

An Exploration of Hybrid Photonic-Plasmonic and Topologically-Protected Resonances in Van der Waals Nanostructures on Gold

A thesis submitted in partial fulfilment for the degree of Doctor of Philosophy

By

Sam Anthony Randerson

School of Mathematical and Physical Sciences
Faculty of Science
The University of Sheffield

June 18, 2025

To my late grandads,
Tony Randerson and Barry Fawcett

Acknowledgements

I would like to thank all the people that guided and supported my PhD journey for the last three and a half years, both those directly involved in my field of study, and those outside of academia. Firstly to my supervisor Sasha, thank you for this incredible opportunity to work within a leading group where I have developed significantly from a professional standpoint, but also personally. From suggesting to ideas through to help with publication, you have always been onside to help with any queries or problems that arose. Likewise to Paul, Yadong, and Alex, who always provided patient and constructive feedback on how to be the best scientist possible. Without their expertise on nanophotonics and scattering-type scanning near-field optical microscopy, this journey would have taken much much longer. To Xuerong, a huge thank you for the immense effort you put into the fabrication of samples not just for myself, but for the whole group. You never fail to deliver even the most painstakingly difficult structures, and without your knowledge I could not have produced the results presented in this thesis. Specifically, I would like to acknowledge Xuerong and Christina (from the University of York) for their contributions towards electron beam lithography and reactive ion etching of the nanostructures covered in this thesis. To Oscar P., thank you for the dedication you showed to the gratings project, taking countless measurements and performing a range of simulations to keep the project on track. I wish you the best of luck with continuing your PhD. Not involved directly in my research but equally important, I would like to thank Dan, Zara, Tim, Charalambos, Anthonin, and Owen, for always being supportive and helping to ease the stresses of PhD with insightful and fun conversations at lunch time. In addition, Oscar H., you gave me consistent support throughout your time in our group, not only in helping me with physics and coding troubles, but also anything that was on my mind outside of work. Your patience and empathy will never be forgotten, thank you.

During my time on this PhD, I also supervised several undergraduate, master's, and placement students. I would like to thank them all for their contributions towards understanding the intricacies of WS_2 nanoantennas on gold. Dominic, Sharada, Ye, Elliott, Will, and Stephen, you always put in 100% effort despite your other commitments, and helped me in developing my own understanding of the subject, furthering my professional skills. From The University of Sheffield, I also acknowledge IT Services for the provision of services for High Performance Computing, which I used extensively throughout my work for complex simulations of a variety of nanostructures.

For the people outside of work, I first thank my family for always being beside me throughout this PhD and life in general. To my mum Louise and dad Garry, thank you for raising me to be the person I am today. You have both always encouraged me to do things I did not think were possible, being kind, understanding, and compassionate, and I will always be so grateful. Also to my sister

Mia, brother Ben, and the newest additional our dog Nellie, thank you all for making my home life so enjoyable and a place to relax and unwind. I would also like to thank my extended family, including both my nanans, Margaret and Janet. You are always happy to chat about what I have been up to and encourage me to be my best self. To my late grandads Barry and Tony, you were always supportive of my decisions and physics journey, and were role models for me to look up to. I only wish I could share this moment of PhD submission with you both. As a child Tony built me a working wooden trebuchet, and Barry was always happy to let me control his extensive model railway, fond memories which I hold dearly to this day, and what I believe sparked my interests in science.

To all my friends, both those I have known since the start of secondary school, to others I met through university, you never fail to bring a smile to my face and keep my spirits up. Ethan and Nick, I always had a fantastic time living with you both throughout our undergraduate courses, and still continue to be great friends to this day. Thank you for all the fun memories and I hope more are to come. To Anne, thank you for the many great times we've had during our PhDs, from the first Christmas meal, to holidays around the UK. You've always been there to chat or hang out and I am grateful for our friendship. Finally to Beck, you have been incredibly strong, supportive, and understanding throughout life, always there to give thoughtful advice for which I am eternally grateful, thank you. I dearly appreciate all those who surround me and I am excited to see what the future holds for us all.

Abstract

Recently, there has been significant movement towards photonic computing chips, offering lower losses, and additional functionality over conventional electronic systems. Layered van der Waals materials are emerging as ideal candidates for nanophotonics, with interlayer adhesive forces that facilitate simple fabrication of multi-layer heterostructures and devices, without the need for lattice matching. Furthermore, transition metal dichalcogenides in particular offer higher refractive indices than silicon and III-V materials, as well as efficient direct band gap emission in the monolayer limit.

Here, I simulate, fabricate, and optically characterise WS_2-based nanostructures to investigate their exotic resonance behaviours. WS_2 nanoantennas on gold are shown to host hybrid Mie-plasmonic modes, with higher quality factors than purely dielectric systems. Via tuning of geometrical parameters, strong mode coupling is observed, resulting in a highly confined supercavity mode with an experimental quality factor of over 260. In simulation, a WS_2 nanoantenna atop a few-layer hBN spacer on gold is characterised, yielding strong Purcell enhancement of coupled single photon emitters, directivity tailoring, and an overall emission enhancement of over 10^7 times stronger than the same emitter in vacuum. WS_2 gratings on gold are further investigated experimentally, where placing structures with opposite topologies together produces a robust Jackiw-Rebbi edge state. This topologically-protected state is highly localised in energy and wave vector space, with a respective 6 meV linewidth and 7° angular emission bandwidth. An active grating heterostructure incorporating an hBN-encapsulated monolayer WSe_2 is further fabricated, exhibiting directional coupling of the photoluminescence to the edge state, with an enhancement of 16 times compared to uncoupled monolayer. Scattering-type scanning near-field optical microscopy measurements of both the Mie-plasmonic modes and Jackiw-Rebbi edge states are finally presented, providing insight into the near-field properties of such resonances.

These results highlight applications of van der Waals nanophotonics in controllable quantum light emission, robust unidirectional waveguiding, lasing, sensing, and more, with easy integration into a range of other material systems.

List of Publications

- **Sam A. Randerson**, Paul Bouteyre, Xuerong Hu, Oscar J. Palma-Chaundler, Alexander J. Knight, Helgi Sigurðsson, Casey K. Cheung, Yue Wang, Kenji Watanabe, Takashi Taniguchi, Roman Gorbachev, Alexander I. Tartakovskii

  "Topological Jackiw-Rebbi States in Photonic Van der Waals Heterostructures"

  arXiv preprint, arXiv:2506.03985, (2025)

- **Sam A. Randerson**, Panaiot G. Zotev, Xuerong Hu, Alexander J. Knight, Yadong Wang, Sharada Nagarkar, Dominic Hensman, Yue Wang, Alexander I. Tartakovskii

  "High Q Hybrid Mie–Plasmonic Resonances in Van der Waals Nanoantennas on Gold Substrate"

  ACS Nano, **18**(25):16208–16221, (2024)

- Panaiot G. Zotev, Paul Bouteyre, Yadong Wang, **Sam A. Randerson**, Xuerong Hu, Luca Sortino, Timur Shegai, Su-Hyun Gong, Andreas Tittl, Igor Aharonovich, Alexander I. Tartakovskii

  "Nanophotonics with Multilayer Van der Waals Materials"

  Nature Photonics - Accepted for Submission

- Yadong Wang, Charalambos Louca, **Sam A. Randerson**, Xuerong Hu, Panaiot G. Zotev, Oscar Palma-Chaundler, Paul Bouteyre, Casey K. Cheung, Roman Gorbachev, Yue Wang, Alexander I. Tartakovskii

  "Exciton-Polaritons in a Monolayer Semiconductor Coupled to Van der Waals Dielectric Nanoantennas on a Metallic Mirror"

  arXiv preprint, arXiv:2506.04979, (2025)

- Paul Bouteyre, Xuerong Hu, **Sam A. Randerson**, Panaiot G. Zotev, Yue Wang, Alexander I. Tartakovskii

  "Simultaneous Observation of Bright and Dark Polariton States in Subwavelength Gratings made from Quasi-Bulk WS_2"

  Optics Express, **33**(10):21173–21182, (2025)

- Panaiot G. Zotev, **Sam A. Randerson**, Xuerong Hu, Yue Wang, Alexander I. Tartakovskii

  "Single Photon Emitters in Monolayer Semiconductors Coupled to Transition Metal Dichalcogenide Nanoantennas on Silica and Gold Substrates"

  arXiv preprint, arXiv:2408.01070, (2024)

- Armando Genco, Charalambos Louca, Cristina Cruciano, Kok Wee Song, Chiara Trovatello, Giuseppe Di Blasio, Giacomo Sansone, **Sam A. Randerson**, Peter Claronino, Rahul Jayaprakash, Kenji Watanabe, Takashi Taniguchi, David G. Lidzey, Oleksandr Kyriienko, Stefano Dal Conte, Alexander I. Tartakovskii, Giulio Cerullo

  "Femtosecond Switching of Strong Light-Matter Interactions in Microcavities with Two-Dimensional Semiconductors"

  arXiv preprint, arXiv:2408.00111, (2024)

- Abimbola Feyisara Adedeji-Olulana, Katarzyna Wacnik, Lucia Lafage, Laia Pasquina-Lemonche, Mariana Tinajero-Trejo, Joshua A. F. Sutton, Bohdan Bilyk, Sophie E. Irving, Callum J. Portman Ross, Oliver J. Meacock, **Sam A. Randerson**, Ewan Beattie, David S. Owen, James Florence, William M. Durham, David P. Hornby, Rebecca M. Corrigan, Jeffrey Green, Jamie K. Hobbs, Simon J. Foster

  "Two Codependent Routes Lead to High-Level MRSA"

  Science, **386**(6721):573–580, (2024)

- Panaiot G. Zotev, Yue Wang, Daniel Andres-Penares, Toby Severs-Millard, **Sam A. Randerson**, Xuerong Hu, Luca Sortino, Charalambos Louca, Mauro Brotons-Gisbert, Tahiyat Huq, Stefano Vezzoli, Riccardo Sapienza, Thomas F. Krauss, Brian D. Gerardot, Alexander I. Tartakovskii

  "Van der Waals Materials for Applications in Nanophotonics"

  Laser & Photonics Reviews, **17**(8):2200957, (2023)

- Charalambos Louca, Armando Genco, Salvatore Chiavazzo, Thomas P. Lyons, **Sam A. Randerson**, Chiara Trovatello, Peter Claronino, Rahul Jayaprakash, Xuerong Hu, James Howarth, Kenji Watanabe, Takashi Taniguchi, Stefano Dal Conte, Roman Gorbachev, David G. Lidzey, Giulio Cerullo, Oleksandr Kyriienko, Alexander I. Tartakovskii

  "Interspecies Exciton Interactions Lead to Enhanced Nonlinearity of Dipolar Excitons and Polaritons in MoS_2 Homobilayers"

  Nature Communications, **14**(1):3818, (2023)

- Toby Severs Millard, Armando Genco, Evgeny M. Alexeev, **Sam A. Randerson**, Seongjoon Ahn, A-Rang Jang, Hyeon Suk Shin, Alexander I. Tartakovskii

  "Large Area Chemical Vapour Deposition Grown Transition Metal Dichalcogenide Monolayers Automatically Characterized through Photoluminescence Imaging"

  npj 2D Materials and Applications, **4**(1):12, (2020)

List of Conference Presentations

- **Nanophotonics Winter School**, Sheffield, (Jan 2025)

  "Topological Edge States in 1D WS_2 Grating Heterostructures and Photoluminescence Enhancement"

  Poster Presentation

- **Graphene Week**, Prague, (Oct 2024)

  "Topological Edge States in 1D WS_2 Grating Heterostructures and Photoluminescence Enhancement"

  Poster Presentation

- **Workshop on Near-field Optical Imaging and Spectroscopy**, Sheffield, (Sep 2024)

  "Probing Topological Edge States in 1D WS_2 Gratings through Scattering SNOM"

  Poster Presentation

- **Nanophotonics Winter School**, Sheffield, (Jan 2024)

  "Van der Waals Nanoantennas on Gold for Hosting High Q Factor Hybrid Mie-Plasmonic Resonances"

  Poster Presentation

- **Materials for Quantum Network**, Cambridge, (Nov 2023)

  "High Q Hybrid Mie-Plasmonic Resonances in Van der Waals Nanoantennas on Gold Substrate"

  Poster Presentation

- **UK Semiconductors**, Sheffield, (Jul 2023)

  "High Q Hybrid Mie-Plasmonic Resonances in Van der Waals Nanoantennas on Gold Substrate"

  Oral Presentation

- **Nanophotonics of 2D Materials**, San Sebsatián, (Jun 2023)

  "High Q Hybrid Mie-Plasmonic Resonances in Van der Waals Nanoantennas on Gold Substrate"

  Poster Presentation

- **Graphene Week**, Munich, (Sep 2022)

  "Strong Directionality Enhancement using WS_2 Nanoantennas on Gold"

  Oral Presentation

- **UK Semiconductors**, Sheffield, (Jul 2022)

  "Strong Directionality Enhancement using WS_2 Nanoantennas on Gold"

  Oral Presentation

- **Graphene**, Aachen, (Jul 2022)

  "Strong Directionality Enhancement using WS_2 Nanoantennas on Gold"

  Poster Presentation

- **QUANTUMatter**, Barcelona, (Jun 2022)

  "Strong Directionality Enhancement using WS_2 Nanoantennas on Gold"

  Oral Presentation

Declaration

I hereby declare that the contents of this thesis are original and my own work, except where specific reference to literature has been made, or where collaborative work is clearly stated in the main text and Acknowledgements section. I confirm that I am aware of The University of Sheffield's guidance on the use of unfair means, and that none of this work has been submitted in whole, or in part towards another degree at this, or any other institution.

Sam Anthony Randerson
June 18, 2025

Table of Contents

Dedication ii

Acknowledgements iii

Abstract v

List of Publications vi

List of Conference Presentations viii

Declaration x

Table of Contents xi

List of Figures xiv

1 Introduction 1

1.1 Context of Research . . . 1

1.2 Scope of Thesis . . . 2

2 Theoretical Background 7

2.1 Introduction . . . 7

2.2 2D Materials Overview . . . 9

2.3 Optoelectronic Properties of Transition Metal Dichalcogenides . . . 10

2.3.1 Crystal Structure . . . 10

2.3.2 Band Gap Transition . . . 11

2.3.3 Excitonic Properties . . . 13

2.3.4 Optical Properties . . . 14

2.4 Nanophotonics in 0D Structures . . . 15

2.4.1 Electromagnetic Waves in a Medium . . . 17

2.4.2 Mie Resonances . . . 18

2.4.3 Optical Anapoles . . . 21

2.4.4 Fabry–Perot Modes . . . 24

2.4.5 Polaritons . . . 25

2.4.6 Friedrich-Wintgen Bound States in the Continuum . . . 27

2.4.7 Purcell Enhancement . . . 29
2.4.8 Plasmonics . . . 31
2.5 Nanophotonics in 1D Periodic Structures . . . 35
2.5.1 Waveguide Modes . . . 35
2.5.2 Grating Modes . . . 36
2.5.3 Diffractive Coupling . . . 38
2.6 Topological Photonics in 1D Periodic Structures . . . 39
2.6.1 Introduction to Topology . . . 39
2.6.2 Topological Insulators . . . 40
2.6.3 Topological Photonics . . . 44
2.6.4 Symmetry-Protected Bound States in the Continuum . . . 44
2.6.5 Jackiw-Rebbi Edge States . . . 47
2.7 Simulation Techniques . . . 49
2.7.1 Finite-Difference Time-Domain . . . 49
2.7.2 Rigorous Coupled-Wave Analysis . . . 51

3 Methods **52**
3.1 Introduction . . . 52
3.2 Fabrication . . . 53
3.2.1 Substrate Preparation . . . 53
3.2.2 Mechanical Exfoliation of van der Waals Materials . . . 54
3.2.3 Flake Searching . . . 57
3.2.4 Electron Beam Lithography Patterning . . . 57
3.2.5 Reactive Ion Etching . . . 59
3.2.6 Flake Transfer . . . 60
3.3 FDTD Simulations . . . 63
3.3.1 Scattering Spectra . . . 63
3.3.2 Near-Field Distributions . . . 64
3.3.3 Purcell Factor and Radiative Rate Enhancement . . . 65
3.3.4 Directivity . . . 66
3.3.5 Band Structure . . . 66
3.3.6 Angle-Resolved Reflectance Contrast . . . 67
3.4 RCWA Simulations . . . 68
3.4.1 Angle-Resolved Reflectance Contrast . . . 69
3.4.2 Near-Field Distributions . . . 69
3.5 Far-Field Spectroscopy . . . 69
3.5.1 Dark Field . . . 70
3.5.2 Angle-Resolved Reflectance Contrast . . . 71
3.5.3 Angle-Resolved Photoluminescence . . . 72
3.6 Near-Field Spectroscopy . . . 73
3.6.1 Scattering-Type Scanning Near-Field Optical Microscopy . . . 73

4 Hybrid Mie-Plasmonic Resonances in WS_2 Nanoantennas on Gold **76**
4.1 Introduction . . . 76
4.2 Simulations of WS_2 Nanoantenna Resonances . . . 78
4.2.1 Multipole Expansion of Mie Resonances in Suspended Nanoantennas . . . 78
4.2.2 Electric Field Distributions in Suspended WS_2 Nanoantennas . . . 80
4.2.3 Introducing the Gold Substrate . . . 81
4.2.4 Electric Field Distributions in WS_2 Nanoantennas on Gold . . . 85
4.2.5 Scattering Radius Dependence for Different Substrates . . . 86
4.3 Experimental Characterisation of WS_2 Nanoantennas on Gold . . . 87
4.3.1 Fabrication of Nanoantennas on Gold . . . 88
4.3.2 Dark Field Scattering Spectra . . . 88
4.3.3 Strong Coupling and Supercavity Mode . . . 93
4.4 Mie-Plasmonic Resonances for Emitter Enhancement . . . 97
4.5 Conclusion . . . 100

5 Topological Edge States in 1D WS_2 Double Gratings **102**
5.1 Introduction . . . 102
5.2 WS_2 Inverted Gratings on Gold . . . 104
5.2.1 Choice of Substrate . . . 104
5.2.2 Grating Parameter Tuning . . . 107
5.2.3 Photonic Band Inversion . . . 109
5.3 WS_2 Double Inverted Gratings for Edge States . . . 111
5.3.1 Fabrication of Double Inverted Gratings . . . 112
5.3.2 Jackiw-Rebbi Edge States . . . 114
5.3.3 Electric Field Simulations . . . 117
5.4 Active WSe_2 Monolayer-Coupled Double Grating Heterostructure . . . 119
5.4.1 Photoluminescence Enhancement Simulations . . . 120
5.4.2 Fabrication of Double Grating Heterostructure . . . 123
5.4.3 Fourier Photoluminescence . . . 126
5.5 Conclusion . . . 129

6 Near-Field Imaging of WS_2 Nanophotonic Structures **133**
6.1 Introduction . . . 133
6.2 Near-Field Imaging of WS_2 Nanoantennas on Gold . . . 135
6.3 Near-Field Imaging of Jackiw-Rebbi Edge States in WS_2 Gratings on Gold . . . 138
6.4 Conclusion . . . 142

7 Conclusion **144**
7.1 Summary of Research . . . 144
7.2 Future Perspective . . . 149

References **151**

List of Figures

2.1 Plots of the electronic density of states for different dimensionalities of semiconductors . . . 9
2.2 Atomic structure of TMD layers . . . 11
2.3 Stacking configurations of TMD layers . . . 12
2.4 Indirect to direct band gap transition of MoS_2 . . . 13
2.5 Effect of dielectric screening on intra-layer excitons . . . 14
2.6 Electronic band structures for different monolayer TMDs including spin-orbit coupling effects and spin-valley locking . . . 15
2.7 Complex refractive indices for the in- and out-of-plane directions of common TMDs 16
2.8 Vector plots of the Mie solutions to Maxwell's equations on the surface of a metallic nanosphere . . . 19
2.9 Calculated multipole expansion of electric and magnetic fields from nanospheres of different materials compared to analytical Mie solutions . . . 21
2.10 Depiction of the near-field composition of an optical anapole . . . 23
2.11 Multipole expansion of the near-fields from a silicon nanodisk in the long-wavelength approximation showing existence of an anapole . . . 24
2.12 Schematics of different types of photonic resonances in a cylindrical dielectric nanoantenna . . . 26
2.13 Schematic of the available resonances of a typical quantum system . . . 28
2.14 Properties of different plasmon-polaritons in metals . . . 33
2.15 Visualisation of photonic waveguide modes . . . 36
2.16 Visualisation of photonic grating modes . . . 37
2.17 Mode dispersion of gratings including radiative losses . . . 39
2.18 Schematic of various basic topological geometries along with everyday objects with the same corresponding topological invariant g . . . 40
2.19 Comparison of topological and trivial insulators . . . 42
2.20 Visualisation of electric field profiles associated with symmetry-protected BIC and corresponding lossy grating mode . . . 45
2.21 Far-field polarisation vortex associated with BICs in k-space . . . 47
2.22 Simulated reflectance contrast showing formation of a photonic Jackiw-Rebbi edge state . . . 48

2.23 Representation of electromagnetic field vector components on a Yee cell in FDTD simulations . . . 50

3.1 Schematic of exfoliation methods on three different substrates . . . 55
3.2 Microscope images of exfoliated van der Waals materials on different substrates . . . 58
3.3 Schematic of TMD nanostructure fabrication process . . . 59
3.4 Illustration of PDMS stamp and PMMA membrane transfer methods . . . 61
3.5 FDTD simulation setup for calculation of scattering spectra and electric field distributions in WS_2 nanoantennas on gold . . . 64
3.6 FDTD simulation setup for calculation of Purcell factor and directivity of a dipole within WS_2 nanostructures on gold . . . 65
3.7 FDTD simulation setup for angle-resolved reflectance contrast from WS_2 double grating structures . . . 68
3.8 Schematic of home-built dark field spectroscopy setup . . . 70
3.9 Schematic of home-built Fourier spectroscopy setup . . . 72
3.10 Schematic of commercial neaspec s-SNOM setup . . . 74

4.1 Rigorous multipole expansion of Mie modes within WS_2 hexagonal nanoantennas suspended in vacuum . . . 80
4.2 Simulated electric field intensity within a WS_2 nanoantenna of height 78 nm and radius 290 nm in vacuum for different resonances . . . 81
4.3 WS_2 nanoantennas from vacuum to gold simulations . . . 83
4.4 Simulated scattering spectra with changing distance between a WS_2 nanoantenna and gold substrate s . . . 84
4.5 Simulated electric field intensity within a WS_2 nanoantenna of height 78 nm and radius 290 nm on gold for different resonances . . . 86
4.6 Simulated normalised scattering intensity of WS_2 hexagonal nanoantennas of height 78 nm with varying radii compared with different substrates . . . 87
4.7 Optical far-field characterisation of WS_2 nanoantennas on gold . . . 89
4.8 Comparison of Fabry–Perot mode theory with FDTD simulations of high index hexagonal monomers with varying height on a gold substrate . . . 91
4.9 Simulated electric field intensity within a WS_2 nanoantenna of height 180 nm and radius 250 nm on a gold substrate for different hybrid resonances . . . 92
4.10 Coupled oscillator model fit to experimental FPP mode and HOAP scattering spectra from WS_2 nanoantennas on a gold substrate . . . 94
4.11 Supercavity mode characterisation for WS_2 dimer nanoantennas on a gold substrate in simulation . . . 96
4.12 Simulated electric field and light extraction enhancement throughout an hBN layer between a WS_2 nanoantenna and gold substrate . . . 98

5.1 Simulated band structure and reflectance of a WS_2 grating on silica and gold substrates . . . 106

5.2 Simulated reflectance contrast of a WS_2 grating on gold upon varying geometrical parameters . . . 108
5.3 Simulated photonic band inversion via a WS_2 grating on gold with a WS_2 slab placed on top . . . 110
5.4 Fabricated gratings parameter check and top flake thickness calibration . . . 113
5.5 Experimental normalised angle-resolved reflectance contrast of WS_2 double inverted gratings on gold substrate showing Jackiw-Rebbi edge state . . . 116
5.6 Simulated electric field distributions within WS_2 single and double inverted gratings on gold for different photonic modes . . . 119
5.7 Simulations of an active WSe_2 monolayer-integrated double grating heterostructure 122
5.8 Images of grating heterostructure fabrication after transfer of encapsulated monolayer WSe_2 . . . 125
5.9 Experimental angle-resolved characterisation of active WSe_2-coupled double grating heterostructure . . . 127

6.1 Experimental near-field characterisation of SPPs launched from WS_2 nanoantennas on gold . . . 136
6.2 AFM and s-SNOM images of a bare gold substrate and low index pillars on a gold substrate at 785 nm excitation . . . 138
6.3 Near-field characterisation of a topological Jackiw-Rebbi edge state in WS_2 double inverted gratings on gold . . . 140

1

Introduction

1.1 Context of Research

The rich world of two-dimensional materials first came to discovery in 2004, with the isolation of single-layer graphene by Konstantin Novoselov and Andre Geim [1] in Manchester, UK. Soon after, additional layered materials such as boron nitride and transition metal dichalcogenides (TMDs) were also cleaved to the monolayer limit, showing remarkable stability at room temperatures [2]. These two seminal works kick-started the field of van der Waals materials research, unveiling the diverse and unique properties that arise from confining materials to the 2D plane. Not only this, but by stacking different 2D materials together through their inherent interlayer attractive forces, near limitless combinations can be fabricated. This enables simple realisation of complex heterostructures and devices with vastly different properties, from superconductors [3] to insulators [4]; semiconductors to semimetals [5]; as well as ferro- and piezoelectrics [6], and more.

Less studied however, is the use of van der Waals materials in multi-layer form for nanophotonic applications. Before delving into this niche, it is important to mention a brief background of the field. Conventional nanophotonics heavily relies on silicon-based components, used to manipulate the propagation, polarisation, frequency, and phase of photons on micro- to nanoscale chips [7]. Silicon has been extremely well studied, boasting lower losses than electronic signal processing used in traditional computing [8], with the ability for wavelength and polarisation multiplexing [9, 10] for greater computational bandwidth. Optical components such as waveguides [11], modulators [12], couplers [13, 14], and detectors [15, 16] can all be made purely from silicon, with cheap material costs and reliable fabrication methods [17]. Silicon photonics is therefore a very versatile platform for all-photonic information processing and quantum technologies [18], but can also be combined with electronic components owing to CMOS compatibility [19]. Van der Waals materials offer nearly all the advantages of silicon photonics [20, 21], with a much broader choice

of intrinsic material parameters, and the ability to stack an arbitrary number of layers onto nearly any substrate or device, thus unlocking the third dimension for nanophotonic structure design. This avoids difficulties associated with III-V materials such as GaAs and AlGaAs, where precise lattice matching [22] and expensive molecular beam epitaxy methods are required to achieve stacked layers with atomically flat interfaces [23]. Using van der Waals materials, one can envisage fabricating an entire quantum chip, consisting of, for example, strained TMD monolayers as deterministic, high single photon purity sources [24, 25], coupled to high refractive index multi-layer waveguides [26, 27], followed by an operation such as signal modulation [28] or use of logic gates via van der Waals heterostructures [29], and finally measurement via a monolayer TMD photodetector component [30–32].

One of the major recent breakthroughs in photonics is the branch of topological photonics, first proposed theoretically in 2008 [33, 34] as a photonic analogue to the quantum Hall conducting edge state in topological insulators [35]. A year later, this phenomenon was observed experimentally in a two dimensional photonic crystal, hosting topologically-protected edge states with inherent immunity to back-reflection [36]. Another advantage of topological states is their intrinsic robustness to defects [37–39]. This occurs due to integer global characteristics of the photonic bands known as topological invariants, as discussed in more depth in this thesis, which can only be changed via large structural changes [40, 41]. It is therefore evident that topologically-protected photonic systems provide a huge leap forward compared to conventional photonics, with the possibility for near lossless, unidirectional waveguiding [42, 43], combined with unparalleled robustness to fabrication imperfections, for advanced control of light at the nanoscale.

1.2 Scope of Thesis

For the work presented in this thesis, I focus primarily on investigating TMD-based nanostructures to explore their exotic resonance phenomena for use in nanophotonics. I thoroughly simulate, fabricate, and optically characterise WS_2 nanoantennas and grating structures on gold, characterising hybridised Mie-plasmonic supercavity modes, and topologically-protected photonic Jackiw-Rebbi edge states respectively. I play to the strengths of TMDs, which exhibit higher refractive indices than silicon, thus enabling deeper sub-wavelength light confinement and manipulation. Furthermore, using their inherent van der Waals attractive forces, I build complex heterostructures using simple transfer techniques, otherwise not possible, or requiring significant fabrication effort with conventional dielectrics like Si and GaAs.

I begin in Chapter 2, by outlining the atomic theory behind TMDs themselves, commenting on their trigonal prismatic crystal structure, and how this impacts their excitonic properties. I also provide refractive indices of different tungsten and molybdenum-based TMDs, followed by a thorough mathematical overview of different resonances able to be hosted within sub-wavelength-sized devices. Fundamental Mie theory will be explained for electromagnetic waves on the surface of a conducting nanosphere, as well as the identification process for optical anapoles, which cause far-field suppression of scattered light. More complex interactions and resonances will then be introduced, including polaritons and optically invisible Friedrich-Wintgen bound states in the

continuum (BIC), before detailing how the discussed modes can lead to a spontaneous emission enhancement of coupled emitters, referred to as the Purcell effect. To complement the purely dielectric resonances, I will then describe the interaction of light with bulk and surface plasmons, resulting in surface plasmon-polaritons. Following the overview of resonances in finite-sized structures, the propagation of light within infinitely repeating, periodic structures such as one dimensional gratings will be explored theoretically. Starting from simple slab waveguide modes, a system Hamiltonian will be built to include photonic band folding and diffractive coupling, thus predicting anti-crossed grating modes in energy and wave vector space, containing symmetry-protected BICs. Such states have topologically protected properties, meaning high robustness to device imperfections. To provide the necessary understanding behind this phenomena, I first introduce topology in a geometry sense, with clear visual aids depicting topological invariants such as the number of holes (genus) of an object. This foundation is built on to explain the discovery of topologically insulating materials, where highly robust conducting edge states form between topological and trivial insulators. Analogies to photonic crystal band structures can then be made, through which I detail the formation of topologically-protected photonic Jackiw-Rebbi edge states, existing along the boundary between devices with BICs characterised by different topological invariants. To finish the theory chapter, I discuss the principles behind two simulation techniques used throughout this thesis, finite-difference time-domain (FDTD), and rigorous coupled-wave analysis (RCWA).

Following the theoretical background, I describe the fabrication, simulation, and experimental methods in Chapter 3. I first detail how to prepare the gold substrates via two methods, electron beam evaporation and template stripping, followed by three mechanical exfoliation techniques to achieve WS_2 on gold, hBN on PMMA, and WSe_2 on PDMS. Electron beam lithography patterning and reactive ion etching recipes are then reported for precise imprinting of designs onto the exfoliated flakes to form nanoantennas and gratings. Utilising the inherent van der Waals interlayer forces of TMDs, I explain two flake transfer methods used to fabricate grating heterostructures, one via a suspended PMMA membrane, and the other using a PDMS stamp on a glass slide. I then detail the FDTD simulation methods used to model the WS_2 nanoantennas on gold, obtaining scattering spectra to identify constituent resonances, followed by calculations of electric field profiles associated with each. By changing the simulation light source to a point dipole emitter, the Purcell factor and corresponding directivity can also be extracted. For the WS_2 gratings, I describe the setup used for simulating the photonic band structure and reflectance contrast throughout wave vector space in FDTD as well as with RCWA. Subsequent to the simulation methods, I then outline the experimental characterisation methods, providing schematics of each setup for reference. I first detail the principles of dark field spectroscopy, used to obtain far-field scattering spectra of nanoantennas on gold, followed by Fourier reflectance contrast and photoluminescence for angle resolved measurements of fabricated gratings. Finally, the near-field probing technique, scattering-type scanning near-field optical microscopy (s-SNOM) will be explained, along with an overview of the pseudoheterodyne detection regime used to isolate the desired signal from the significant background.

Starting in Chapter 4, I present, analyse, and discuss the results of my investigations into the resonant behaviour of WS_2 nanoantennas on a gold substrate. I first provide an overview of histor-

ical and more recent works in the field of photonic and plasmonic nanoresonators, highlighting the relative lack of hybrid devices and potential advantages of such, especially incorporating TMDs with metals. To fully understand the effect of using a metallic substrate, I begin by simulating WS_2 nanoantennas suspended in vacuum, using a rigorous multipole expansion technique to identify all of the constituent Mie resonances, and anapole conditions within nanoantennas of different height and radius. I then gradually introduce a gold substrate in simulation, plotting the respective scattering spectra to clearly visualise the change in mode structure between the all-dielectric, and hybrid dielectric-metallic regime. Increased quality factor of the Mie modes is observed, but more importantly, additional Fano-shaped modes appear when the nanoantennas are ~ 5 nm from the gold substrate. Via simulation of the electric field distributions of each mode, the Fano-shaped peaks are identified as hybrid Mie-plasmonic (MP) resonances, with order of magnitude stronger field confinement than Mie modes alone. I then investigate the behaviour of each resonance under tuning of the nanoantenna radius in simulation, with comparison to nanoantennas on SiO_2 and vacuum substrates to confirm that the MP mode does not exist in purely dielectric systems. Through experimental dark field spectroscopy measurements, I observe excellent agreement with all the modes seen in simulation over a range of nanoantenna radii and heights, with the MP mode yielding a 33 times larger quality factor than for non-hybrid Mie modes in WS_2 nanoantennas on SiO_2. For nanoantennas on gold with larger heights of 180 nm, Fabry–Perot and hybridised Fabry–Perot-plasmonic modes are also identified in the experimental and simulated scattering spectra, via comparison to theory and simulated electric field distributions. By then tuning the Fabry–Perot-plasmonic mode into resonance with a higher-order anapole condition, a distinct anti-crossing of the two spectral features occurs, exhibiting strong coupling with a Rabi splitting of 48 ± 5 meV. This combined with a sharp increase in quality factor up to 263 ± 28 at the point of minimum energy splitting, along with suppression of the mode amplitude, give indication of the presence of a highly confined supercavity mode in experiment. To finish the chapter, I perform simulations of a WS_2 nanoantenna on a 5 nm hBN spacer on gold, as a potential application of the hybrid Mie-plasmonic mode for emission enhancement of coupled single photon emitters. By modelling a dipole emitter within the hBN, I calculate a maximum Purcell factor of over 700, and a vertical directivity of $\sim 50\%$ for the MP mode, with electric field confinement of over 2600. These factors combined yield an overall emission enhancement of 10^7 times that of the same emitter in vacuum, indicating strong potential for use within low quantum yield systems, where the rate of single photon emission needs to be increased to a usable level, e.g. for computing, whilst also boasting directional control.

Following the work on WS_2 nanoantennas, Chapter 5 explores photonic and topological effects in WS_2 gratings, and grating heterostructures on gold. The motivation behind using a gold substrate over dielectrics such as SiO_2 is first discussed, with corresponding simulations of the photonic band structure and reflectance contrast of WS_2 gratings on each. Next, the impact of varying grating structural parameters such as the thickness, period, and filling factor is simulated using RCWA, highlighting the difficulty in complete band gap engineering. This problem is solved via the addition of a WS_2 slab on top of the gratings, thus reducing the effective refractive index contrast between the high and low index sections of the grating. The effect is to decrease the size of the band gap through altering the coupling between forwards and backwards grating modes, therefore

allowing the band gap to be closed and reopened via tuning of the filling factor. This photonic band inversion fundamentally changes the topology of the associated bands, which is observed via the formation of a topologically protected edge state at the centre of the band gap, when gratings with BICs on different energy branches are placed adjacent to one another. Such double inverted WS_2 gratings on gold are then fabricated via standard nanopatterning and etching techniques, followed by PMMA transfer of the top WS_2 slab, showing excellent agreement with theory and simulation. This is one of the first experimental realisations of the topologically-protected photonic Jackiw-Rebbi edge state in 1D gratings, exhibiting strong energy confinement with a mode linewidth of 6 meV, as well as highly directional emission with a 7° angular bandwidth perpendicular to the grating axis. The full modal dispersion in wave vector space was subsequently mapped in experiment, where the edge state extended throughout the full range of measured angles ($\pm 44°$) in the direction parallel to the grating axis, with a parabolic energy shift. In simulation, the electric field distributions of each mode are presented, highlighting the symmetric and anti-symmetric nature of the lossy mode and BIC about the grating unit cell respectively, leading to coupling or non-coupling to the radiative continuum. The near-field of the Jackiw-Rebbi edge state shows strong localisation to the boundary between the adjacent gratings in real space, with a calculated spatial confinement of 1.45 μm. By incorporating an hBN-encapsulated monolayer WSe_2 between the WS_2 grating and top slab, I simulated the directivity and emission enhancement of photoluminescence emission from the monolayer coupled to the edge state, exhibiting a potential increase of over 1000 compared to monolayer alone. The five-layer grating heterostructure was subsequently fabricated via multiple transfers, yielding a Jackiw-Rebbi edge state around the WSe_2 exciton energy of 1.65 eV. Through experimental angle-resolved photoluminescence measurements, coupling of the WSe_2 emission to the individual grating modes was observed, following the dispersion of the modes recorded in reflectance contrast. This resulted in clear enhancement of the photoluminescence compared to uncoupled WSe_2 emission in a reference heterostructure, where no grating modes were present. When measuring the region between the two adjacent gratings, the photoluminescence was increased further, thus indicating coupling to the Jackiw-Rebbi edge state. By integrating over the edge state linewidth in both energy and wave vector, a maximum enhancement of 16 was calculated, compared to emission from encapsulated monolayer WSe_2 uncoupled from the edge state. These results thus highlight the utility of TMD-based grating structures for reliably producing complex heterostructures able to induce a variety of light-matter interactions for on-chip photonic circuitry, with the added robustness of topological protection against device imperfections.

The experimental results are finalised in Chapter 6, where I present near-field scans of the previously studied WS_2 nanoantennas and double inverted gratings on gold measured via s-SNOM. The chapter begins with an overview of the principles of s-SNOM, stating its advantages in beating the diffraction limit compared to conventional far-field spectroscopy techniques. Different probing mechanisms are discussed, highlighting the ability to either map complex refractive indices in the weakly interacting regime, or probe confined electric fields in the strongly interacting regime, both down to $\sim$ 20 nm spatial resolution. Applying this measuring technique to nanoantennas on gold, clear surface plasmon-polariton interference patterns are observed on the substrate sur-

face in both the amplitude and phase scans, forming concentric rings around each nanoantenna. By scanning nanoantennas of different radii or changing the incident wavelength, the response of the interference patterns changes. The relative intensity of the patterns around each nanoantenna strongly correlates to peaks in the respective scattering spectra, as identified in dark field spectroscopy measurements from Chapter 4. Further scans of low index pillars on gold show negligible SPP response, thus indicating that SPPs can only be launched via excitation of confined, hybrid Mie resonances present in high index structures. I then switch to measuring the WS_2 double inverted gratings on gold via s-SNOM, with precise orientation of the incident light along the grating axis. By scanning at 736 nm wavelength, i.e. the Jackiw-Rebbi edge state energy extrapolated to $\sim 60°$ incident angle, clear increased scattering from the boundary between the adjacent gratings was observed. Multiple wavelengths are then scanned showing a suppression in signal, thus proving that the boundary-localised scattering can be attributed to direct probing of the Jackiw-Rebbi edge state. The results agree well with electric field profile simulations at the tip position, providing experimental evidence of the highly spatially confined nature of the topologically-protected Jackiw-Rebbi edge state. The s-SNOM results from this chapter therefore accompany Chapters 4 and 5, providing a full characterisation of photonic, plasmonic, and topological resonances in van der Waals nanostructures on gold in both the near- and far-field.

To conclude, I summarise the work of this thesis in Chapter 7, emphasising the key results. I also discuss the context in terms of using of van der Waals materials in photonic circuits, as a robust and versatile addition to conventional silicon photonics. Finally, I provide a future perspective, suggesting specific ways in which the structures studied in this thesis could be used to further research in the field, for example using nanoantenna metasurfaces for nanoholography, or stacked gratings to achieve macroscopic moiré effects.

2

Theoretical Background

2.1 Introduction

This chapter will focus on providing a strong mathematical and theoretical foundation for understanding the results presented later in Chapters 4, 5, and 6. For each topic or theory, I reference key historical literature marking the lead up to, and fruition of the discovery, followed by more contemporary works that apply the models to experimental systems. To begin, I overview the definition of two dimensional semiconductor materials, comparing their associated density of states with that of other dimensionalities to mark the distinction. I then discuss the optoelectronic properties of the transition metal dichalcogenide family of layered van der Waals materials, first commenting on their atomic structure, and how this impacts the electronic band structure of the crystal. Through consideration of dielectric screening and quantum confinement effects, I explain the transition between an indirect and direct band gap when TMDs are thinned to the monolayer limit. Spin-orbit coupling and spin-valley locking are also detailed, resulting in splitting of the conduction and valence bands, and degeneracy lifting in the Brillouin zone for chiral excitation respectively. To finish this section, I present the complex refractive indices of four different TMDs, depicting their varied optical responses for versatile nanophotonic applications.

To introduce the theory behind photonic resonance phenomena, I start by considering light propagation in a linear dielectric medium, describing how the relative permittivity of the material affects the polarisation of the travelling light, and thus its wave speed. Maxwell's equations are then listed in differential form, governing the complete propagation of electromagnetic waves in a medium, and thus setting the basis for describing a wide variety of photonic resonances. I first provide a theoretical overview of Mie resonances on the surface of a conducting metallic nanosphere through plots of the analytical solutions to Maxwell's equations. For more arbitrary geometries, I present equations defining numerical solutions of the scattering coefficients from each multipolar

contribution, for easy identification of Mie resonances in scattering spectra. Using a long wavelength approximation, the electric dipole mode equation is decomposed into two components, thus allowing the identification of optically dark anapole conditions. I then derive the mathematical description of Fabry–Perot modes, existing as simple standing waves between two reflective surfaces. Interactions of photonic resonances with excitons are then discussed, forming new half-light, half-matter quasiparticles called polaritons, as described by an appropriate strong coupling Hamiltonian. Additional strong hybridisation between two photonic modes are also mathematically defined, resulting in perfectly confined resonances with infinite quality factor known as Friedrich-Wintgen bound states in the continuum (BICs). Moving to the weak coupling regime, I then outline the theory behind the Purcell effect, introducing two different definitions that describe the spontaneous emission enhancement of emitters within modified local photonic environments. This section is finished by a thorough review of plasmonic resonances, detailing the behaviour of electrons in metallic materials through the historical Drude model. Then, via solving Maxwell's equations using the Drude model permittivity, localised light-matter quasiparticles known as surface-plasmon polaritons emerge, with distinct dispersions in wave vector space.

Adding to the library of nanophotonic resonances, I next consider eigenmodes of infinitely extending waveguides and periodic grating structures. The dispersions of counter-propagating forwards and backwards modes in high index waveguide slabs are first derived, bound to the structure via total internal reflection. Adding to the model, a modulation of the refractive index is then introduced, thus leading to folding of the photonic bands into the first Brillouin zone. By building a system Hamiltonian, strong coupling between the forwards and backwards modes is visualised via solving the matrix eigenvalue problem. Further inclusion of losses into the system leads to the formation of a lossless symmetry-protected BIC on the lower energy branch at zero wave vector, and a corresponding broad linewidth mode on the upper energy branch that takes all the losses. Topological effects are then discussed, by first introducing the topology of two dimensional manifolds and everyday objects for visual reference. Following this, I detail the history of the discovery of topological insulators, starting from the observation of edge-localised electron motion via the quantum Hall effect. To understand this phenomenon, I explain the significance of the Berry curvature of the electronic bands and how to calculate it, before integrating over all energy levels to obtain a topological invariant known as the Chern number. By combining systems with different integer Chern numbers, I describe how the electronic band gap must close and reopen to change the topology of the bands, thus resulting in topologically-protected, highly localised edge states. I then outline the subsequent array of research into topological photonics, as an optical analogue to topological insulators. The inherent topological properties of BICs are also explored, with an equivalent topological invariant to the Chern number calculated as the winding number of the associated polarisation of the state around a vortex in wave vector space. As with topological insulators, I explain how combining systems with BICs of different topologies leads to the formation of a robust edge-localised state, referred to in literature as a Jackiw-Rebbi edge state.

To finish this theoretical chapter, I describe the working principles the finite-difference time-domain, and rigorous coupled-wave analysis simulation approaches, including relevant literature on their initial implementations.

2.2 2D Materials Overview

By definition, two-dimensional (2D) materials are those that are reduced in one dimension to the absolute limit of a single plane with thickness of a single atomic unit cell. One can see, however, that the phrase "2D materials" has become more of an umbrella term for the vast array of semiconductors [44], insulators [45], and more recently even metals [46], which can be thinned down to single layers in practice. Fundamentally, a true atomically thin 2D material experiences a change to its electronic density of states [47] compared to that of the same material in bulk 3D form, owing to restrictions placed on available electronic energy states in wave vector space [48]. Plots of the density of states for 3D semiconductors ranging down to the 0D limit are shown in Figure 2.1.

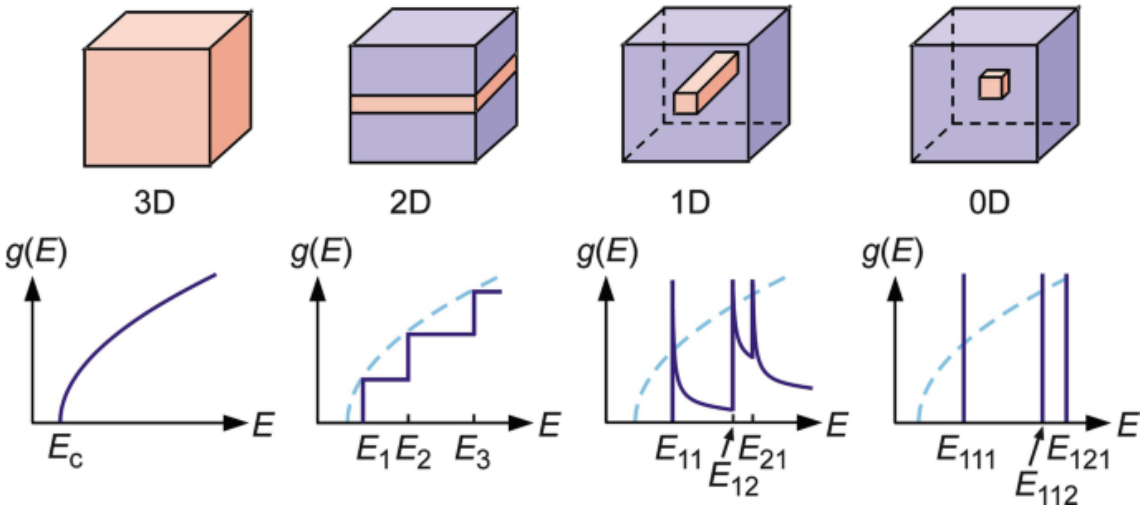


Figure 2.1: **Plots of the electronic density of states for different dimensionalities of semiconductors.** From left to right: 3D bulk material, 2D plane of material, 1D wire of material, 0D dot of material. $g(E)$ is the density of states, E_c is the conduction band edge energy, and E_n represent increasing discretised energy levels where n is a positive integer. Figure used with permission of Springer Nature BV, from Semiconductor Physics, Karl W. Böer and Udo W. Pohl, 1st ed. 2018; permission conveyed through Copyright Clearance Center, Inc.

In 3D, the density of states is proportional to the square root of the energy $E^{1/2}$ [48], where there are very few states available near to the conduction band edge E_c, and further increasing states at higher energies owing to degeneracy. In 2D, however, the density of states does not depend on energy. There are immediately many more available states above the conduction band edge with further discrete energy levels as in the particle-in-a-box model [47]. This step function governs the band-to-band transitions of electrons in the material.

In this thesis I will focus on 2D materials in both their 2D form (monolayer), and as a 3D bulk crystal where many layers are stacked together. More specifically, I consider a family of materials known as transition metal dichalcogenides (TMDs) for which the optoelectronic properties can vary drastically between the 3D and 2D regimes as discussed further below.

2.3 Optoelectronic Properties of Transition Metal Dichalcogenides

In this section, I will detail the fundamental atomic structure of the TMD family of materials, and how this governs their electronic and optical responses. I first illustrate the general crystal structure, composed of individual layers with strong in-plane bonds, and much weaker out-of-plane van der Waals forces. The distribution of electronic orbitals associated with each atom is then described, enabling understanding of the formation of energy bands, and the process behind the indirect to direct band gap transition upon reduction of the layer number to a single plane of material. Excitonic properties of TMDs are then discussed, taking into account spin-orbit coupling effects that cause splitting of the valence and conduction band, yielding four different energy excitons, namely A and B, both with bright and dark variants respectively. Further spin-valley locking is also explained, allowing selective excitation of normally degenerate opposite sides of the Brillouin zone via right and left circularly polarised light. Finally, I present the complex refractive indices of four different TMDs, highlighting the range of exciton energies and strengths available, as well as the different transparency windows in the upper visible wavelength range.

2.3.1 Crystal Structure

Amongst the large species of 2D materials lie the transition metal dichalcogenides, which are fundamentally 2D planes of transition metal atoms (e.g. W or Mo) encased on either side by chalcogen atoms (e.g. S or Se) to form a trigonal prismatic [49] crystal as illustrated in Figures 2.2 (a), (b), and (c). By convention, the chemical formula is written as MX_2, where M represents the transition metal and X the chalcogen. Figure 2.2 (c) depicts the hexagonal arrangement of atoms in-plane which yields a hexagonal Brillouin zone in reciprocal space [49, 50] as in Figure 2.2 (d). Each monolayer of TMD contains strong in-plane covalent bonds [51], giving high tensile strength and stiffness [52–54], but only weak van der Waals [21, 51] forces between adjacent layers. This enables individual layers of up to hundreds of microns in lateral size [55] to be separated with relative ease using a technique known as mechanical exfoliation, first demonstrated by Konstantin Novoselov and Andre Geim in 2004 using Scotch tape [1]. Such van der Waals forces also give good adhesion to a wide variety of substrates making for easy and versatile measurements.

Delving deeper into their atomic structure, we see from Figure 2.2 (b) that each monolayer is reflection symmetric in the out-of-plane direction but has broken inversion symmetry in-plane [50, 56]. By stacking two monolayers with a 180° relative rotation about the out-of-plane axis, the in-plane inversion symmetry can be restored as in Figures 2.3 (a) and (b). This configuration is known as hexagonal, or 2H, and is the lowest energy type of stacking and therefore the most commonly found [57]. There is also another stable form of stacking involving a translational shift between layers with no rotation so that a rhombohedral unit cell is produced as in Figures 2.3 (c) and (d). This is known as 3R and has broken inversion symmetry [49, 57] as with a single monolayer, which will be important when considering excitonic properties later in this chapter.

Within each layer, every individual atom has associated electronic orbitals that would be discrete in energy if alone in space. However, when atoms are packed together in close proximity, there is an overlap of electronic wavefunctions from neighbouring atoms, thus resulting in a splitting of

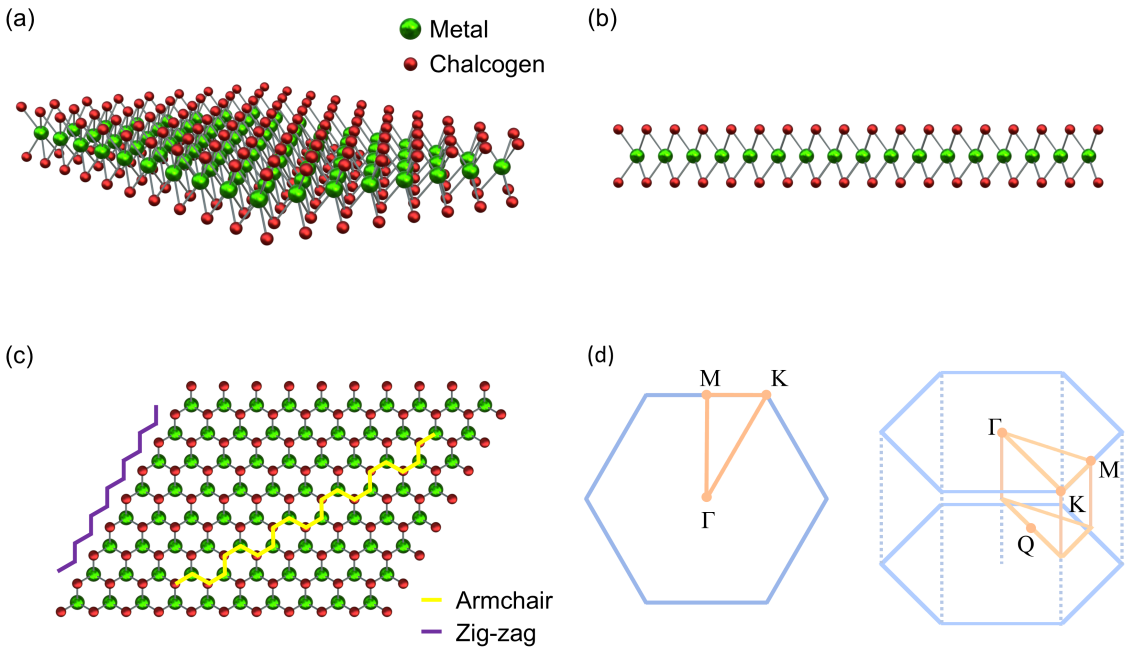


Figure 2.2: **Atomic structure of TMD layers. (a)-(c)** Schematics showing isometric, side, and top-down views of a TMD monolayer respectively. Green spheres represent the metal atoms, and red the chalcogens. Armchair and zig-zag crystal axes are highlighted in yellow and purple respectively. **(d)** First Brillouin zone of the TMD crystal lattice in reciprocal space. Letters mark various symmetry points or lines of interest.

the energy levels as in the tight-binding model. Now considering many atoms making up a crystal lattice, the energy levels of the many electrons overlap to the point where the splitting between each becomes negligible, and can therefore be considered a continuous spectrum, i.e. an energy band [47, 48]. An alternative model is to assume a nearly-free electron that experiences a continuously varying, periodic lattice potential owing to the repeating atomic unit cell. Its wavefunction $\psi_n(\boldsymbol{r})$ can therefore be expressed in Bloch form [58],

$$\psi_n(\boldsymbol{r}) = e^{i\boldsymbol{k}\cdot\boldsymbol{r}} u_n(\boldsymbol{r}), \tag{2.1}$$

where $n = 1, 2, 3, ...$ is the energy level, $\boldsymbol{r}$ is the real space positional vector, $\boldsymbol{k}$ is the reciprocal space crystal momentum vector, and $u_n(\boldsymbol{r})$ is a function with periodicity of the lattice. The energy bands also disperse with wave vector $\boldsymbol{k}$ over the Brillouin zone, leading to the characteristic electronic band structure diagrams of materials that are often found in literature. The behaviour and effects of these band structures will be discussed further in the following sections.

2.3.2 Band Gap Transition

One of the more interesting properties of TMDs in particular compared to other van der Waals materials, is their ability to switch from an indirect band gap semiconductor to having a direct band gap when changing from multi-layer to monolayer [50, 56, 59, 60] as in Figure 2.4 (a). We can observe that the indirect band gap initially exists between the valence band at the Γ point and the conduction band at the Q point for bulk TMDs [50]. However, during the transition to monolayer,

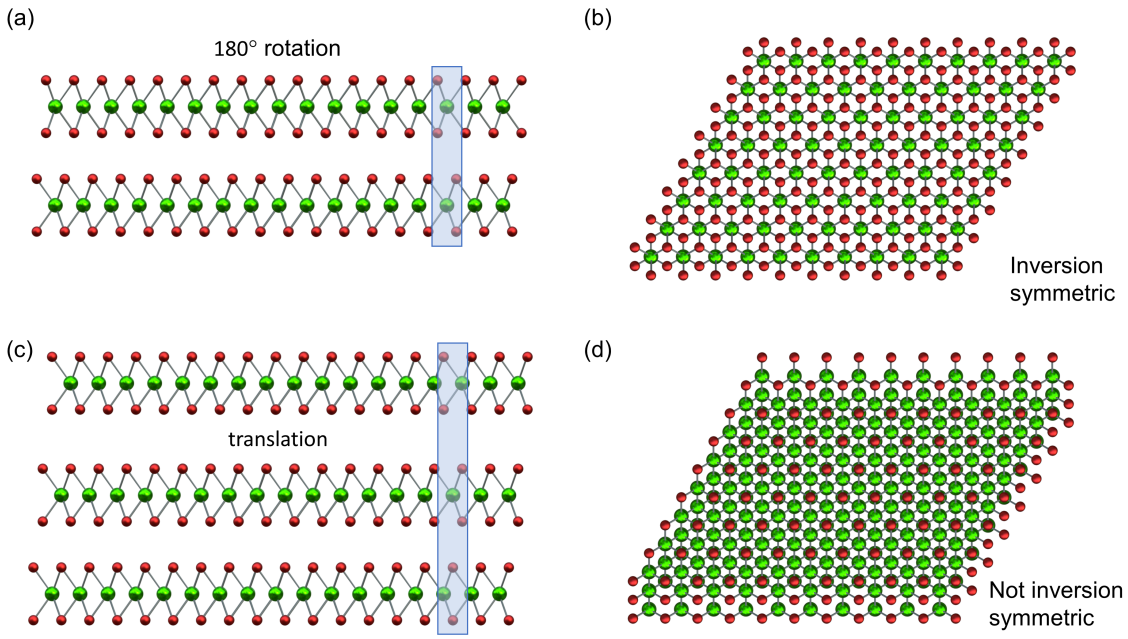


Figure 2.3: **Stacking configurations of TMD layers. (a)**, **(b)** Side and top-down views of hexagonal (2H) stacking arrangement where one layer is rotated 180° to the other to reinstate inversion symmetry. **(c)**, **(d)** Side and top-down views of rhombohedral (3R) stacking involving three layers with a translational shift giving no inversion symmetry. Blue regions in **(a)** and **(c)** aid to visualise the interlayer atomic alignment.

the valence band edge at the Γ point decreases significantly in energy, along with an increase of the conduction band edge at the Q point and a small reduction at the K point [59, 61], thus causing the shift to a direct band gap at the K point.

In order to understand why this shifting of band edges occurs, we must consider the configuration of electronic orbitals from individual atoms in each monolayer. Figures 2.4 (b) and (c) show the relative weight of each different electronic orbital that contribute to the overall valence and conduction bands of MoS_2. The out-of-plane (z) orbitals primarily contribute to the valence band at the Γ point and the conduction band at the K point [62–64] as shown by the larger markers. These out-of-plane orientated orbitals are susceptible to quantum confinement effects [47] when the material is thinned to a single layer, therefore causing a decrease in energy of the valence band and conduction band edges at the Γ and K points respectively. Conversely, the conduction band edge at the Q point and the valence band edge at the K point are governed mostly by in-plane (x, y) orbitals of the metal and chalcogen atoms [62–64], and so they have a negligible shift upon reduction of the number of layers. The result of these two effects is a transition from an indirect band gap to a direct band gap at the K point. This allows for much more efficient photoluminescence (PL) of monolayer TMDs compared to their multi-layer forms, via fully radiative recombination of an electron in the conduction band with a hole in the valence band, without the need of a phonon exchange [59].

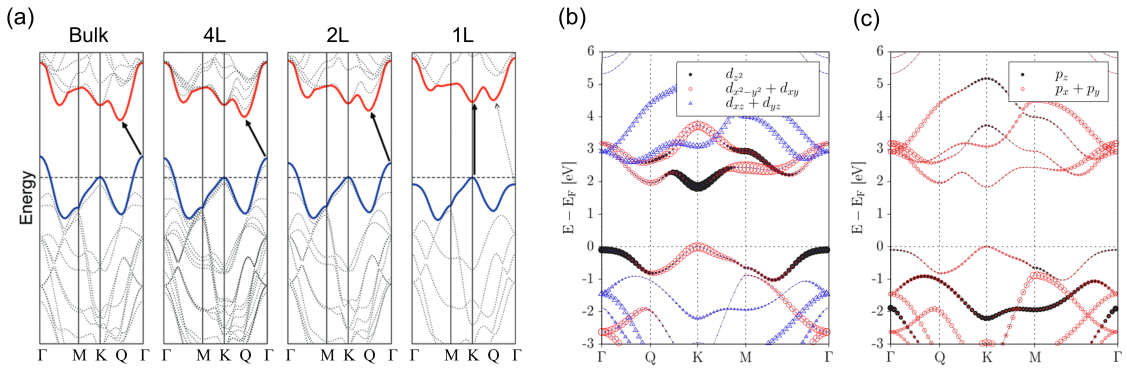


Figure 2.4: **Indirect to direct band gap transition of MoS_2. (a)** Electronic band structure of MoS_2 from multi-layer down to a single monolayer adapted from [59]. Indirect to direct band gap transition visible between bilayer and monolayer as indicated by the black arrows. **(b), (c)** Weighting of the contributions of d and p electronic orbitals respectively to the MoS_2 band structure adapted from [62]. Larger marker sizes for both in-plane (x, y) and out-of-plane (z) orbital contributions correspond to higher weighting.

2.3.3 Excitonic Properties

Transition metal dichalcogenide monolayers also show prominent excitonic effects with high oscillator strengths even at room temperature [50]. Such bound electron-hole quasiparticles exist at the edges of the step-like energy bands from Figure 2.1, formed when an electron near the top of the valence band gains enough energy to transition across the direct band gap to the bottom of the conduction band. This leaves behind a negatively charged hole which is bound to the electron by the Coulomb interaction [48]. These quasiparticles are well-described as Wannier-Mott excitons [65, 66], as despite their high binding energies of around 100 meV [67] (usually typical of Frenkel excitons [68]), they have much larger Bohr radii of around 1-2 nm [67], which spans over multiple unit cells of the crystal lattice. The reason behind the high binding energies is due to reduced dielectric screening [48, 69] when in monolayer form as shown in Figure 2.5, which also depicts how sensitive these excitons can be to their surrounding environment.

Until this point I have so far neglected the effects of spin-orbit coupling [70]. This causes an appreciable energy splitting of the valence band at the K points allowing two transitions of different energies to the conduction band, hence permitting two excitons which we name A and B (A being the lowest energy) [62, 71, 72]. Furthermore, a smaller spin-orbit splitting of the conduction band arises leading to the formation of both spin-allowed (bright) and spin-forbidden (dark) excitonic states [72, 73], as shown in Figures 2.6 (a) and (b) for Mo- and W-based TMDs respectively. Bright excitons can be easily created through absorption of a photon, however the dark excitons require a phonon exchange and must decay through non-radiative channels. There exist also inter-valley dark excitons [74–77], however I will not cover these in depth as all the experimental results in this thesis will focus primarily on utilising bright excitons. It is also important to note that different TMDs can have spin-orbit splitting of opposite signs owing to their electronic orbital configurations, thus leading to different types of excitons as their ground state. For example, in Mo-based TMDs the ground state consists of a spin-allowed bright A exciton, however for W-based TMDs the split conduction bands are flipped in energy, and so the ground state is a spin-forbidden dark

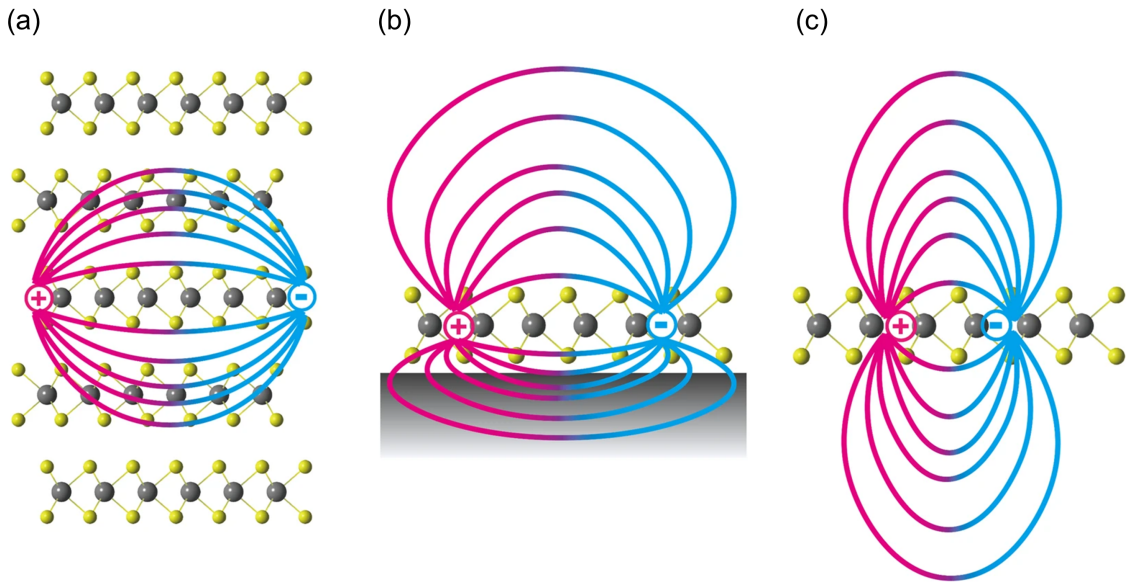


Figure 2.5: **Effect of dielectric screening on intra-layer excitons.** **(a)** Exciton in multi-layered TMD experiencing appreciable dielectric screening. **(b)** Exciton in a monolayer TMD on a substrate showing confinement of the electric field in the substrate due to screening. **(c)** Exciton in suspended monolayer experiences the least screening and hence its associated fields project the furthest into the surrounding environment. Adapted from [69].

exciton. This means that the lowest energy bright A exciton exists at slightly higher energy than the electronic band gap for W-based TMDs, as illustrated by the double headed arrows in Figure 2.6 (b).

Another consequence of the spin-orbit interaction associated with monolayer TMDs is their inherent spin-valley locking [66, 78, 79]. In the bulk 2H stacked form, there exists inversion symmetry in-plane and so the two opposite K valleys are degenerate. However, since monolayers have broken in-plane inversion symmetry as discussed in Section 2.3.1, the K valleys host opposite spin states and can be denoted as K^+ and K^- (or K and K'). This is depicted in Figures 2.6 (a) and (b), and means that each valley can be selectively excited using either left (σ^+) or right (σ^-) circularly polarised light, therefore opening up another degree of freedom for light-matter interactions using TMDs.

2.3.4 Optical Properties

As well as the rich electronic phenomena discussed previously, TMDs also possess remarkably high refractive indices along with extremely low losses above $\sim$ 700 nm wavelength and across a large portion of the near infra-red range (note that experimental data only exists up to 1.7 µm wavelength [80]). Owing to the uniaxial crystal structure as discussed in Section 2.3.1, light experiences a different refractive index when passing through the material in-plane compared to out-of-plane, and hence TMDs are inherently anisotropic materials. This is shown in Figure 2.7, which presents experimentally measured complex refractive indices for four of the most well-studied TMDs: WS_2, WSe_2, MoS_2, and $MoSe_2$ in both the in- and out-of-plane directions. Towards the lower end of the visible wavelength range we see typical dielectric responses due to the excitons [81] discussed in

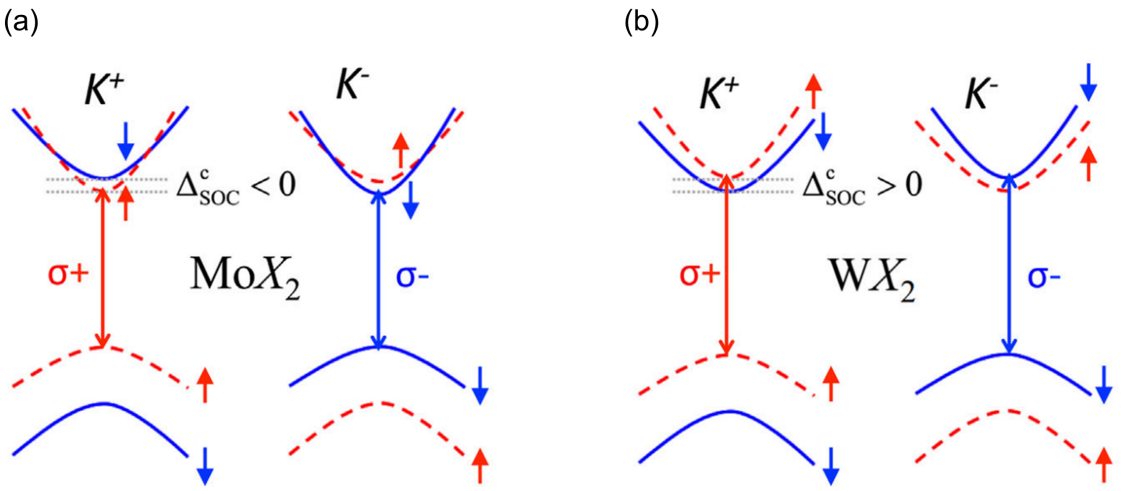


Figure 2.6: **Electronic band structures for different monolayer TMDs including spin-orbit coupling effects and spin-valley locking. (a)** Mo-based TMD band structure showing large spin-orbit splitting of the valence band and a smaller splitting (Δ^c_{SOC}) of the conduction band, leading to a number of spin-allowed (bright) and spin-forbidden (dark) exciton transitions. Single headed arrows denote spins of individual bands, whilst double headed arrows show the lowest energy (A) exciton transition. Left and right schematics correspond to the K^+ and K^- valleys which can be accessed only by either left (σ^+) or right (σ^-) circularly polarised light respectively. **(b)** Band structure for W-based TMDs showing lowest energy transition is spin-forbidden due to conduction band spin-orbit coupling of the opposite sign. The A exciton exists between the top valence band and the upper conduction band in contrast to Mo-based TMDs. Adapted from [72].

Section 2.3.3. These manifest in the refractive index data as asymmetric Fano curves [82] in the real part (n), and as a Lorentzian peak in the absorption (k). For example, in WS_2 the A exciton appears at around 625 nm as shown by the sharp features in both n and k of the in-plane complex refractive index in Figure 2.7 (c). At wavelengths below the exciton, the absorption increases significantly due to exciting the crystal above the band gap, meaning that incident light is lost to both the creation of excitons, and inter-band transitions. The high refractive indices combined with low losses at wavelengths above the A exciton make TMDs an ideal candidate for confining and manipulating light on the nanoscale [83], and studying exotic light-matter interactions as discussed further in Sections 2.4 and 2.5.

2.4 Nanophotonics in 0D Structures

Now that I have covered the fundamental material properties of TMDs, I will shift focus to how they can be used within the field of nanophotonics. In short, nanophotonics covers the manipulation of light on nanometer length scales, and to understand this further I will introduce a variety of different ways that light can be bound within nanostructured materials, also known as photonic resonances or modes. In this section I will focus on nanoresonators of sizes on the order of the wavelength of visible light, and hence they can be considered as zero-dimensional (0D) structures. To begin I will introduce fundamental Mie resonances, detailing how the size and shape of nanoparticles strongly influences their light-scattering behaviour. I will then discuss the anapole condition, an

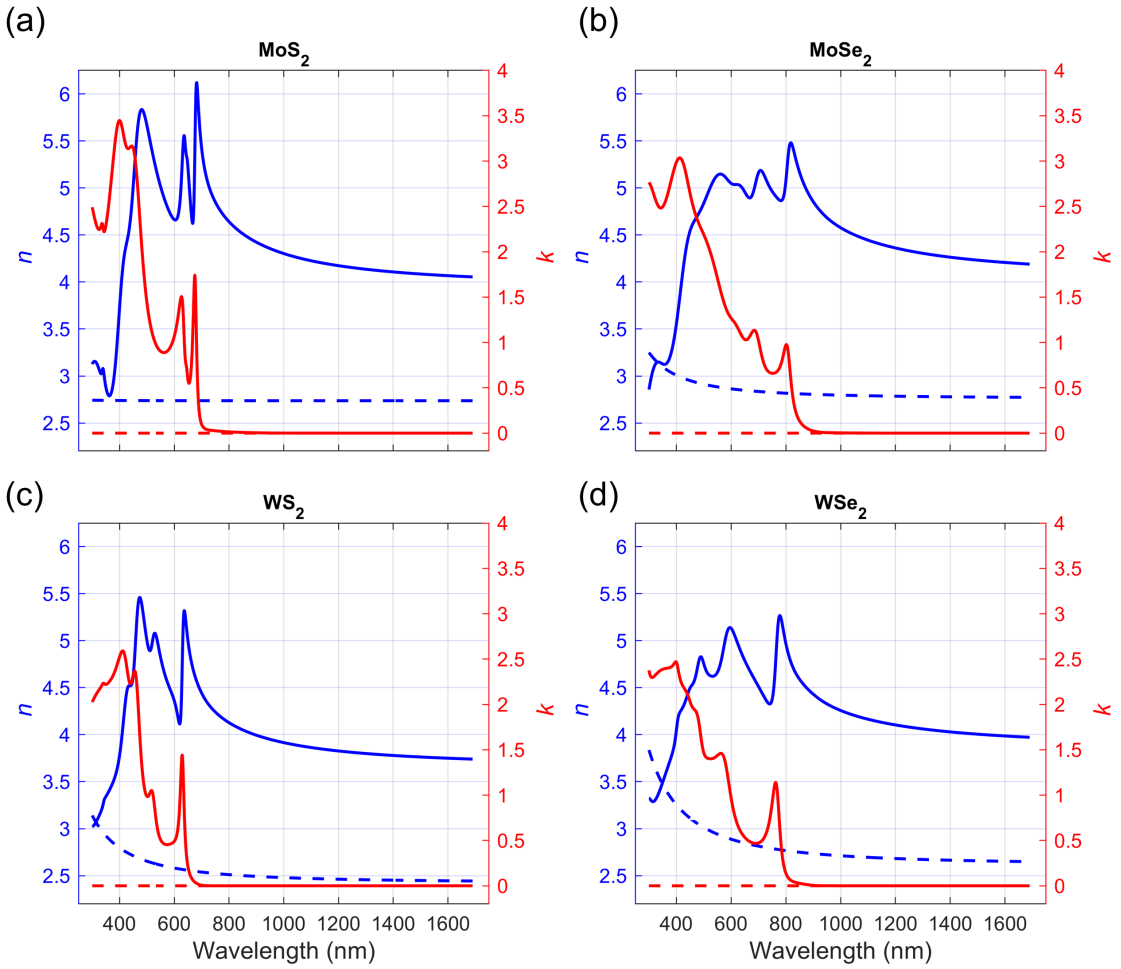


Figure 2.7: **Complex refractive indices for the in- and out-of-plane directions of common TMDs. (a)-(d)** MoS_2, $MoSe_2$, WS_2, and WSe_2 complex refractive indices respectively using data from [80]. Blue lines correspond to real part of refractive index n, and red lines the imaginary part k. Solid lines correspond to in-plane data and dotted lines out-of-plane. Same scales used with each material for direct comparison.

optically dark state formed from the interplay of different Mie modes. Fabry–Perot modes will also be covered, along with how such photonic cavities can introduce strong coupling with excitons forming a new quasiparticle named the polariton. Following on from this, I will explore strong coupling of two photonic modes resulting in the formation of Friedrich-Wintgen bound states in the continuum. Looking towards the weak coupling regime, I will then explain the fundamentals of spontaneous emission enhancement, also known as the Purcell effect, and its context within the field of nanophotonics. Finally, I provide a theoretical background for the field of plasmonics, explaining what plasmons are and how they can interact with incident light to form additional types of nanoscale resonances, thus further adding to the ways in which light-matter interactions can be manipulated on the nanoscale.

2.4.1 Electromagnetic Waves in a Medium

When electromagnetic (EM) radiation propagates through a medium its behaviour is characterised by the intrinsic refractive index, as well as the shape and size of the object. Considering first the material itself, in a metal there is no electronic band gap and the Fermi level lies within the overlapping conduction and valence bands, thus giving many entirely free charge carriers that can move throughout the material as described by the Drude model [84, 85]. Dielectric materials such as TMDs do not inherently contain free charge carriers owing to their significant band gap [47]. The electrons and holes are bound to atoms on the crystal lattice, and cannot move freely between lattice sites without some form of external excitation. However, the charge carriers can still oscillate about their host atom. When illuminated by EM waves, the bound charges align with the incident field creating a net dipole moment per unit volume, also known as polarisation. Since TMDs are anisotropic materials, the polarisation response will be different depending on the angle of the incident light. For this thesis I will consider mainly the in-plane polarisation $\boldsymbol{P}^{\text{in}}$, which can be defined as

$$\boldsymbol{P}^{\text{in}} = \epsilon_0 \chi^{\text{in}} \boldsymbol{E}^{\text{in}}, \tag{2.2}$$

where ϵ_0 is the electric permittivity of free space, and χ^{in} is the in-plane electric susceptibility of the material given as a function of the material's in-plane relative permittivity ($\epsilon_{\text{r}}^{\text{in}}$):

$$\chi^{\text{in}} = \epsilon_{\text{r}}^{\text{in}} - 1. \tag{2.3}$$

Before going further it is important to note that Equation 2.2 makes the assumption that $\boldsymbol{P}^{\text{in}}$ varies linearly with $\boldsymbol{E}^{\text{in}}$, which is only true for linear media. TMDs present a rich variety of non-linear behaviours, however these are not the focus of this thesis and so I will safely ignore their effects.

Concerning the propagation of light in a medium, Equation 2.2 neatly describes how EM waves change speed in materials of different refractive indices. The higher the refractive index (or relative permittivity), the higher the polarisation (or net dipole moment of the charge carriers), and so the higher the amplitude of the dipolar oscillations. If we first consider an infinitesimally thin layer of material under illumination, the fields created by the oscillating dipoles in the layer will have the same frequency as the incident wave in the steady state but much lower amplitude. There will also be a phase lag between the incident wave and the dipolar waves as the bound charges have finite mass, and so take a non-zero time to accelerate and begin oscillating. The dipolar waves then interfere with the incident wave causing an infinitesimal backwards shift in phase. Now, by adding together many layers of material, the incident wave experiences an infinitesimal backwards phase shift from each infinitesimally thin layer thus creating the overall effect of a shortening of the wavelength, and therefore a reduction of the wave speed [86]. Since TMDs boast high refractive indices, EM radiation propagating within them is significantly reduced in wavelength, thus enabling strong confinement of light to sub-vacuum-wavelength scales not normally possible with low index materials.

So far I have focused primarily on the electric response of dielectrics, however this is only half of the story. By also considering the magnetic susceptibility, a complete description of the

behaviour of EM waves in a medium can be expressed through the Maxwell-Heaviside equations,

$$\nabla \cdot \boldsymbol{D} = \rho, \tag{2.4}$$

$$\nabla \cdot \boldsymbol{B} = 0, \tag{2.5}$$

$$\nabla \times \boldsymbol{E} = -\frac{\partial \boldsymbol{B}}{\partial t}, \tag{2.6}$$

$$\nabla \times \boldsymbol{H} = \boldsymbol{j} + \frac{\partial \boldsymbol{D}}{\partial t}, \tag{2.7}$$

where $\boldsymbol{D}$, $\boldsymbol{B}$, $\boldsymbol{E}$, and $\boldsymbol{H}$ are the electric displacement field, magnetic flux density, electric field strength, and magnetic field strength respectively, $\boldsymbol{j}$ is the current density, and ρ is the free charge density. In Section 2.4.2 I will explain in more depth how solving the Maxwell-Heaviside equations can give insight into a variety of photonic resonances in nanoscale structures.

2.4.2 Mie Resonances

In Section 2.4.1 I discussed how the intrinsic material refractive index governs the propagation of light within a dielectric medium. Now I will explore how forming shapes such as spheres and pillars of sizes on the order of the incident wavelength can trap and manipulate light on the nanoscale further. The theory for light scattering from particles of these sizes was originally proposed by Gustav Mie in 1908 [87], who solved Maxwell's equations analytically for a plane wave incident upon a metallic nanosphere. The solutions allow one to calculate both the electric and magnetic fields inside, on the surface of, and outside of the nanosphere. In the case of a metallic medium, the incident light causes the free charge carries to oscillate as described in Section 2.4.1. However, owing to boundary conditions imposed by the spherical geometry and the size comparable to the incident wavelength, resonances akin to standing waves can be established. For a metal, these modes propagate on the surface of the particle, but for a dielectric they can be confined completely inside. For example, the surface fields originally calculated by Mie for a metallic nanosphere are visualised in Figure 2.8, and show increasing orders of the allowed electric and magnetic Mie resonances. These orders are termed multipole moments, consisting of electric and magnetic dipoles, quadrupoles, octupoles, and so on, named this way owing to the net field pattern produced by the sum off all the oscillating dipoles of the particle. Most interestingly for the work in this thesis, once all of the fields associated with the nanosphere are known, partial scattering cross-sections in the far-field can be calculated for each different multipole moment, and then compared with simulation and experiment.

I will spare delving into a lengthy derivation of the Mie solutions to Maxwell's equations as these are well defined in [87], but more importantly these only apply to the very specific case of a nanosphere suspended in a homogeneous dielectric medium. This thesis will focus on more complex geometries such as hexagonal pillars on different substrates, and so I will turn my attention towards more general expressions that can be used for any shape or size object. Furthermore, I will focus on the scattering cross-sections associated with each multipole moment which tell us how much light in total is redirected by each different Mie mode. This is useful as it corresponds to

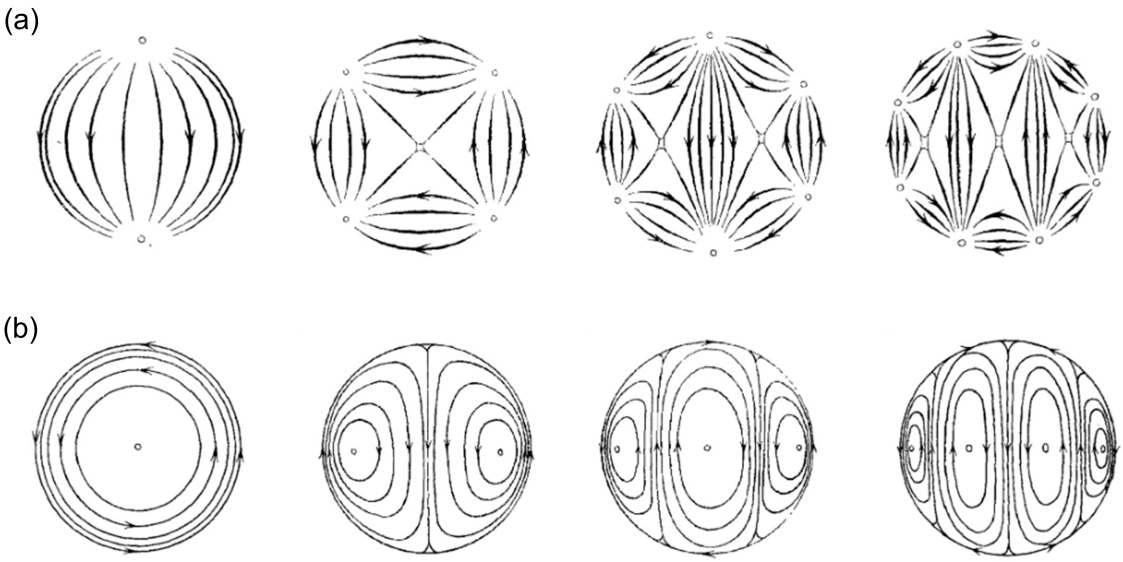


Figure 2.8: **Vector plots of the Mie solutions to Maxwell's equations on the surface of a metallic nanosphere. (a)** Top row corresponds to the electric field distributions of the first four electric Mie modes. **(b)** Bottom row corresponds to the electric field distributions of the first four magnetic modes. Adapted from [87].

a specific measurable quantity for each different multipole moment that can be easily compared, unlike the electric/magnetic field strengths which vary strongly depending on both the type of Mie mode, and the position within the nanoparticle. Once the multipole moments and their respective scattering cross-sections are known, then one can fully describe how EM fields couple to arbitrarily shaped nanoparticles, and how such incident light is then scattered to the far-field.

In order to calculate the scattering contribution from each partial multipole moment, the electric and magnetic field strength vectors, $\boldsymbol{E}^{\omega}(\boldsymbol{r})$ and $\boldsymbol{H}^{\omega}(\boldsymbol{r})$, at each point $\boldsymbol{r} = (x, y, z)$ must be known throughout a given nanoparticle under plane wave illumination at normal incidence with angular frequency ω. For the results in this thesis, these values are calculated using finite-difference time-domain simulations which will be explained in more depth in Sections 2.7.1 and 3.3. The displacement current density within the nanoparticle, i.e. the rate of change of the oscillating dipolar fields, is given by [88]

$$\boldsymbol{J}^{\omega}(\boldsymbol{r}) = -i\omega\epsilon_0(\tilde{n}^2 - 1)\boldsymbol{E}^{\omega}(\boldsymbol{r}) \tag{2.8}$$

where $\tilde{n}$ is the complex refractive index. From this, Alaee *et al.* showed that the exact multipole moments can be written as [89]

$$\text{ED}: \quad p_\alpha = -\frac{1}{i\omega}\left\{\int J^\omega_\alpha j_0(kr)\,\mathrm{d}^3\boldsymbol{r} + \frac{k^2}{2}\int\left[3(\boldsymbol{r}\cdot\boldsymbol{J}^\omega)r_\alpha - r^2 J^\omega_\alpha\right]\frac{j_2(kr)}{(kr)^2}\,\mathrm{d}^3\boldsymbol{r}\right\}, \tag{2.9}$$

$$\text{MD}: \quad m_\alpha = \frac{3}{2}\int(\boldsymbol{r}\times\boldsymbol{J}^\omega)_\alpha\frac{j_1(kr)}{kr}\,\mathrm{d}^3\boldsymbol{r}, \tag{2.10}$$

$$\text{EQ}: \quad Q^{\mathrm{e}}_{\alpha\beta} = -\frac{3}{i\omega}\left\{\int\left[3(r_\alpha J^\omega_\beta + r_\beta J^\omega_\alpha) - 2(\boldsymbol{r}\cdot\boldsymbol{J}^\omega)\delta_{\alpha\beta}\right]\frac{j_1(kr)}{kr}\,\mathrm{d}^3\boldsymbol{r}\right. \tag{2.11}$$

$$\left. + 2k^2\int\left[5r_\alpha r_\beta(\boldsymbol{r}\cdot\boldsymbol{J}^\omega) - r^2(r_\alpha J^\omega_\beta + r_\beta J^\omega_\alpha) - r^2(\boldsymbol{r}\cdot\boldsymbol{J}^\omega)\delta_{\alpha\beta}\right]\frac{j_3(kr)}{(kr)^3}\,\mathrm{d}^3\boldsymbol{r}\right\},$$

$$\text{MQ}: \quad Q^{\mathrm{m}}_{\alpha\beta} = 15\int\left[\,r_\alpha(\boldsymbol{r}\times\boldsymbol{J^\omega})_\beta + r_\beta(\boldsymbol{r}\times\boldsymbol{J^\omega})_\alpha\right]\frac{j_2(kr)}{(kr)^2}\,\mathrm{d}^3\boldsymbol{r} \tag{2.12}$$

for the electric dipole (ED) p_α, magnetic dipole (MD) m_α, electric quadrupole (EQ) $Q^{\mathrm{e}}_{\alpha\beta}$, and magnetic quadrupole (MQ) $Q^{\mathrm{m}}_{\alpha\beta}$, where $\alpha,\beta = (x,y,z)$, k is the wavenumber, and $j_n(\rho)$ are the spherical Bessel functions of the first kind. To now calculate the total scattering cross-section from a given nanoparticle illuminated by a plane wave at normal incidence, the partial scattering cross-sections from each multipole in all directions must be summed:

$$\begin{aligned} C^{\text{total}}_{\text{sca}} &= C^{p}_{\text{sca}} + C^{m}_{\text{sca}} + C^{Q^{\mathrm{e}}}_{\text{sca}} + C^{Q^{\mathrm{m}}}_{\text{sca}} + \cdots \\ &= \frac{k^4}{6\pi\epsilon_0^2\left|\boldsymbol{E}_0\right|^2}\left[\sum\left(\left|\boldsymbol{p}\right|^2 + \frac{\left|\boldsymbol{m}\right|^2}{c}\right) + \frac{1}{120}\sum\left(\left|k\boldsymbol{Q}^{\mathrm{e}}\right|^2 + \left|\frac{k\boldsymbol{Q}^{\mathrm{m}}}{c}\right|^2\right) + \cdots\right], \end{aligned} \tag{2.13}$$

where $\left|\boldsymbol{E}_0\right|^2$ is the electric field intensity of the incident radiation, and c is the vacuum speed of light. As can be seen from Equation 2.13, the total scattering cross-section is an infinite sum of increasing order partial multipole moments. However, for the structures considered in this thesis, the first four terms serve as an accurate enough description of the total scattering, with higher order multipoles adding a negligible effect.

To prove the validity of Equation 2.13, Alaee *et al.* compared their results of the aforementioned multipole expansion method with the analytical Mie solutions for dielectric and gold nanospheres as shown in Figures 2.9 (a) and (b). For both materials, they found excellent agreement between the two methods, and further showed that Equations 2.9-2.12 also work well for arbitrary geometries such as coupled nanodisks [89] as in Figure 2.9 (c). Furthermore, Alaee *et al.* compared their exact multipole expansion formula to a previously popular method in which a long wavelength approximation was used, assuming the nanoparticle is much smaller than the wavelength of the incident light [90, 91]. For larger particles this approximate method was shown to break down, and thus introduces a large error as shown in Figure 2.9 (d).

The exact multipole expansion formulation will be used later in this thesis to decompose simulated total scattering spectra of various different nanostructure geometries and sizes, into partial scattering cross-sections associated with different multipole moments. This will be of great use in beginning to characterise the rich variety of photonic resonances available in nanostructured

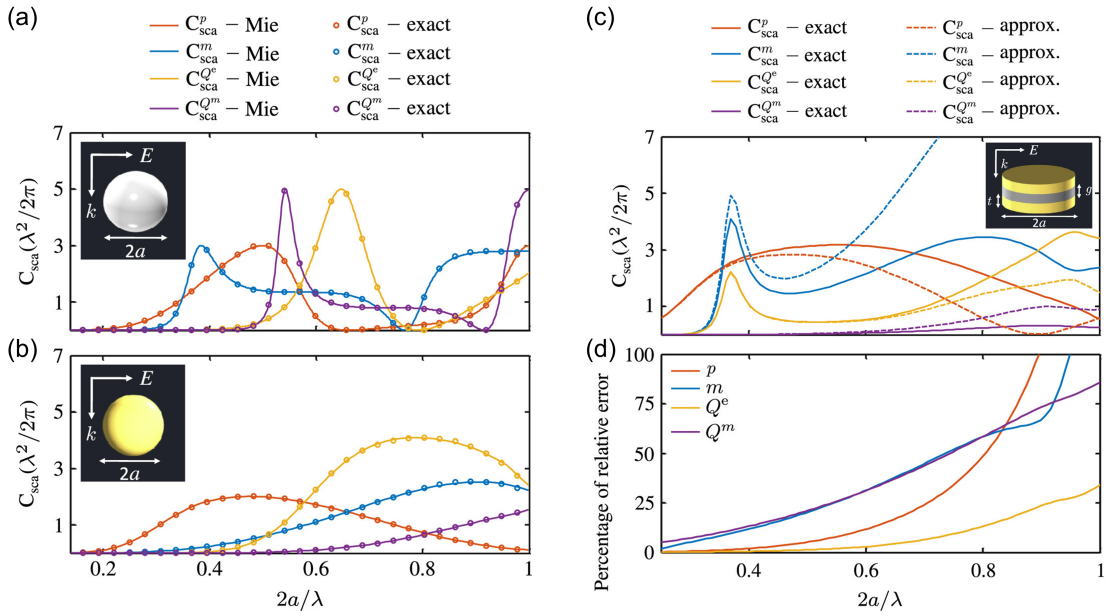


Figure 2.9: **Calculated multipole expansion of electric and magnetic fields from nanospheres of different materials compared to analytical Mie solutions.** **(a)** Partial scattering cross-sections of the electric and magnetic dipoles (C^{p}_{sca}, C^{m}_{sca}) and quadrupoles ($C^{Q^{\text{e}}}_{\text{sca}}$, $C^{Q^{\text{m}}}_{\text{sca}}$) from a dielectric nanosphere. Solid lines correspond to the analytical Mie solutions, and circle markers correspond to the calculated multipole expansions using Equations 2.9-2.12. **(b)** Same for a gold nanosphere. **(c)** Multipole expansion method applied to a coupled nanodisk structure. Here the solid lines correspond to the multipole expansion and dashed lines to a previously used approximate method involving a long-wavelength assumption. **(d)** Percentage error between the exact and approximate multipole expansions from **(c)**. For each multipole moment the error of the approximate method increases as the nanostructure becomes of comparable size to the incident wavelength or larger. Adapted from [89].

TMDs on different substrates, and better understanding how one can manipulate light on such length scales.

2.4.3 Optical Anapoles

Anapoles differ from Mie resonances in that they are not individual eigenmodes of a given resonator [92]. Rather they are a specific condition that the electric dipole moment must meet in order for its radiation to be completely suppressed in the far-field, thus yielding an optically dark state [93–96]. Anapoles can also be differentiated from radiationless bound states in the continuum. The anapole can only exist under external excitation, whereas BICs exhibit self-sustained oscillations without requiring any external fields [92, 97]. These bound states will be discussed in more depth later in Sections 2.4.6 and 2.6.4. To understand why anapoles occur in a more didactic way, it is helpful to consider splitting the previously defined spherical electric dipole moment $|\boldsymbol{p}|$ into two components, $|\boldsymbol{p}^{\text{Car}}|$ and $|-ik\boldsymbol{T}^{\text{Car}}|$, corresponding to the so-called Cartesian electric and toroidal dipole components respectively [89, 98, 99]. This is achieved using the long-wavelength approximation mentioned in Section 2.4.2, which simplifies the spherical Bessel functions to

$$j_0(kr) \approx 1 - \frac{(kr)^2}{6}, \tag{2.14}$$

$$j_2(kr) \approx \frac{(kr)^2}{15}. \tag{2.15}$$

Substituting these back into Equation 2.9 we arrive at

$$p_\alpha \approx -\frac{1}{i\omega}\left\{\int J_\alpha^\omega \, \mathrm{d}^3\boldsymbol{r} + \frac{k^2}{10}\int\left[(\boldsymbol{r}\cdot\boldsymbol{J}^\omega)r_\alpha - 2r^2 J_\alpha^\omega\right]\mathrm{d}^3\boldsymbol{r}\right\}, \tag{2.16}$$

which can be split into two components,

$$p_\alpha^{\mathrm{Car}} \approx -\frac{1}{i\omega}\int J_\alpha^\omega \, \mathrm{d}^3\boldsymbol{r}, \tag{2.17}$$

$$T_\alpha^{\mathrm{Car}} \approx -\frac{1}{i\omega}\frac{k^2}{10}\int\left[(\boldsymbol{r}\cdot\boldsymbol{J}^\omega)r_\alpha - 2r^2 J_\alpha^\omega\right]\mathrm{d}^3\boldsymbol{r}, \tag{2.18}$$

where p_α^{Car} takes the form of a general electric dipole moment [100] assuming the nanostructure under illumination is much smaller than the incident wavelength. T_α^{Car} can be thought of as a Cartesian toroidal dipole moment owing to the torus-shaped radiation pattern as shown in Figure 2.10 (a). Previously this was thought to be a third type of multipole moment along with electric and magnetic multipoles [89, 99], however it is clear from Equation 2.16 that the toroidal moment is simply a higher-order component of the electric dipole.

Now, by substituting 2.16 back into Equation 2.13 we can write

$$C_{\mathrm{sca}}^{\mathrm{total}} \approx \frac{k^4}{6\pi\epsilon_0^2\left|\boldsymbol{E}_0\right|^2}\left[\sum\left(\left|\boldsymbol{p}^{\mathrm{Car}} + ik\boldsymbol{T}^{\mathrm{Car}}\right|^2 + \frac{\left|\boldsymbol{m}\right|^2}{c}\right) + \frac{1}{120}\sum\left(\left|k\boldsymbol{Q}^{\mathrm{e}}\right|^2 + \left|\frac{k\boldsymbol{Q}^{\mathrm{m}}}{c}\right|^2\right) + \cdots\right]. \tag{2.19}$$

The anapole condition occurs when the total scattering in all directions from the overall electric dipole moment is reduced to zero, which can be neatly written as $\boldsymbol{p}^{\mathrm{Car}} + ik\boldsymbol{T}^{\mathrm{Car}} = 0$ [88]. Importantly, this only happens when the contributions from the Cartesian electric and toroidal dipole components are equal in magnitude, but also with opposite phases so that their scattered radiation patterns perfectly cancel each other out in the far-field. For example, Figure 2.11 shows the long-wavelength approximated multipole expansion for a dielectric nanodisk by Hinamoto *et al* [88]. They observed that the scattering cross-sections of the Cartesian electric and toroidal dipole components are equal (Figure 2.11 (b)) at roughly the same wavelength as the point where the phases of the two components are equal in magnitude but with opposite signs (Figure 2.11 (c)). Here the anapole condition is met, and there is a corresponding suppression of the total scattering from the nanostructure. This characteristic of anapoles enables potential uses in cloaking devices [92, 94, 95, 101], where incident radiation simply passes through a nanostructure without scattering, meaning the object cannot be detected.

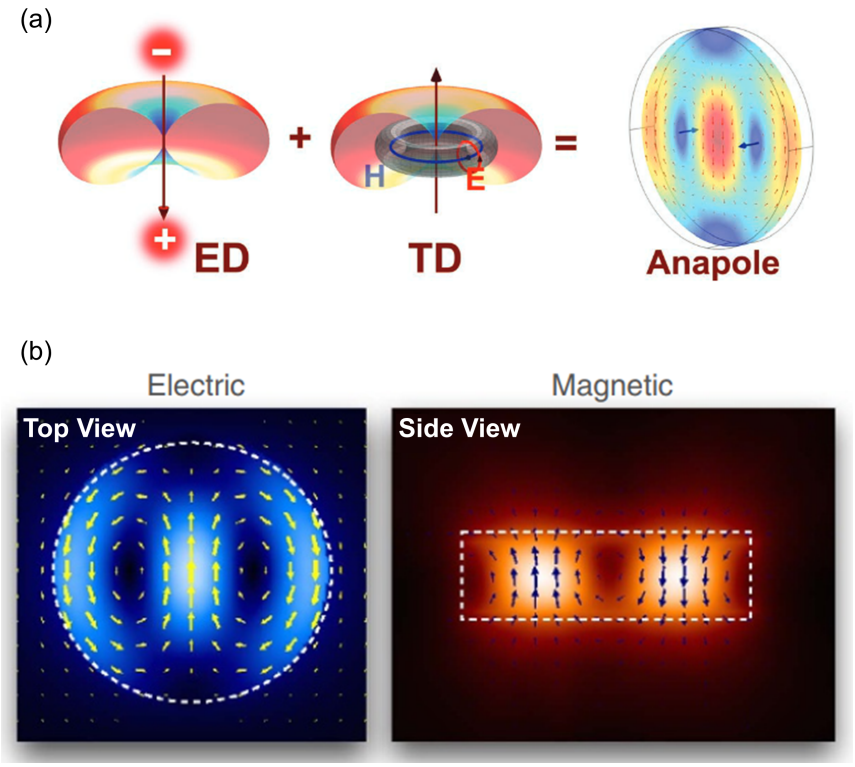


Figure 2.10: **Depiction of the near-field composition of an optical anapole.** **(a)** Left: cross-sectional schematic of the Cartesian electric dipole component shown as two opposite charges separated by some distance. Torus shape depicts the radiation pattern as expected of an oscillating electric dipole. Middle: Cartesian toroidal dipole component illustrated by a circulating magnetic field (blue ring) with induced radially arranged electric field loops. Radiation pattern produced is identical to the Cartesian electric dipole component but 180° out of phase, thus the two destructively interfere and cancel out. Right: Plot of the electric field vector through the centre of a dielectric nanosphere exhibiting a superposition of Cartesian electric and toroidal dipole components comprising the anapole condition. Adapted from [95]. **(b)** Left and right panels show the electric and magnetic field vectors respectively for an anapole in a silicon nanodisk geometry. Adapted from [94].

Perhaps initially counter-intuitive, is the fact that the total scattering cross-section in Figure 2.11 (b) is less than the individual contribution from the Cartesian electric dipole component $|\boldsymbol{p}^{\mathrm{Car}}|$. This is where the distinction between the spherical electric dipole moment $|\boldsymbol{p}|$ from Equation 2.13 must be carefully distinguished from the Cartesian electric dipole moment $|\boldsymbol{p}^{\mathrm{Car}}|$ from Equation 2.19, which is just a *component* of the spherical electric dipole moment: $|\boldsymbol{p}|^2 \approx |\boldsymbol{p}^{\mathrm{Car}} + ik\boldsymbol{T}^{\mathrm{Car}}|^2$. I use the approximate symbol here as this is still under the small particle, long-wavelength assumption. It is now evident that when multiplying out the right hand side there will be additional cross-terms, especially since both $|\boldsymbol{p}^{\mathrm{Car}}|$ and $|\boldsymbol{T}^{\mathrm{Car}}|$ are complex numbers. These cross-terms contribute both positively and negatively to the overall *spherical* electric dipole moment so that its sum, along with the other multipole moments, adds to the total displayed in Figure 2.11 (b). This means that the individual *Cartesian* electric dipole component $|\boldsymbol{p}^{\mathrm{Car}}|$ can have a larger scattering coefficient than the total *spherical* electric dipole moment $|\boldsymbol{p}|$. The primary motive of this toroidal dipole formulation however, is to distinguish if and where in wavelength the anapole condition is met,

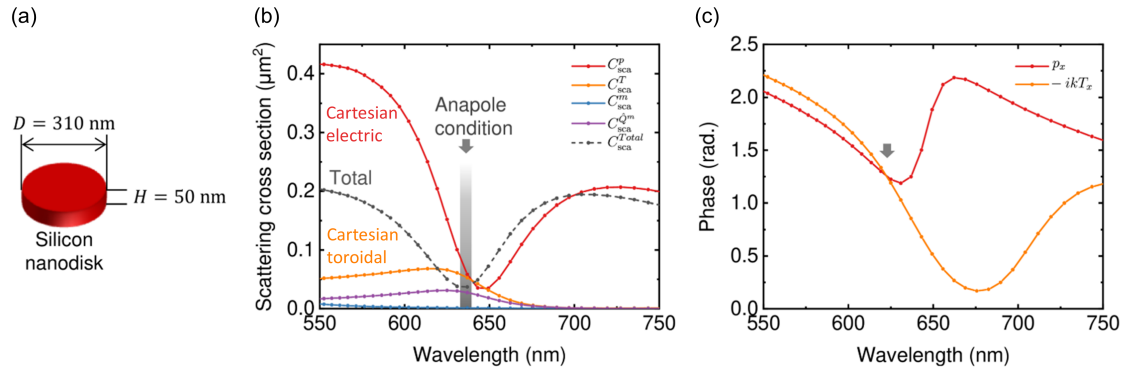


Figure 2.11: **Multipole expansion of the near-fields from a silicon nanodisk in the long-wavelength approximation showing existence of an anapole.** **(a)** Schematic of the nanodisk structure where D and H correspond to the diameter and height respectively. **(b)** Multipole expansion plot where the red and orange curves correspond to the Cartesian electric $|\boldsymbol{p}^{\text{Car}}|$ and Cartesian toroidal $|ik\boldsymbol{T}^{\text{Car}}|$ components of Equation 2.19. Blue and purple curves correspond to the magnetic dipole and quadrupole moments respectively. **(c)** Phase components of $\boldsymbol{p}^{\text{Car}}$ and $-ik\boldsymbol{T}^{\text{Car}}$ in the direction parallel to the polarisation of the incident wave x. Adapted from [88].

rather than to assign specific scattering values to the individual multipole moments, which can be calculated exactly with Equation 2.13.

Whilst the far-field response for the anapole condition is net-zero plane wave scattering in all directions, the associated near-fields within the host nanostructure are non-zero. Plots of the electric and magnetic field distributions for the first-order anapole are presented in Figures 2.10 (a) and (b). For the case of nanospheres and nanoantennas, the field distribution of the anapole generally exhibits the same symmetric pattern, with a central field maximum and two outer maxima along the direction perpendicular to the polarisation axis of the incident light [94, 95, 102–105]. Higher-order anapole states are also possible, which show an increasing number of field maxima in the direction perpendicular to the polarisation axis [106–108]. Notably, the near-fields associated with anapole conditions are very well-confined within the host nanostructures as in Figures 2.10 (a) and (b). This means that there is little leakage of the fields to the surrounding environment, and so very low energy losses per cycle. As a result, anapoles generally appear in far-field scattering spectra as narrow linewidth spectral features with high quality (Q) factors. In this thesis, many of the resonances studied will be characterised by their Q factor which takes the form $Q = \lambda_0/\Delta\lambda$, where λ_0 is the peak resonance wavelength, and $\Delta\lambda$ is the full width at half maximum (FWHM) of the peak. This gives a quantitative idea of how well confined and lossless a given resonance is.

2.4.4 Fabry–Perot Modes

Another fundamental type of resonance, able to exist in any medium for any type of wave whether transverse (e.g. electromagnetic) or longitudinal (e.g. sound), are simple standing waves. A Fabry–Perot (FP) mode is a subcategory of standing waves associated only with confined electromagnetic radiation across the whole EM frequency spectrum. The term originates from a light interferometer (or etalon) developed by Charles Fabry and Alfred Perot in 1896 [109, 110], used to analyse the spectroscopic components of light emission from atoms through standing EM waves. The inter-

ferometer cavity length could be varied until constructive interference of incident light with itself was observed. Then the wavelength could be easily calculated by rearranging

$$L = \frac{m\lambda}{2n}, \tag{2.20}$$

where L is the cavity length, λ is the incident wavelength, m is a positive integer starting from one, and n is the real part of the complex refractive index. For a Fabry–Perot interferometer used in air $n = 1$, however when applying this formula to micro- and nanocavities, it is evident that by using high refractive index materials such as TMDs, one can confine light to much smaller sub-wavelength-sized cavities. At this point it is important to clarify the difference between Fabry–Perot modes and the Mie modes discussed in Section 2.4.2, as they both appear to be sub-wavelength resonances analogous to standing waves. Of course Equation 2.20 governing the propagation of FP modes is very different to that of the Mie multipole moments (Equations 2.9-2.12), but the way the light propagates for the two types of modes can be distinguished more obviously from Figure 2.12. For the case of a cylindrical resonator, the Mie modes primarily reflect from the side walls, propagating back and forth in the direction perpendicular to the incident wave. In contrast, for a cavity system with no lateral confinement, Fabry–Perot modes propagate parallel to the incident wave, travelling between the top and bottom faces of the cavity as in Figure 2.12 (a) and (b). Note that in more complex structures these modes will be less simple to illustrate schematically.

An alternative but equivalent way to define Fabry–Perot modes, is to consider the phase accumulation of the propagating wave per cycle of the resonance. In order for constructive interference to occur, the wave must acquire an integer number of 2π phase after every cycle. Taking into account any phase changes upon reflection from the bottom (ϕ_b) and top (ϕ_t) faces, we can write

$$2nkL + \phi_\mathrm{b} + \phi_\mathrm{t} = 2m\pi, \tag{2.21}$$

where k is the wavenumber and n is the refractive index of the cavity medium, thus the term $2nkL$ defines the phase accumulated over distance $2L$. This formulation will be used later in Section 4.3.2 to model nanoresonators on a substrate, where depending on the substrate material used, there can be different phase changes upon reflection for the top and bottom faces.

2.4.5 Polaritons

Now that I have described both photonic resonances (i.e. Mie and Fabry–Perot modes) and material properties (i.e. TMD excitons), I will introduce the concept of polaritons, which are a quasiparticle consisting half of electromagnetic waves and half of quantised dipolar oscillations. Their initial existence was first proposed by Kirill Borisovich Tolpygo in 1950 [112], who theoretically considered coupling of photons with ionic lattice vibrations, which we now term phonon-polaritons. The term polariton itself was first coined a number of years later by John Hopfield [113], and has now grown into a very active field of research. In this thesis I will focus mostly on surface-plasmon-polaritons which will be described in more detail in Section 2.4.8, however it is helpful to be aware of other types of polaritons that can exist within TMD nanoresonator systems.

One such example is exciton-polaritons, that can be observed through the use of mirrored (or

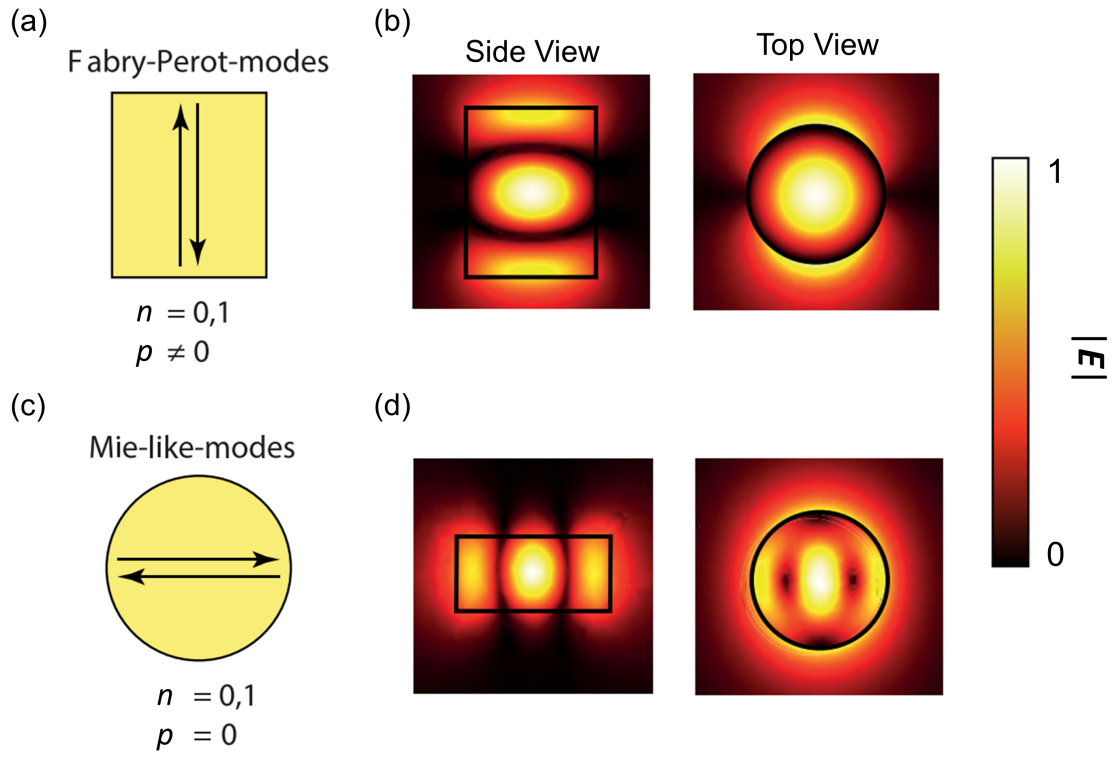


Figure 2.12: **Schematics of different types of photonic resonances in a cylindrical dielectric nanoantenna.** **(a)** Side view of a tall nanoantenna where the illumination is incident from the top down. Double arrows depict the propagation of a Fabry–Perot mode. n and p represent the azimuthal and axial wavenumbers respectively. **(b)** Normalised electric field ($|\boldsymbol{E}|$) profiles through slices of the nanoantenna from the side and top views respectively, showing vertically arranged field maxima indicative of a Fabry–Perot mode. **(c)** Top-down view of a wider nanoantenna showing a Mie-like resonance propagating perpendicular to the incident light. **(d)** Normalised electric field profiles from the side and top views showing horizontally arranged field maxima indicative of Mie-like modes. Adapted from [111].

distributed Bragg reflector-based) microcavities [114–116]. Here, a cavity is used to create a confined photonic mode, i.e. a standing wave, and a material with an optically active exciton is placed inside at the anti-node of the resonance. Through tuning of the cavity length, the photonic mode can be brought into resonance with the exciton energy. At this point two different coupling regimes are possible, either weak or strong coupling [117]. This can depend on several factors such as the overlap of exciton and photonic mode wavefunctions in space, the exciton oscillator strength, and the cavity Q factor [118]. In the weak coupling regime, the two oscillators exchange energy slower than the decoherence time. Physically this means that in general the cavity loses photons to the environment before they can be used to excite the excitons, and the excitons decay non-radiatively (e.g. through phonons) more than they do radiatively, so cannot be trapped in the cavity. The result is that the two oscillators are degenerate in energy and would show a spectral crossing upon tuning the cavity length. In contrast, strong coupling describes the regime where the losses of each oscillator are smaller than the coupling between them, i.e. [118]

$$\Omega > \gamma_{\text{pho}} + \gamma_{\text{exc}}, \tag{2.22}$$

where Ω is the coupling strength between the two oscillators, and γ_{pho}, γ_{exc} are the linewidths of the photonic mode and exciton respectively. This means that the radiative decay of the excitons exceeds the non-radiative rate, and so the emitted photons can be used to pump the cavity mode. In turn, the high Q factor cavity confines the photons well, allowing them to re-excite the excitons before being lost to the environment, thus continuing the cycle. In this case, the energies of each oscillator become non-degenerate and split into a upper and lower polariton branch yielding a spectral anti-crossing upon tuning the cavity length [114, 118].

This behaviour can be described more rigorously by using a coupled oscillator model [117] with the Hamiltonian

$$H = \begin{pmatrix} E_{\text{pho}} & \hbar\Omega \\ \hbar\Omega & E_{\text{exc}} \end{pmatrix} - i\hbar \begin{pmatrix} \gamma_{\text{pho}} & 0 \\ 0 & \gamma_{\text{exc}} \end{pmatrix}, \tag{2.23}$$

where E_{pho} and E_{exc} are the resonance peak energies of the photonic mode and exciton respectively. By solving for the eigenvalues of Equation 2.23, an upper and lower polariton branch emerge. This means that the individual photons and electrons can no longer be distinguished, and thus a combined quasiparticle is observed. From this model the exciton and photon fraction of the polariton can also be calculated, and at the point of minimum energy splitting between E_{pho} and E_{exc}, the system can be considered exactly half material exciton and half cavity photon [118, 119].

Another way exciton-polaritons can be achieved that is more relevant to the work in this thesis, is by using dielectric nanoresonators as a cavity. Mie modes within these nanostructures have also been shown to strongly couple to excitons in materials such as TMDs [102, 120], characterised by anti-crossings in scattering spectra. In this case, no microcavity system is needed as the resonator itself hosts the photonic mode, which can directly interact with excitons inside, thus reducing the size of polaritonic devices by orders of magnitude.

Polariton systems in general offer a solid platform for understanding a vast array of light-matter interactions on the nanoscale, from scaling up quantum phenomena through Bose-Einstein condensation [121], to potential for achieving room-temperature superconductivity [122]. They exhibit advantages of both photonic and excitonic systems, such as low effective mass along with strong non-linear effects [116], making them potentially useful for a range of nanophotonic devices and applications.

2.4.6 Friedrich-Wintgen Bound States in the Continuum

First predicted theoretically by John von Neumann and Eugene Wigner in 1929 [123], bound states in the continuum (BICs) are, by name, a seemingly counter-intuitive phenomena. To understand their physical origin, we must first consider a finite quantum well system. There will exist several discrete (or bound) energy levels within the well, and a continuum of states for energies outside of the well. This is analogous to electrons in semiconductors, where there are bound electrons at discrete energy levels below the band gap, and a continuous spectrum of available energy states in the conduction band. Looking more towards photonics, another analogy is optical waveguides. In this case, the bound states are represented by guided modes existing below the light cone, meaning that photons cannot couple out perpendicular to the waveguide. The continuum of states thus

corresponds to leaky resonances that can escape the waveguide and carry energy away. A BIC, by nature, therefore goes against this logic, existing as a non-leaky resonance within the continuum of states, boasting a theoretically zero linewidth and thus infinite Q factor [123, 124]. This means that BICs do not require external excitation to sustain oscillations, and are often referred to as embedded eigenstates of a system [92]. A schematic is presented in Figure 2.13, depicting bound states, leaky resonances, and BICs.

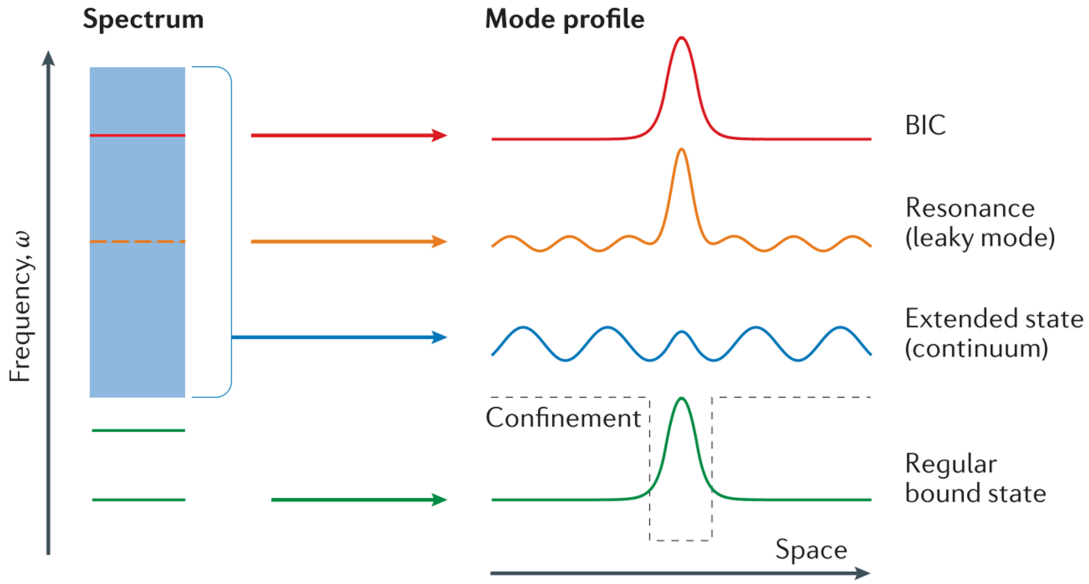


Figure 2.13: **Schematic of the available resonances of a typical quantum system.** Dashed black line depicts the walls of a finite quantum well. Green curve corresponds to a regular bound state within the discrete energy levels that does not couple to the continuum. Blue curve represents the continuum of available energy states outside of the quantum well. Orange curve corresponds to a regular leaky resonance within the continuum that loses energy via coupling to the extended states. Red curve corresponds to a BIC that exists within the continuum of energies but is completely bound and so does not couple to any extended states. Figure from [124].

Since their initial prediction, there have been a plethora of different systems proposed and realised in which many different types of BICs can exist. In this thesis I will focus on two types in particular, first Friedrich-Wintgen BICs [125], and then later in Section 2.6.4, symmetry-protected BICs. Normally these infinite Q factor states exist in periodic structures where at least one dimension extends to infinity, such as 1D coupled waveguide arrays [126], or 2D photonic crystal cavities [127–129]. Friedrich-Wintgen BICs differ in this regard as they can exist in finite-sized structures such as nanoantennas [111, 130–135]. They occur as a result of two different interfering photonic modes (e.g. a Mie and Fabry–Perot mode) in the same spatial location [125] under the strong coupling regime. By varying a continuous parameter, for example nanoantenna radius, the BIC signature is seen as an anti-crossing between two different resonances when tuned to the same energy. The Hamiltonian for the system can be written as [124, 136]

$$H = \begin{pmatrix} \omega_1 & \Omega \\ \Omega & \omega_2 \end{pmatrix} - i \begin{pmatrix} \gamma_1 & \sqrt{\gamma_1\gamma_2} \\ \sqrt{\gamma_1\gamma_2} & \gamma_2 \end{pmatrix}, \tag{2.24}$$

where $\omega_{1,2}$ and $\gamma_{1,2}$ are the resonance frequencies and radiation rates of each mode respectively, Ω represents the coupling between modes, and the term $\sqrt{\gamma_1\gamma_2}$ represents the combined losses of the coupled modes via the continuum. Solving for the eigenvalues of Equation 2.24, it can been shown that under the condition

$$\Omega(\gamma_1 - \gamma_2) = \sqrt{\gamma_1\gamma_2}(\omega_1 - \omega_2), \tag{2.25}$$

one of the eigenvalues become purely real, and the other takes all of the losses [124, 125]. Physically this means that one mode tends to zero linewidth at the point of minimum energy splitting, and thus has an infinite Q factor, whilst the linewidth of the other mode grows to the sum of the linewidths of the original two modes. These high Q factor states have also been termed supercavity modes in literature [130, 132, 137].

A true Friedrich-Wintgen BIC cannot be measured experimentally in the far-field as it perfectly confined and so light cannot couple in or out of the state. However, in reality nanoresonators are not perfectly fabricated and may have some imperfections, thus allowing some light to couple into the BIC. Here it is common to use the term quasi-BIC, as the linewidth will be non-zero and the Q factor will be non-infinite. Deliberate symmetry-breaking has also been carried out by cutting away sections of previously symmetric nanoresonators, thus enabling quasi-BICs to be probed and manipulated more easily [133]. Owing to their well-confined near-fields, quasi-BICs enable strong Purcell enhancement of quantum emitters [135], however they boast a wealth of other properties that are currently under high research effort. For example, quasi-BICs can be tuned for highly directive light scattering [131, 133, 135], they can be used for lasing [132], and can also boost non-linear effects such as second and third harmonic generation [131, 138, 139]. All of these exotic phenomena make BICs an ideal candidate for use in nanophotonic circuits, where their many degrees of freedom can be exploited for advanced control of light on-chip.

2.4.7 Purcell Enhancement

So far I have considered only consequences of light-matter interactions in the strong coupling regime. However, the weak coupling regime also has its advantages. One of these is the spontaneous emission rate enhancement of emitters, also known as Purcell enhancement. This effect was first documented by Edward Purcell in 1946 when studying the radiative lifetimes of nuclear magnetic spins, which appeared to reduce in the presence of a coaxial cable cavity [140]. As it turned out, the nuclear spins experienced weak coupling to the cavity, which increased the local density of photonic states available to emit into, and therefore increased the emission rate [141]. This can be understood by considering Fermi's golden rule [142, 143],

$$\gamma_{\mathrm{i}\to\mathrm{f}} = \frac{2\pi}{\hbar}|\langle \mathrm{f}|H'|\mathrm{i}\rangle|^2\rho(E_\mathrm{f}), \tag{2.26}$$

where $\gamma_{\mathrm{i}\to\mathrm{f}}$ is the radiative rate between the initial $|\mathrm{i}\rangle$ and final $\langle\mathrm{f}|$ states, H' is the perturbing Hamiltonian, and $\rho(E_\mathrm{f})$ is the density of final states at energy E_f. Here it is evident that by increasing the density of final states (i.e. photonic modes to emit into), the radiative rate of the emitter will also increase proportionally. For an emitter within a photonic cavity, there are a finite number of

discrete energy levels available (i.e. Mie or Fabry–Perot modes) as opposed to the continuum of states a vacuum can host. However, the important part is the density of these states, which for quantised cavity energy levels is much larger than the density of states in vacuum. The Purcell factor, F_{P}, can then be defined as the ratio of spontaneous emission of an emitter placed within a cavity $\gamma^{\mathrm{cav}}_{\mathrm{i}\to\mathrm{f}}$, compared to the same emitter within a homogeneous dielectric medium $\gamma^{\mathrm{hd}}_{\mathrm{i}\to\mathrm{f}}$,

$$F_{\mathrm{P}} = \frac{\gamma^{\mathrm{cav}}_{\mathrm{i}\to\mathrm{f}}}{\gamma^{\mathrm{hd}}_{\mathrm{i}\to\mathrm{f}}}. \tag{2.27}$$

This general definition of the Purcell factor is applicable to any emitter placed in any arbitrary photonic environment where the local density of final states is modified. However, another equivalent formulation of the Purcell factor specifically for photonic cavities also exists [140, 141, 144]:

$$F_{\mathrm{P}} = \frac{3}{4\pi^2}\left(\frac{\lambda_0}{n}\right)^3 \frac{Q}{V_{\mathrm{eff}}}, \tag{2.28}$$

where λ_0 is the vacuum wavelength of the emission, n is the refractive index of the cavity material, Q is the cavity quality factor, and V_{eff} is the effective mode volume. This definition can be explained more in terms of what is happening within the cavity physically, rather than through the notion of available energy states. When a photon is emitted from within the cavity at the correct wavelength, it becomes trapped in a photonic mode. Similar to a standing wave, the photon travels back and forth, resonating for a while until it encounters the emitter again. At this point the photon re-drives the oscillations of the emitter, causing a higher rate of spontaneous emission compared to the same emitter in a homogeneous dielectric.

In order to achieve maximal enhancement, one should aim for a high Q factor cavity with a very small effective mode volume as per Equation 2.28. V_{eff} describes how tightly confined the fields of a given cavity mode are, and can be defined as [145]

$$V_{\mathrm{eff}} = \frac{\int \epsilon(\boldsymbol{r})|E(\boldsymbol{r})|^2 \,\mathrm{d}V}{\max[\epsilon(\boldsymbol{r})|E(\boldsymbol{r})|^2]}, \tag{2.29}$$

where $\epsilon(\boldsymbol{r})$ is the electric permittivity of the cavity material as a function of position, $\boldsymbol{r}$, and $|E(\boldsymbol{r})|^2$ is the electric field intensity at position, $\boldsymbol{r}$. This means that to reduce V_{eff}, the maximum field strength of the cavity mode needs to be high. This can be achieved with a strong local change in $\epsilon(\boldsymbol{r})$, for example with a sub-wavelength-sized air slot in a high index photonic crystal cavity [146], or ultra-small gaps between nanoantennas [147]. Geometrical techniques like these enable electric fields to be confined to deep sub-wavelength volumes, significantly beating the diffraction limit with even stronger confinement than typical high index material nanoresonators alone [102, 103].

Unfortunately, the formalism of Equation 2.28 only works for scenarios where the emitter is point-like compared to the size of the cavity. For Mie-resonant structures of sizes on the order of tens of nanometers, this assumption no longer holds as the excitons have considerable Bohr radii of around 1-2 nm [148], and thus Equation 2.28 breaks down. In addition, for arbitrarily-shaped nanostructures a rigorous definition of the effective mode volume is non-trivial to calculate. Therefore, for the nanoantennas and gratings presented in Chapters 4 and 5 of this thesis, I will use the more general form of the Purcell factor from Equation 2.27.

The Purcell effect can be used for enhancing or suppressing the radiative rate of a range of emitters. For example, it is often used to aid quantum dot performance by offsetting their intrinsically low out-coupling efficiency [149–151], or more relevant to the work in this thesis, single photon emitters in TMD monolayers, which have inherently weak emission due to low quantum yield [152–154].

2.4.8 Plasmonics

So far in this section I have focused mainly on the explanation of different types of photonic resonances that exist within purely dielectric nanostructures. Such materials contain bound charges as described in Section 2.4.1, that oscillate and form confined photonic resonances through interaction with an external driving EM field. Many dielectrics can be described macroscopically as having a positive electric permittivity, where EM waves can enter deep within the material whilst experiencing little loss. Metallic nanoresonators on the other hand, contain a vast amount of unbound electrons with no restoring force to any particular lattice site [47]. Together with the positive metal ions, the system can be considered as a neutral plasma, and thus can be described via the Drude-Lorentz model [84, 85, 155],

$$\epsilon_{\mathrm{r}}^{\mathrm{m}}(\omega) = 1 - \frac{\omega_{\mathrm{p}}^2}{(\omega^2 + i\gamma\omega_{\mathrm{p}}^2)}, \tag{2.30}$$

where $\epsilon_{\mathrm{r}}^{\mathrm{m}}(\omega)$ is the relative electric permittivity of the metal as a function of angular frequency, γ is the damping rate, and ω_{p} is the so-called plasma frequency,

$$\omega_{\mathrm{p}} = \left(\frac{Ne^2}{\epsilon_0 m_0}\right)^{\frac{1}{2}}. \tag{2.31}$$

Here N is the number of electrons per unit volume, e is the electronic charge, ϵ_0 is the permittivity of free space, and m_0 is the free electron mass. Assuming no damping,

$$\epsilon_{\mathrm{r}}^{\mathrm{m}}(\omega) = 1 - \frac{\omega_{\mathrm{p}}^2}{\omega^2}, \tag{2.32}$$

and therefore is is possible to obtain a negative permittivity for $\omega < \omega_{\mathrm{p}}$, unlike the case for conventional dielectrics. For most metals, the plasma frequency sits within the ultra-violet spectral range [156], and corresponds to the fundamental resonant frequency of the bulk electron plasma within the metal. By substituting $\omega = \omega_{\mathrm{p}}$ into Equation 2.32, we obtain $\epsilon_{\mathrm{r}}^{\mathrm{m}}(\omega_{\mathrm{p}}) = 0$. Then, by considering Gauss's law (Equation 2.4) with a zero free charge density owing to the neutral plasma, one can write

$$\boldsymbol{\nabla} \cdot \boldsymbol{D} = \boldsymbol{\nabla} \cdot (\epsilon_0 \epsilon_{\mathrm{r}}^{\mathrm{m}} \boldsymbol{E}) = 0. \tag{2.33}$$

Normally, for materials with non-zero permittivity the condition $\boldsymbol{\nabla} \cdot \boldsymbol{E} = 0$ must hold, which forces solutions to be transverse waves such as EM radiation. However, for $\epsilon_{\mathrm{r}}^{\mathrm{m}} = 0$ the opposite is true ($\boldsymbol{\nabla} \cdot \boldsymbol{E} \neq 0$), and so longitudinal waves can become solutions. These manifest in the form of self-sustained, quantised oscillations of the electron plasma in energy units of $\hbar\omega_{\mathrm{p}}$, also known

as bulk plasmons [157]. Since Equation 2.31 only depends on material and physical constants and not the wave vector, the bulk plasmons must be dispersionless. It is important to note that since bulk plasmons oscillate purely longitudinally, transverse EM waves cannot directly couple in to excite them, and so other techniques such as electron energy-loss spectroscopy are required to probe them. This involves using a high energy electron beam to excite plasmons through inelastic scattering [158–160].

Shifting focus back to light propagation in metals, one can visualise the photon dispersion by relating the angular frequency to the wave vector through its speed,

$$\omega^{\mathrm{m}} = \frac{ck}{\sqrt{\epsilon_{\mathrm{r}}^{\mathrm{m}}}}, \tag{2.34}$$

where ω^{m} is the photon angular frequency in a metal with permittivity $\epsilon_{\mathrm{r}}^{\mathrm{m}}$. By now substituting Equation 2.32 into Equation 2.34 we arrive at

$$\omega^{\mathrm{m}} = \sqrt{(ck)^2 + \omega_{\mathrm{p}}^2}, \tag{2.35}$$

corresponding to the angular frequency of a photon in a Drude-Lorentz metal. This dispersion is illustrated by the green line in Figure 2.14 (a), which reaches the plasma frequency at zero wave vector. As the wave vector increases, the photon dispersion in a metal tends to the case of a photon in a dielectric, as depicted by the blue line. Here, the dielectric is modelled with a constant permittivity of unity, hence $\omega^{\mathrm{d}} = ck$, where ω^{d} is the angular frequency of a photon in the dielectric, yielding a linear dispersion. Below the green line, there can be no propagation as a pure photon within the metal. Mathematically this explains why metals appear almost completely reflective below the plasma frequency. Energy must be conserved, and if the photon cannot exist within the metal, it must be reflected or absorbed. Above the plasma frequency the photon is allowed to propagate, and so metals appear transparent at higher frequencies up into the ultra-violet range.

For a more physically intuitive description, one must consider the oscillations of free electrons under an external driving EM wave. For $\omega < \omega_{\mathrm{p}}$, the electron plasma effectively screens the incident wave, yielding an evanescent wave on the inside of the metal that quickly decays as described by its skin depth [162]. At these low frequencies, the electrons can oscillate almost instantaneously in response to the external driving field, however with opposite phase. This has the effect of cancelling the fields out on the inside of the metal, and launching a counter-propagating EM wave on the outside, resulting in near-unity reflection. However, for $\omega > \omega_{\mathrm{p}}$, the incident frequency is too high and so the electrons cannot respond as quickly as in the previous case. This results in an overall lower amplitude of electron plasma oscillations that cannot interact with the incoming wave as strongly, and so the majority is transmitted, as with positive permittivity dielectrics. For the work in this thesis, I will focus on light within the visible spectrum and thus below the plasma frequency, therefore leading to strong reflections.

So far I have only described photons and bulk plasmons which can propagate anywhere within a metal, however another form of plasmon localised to boundaries between metals and dielectrics also exists known as the surface plasmon [163, 164]. In contrast to the purely longitudinal bulk plasmons described before, the field distribution of surface plasmons has components both parallel

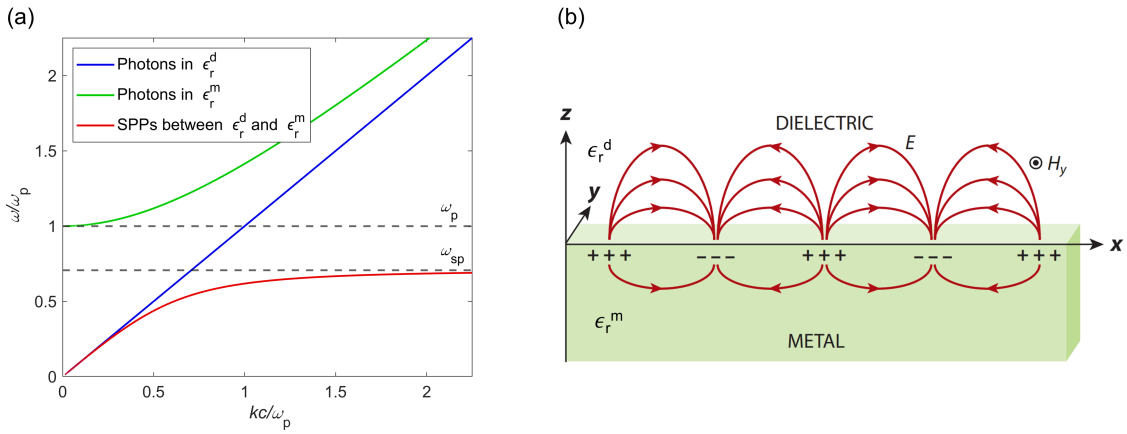


Figure 2.14: **Properties of different plasmon-polaritons in metals. (a)** Dispersion relation normalised to the plasma frequency for photons within a metal with Drude-Lorentz permittivity from Equation 2.30, and surface plasmons-polaritons (SPPs) at the boundary between a metal and a dielectric, shown by the green and red curves respectively. ϵ^{d} and ϵ^{m} correspond to the relative permittivity of the dielectric and metal respectively. Blue curve represents the linear dispersion of photons in a vacuum, also referred to as the light cone. Black dashed lines labelled ω_{p} and ω_{sp} correspond to the plasma frequency and surface plasma frequency respectively. **(b)** Schematic of the electric field lines associated with an SPP propagating in the x direction, showing components both parallel and perpendicular to the propagation direction. Adapted from [161].

and perpendicular to the direction of travel, as depicted in Figure 2.14 (b). This characteristic allows external transverse EM waves to couple in and excite surface plasmons under the condition of wave vector-matching, thus giving rise to a new polaritonic quasiparticle, the surface plasmon-polariton [165, 166].

Their existence can be proved by solving Maxwell's equations for a transverse-magnetic (TM) wave propagating in the x direction along the boundary between a metal of permittivity $\epsilon_{\mathrm{r}}^{\mathrm{m}}$, and a dielectric of permittivity $\epsilon_{\mathrm{r}}^{\mathrm{d}}$ as in Figure 2.14 (b). The system can be described by simple plane waves along the x direction that decay exponentially along z, normal to the interface:

$$\boldsymbol{E}^{\mathrm{d}} = E_{0,j}^{\mathrm{d}} e^{i(k_x^{\mathrm{d}} x - \omega t)} e^{-k_z^{\mathrm{d}} z}, \tag{2.36}$$

$$\boldsymbol{H}^{\mathrm{d}} = H_{0,j}^{\mathrm{d}} e^{i(k_x^{\mathrm{d}} x - \omega t)} e^{-k_z^{\mathrm{d}} z}, \tag{2.37}$$

$$\boldsymbol{E}^{\mathrm{m}} = E_{0,j}^{\mathrm{m}} e^{i(k_x^{\mathrm{m}} x - \omega t)} e^{+k_z^{\mathrm{m}} z}, \tag{2.38}$$

$$\boldsymbol{H}^{\mathrm{m}} = H_{0,j}^{\mathrm{m}} e^{i(k_x^{\mathrm{m}} x - \omega t)} e^{+k_z^{\mathrm{m}} z}, \tag{2.39}$$

where $\boldsymbol{E}^{\mathrm{d,m}}$ and $\boldsymbol{H}^{\mathrm{d,m}}$ are the electric and magnetic field strength vectors in the dielectric and metal respectively, $E_{0,j}^{\mathrm{d,m}}$ and $H_{0,j}^{\mathrm{d,m}}$ are the field amplitudes in direction $j = x, y, z$, and $k_j^{\mathrm{d,m}}$ are the wave vectors in each respective medium for a given direction. We must also apply some boundary conditions across the interface to ensure continuity:

$$E_x^{\mathrm{d}} = E_x^{\mathrm{m}}, \tag{2.40}$$

$$H_y^{\mathrm{d}} = H_y^{\mathrm{m}}, \tag{2.41}$$

$$\epsilon_{\mathrm{r}}^{\mathrm{d}} E_z^{\mathrm{d}} = \epsilon_{\mathrm{r}}^{\mathrm{m}} E_z^{\mathrm{m}}. \tag{2.42}$$

These conditions force the wave vector in the x direction to be the same on either side of the boundary. Finally, by substituting Equations 2.36-2.39 back into Maxwell's equations and enforcing the boundary conditions of Equations 2.40-2.42, one arrives at

$$k_x = \frac{\omega}{c}\left(\frac{\epsilon_{\mathrm{r}}^{\mathrm{d}}\epsilon_{\mathrm{r}}^{\mathrm{m}}}{\epsilon_{\mathrm{r}}^{\mathrm{d}} + \epsilon_{\mathrm{r}}^{\mathrm{m}}}\right)^{\frac{1}{2}}, \tag{2.43}$$

which fully describes the dispersion of surface plasmon-polaritons along the boundary between a Drude-Lorentz metal, where $\epsilon_{\mathrm{r}}^{\mathrm{m}}$ corresponds to Equation 2.32, and a dielectric. This curve is plotted in Figure 2.14 (a) in red and lies entirely below the light cone, meaning that SPPs are a type of guided mode. Owing to the momentum mismatch between the blue and red curves, a photon in the dielectric cannot directly excite an interfacial SPP, and vice versa. Therefore, to excite SPPs with photons, other methods are required such as evanescent excitation via a prism [166], or by introducing local inhomogeneities such as a rough metallic surface [164], or pre-fabricated nanostructures [167–169] to launch the SPPs. From Figure 2.14 (a) it is also evident that the SPP dispersion asymptotes at a certain frequency we denote ω_{sp}. This is named the surface plasma frequency, and corresponds to the fundamental resonance frequency of the electron plasma at a dielectric-metal interface. To find an expression for ω_{sp}, we first take the limit of Equation 2.43 for $k_x \to \infty$, thus giving $\epsilon_{\mathrm{r}}^{\mathrm{d}} = -\epsilon_{\mathrm{r}}^{\mathrm{m}}$ at the surface plasma frequency. Then by substituting into Equation 2.32 we get

$$\omega_{\mathrm{sp}} = \frac{\omega_{\mathrm{p}}}{\sqrt{1 + \epsilon_{\mathrm{r}}^{\mathrm{d}}}}, \tag{2.44}$$

proving that ω_{sp} is always less than ω_{p}. Between these two frequencies there is effectively a band gap where no propagating plasmon modes can exist, only exponentially decaying evanescent fields inside the metal, and strong reflection on the outside.

Surface plasmon-polaritons have proved to be useful for nanophotonics owing to their very strong, sub-wavelength electric field confinement. This opens up possibilities for Purcell enhancement of coupled emitters [169–174], waveguiding [175, 176], switching [177, 178] and sensing [179, 180]. Their main downfall against dielectric resonances, however, is comparatively high losses. This is where hybrid metallic-dielectric devices can help to offset these disadvantages, allowing advanced and efficient control of light-matter interactions at the nanoscale. Characterisation of such hybrid devices will be the main focus of Chapter 4 of this thesis.

2.5 Nanophotonics in 1D Periodic Structures

In this section, I will move away from finite-sized, 0D nanoresonators, to structures that extend quasi-infinitely in a single dimension. A very simple but prominent example in nanophotonics is the 1D grating. However, as I shall detail, the physics of such gratings is extremely diverse, making them an ideal platform for studying a range of light-matter interactions on nanometer length scales. First I will cover the basics of dielectric photonic waveguides, and how they are used to confine and direct light beneath the light cone. I will then build on this concept by introducing a periodic modulation of the refractive index to form a 1D grating, showing how this results in a band-folding of the photonic bands into the light cone. I will also consider the effects of adding diffractive coupling between photonic modes, thus relieving the energy degeneracy at the Γ point and yielding an energy splitting. Finally, radiative losses will be added to the model, resulting in the formation of a symmetry-protected bound state in the continuum. This theory will form the basis for Sections 2.6.4 and 2.6.5 on topological edge states in 1D grating nanostructures, and the experimental results presented in Chapter 5.

2.5.1 Waveguide Modes

Before exploring 1D gratings, we must first understand simple photonic waveguides [181, 182]. Consider a high refractive index dielectric slab suspended in vacuum with thickness t and width l, that extends infinitely in the x direction as shown in Figure 2.15 (a). One can envisage counter-propagating forwards $\langle f|$ and backwards $|b\rangle$ photonic modes trapped within the slab owing to total internal reflection. Here the propagation direction is in x, and the polarisation is along the y axis. The dispersion of these modes can be plotted using

$$E_{\text{wm}} = \hbar \frac{c}{\sqrt{\epsilon_{\text{d}}}} \sqrt{k_x^2 + \frac{p^2\pi^2}{l^2} + \frac{q^2\pi^2}{t^2}}, \tag{2.45}$$

where E_{wm} is the waveguide mode energy, $\hbar$ is the reduced Planck's constant, c is the vacuum speed of light, and ϵ_{d} is the relative permittivity of the dielectric slab, which is assumed to be isotropic. k_x corresponds to the wave vector in the propagation direction, p and q are the integer mode orders in the y and z directions respectively, and l and t correspond to the width and thickness of the slab in the y and z directions respectively. Equation 2.45 is plotted in Figure 2.15 (b) for a waveguide with parameters $l = 200$ nm and $t = 100$ nm for three different mode orders, depicting the allowed energies of propagation for given wave vectors within the slab. The fundamental waveguide mode of lowest energy is plotted in orange, labelled $p = 0, q = 0$, and shows a completely linear dispersion in wave vector space. As the mode order increases, the dispersions become more parabolic at low $|k_x|$, eventually tending towards the same linear gradient as the fundamental mode when $|k_x|$ is increased. The dispersion for photons in vacuum ($\epsilon_{\text{vac}} = 1$) is plotted in blue, and defines the boundaries of the light cone. Anything outside of the light cone cannot couple in or out of the slab as there are no matching free space photon wave vectors for the same energy. Therefore, the orange, green, and red dispersions lie expectedly below the light cone, since the photons are completely trapped within the structure. This makes waveguide modes very useful for directing light around a

chip, like with electrical wires in a computer. However, another component is needed for inserting and extracting photonic signals if they are to be used in computing, i.e. a grating coupler.

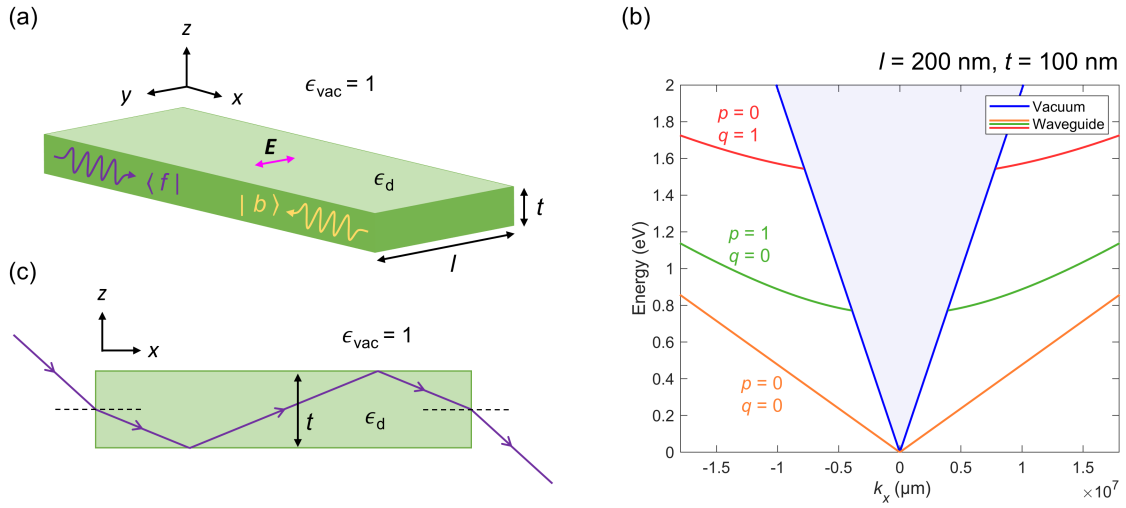


Figure 2.15: **Visualisation of photonic waveguide modes. (a)** Schematic of a vacuum-suspended slab waveguide of thickness t, width l, and permittivity ϵ_d, that extends infinitely in the x direction. $\langle f|$ and $|b\rangle$ correspond to the forwards and backwards propagating modes respectively in the x direction, with polarisation of the electric field, $\boldsymbol{E}$, along the y axis as denoted by the pink double arrow. **(b)** Normalised dispersion relations with respect to the wave vector along the x axis of a slab waveguide with $l = 200$ nm and $t = 100$ nm. Blue lines correspond to photons propagating in vacuum, i.e. the light cone. Orange, green, and red curves correspond to waveguide modes of increasing order denoted by integers p and q for the y and z directions respectively. Guided modes lie outside of the light cone for all wave vectors and orders. **(c)** Side view of a finite-sized waveguide depicting total internal reflection along x. Light can only enter and exit via the end faces for a relatively small range of angles. Dashed lines represent surface normals of the end faces.

2.5.2 Grating Modes

If we now consider the slab from Section 2.5.1 did not extend infinitely in x, the modes would be able to partially transmit through the end faces and couple out for a small range of angles as in Figure 2.15 (c). Extending this concept further, to induce more out-coupling along the whole length of the structure, additional end faces are needed along x. One can therefore introduce a periodic modulation of the refractive index as shown in Figure 2.16 (a), where the refractive index of the gaps between grating segments is unity to mimic that of air. Here we define the grating axis as parallel to the high index wires, i.e. along y. A propagating wave perpendicular to the grating axis now experiences many dielectric-air boundaries on its way through the structure as in Figure 2.16 (b), being partially reflected and transmitted (with refraction) at each. For certain wavelengths and wave vectors, these multiple reflections and refractions will result in light being ejected from many locations along the structure, not previously possible with only two end faces. In addition, light can be coupled in and out at much greater angles compared to a standard waveguide, thus allowing detection via conventional far-field optics. Similar to an optical fibre, a waveguide can only sustain total internal reflection for a narrow range of incident angles. In contrast, a grating is formed of many nanoscale segments, which each act similar to the Mie resonators discussed in Section 2.4.2.

Therefore, light incident completely normal to the grating plane can excite collective resonances of the bound charges in the structure which scatter over a range of angles, including perpendicular to the source. In reverse, we thus expect gratings to be able to couple normally purely in-plane waveguide modes to the far-field, hence pushing their dispersions into the light cone as in Figure 2.16 (c). Here, only the fundamental grating mode is considered for simplicity, however higher order modes also follow the same principles.

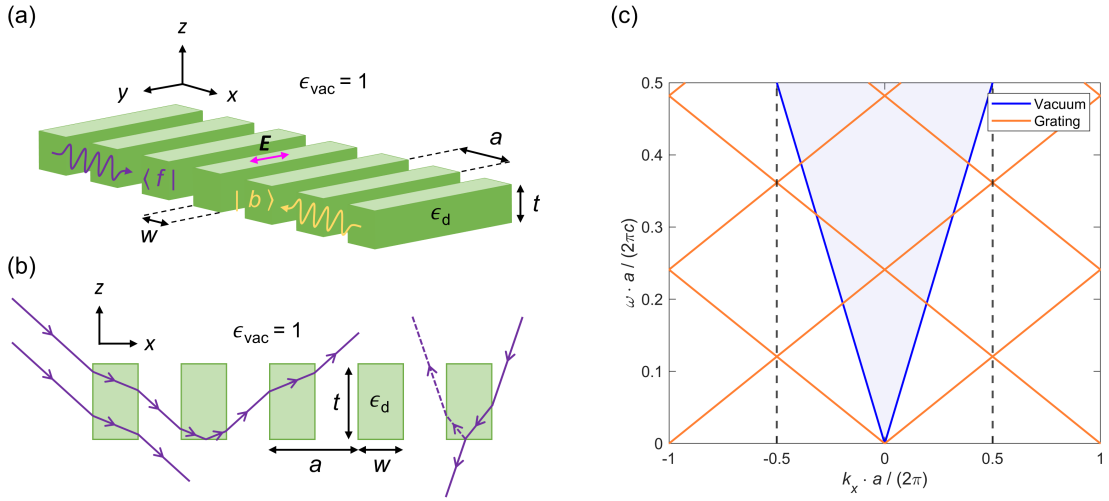


Figure 2.16: **Visualisation of photonic grating modes. (a)** Schematic of vacuum-suspended grating structure with periodically varying refractive index between unity (air) and ϵ_d. Structure is characterised by parameters t, a, and w, corresponding to the thickness, grating period, and segment width respectively. As with the waveguide structure, there are forwards $\langle f|$ and backwards $|b\rangle$ propagating modes polarised along y as shown by the pink double arrow. **(b)** Side view of the grating structure depicting the multiple reflections and refractions now possible as opposed to a slab waveguide. Dashed purple line represents partial reflection. **(c)** Normalised dispersion relation with respect to the wave vector along the x axis. Blue and orange lines correspond to photons propagating in vacuum (i.e. the light cone), and in the grating depicted in **(a)** respectively. A band-folding effect is seen where dispersions from adjacent segments of the grating overlap within the light cone, enabling free-space photons to couple in and out. Black dashed lines represent the edges of the 1st Brillouin zone at $\pm\pi/a$.

Since the structure is periodic in real space, it must also be periodic along the same direction in reciprocal space (k_x), analogous to having many small waveguides placed in a line. This means that the dispersions from Figure 2.15 (b) can be repeated every $2\pi/a$, where a is the length of each unit cell, also known as the grating period. The modes are therefore band-folded into the first Brillouin zone by the grating [183, 184], causing them to now pass through the light cone and couple to the radiative continuum as in Figure 2.16 (c). This results in a band structure similar to that of electrons subject to a periodic lattice potential, e.g. in a dielectric as described previously in Sections 2.3.1 and 2.3.2. However, in this case the electrons are switched for photons, and the periodic lattice potential is switched for a periodic refractive index modulation.

2.5.3 Diffractive Coupling

So far I have considered a simple model which neglects any coupling between the forwards and backwards modes within the grating. However, in reality there is an energy exchange between the two modes, and so they cannot be degenerate in energy for the same wave vector. This can be proved mathematically by constructing a Hamiltonian for the two modes with a coupling strength between them, U:

$$H = \begin{pmatrix} E_0 + E_{\text{wm}} & U \\ U & E_0 - E_{\text{wm}} \end{pmatrix} + i\hbar\gamma \begin{pmatrix} 1 & 1 \\ 1 & 1 \end{pmatrix}, \tag{2.46}$$

where E_0 is the mid-gap energy, and γ represents the radiative losses of the system. I later show the validity of this model in Chapter 5, where excellent agreement with simulations and experimental data of the dispersions from WS_2 gratings is observed. The eigenvalues of Equation 2.46 are then given by

$$E_{\text{up,lo}} = E_0 + i\hbar\gamma \pm \sqrt{E_{\text{wm}}^2 + U^2 - \hbar^2\gamma^2 + 2i\hbar\gamma U}, \tag{2.47}$$

which forms two distinct upper and lower energy branches $E_{\text{up,lo}}$, different to the two uncoupled forwards and backwards modes before. It is no longer useful to think about $\langle f|$ and $|b\rangle$ as in this model, they are now strongly coupled and indistinguishable. The new upper and lower energy modes are plotted in Figure 2.17 (a), which shows a clear energy splitting for $k_x = 0$. Physically, this is analogous to a Bragg mirror, where constructive and destructive interferences between the many reflections from each layer result in a stop band of wavelengths that incur unity reflection [185, 186].

Interestingly, the lower energy branch appears to disappear with a vanishing linewidth at the Γ point ($k_x = 0$), as in Figures 2.17 (a) and (b). This can be explained by looking at the eigenvalues from Equation 2.47. By setting k_x to zero we find that

$$E_{\text{up}} = E_0 + U + 2i\hbar\gamma, \tag{2.48}$$

$$E_{\text{lo}} = E_0 - U, \tag{2.49}$$

proving that the lower energy mode becomes completely lossless, and therefore has zero linewidth. To make up for this, the upper energy branch takes on all the losses of the system, and so increases in linewidth as in Figures 2.17 (a) and (b). In this case, the lower energy branch is termed a symmetry-protected BIC [124, 187–190] at $k_x = 0$, and is inaccessible to light at normal incidence. The only way to access it without changing the structure is via angle-resolved measurements, where $|k_x|$ is increased to effectively break the symmetry and reveal a quasi-BIC [190, 191]. These type of BICs are fundamentally different from those discussed in Section 2.4.6 as they can only exist in high-symmetry periodic structures [124, 136], and will be discussed in more detail in Section 2.6.4.

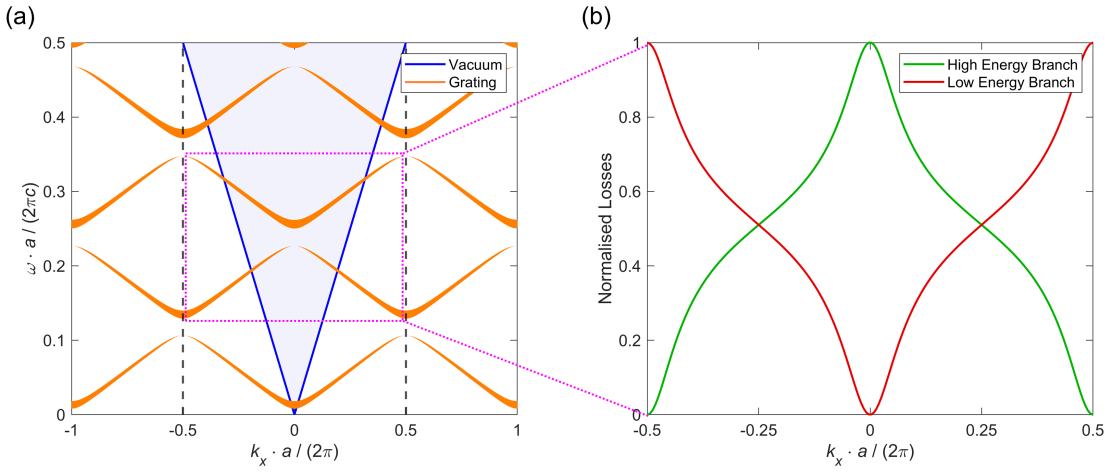


Figure 2.17: **Mode dispersion of gratings including radiative losses. (a)** Dispersion relation using the eigenvalues from Equation 2.47. Blue lines depict the edges of the light cone, and orange curves are the upper and lower coupled energy eigenmodes with linewidths equal to the losses. In this case, the upper energy branches take all the losses at $k_x = 0$ shown by their broad linewidth, and the lower energy branches become symmetry-protected BICs with zero linewidth. Anti-crossings are seen at all points where the previously uncoupled forwards and backwards modes from Figure 2.16 (c) intersect. **(b)** Normalised losses of the upper (green) and lower (red) energy branches enclosed by the pink dashed box in **(a)**. As one mode reaches zero losses, the other reaches its maximum and vice versa.

2.6 Topological Photonics in 1D Periodic Structures

The following section will discuss the theory behind the rapidly evolving field of topological photonics, which promises unprecedented quality on-chip waveguiding and light manipulation owing to intrinsically high robustness to defects, and complete protection against back-reflection. The concept of topology itself, however, can seem rather abstract at first. Therefore, I will begin by explaining the mathematical definition of topology with visual examples in geometry. This will then lead into my discussion of the discovery of topological insulators, which are insulating in the bulk, but host highly robust conductive surface electronic states. I will then focus on analogies of this regime to photons in periodic crystals, from which the field of topological photonics was born. More specifically, I will describe the topological nature of previously mentioned symmetry-protected BICs in 1D grating nanostructures, before finishing with a discussion of their role in the formation of highly localised Jackiw-Rebbi edge states.

2.6.1 Introduction to Topology

In mathematics, topology concerns the study of geometrical parameters under continuous deformation of a closed surface without tearing, joining, or passing through itself. A classic example is the doughnut and coffee mug as depicted in Figure 2.18 (b). The doughnut (or torus) can gradually morph into a coffee cup without performing any of the stated forbidden actions and vice versa. Therefore, the two objects are considered to be topologically identical. In contrast, a sphere can never deform into a torus without puncturing a hole in the structure, and so spheres and toruses are

topologically distinct from one another.

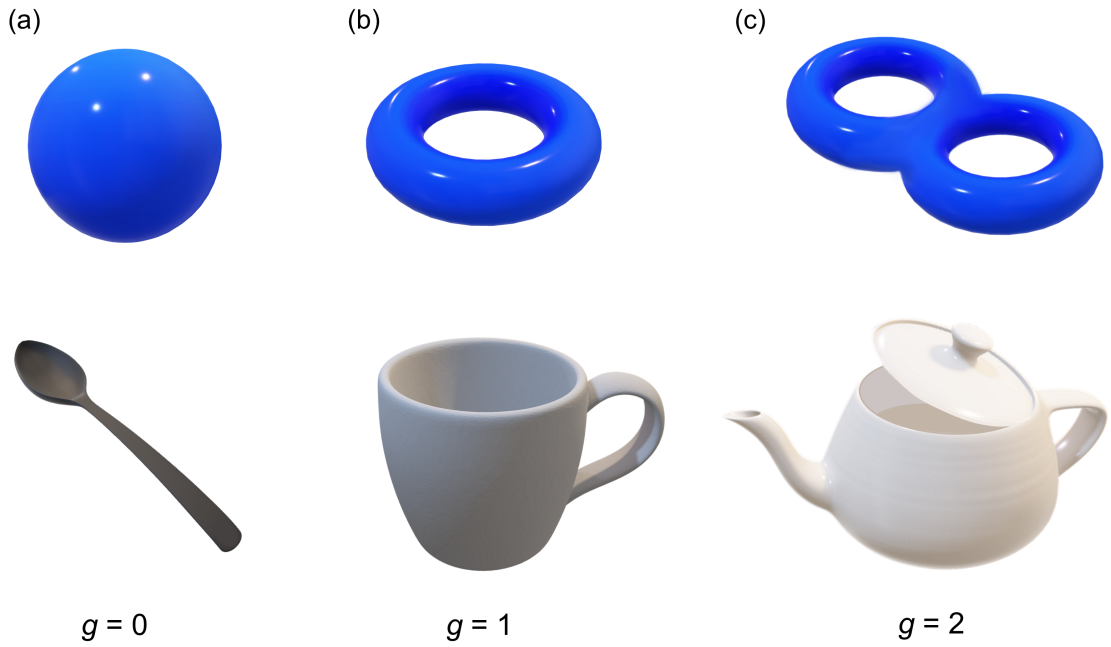


Figure 2.18: **Schematic of various basic topological geometries along with everyday objects with the same corresponding topological invariant g. (a)** Sphere and a spoon both have a genus of 0 as there are no holes in either. **(b)** Torus and mug have a single hole and therefore a genus of 1. **(c)** Linked toruses and teapot both have two holes and a genus of 2. Each basic geometry in the top row can be continuously deformed into its corresponding everyday object in the bottom row without tearing points apart, joining points, or passing points through each other.

Importantly, for any object this property can be quantised into an integer known as a topological invariant. In the case of geometry, this topological invariant is known as the genus, and describes the number of holes within a closed surface. More rigorously, this can be defined using the Gauss-Bonnet theorem [192],

$$\frac{1}{2\pi}\oint_S \kappa \, \mathrm{d}A = 2(1-g), \tag{2.50}$$

where κ is the Gaussian curvature of a 2D closed surface S integrated over its surface area A, and g is the genus. This results in $g_{\text{sphere}} = 0$ and $g_{\text{torus}} = 1$ as expected. Topological invariants are thus useful ways to condense many geometrical parameters down into a single number for simplifying problems where their exact shape and size do not matter, but their general form does. I will now link this concept to the motion of electrons within special types of materials known as topological insulators, where interesting macroscopic behaviour can result.

2.6.2 Topological Insulators

In order to understand how topological concepts can be applied photonics, I must first cover a brief introduction to the formerly discovered field of topological insulators, from which several analogies can be made. From a macroscopic standpoint, topological insulators are insulating materials in the bulk, but host conductive and non-dissipative electronic states around their edges (in 2D) or surfaces

(in 3D), which are highly robust to defects or changes in device geometry. Furthermore, such edge states can display spin-selective chirality, where electrons of different spins are forced to propagate in opposite directions and are therefore completely immune to back-reflection. The reason behind these unique properties is in the topological phase of the material and its surroundings.

As a brief recap, ordinary (trivial) insulators contain charges strongly bound to lattice sites with a significant energy gap between the filled valence, and empty conduction bands as depicted in Figures 2.19 (a) and (b). The first experimental observation of topological phases in condensed matter was by Klaus von Klitzing *et al.* in 1980, where they measured the quantum Hall effect in a 2D electron gas within a silicon metal-oxide-semiconductor field-effect transistor [35]. This involved applying a strong magnetic field perpendicular to the 2D electron gas plane, therefore causing the confined electrons to move with circular in-plane orbits at a cyclotron frequency ω_c. A schematic is shown in Figure 2.19 (d), along with the resulting energy band structure in the form of quantised Landau levels in Figure 2.19 (e) as given by

$$E_m = \hbar\omega_c\left(m + \frac{1}{2}\right), \tag{2.51}$$

where $m = 0, 1, 2, ...$ Upon application of an electric field, a quantised Hall voltage [193] was measured giving an extremely well-defined Hall conductivity of

$$\sigma_{xy} = \frac{Ne^2}{h}, \tag{2.52}$$

where N is an integer corresponding to the number of filled Landau levels [194]. σ_{xy} is completely unaffected by device geometry, and so similar to the genus in Section 2.6.1, N represents a topological invariant of the quantum Hall (QH) conducting state.

Another interesting observation was that the QH states were found to be localised entirely around the edges of the 2D electron gas. To understand why this happens I must first introduce the concept of geometric phase, also known as Berry phase [195]. Consider a quantum system that is varied continuously and gradually in k-space, so that the eigenstate, $|\psi(\boldsymbol{k}(t))\rangle$, slowly adapts to the new parameters over time t, and thus always has a well-defined energy eigenvalue. This is known as an adiabatic transformation [196]. Now constrain the transformation to a closed loop back to the original eigenstate between time $t = 0$ and $t = t_f$, thus giving $|\psi(\boldsymbol{k}(0))\rangle = |\psi(\boldsymbol{k}(t_f))\rangle$. The total phase gained over this closed loop in parameter space must also be accounted for. This is comprised of two contributions, namely the dynamic and geometric (Berry) phases [195, 197]. The dynamic phase is simply the phase gained over the time taken to complete the closed loop, whereas the geometric phase is independent of time and depends only on the path taken through parameter space. The consequence of this adiabatic transformation is that a system can remain in the same quantum state, but gain an additional phase,

$$|\psi\rangle \rightarrow e^{(i\phi_B - iEt/\hbar)}\,|\psi\rangle\,, \tag{2.53}$$

where $e^{-iEt/\hbar}$ is the dynamic phase contribution, and ϕ_B is the Berry phase. Integrated around a closed loop in k-space L, the Berry phase is given by

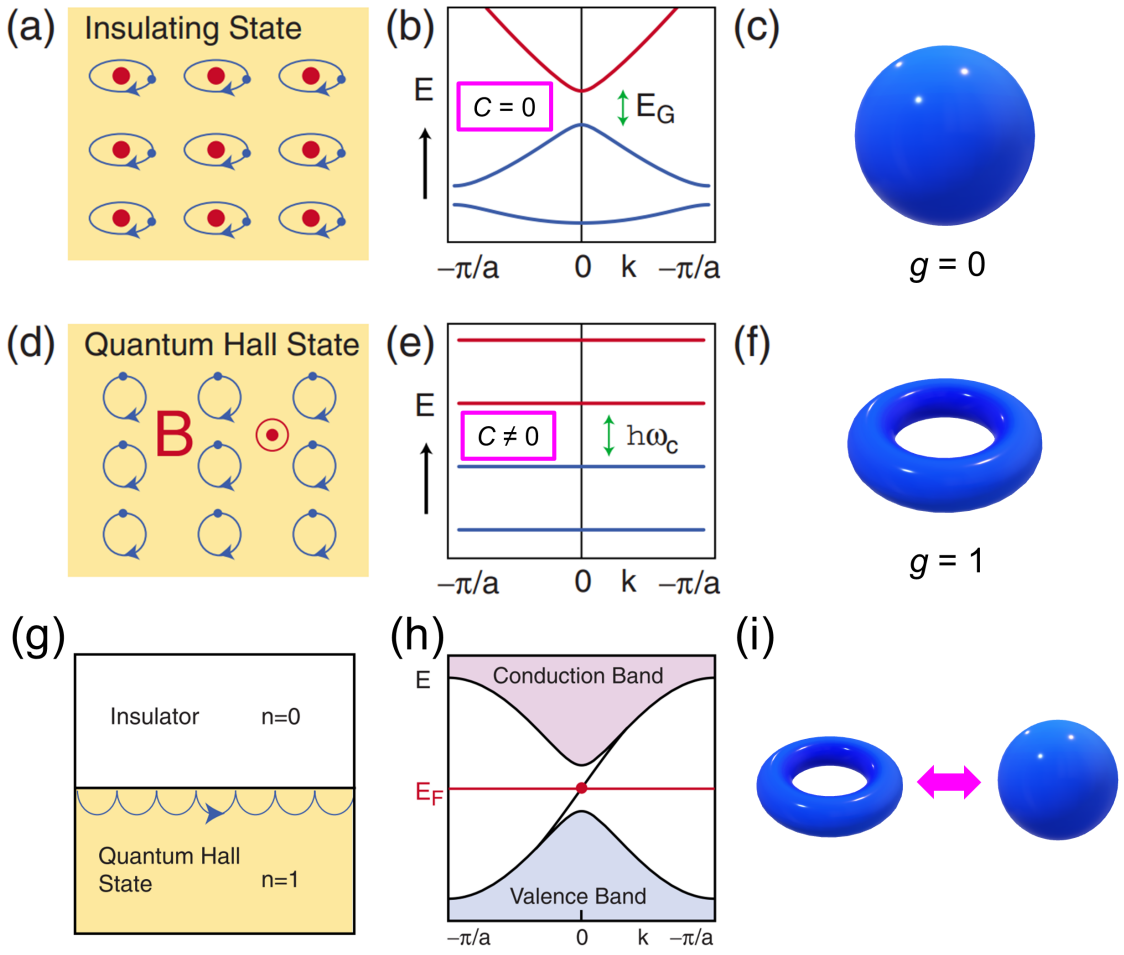


Figure 2.19: **Comparison of topological and trivial insulators. (a)** Schematic of electrons (blue) bound to an ionic lattice (red) in a trivial insulator. **(b)** Band structure of trivial insulator showing a distinct energy gap E_{G} and a Chern number C of zero as denoted by the pink box. **(c)** Comparison to geometrical topology with a sphere of genus zero. **(d)** Schematic of electrons in a 2D electron gas under a strong perpendicular magnetic field B resulting in a topological quantum Hall state. **(e)** Band structure of topological quantum Hall state comprised of discrete Landau levels. Chern number for topological insulators is non-zero. **(f)** Torus as a non-zero genus geometrical analogy. **(g)** Schematic of a trivial insulator (top) in contact with a topological insulator (bottom) hosting a conducting, edge-localised quantum Hall state. Electron moves in a skipping motion in one direction only. **(h)** Band structure showing unidirectional dispersion of the edge state resulting from a closing of the band gap at the interface between the two topologically distinct insulators. E_{F} denotes the Fermi level. **(i)** Geometrical topology analogy showing how a torus can only turn into a sphere by closing the hole and thus changing the genus, and vice versa. Adapted from [194].

$$\phi_{\mathrm{B}} = i \oint_L \langle \psi_m(\boldsymbol{k}) | \nabla_{\boldsymbol{k}} | \psi_m(\boldsymbol{k}) \rangle \, \mathrm{d}\boldsymbol{k}, \tag{2.54}$$

where the function

$$\boldsymbol{\mathcal{A}}_m(\boldsymbol{k}) = i \langle \psi_m(\boldsymbol{k}) | \nabla_{\boldsymbol{k}} | \psi_m(\boldsymbol{k}) \rangle \tag{2.55}$$

is known the Berry connection. A classical analogy to this is the Foucault pendulum [198]. The

pendulum always acquires some dynamic phase as it swings, however its geometric phase depends on is location on Earth. By changing the latitude, the pendulum will trace a different path in real space as the Earth rotates, and thus gains a different geometric phase.

Returning to the quantum Hall effect, the cyclical motion of the electrons results in an acquired Berry phase, which is gauge invariant and an observable quantity. The Berry curvature for a given energy state m can then be defined as the curl of the Berry connection,

$$\boldsymbol{\mathcal{F}}_m(\boldsymbol{k}) = \nabla_{\boldsymbol{k}} \times \boldsymbol{\mathcal{A}}_m(\boldsymbol{k}). \tag{2.56}$$

In analogy with the Gaussian curvature of a 2D manifold from Section 2.6.1, by integrating the Berry curvature over the entire surface of the Brillouin zone (i.e. a torus), and summing over all N filled Landau levels, a topological invariant known as the total Chern number is defined [194]:

$$C = \sum_{m=1}^{N} \frac{1}{2\pi} \int_{\mathrm{BZ}} \boldsymbol{\mathcal{F}}_m(\boldsymbol{k})\, \mathrm{d}^2\boldsymbol{k}. \tag{2.57}$$

Relating this back to Equation 2.52, it is found that N and C are in fact equivalent [199], thus proving the topological nature of the quantum Hall conducting state.

Similar to the genus of geometrical objects in real space, the Chern number allows for the topology of different condensed matter systems in k-space to be rigorously defined. If one calculates the Chern number for trivial insulators such as air, it is different to that of topological insulators such as the 2D electron gas under a strong magnetic field studied by von Klitzing *et al*. This means that they are topologically distinct, and there is no way to adiabatically transform one regime into the other. Looking back to the band structures in Figures 2.19 (b) and (e), the trivial insulator has a Chern number of zero, however for the topological insulator $C \neq 0$, similar to the genus of the sphere and torus in Figures 2.19 (c) and (f) respectively. The trivial band structure cannot continuously deform into a topological band structure without closing the band gap and reopening, which is forbidden during adiabatic transformation, analogous to joining or tearing points on a 2D manifold. Therefore, placing a topological insulator in air creates a boundary between two different topologies where the band gap must close as shown in Figure 2.19 (h). A closed gap means that electrons can very easily be excited to the conduction band, and so a conducting edge state is formed. The unidirectional motion of the electrons at the boundary is depicted in Figure 2.19 (g). They are described by a skipping motion which can be visualised by imagining the quantum Hall state cyclotron orbits from Figure 2.19 (d) being constrained to an edge and thus cut in half. The electrons must remain within the topological insulator, and thus effectively bounce off the boundary moving in a single direction around the entire edge [194].

One of the main drawback of von Klitzing's findings on quantum Hall states, was the very strong magnetic field of 18 T required to sustain the state [35]. Later in 1988, Haldane proposed a model of observing topological conducting edge states on a 2D honeycomb lattice, namely graphene-like systems, without the requirement of an external magnetic field and associated Landau levels [200]. The model worked via local internal magnetic fields where the net magnetic flux through each unit cell summed to zero. Following on from this, electron spin-orbit coupling was discovered to lead to a similar effect without the presence of any internal or external magnetic fields in so-called

spin Hall insulators [201]. A more experimentally practical model was later developed in 2005 by Kane and Mele, who developed Haldane's model by adding spin-orbit coupling effects [202]. They predicted graphene-like systems to become spin Hall insulators at low temperatures, with a topologically insulating bulk phase, and conducting quantum spin Hall (QSH) states around the edges that are non-dissipative and insensitive to disorder. Another seminal example of a topological insulator is the HgTe quantum well. It was first theoretically proposed to support chiral QSH states by Bernevig *et al.* in 2006 [203], and subsequently became the first topological insulator to be experimentally confirmed, without the need for an external magnetic field, a year later [204].

2.6.3 Topological Photonics

Extensive research into topological insulators set up most of the ground work for the prediction and realisation of topological photonics platforms. Similar with analogies between electronic and photonic band structures, it was theoretically shown by Haldane and Raghu that photonic bands in structures with periodic refractive indices could also be characterised by topological invariants [33, 34]. As with topological insulators, by placing a system with a topological photonic band structure in contact with one of trivial band structure, the band gap must close at the interface to change the Chern number, thus resulting in a robust, unidirectional, edge-localised state. This was observed experimentally by Wang *et al.* in 2009, at the interface between a metal and a gyromagnetic 2D photonic crystal [36].

For trivial integrated photonic circuits, back-reflection is a major issue causing both loss of signal strength, and undesirable interference effects within components such as waveguides. Now add to this imperfections in the fabrication, and consider single photon sources such as those required for quantum computing, and one can envisage the difficulty in reliably manipulating and transporting light with such nanophotonic devices. The emerging field of topological nanophotonics is thus a huge leap forward, providing not only immunity to back-reflection and device imperfections, but an additional degree of freedom along with polarisation, wavelength, phase etc. for further advanced control of light. The effects of photonic band topology have already been exploited in a number of systems, including waveguide arrays [205, 206] for applications in on-chip quantum computing; in coupled resonators [207–209], promising uses in optical filters and switches, as well as robust single photon sources; and in polaritonic systems [210–212], showing unidirectional propagation, lasing, and potential for enhancing non-linear effects. My focus will be to explore how the photonic band topology associated with symmetry-protected BICs in a 1D dielectric grating, can lead to highly-localised Jackiw-Rebbi edge states which can greatly enhance coupled emitters.

2.6.4 Symmetry-Protected Bound States in the Continuum

In Section 2.5.3, I discussed how diffractive coupling between photonic modes in a 1D grating can lead to an energy splitting at zero wave vector. By accounting for radiative losses, the eigenvalues defined in Equations 2.48 and 2.49 describe a lossy mode with double the linewidth of the original uncoupled modes, and a zero linewidth mode known as a symmetry-protected BIC. Figure 2.20 (a) presents the simulated angle-resolved reflectance from a lossless dielectric grating with refractive index $n = 3$, period $a = 500$nm, thickness $t = 100$ nm, and filling factor $FF = 0.7$. The lossy

mode and BIC are clearly observed at $k_x = 0$, labelled in yellow and purple respectively, with strong agreement to the model plotted in Figure 2.17 using Equation 2.46. This type of BIC can only occur in systems with inherent reflection or rotational symmetry [124, 129, 190], thus distinguishing them from the previously described Friedrich-Wintgen BICs [125] from Section 2.4.6, that can exist in any shaped resonator but only under careful parameter tuning [124, 213]. As with any other type of BIC, symmetry-protected BICs are completely confined to their host structure with no coupling to external radiation channels, thus leading to an infinite quality factor. However, rather than being described by two photonic modes that have been tuned to achieve complete destructive interference outside of a structure like a Friedrich-Wintgen BIC, symmetry-protected BICs are non-radiative owing to an inherent symmetry mismatch between their mode profile and that of external far-field radiation channels [128, 129, 214–216]. This can be seen in Figure 2.20 (c) for a symmetry-protected BIC hosted within a 1D grating, where the mode profile is anti-symmetric about the unit cell and thus does not couple to the continuum [215, 216]. In contrast, the lossy mode is symmetric, and therefore able to couple to radiative states and propagate away as in Figure 2.20 (b). Because of this symmetry condition, symmetry-protected BICs can only occur at the Γ point.

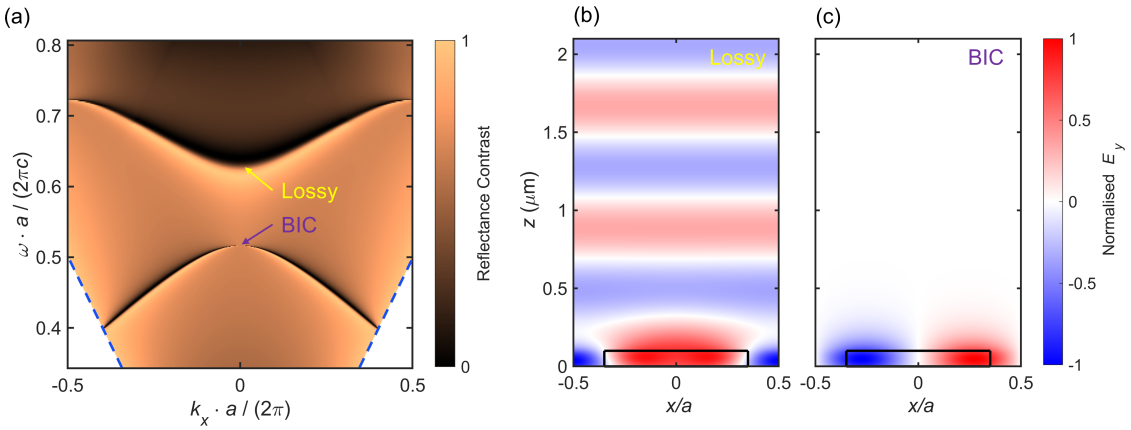


Figure 2.20: **Visualisation of electric field profiles associated with symmetry-protected BIC and corresponding lossy grating mode. (a)** Simulated angle-resolved reflectance contrast of a lossless dielectric grating with refractive index $n = 3$ suspended in air under incident illumination. Grating period, thickness, and filling factor are 500 nm, 100 nm, and 0.7 respectively. Broad linewidth lossy mode (labelled in yellow) can be seen on the upper energy branch, along with a zero linewidth symmetry-protected BIC (labelled in purple) on the lower energy branch at the Γ point. Blue dashed lines denote the edge of the light cone. **(b), (c)** Normalised y component of the electric field in the x-z plane for the lossy and BIC modes respectively. Grating unit cell outlined in black. Lossy mode shows a symmetric field pattern about the centre of the unit cell with clear coupling to outgoing waves in the positive z direction. BIC exhibits an anti-symmetric field pattern, with no coupling to the continuum.

Another type of BIC that can occur in periodic structures is the accidental BIC [124, 128, 129, 217, 218]. These states differ from symmetry-protected BICs in that they are not determined by the geometrical symmetry of the unit cell, and therefore are not limited to the Γ point. Like Friedrich-Wintgen BICs, they exist owing to a destructive interference effect between several photonic modes brought into resonance via so-called accidental symmetries of the system [128, 217]. However, unlike Friedrich-Wintgen BICs, they do not require precise geometrical parameter tuning to exist,

with any small structural changes simply resulting in a shift of the accidental BIC in k-space [129]. As with symmetry-protected BICs, since they are robust to changes in the resonator geometry, one must consider that there could be topological effects at play. The work I present later in this thesis consists only of Friedrich-Wintgen and symmetry-protected BICs, and so I do not describe accidental BICs in depth here, however their existence is important to note, and I direct the reader to Refs. [128, 217, 218] for further information.

Pioneering work by Bo Zhen *et al.* in 2014 unveiled the topological nature of both symmetry-protected and accidental BICs in 2D photonic crystals [129]. Figure 2.21 (a) shows a schematic of the scattered light from a photonic crystal propagating in the direction given by the wave vector $\boldsymbol{k}$. The polarisation direction is therefore given by the orthogonal vector $\boldsymbol{E}$, with in-plane components E_x and E_y. For a BIC, there can be no out-of-plane wave vector, and so the condition $E_x = E_y = 0$ must hold. By plotting the in-plane polarisation vector $\boldsymbol{E}_{//}$ in 2D k-space (grey double arrows in Figure 2.21 (b)), one can visualise where BICs will arise via the intersection of so-called nodal lines. These are given by the green and red curves corresponding to $E_x = 0$ and $E_y = 0$ respectively. In the leftmost panel of Figure 2.21 (b), the nodal lines do not cross, therefore no BIC exists for this system. This is in contrast to the other three panels, which have at least one crossing and therefore a BIC depicted by the filled red circle. The key finding by Zhen *et al.*, however, was that $\boldsymbol{E}_{//}$ winds around a BIC in a counter-clockwise closed loop in k-space, characterised by an integer topological invariant q. This is known as the winding number and is given by [129]

$$q = \frac{1}{2\pi} \oint_L \nabla_{\boldsymbol{k}} \cdot \phi(\boldsymbol{k}) \, \mathrm{d}^2\boldsymbol{k}, \tag{2.58}$$

where $\phi(\boldsymbol{k}) = \arg[E_x(\boldsymbol{k}) + iE_y(\boldsymbol{k})]$ is the angle of $\boldsymbol{E}_{//}$, and L represents a counter-clockwise closed loop in k-space. The winding number has a very similar form to both the genus and Chern number in Equations 2.50 and 2.57 respectively, and is a global property of the BIC, thus remaining constant under small structural changes.

The winding behaviour of the polarisation vector around a BIC is known as a polarisation vortex [124, 129, 218], and q is exactly the number of times $\boldsymbol{E}_{//}$ makes a full 2π rotation in a single closed loop in k-space. Looking back to Figure 2.21 (b), the leftmost panel with no BIC shows no full rotation of $\boldsymbol{E}_{//}$ and thus has a winding number of zero. The two central panels have $q = \pm 1$ as the polarisation rotates in opposite directions around the same closed loop, giving two topologically distinct states. Finally, the rightmost panel depicts two full clockwise rotations of $\boldsymbol{E}_{//}$ and thus $q = -2$. In this way, the existence of a BIC can be experimentally confirmed via measurement of the winding of its far-field polarisation response, and thus its topological charge can be calculated. The topological nature of symmetry-protected BICs further adds to the possible applications of such states. As well as lasing [219–221], non-linear effect boosting [222–225], and Purcell enhancement [226], all possible with Friedrich-Wintgen BICs, the topology of symmetry-protected BICs allows for more exotic phenomena such as vector beams [227, 228], and the realisation of robust, highly localised, unidirectional propagating edge modes ideal for waveguiding [229].

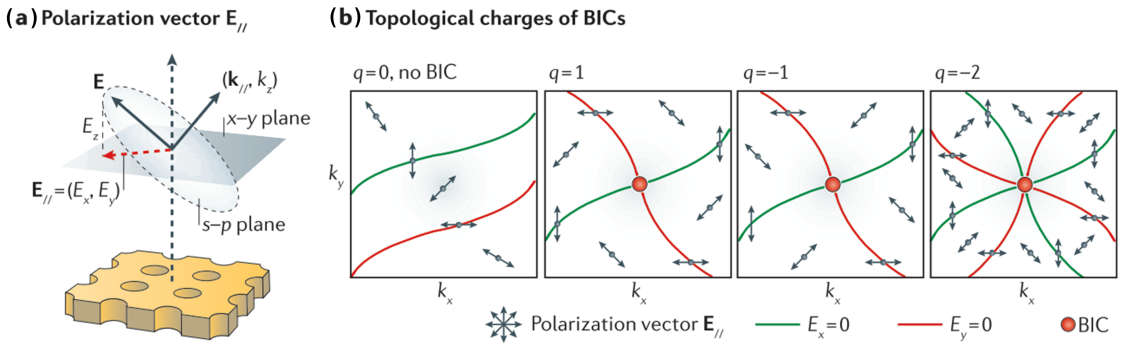


Figure 2.21: **Far-field polarisation vortex associated with BICs in k-space. (a)**. Schematic of a 2D photonic crystal showing an example wave vector $\boldsymbol{k}$ with orthogonal polarisation vector $\boldsymbol{E}$ of a scattered wave. Red dashed arrow depicts the projection of $\boldsymbol{E}$ onto the x-y plane $\boldsymbol{E}_{//}$. **(b)** In-plane polarisation vector $\boldsymbol{E}_{//}$ in k-space given by the grey double arrows, where the green and red curves are nodal lines of the E_x and E_y components respectively. In the leftmost panel, the nodal lines never intersect, resulting in no BIC and a winding number q of zero. In the middle two panels the nodal lines cross, and the polarisation vector winds around the intersection. This point has no clearly defined far-field polarisation, thus yielding a BIC. Depending on the relative sign of the polarisation as each nodal line is crossed, the winding number can be positive or negative leading to two topologically distinct BICs. The rightmost panel depicts a scenario with $q = -2$ showing twice the number of nodal lines, and again is topologically distinct from the other three cases. Adapted from [124].

2.6.5 Jackiw-Rebbi Edge States

In 1976, Roman Jackiw and Claudio Rebbi published a solution to the 1D Dirac equation [230] for the interaction between solitons [231] and a fermionic field [232]. Equivalently, the model can be thought of as describing a relativistic fermionic field with position-dependent mass [233]. If two systems with opposite mass are brought together, a zero-energy solution can be found at the interface between them. This so-called Jackiw-Rebbi edge state is highly confined in space, but most importantly it is highly robust to changes in the masses, as long as the signs are kept opposite on each side of the boundary [234]. The Jackiw-Rebbi solution was, therefore, a precursor to the discovery of topological insulators.

More recently, optical analogues of Jackiw-Rebbi edge states began to emerge in systems such as photonic crystals [235], and nanoresonator chains [236]. Furthermore, binary waveguide arrays [237, 238] showed similar phenomena based on the non-topological Rice-Mele model [239], which reduces to the Jackiw-Rebbi model in the long-wavelength limit. Most applicable to the work in this thesis, however, is the theoretical prediction of Jackiw-Rebbi edge states in nanophotonic gratings by Lee *et al.* [37]. They began by simulating a dielectric grating hosting a symmetry-protected BIC on the lower energy branch and a lossy mode on the upper energy branch as in Figure 2.22 (a). The grating can be characterised by a filling factor F (i.e. the width of each grating segment w divided by the grating period a), and refractive indices of the grating n_{g} and surrounding medium n_{m}. A variable δ was then defined as $\delta = (n_{\mathrm{g}} - n_{\mathrm{m}})/2F$, where by tuning this parameter, the band gap was gradually closed as in Figure 2.22 (b), and then reopened again as in Figure 2.22 (c). After this tuning, the BIC had switched to the upper energy branch, and the lossy mode to the

lower branch. Importantly, similar to closing the electronic band gap of topological insulators in Section 2.6.2, the topological charge of the BIC must change on closing the photonic band gap. This means that the BIC on the lower energy branch is topologically distinct from the BIC on the upper energy branch, and as such they are denoted as trivial and topological phases respectively. Returning to the Jackiw-Rebbi model, analogies can be made between the Dirac mass and the BIC topological charge, and so the model was applied to photonic gratings [37]. As long as the topological phases of two gratings are distinct, when brought together in real space, a zero-energy state (i.e. situated at the centre of the band gap) is formed [37, 232, 234] as shown in Figure 2.22 (d). This is the photonic Jackiw-Rebbi edge state, and is characterised by strong confinement in 1D along the boundary between the two gratings, whilst decaying exponentially perpendicular to the grating axis. In addition, such edge states can only exist at the Γ point, and are dispersionless in k-space perpendicular to the grating axis.

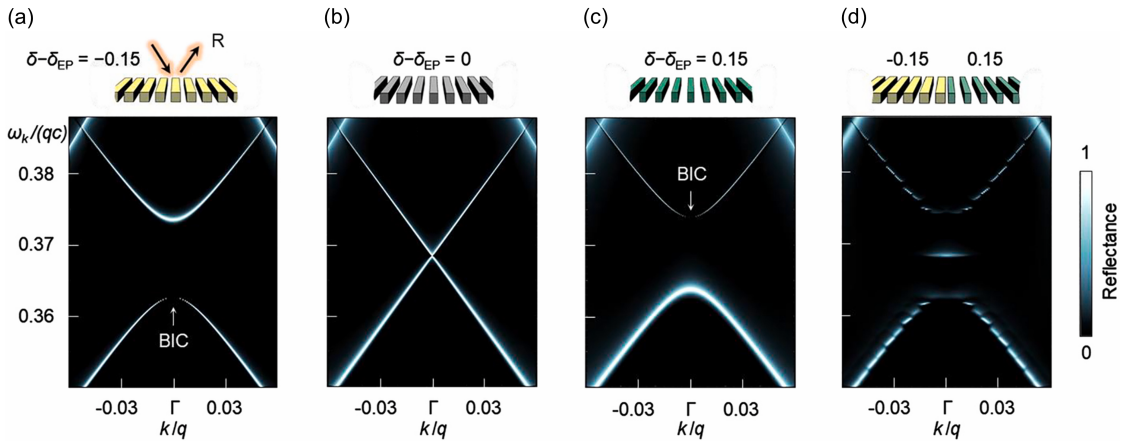


Figure 2.22: **Simulated reflectance contrast showing formation of a photonic Jackiw-Rebbi edge state. (a)** Normalised angle-resolved reflectance contrast of a trivial dielectric grating hosting BIC on the lower energy branch. ω_k is the angular frequency, $q = 2\pi/a$ where a is the grating period, k is the wave vector in the direction perpendicular to the grating axis, δ is a tuning parameter based on the refractive indices and filling factor F, and δ_{EP} is the tuning parameter for the closed band gap case exhibiting exceptional points (EPs) [240]. **(b)** Filling factor and refractive index tuned grating to achieve a closed band gap. **(c)** Further tuned grating showing reopened band gap with topological phase BIC on the upper energy branch. **(d)** Combination of trivial and topological gratings results in a highly localised, dispersionless Jackiw-Rebbi edge state at the mid-gap energy. Adapted from [37].

As with other topologically protected phenomena, 1D photonic Jackiw-Rebbi edge states are predicted to be highly robust against local defects [37], however they do not provide immunity against back-reflection [241] unlike quantum Hall edge states. This means that potential applications lean more towards nanoscale beam-shaping [242], precise spectral filtering [241], and lasing, as opposed to unidirectional waveguiding. In the experimental work I present in Chapter 5 of this thesis, I will use the theory discussed in this section to design, simulate, and fabricate TMD-based gratings with topologically distinct BICs. To the best of my knowledge, I will present the first realisation of photonic Jackiw-Rebbi states in 1D grating structures, demonstrating their strong localisation in energy, real space, and reciprocal space, along with coupling of photoluminescence

from transferred monolayer WSe_2.

2.7 Simulation Techniques

Now that the physical and mathematical theory behind the work in this thesis has been explored, I shall detail the workings behind the two main simulation methods I will use to model how light interacts with TMD-based nanostructures. The first is the finite-difference time domain (FDTD) method, which is a broadly applicable technique, able to simulate almost any structure within the confines of computational power. The second technique is known as rigorous coupled-wave analysis (RCWA), which is intended only for infinitely repeating, periodic structures, with the benefit of faster simulation time and greater reliability than other methods. Both FDTD and RCWA have proved invaluable to the work I present later in this thesis, allowing accurate design and optimisation of nanostructures before fabrication, with excellent agreement to experimental measurements after.

2.7.1 Finite-Difference Time-Domain

In order to model the interactions of light within nanoscale structures and devices, Maxwell's equations need to be solved for the desired boundary conditions. In general however, they cannot be solved analytically except for a few special cases, for example Mie scattering from a sphere as described in Section 2.4.2. Therefore, a numerical finite-difference technique was developed to iteratively solve Maxwell's equations on a discrete spatial mesh in small time steps. The first implementation of this method is accredited to Kane Yee from work published in 1966, whereby he accurately modelled light scattered from a perfectly conducting square in two dimensions [243]. To do this, Yee first adapted the differential forms of Maxwell's equations (2.4-2.7) into a set of four finite-difference equations. The real breakthrough however, was the assignment of each vector component of the electric and magnetic fields to different locations on a discretised square mesh in space. Each cube of the mesh, known subsequently as a Yee cell, contains electric field components at the centre of each edge, oriented parallel to the edge. Each face then contains magnetic field components at the centre, oriented perpendicular to the face. This is represented schematically in Figure 2.23 (a), and forms the basis of the FDTD method. Equally, the system can be defined as having the electric field vectors perpendicular to the faces and magnetic components along the edges, it is merely a matter of convention and perspective. This is depicted in Figure 2.23 (b), where the two planes can be integrated in 3D to form the full cubic cell from 2.23 (a).

Once the spatial mesh was defined, Yee then proved that with small enough time steps, the finite-difference Maxwell's equations could be iteratively solved from the initial conditions of an injected plane wave, thus simulating its propagation through each point in space and time. Note that careful consideration of the size of each Yee cell and time step must be taken into account to ensure stability. For the most accurate results, the mesh size should be a fraction of the incident wavelength, so that the fields do not significantly differ from one cell to the next [243]. The time step Δt must then adhere to the Courant numerical stability criterion based on the mesh size [244]

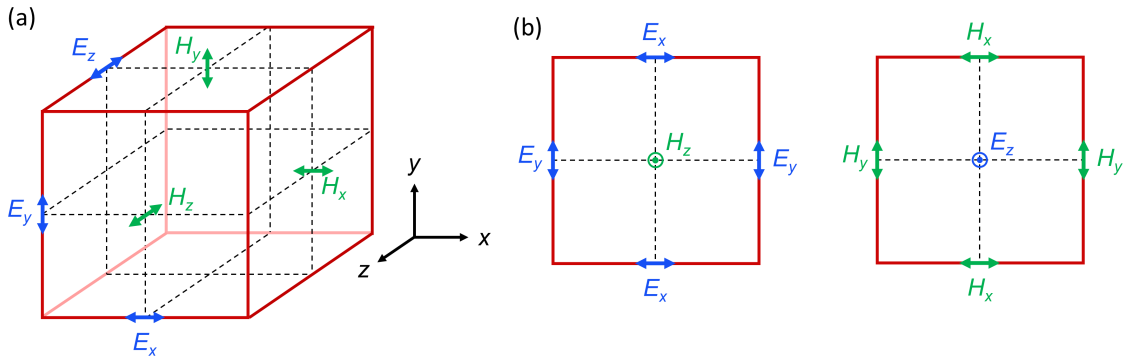


Figure 2.23: **Representation of electromagnetic field vector components on a Yee cell in FDTD simulations. (a)** Full 3D schematic of Yee cell showing electric field components parallel to the edges of the cube, and magnetic components perpendicular to the faces. Each component vector is placed at the centre of its respective edge or face. Only one of each component is shown for clarity. **(b)** Two ways to visualise the distribution of field components on the Yee cell in 2D, showing all respective components for both cases.

$$\sqrt{\Delta x^2 + \Delta y^2 + \Delta z^2} > c_{\max} \Delta t, \tag{2.59}$$

where Δx, Δy, and Δz are the lengths of the Yee cell in each respective dimension, and $c_{\max}$ is the maximum light speed within the medium of the cell. Without these constraints on mesh size and time step, the fields within the simulation would likely diverge, leading to false results. However, reducing the mesh size and time step too far begin to exponentially increase simulation time and computational power needed, whilst giving diminishing returns on the level of accuracy. Careful convergence testing should therefore be carried out for all FDTD simulations, where a balance has to be struck between available time and resources, and the accuracy required. An advantage of FDTD, however, is that results can be evaluated for a broad range of frequencies with little extra time and computational cost, owing to it being a time-domain method, thus allowing efficient frequency tuning.

In the 1960's, the lack of high computing power limited the complexity of simulations that could be carried out using the FDTD method. However, with modern day systems, a huge variety of intricate nanostructures can now be modelled with high degree of accuracy. For the FDTD simulations in this thesis, I use the commercial software package Lumerical. This provides all the functionality of FDTD, whilst having a clear graphical user interface to design complex nanostructures, along with advanced scripting, parameter sweep, and results analysis tools. In addition, owing to implementation of a range of symmetry and boundary conditions, simulation time and computational power can be significantly reduced for symmetric and/or periodic structures, as will be considered in Chapters 4 and 5. The FDTD method is widely considered to be the gold-standard for modelling nanophotonic devices, with broad and versatile applicability to suit a range of research and industrial needs.

2.7.2 Rigorous Coupled-Wave Analysis

As opposed to FDTD, rigorous coupled-wave analysis (RCWA) works within the frequency domain, through the use of Fourier transforms. Specifically, RCWA is designed to model light interacting with stratified media, however modulations in refractive index can be accommodated in the direction normal to the layers if they are infinitely periodic. This makes RCWA ideal for evaluating the diffracted light from 1D gratings or 2D photonic crystals. The first implementations of such a technique appear to be from as early as 1935, when Raman and Nath studied the effect of light diffraction when propagating through high frequency sound waves using Fourier transforms [245]. Similar to a 1D grating, the oscillating sound waves formed a standing wave with high and low pressure regions, thus forming a periodic modulation in the refractive index. Further seminal work in the 1960s proved the technique to work well for devices such as holograms [246] and dielectric gratings [247], however it was not until 1981 that Moharam and Gaylord coined the term rigorous coupled-wave analysis [248]. They presented an approach that was simple to implement via computer, which was further optimised by Lifeng Li in 1996 [249], enabling significantly improved convergence.

Fundamentally, RCWA works by splitting the simulated fields into two distinct regions. Within the refractive index modulated media, the light is modelled as guided modes. Once it leaves the structure, plane wave expansions are used at the boundary to propagate the light away to the far-field [250]. The key to efficient solving of Maxwell's equations within the simulated structures is through expressing the periodically changing permittivity in terms of a series of Fourier transforms. This allows Maxwell's equations to also be expressed in the same way, and thus expanded into a set of separate eigenmodes for each layer [249]. The eigenmodes are then combined, ensuring field continuity at the interface between each layer, allowing reflection and transmission coefficients to be obtained. Finally, these coefficients are used to determine overall measurable quantities, such as reflectance, diffraction angles, field distributions etc. [251]. As opposed to FDTD, there is only a single parameter that controls the accuracy of RCWA simulations, the truncation point of the Fourier series. The more terms are considered, the greater the accuracy of the simulated fields will be, however at increasing computational cost. Again, a balance between time and accuracy must be considered before beginning such simulations, however, RCWA has the advantage of normally converging quicker than FDTD. In addition, numerical instabilities can arise from a range of factors with FDTD, usually owing to the user-set boundary conditions or material properties, and so the simulation can still produce inaccurate results irrespective of mesh optimisation. This means that whilst FDTD is an overall more versatile technique, a greater deal of care must be taken with FDTD simulations to ensure accuracy. In contrast, RCWA is much more robust with only one accuracy-tuning parameter, however only works for the specific application of periodic structures.

For the RCWA simulations I perform in this thesis, I use a Python implementation of the base technique that utilises Li's convergence optimisation [249], amongst other formulations to ensure stability and computational efficiency. The package is named S^4 [252], and contains all the functionality required to model periodic, stratified media, and extract useful results. This will be particularly useful for efficient simulation of the periodic 1D grating structures I investigate in Chapter 5, enabling precise design of structures for fabrication.

3

Methods

3.1 Introduction

This chapter will focus on the technical details behind the methods I used to simulate, fabricate, and experimentally characterise van der Waals nanostructures. I begin with a comprehensive account of the fabrication process behind WS_2 nanoantennas and grating structures on gold. Firstly, preparation of the substrates will be discussed via two different methods, with a comparison of advantages and disadvantage of each. I will then detail how to mechanically exfoliate van der Waals materials onto a variety of substrates by hand using the Scotch tape method, before explaining the flake search and selection process. Conventional semiconductor nanofabrication recipes for patterning and etching will then be covered, utilising electron beam lithography and reactive ion etching to produce nanostructures of desired shapes. As a final fabrication step, I will describe two different methods for transfer of van der Waals materials via a PMMA membrane or PDMS stamp to build complex heterostructures.

After fabrication, the setup of various simulation techniques will be covered. I explain how I modelled the scattering spectra and electric field distributions of resonances within WS_2 nanoantennas on gold, along with the Purcell factor and directivity associated with a dipole placed within such systems using finite-difference time-domain simulations. Similar methods will be described for WS_2 double grating structures, in addition to modelling the photonic band structure and angle-resolved reflectance. I will also detail implementation of rigorous coupled-wave analysis, for efficient calculation of angle-resolved reflectance in single, periodic WS_2 grating structures.

For experimental characterisation of van der Waals nanostructures I utilised several far-field spectroscopy techniques. For the WS_2 nanoantennas on gold, I describe the dark field spectroscopy setup used for measurement of the scattering spectra, and thus characterisation of photonic resonances. I then explain how I used a home-built Fourier spectroscopy setup to measure both the

angle-resolved reflectance contrast and photoluminescence from passive and active WS_2 grating structures respectively, enabling clear visualisation of mode dispersions in k-space. Finally, a thorough description of the working principles and setup of the s-SNOM system is provided. Through a pseudoheterodyne interferometric detection regime, I detail how the background signal can be almost completely suppressed, allowing measurement of near-field interactions between a probing tip and the fabricated nanostructures down to tens of nanometres resolution.

The methods discussed in this chapter underpin all of the contributing research presented in experimental Chapters 4, 5, and 6, providing a vast range of design, fabrication, and characterisation potential.

3.2 Fabrication

In this section, I will detail the fundamental nanofabrication techniques behind the realisation of van der Waals material nanophotonic devices. For the most part, standard semiconductor fabrication methods can be applied, however van der Waals materials also have the advantage of simple transfers, allowing any number of different layers to be stacked together. I will begin by introducing the gold substrates used for both the WS_2 nanoantennas and gratings, and the two main methods by which they were prepared. Next, I explain the subtle differences in mechanical exfoliation of different van der Waals materials onto substrates with varying surface properties, including bulk WS_2 on gold, few-layer hBN on PMMA, and single layer WSe_2 on PDMS. After exfoliation, a brief overview of flake searching will be given, followed by the steps required for flake patterning via electron beam lithography. I will then describe the reactive ion etching process, along with the parameters used to imprint the designed patterns upon the TMD flakes. Finally, I will detail two different methods for transfer of both bulk and single layer van der Waals materials onto a target etched device to achieve complex heterostructures.

3.2.1 Substrate Preparation

All of the TMD-based nanostructures investigated in this thesis were fabricated on gold substrates of 99.99% purity. The substrates were manufactured in collaboration with the University of York using two different techniques, electron beam evaporation, and template-stripping. For the e-beam evaporated gold samples, a commercial silicon wafer was used as a base, before evaporating 10 nm of either titanium or nickel, and then 150 nm of gold. The Ti/Ni layer was necessary to increase adhesion between the Si wafer and gold, which would otherwise peel apart during exfoliation. I measured low RMS roughness values of the e-beam evaporated gold substrates of 1.2 and 2.5 nm using the Ti and Ni layers respectively.

Template-stripping works by first evaporating the gold onto an ultra-flat Si wafer, before placing a glass slide coated with an epoxy glue in contact with the gold. Once set, the slide is lifted, taking with it an extremely flat gold surface with a measured RMS roughness down to 0.7 nm. For the WS_2 nanoantennas presented in Chapter 4, both types of gold substrate were tested, yielding very similar results. The main disadvantage of the template-stripped substrates was degradation of the glue during solvent cleaning, thus significantly reducing the smoothness of the gold surface.

Therefore, for all subsequent nanoantennas and grating structures, e-beam evaporated gold on Si was used, able to withstand harsh cleaning techniques.

3.2.2 Mechanical Exfoliation of van der Waals Materials

In order to fabricate nanostructures from layered van der Waals materials, flakes of material must first be attached to a stable substrate. One of the most simple methods which produces the highest crystal quality structures is mechanical exfoliation. Owing to the inherent van der Waals attractive forces, these materials can be exfoliated directly onto almost any desired substrate. However, there are some slight adjustments that must be made during the process depending on the mechanical properties of the chosen substrate, in order to achieve the best yield.

Bulk WS_2 on Gold

I will first detail exfoliation of bulk WS_2 onto hard and flat substrates, such as gold, SiO_2 and Si through the Scotch tape method. Before starting the exfoliation, I thoroughly cleaned the 10×10 mm gold substrates by submersion first in acetone for 2-3 minutes, swirling the beaker once per minute to agitate and lift any surface contamination. The substrates were then swiftly transferred into a beaker of isopropyl alcohol (IPA) to remove the excess acetone residue before it dried. I also intermittently swirled the IPA beaker, and removed the substrates after 1-2 minutes, before drying with a compressed nitrogen gas gun. As a final step, the substrates were subjected to a brief oxygen-plasma cleaning of 45 seconds to remove any remaining contamination, resulting in an ultra-clean, ultra-flat gold surface. Bulk WS_2 crystal from HQ-Graphene was then placed onto one half of the sticky side of a $\sim 4 \times 8$ cm piece of Nitto Denko ELP BT-150E-CM low adhesion tape, as depicted by step 1 in Figure 3.1. This rectangular shape was used so that one side could be handled with nitrile gloves, leaving the other side containing the crystal free from contamination. With the protective backing then replaced to form a seal around the crystal, slight pressure between two thumbs was applied to promote adhesion to the tape as in step 2 of Figure 3.1. I then peeled off the protective backing once again, and removed the bulk WS_2 with tweezers whilst flexing the tape slightly to facilitate detachment. At this stage, millimetre-sized thin crystal should be present on the blue tape with a very shiny mirror-like appearance, indicating high crystalline quality. On occasion no crystal would adhere, in which case I simply repeated the previous step with slightly increased pressure.

The next step was to thin out the crystal onto three more rectangles of tape. I first removed the backing from one piece of tape and placed the sticky side in contact with the sticky side of the tape containing the WS_2 crystal. I then peeled them apart slowly ($\sim$ 2 cm/s) yielding crystal on both tapes. This process was then repeated up to four times in total, each time placing the tapes together with a lateral shift and/or twist to spread out the flake coverage over an area of ~ 3 cm^2, as demonstrated schematically in step 3 of Figure 3.1. Repeating this process too much leads to lots of very thin flakes with small lateral sizes and vice versa, therefore this process can be tailored depending on the flake parameters desired. I then took the final two tapes and adhered them to the first two, thus spreading the crystal over a total of four tapes.

To exfoliate the WS_2 onto the cleaned gold substrates, I first placed two substrates towards either

end of a rectangular glass slide as in step 4 of the yellow box in Figure 3.1. I then slowly applied the prepared tapes in a rolling motion from one side of the substrate to the other, ensuring that regions of high flake density were positioned over the substrates, and that as few bubbles as possible formed. I repeated this for the second substrate, before cutting away excess tape overhanging the edges of the glass slide. The slide was then heated on a hot plate to 105°C for 1 minute to allow the tape to conform to the surface well, and promote adhesion between the flakes and the gold. The tapes were subsequently removed from the heat and allowed to cool for $\sim$ 1 minute, by which time the tape often began to peel itself off as it contracted. The final step was to peel the tape off with tweezers by hand as slowly as physically possible without stopping or changing speed. This speed is crucial to avoid flakes being removed with the tape, and to exfoliate flakes with large lateral sizes. I found that gripping a corner of the tape and bending it back on itself enabled resting of the hand on the worktop, thus enabling a stable and uniform peel to increase flake yield. Through this process I was able to achieve uniform flake coverage with a range of thickness from $<$ 10 nm up to $\sim$ 450 nm, with lateral sizes between 50-700 µm.

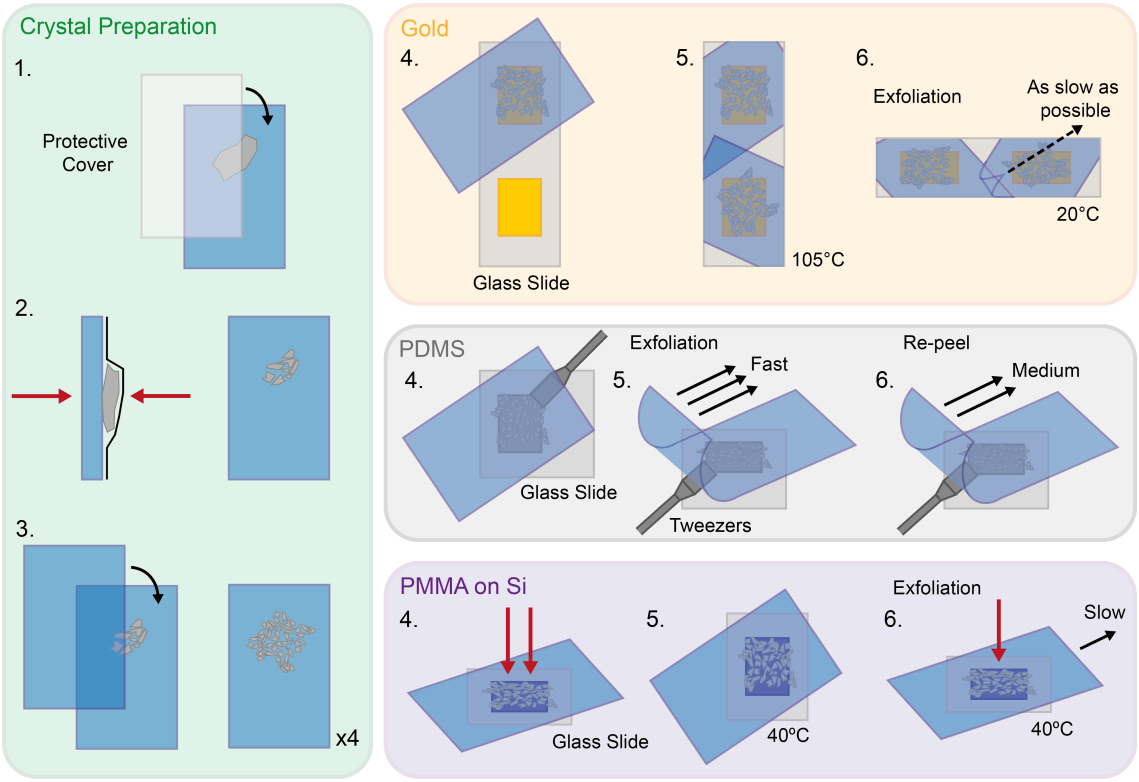


Figure 3.1: **Schematic of exfoliation methods on three different substrates.** Left panel in green outlines method for preparing and thinning bulk crystal on low adhesion tape. Red arrows denote directions to apply pressure to promote flake adhesion. Right panels depict exfoliation methods for van der Waals materials on gold, PDMS, and PMMA on Si substrates, corresponding to the yellow, grey, and purple boxes respectively.

Monolayer WSe_2 on PDMS

To exfoliate single layers of TMDs, softer viscoelastic polymer substrates such as PDMS give the best yield. To prepare the PDMS stamp, I first cleaned a square glass slide with IPA, followed

by drying via compressed nitrogen. I then cut small rectangles of PDMS $\sim 10 \times 15$ mm in size, before removing the thin top protective film. I then peeled the PDMS layer from the hard plastic backing, and slowly placed it onto the top half of a glass slide in a rolling motion to ensure full contact without any bubbles. The off-centre placement of the PDMS is to ensure that there is room to attach the transfer arm to the slide later, without obstructing the view of the monolayer.

After preparing the PDMS, I used the same process as in the previous section to thin the WSe_2 crystal onto four separate tapes. Whilst holding one corner of the PDMS down with a pair of flat-headed tweezers, I then laid the tape down slowly (again in a rolling motion) using another pair of tweezers in the opposite hand, ensuring good contact with the PDMS. This is illustrated schematically in step 4 of the grey box in Figure 3.1. With the flat-headed tweezers still holding the PDMS down, I then folded the end of the tape back on itself in the direction it came from without peeling the PDMS and tape apart yet, as depicted by step 5. In a swift motion, akin to ripping off a plaster, I peeled the tape away from the PDMS, leaving a covering of flakes behind. This was all done at room temperature. The high speed here is crucial for good flake coverage on PDMS due to its viscoelasticity. This means that on short time scales, the material behaves with strong adhesion, thus allowing thin layers of crystal to be exfoliated [253]. On longer time scales, the PDMS is less adhesive, and so can be used to release flakes during transfers as explained later in Section 3.2.6. To increase the monolayer yield, I performed additional re-peels on each PDMS stamp. This involved taking a fresh piece of tape and sticking it to the WSe_2-coated PDMS, before peeling the tape off at a medium speed. Again, the speed here is crucial, it must not be as fast as the initial exfoliation otherwise all the flakes will be removed, nor too slow otherwise nothing will adhere to the tape. As a rough guide, ~ 10 cm/s speed should be used so that the top layers of thicker WSe_2 are removed, thus increasing the chances of leaving monolayers behind on the PDMS. In addition, the fluidity of movement in the step is just as important as the speed. The tape should be peeled in one motion at uniform speed, so that the detachment is as smooth as possible to avoid damaging any monolayers. For each PDMS stamp, I flake searched (as described in Section 3.2.3) after the initial exfoliation, then if no monolayers were present, I re-peeled and flake searched again until either a monolayer was found or all the flakes had been removed. Using this method, I was able to exfoliate 1-2 useable monolayers of ~ 50 µm or larger per full day after practising the peeling techniques, assuming good bulk crystal quality.

Few-layer hBN on PMMA

The hBN exfoliation process was slightly different to the two previous exfoliations owing to the size of the bulk crystals. For TMDs, the bulk crystal from HQ-Graphene is generally ~ 10 mm in lateral size, whereas the hBN from Tsukuba NIMS exists in much smaller flakes of < 1 mm. I therefore cut a very thin strip of tape $\sim 1 \times 30$ mm in size and, holding with tweezers at both ends, bent the tape to form a 'U' shape with the sticky side down. I then dabbed the tape onto the hBN crystals, picking up several small flakes, before depositing onto the centre of larger rectangle of tape ($\sim 5 \times 10$ cm) in several nearby locations, until all of the hBN was on the larger piece. Similar to the previous techniques, I then thinned out the hBN, however this time using the same piece of tape, folding it in on itself up to four times, thus spreading the hBN out. As a final step, I

took another large rectangle of tape and adhered it to the first, splitting the remaining hBN between the two. Both of these tapes could then be used for up to five exfoliations.

I used substrates consisting of a silicon base, followed by a PVA sacrificial layer, topped with several hundred nanometres of spin-coated PMMA. Similar to the exfoliation process on gold, I placed the substrates on a glass slide, before slowly applying one of the hBN-covered tapes in a rolling motion. However, in this case the aim was to exfoliate few-layer hBN < 5 nm thick, rather than bulk crystal as with the WS_2. To do this, maximal adhesion to the PMMA was needed, therefore I applied significant pressure to the tape-covered substrates as shown in step 4 of the purple box in Figure 3.1. I placed the ball of the thumb on top of the sample and initially applied uniform pressure using just the hand. Then for around one minute, I positioned most of my body weight over the sample to press the hBN firmly into the PMMA. Owing to the softness of the polymer, this process did not cause damage to the hBN flakes. I then heated the sample to 40°C on a hotplate for 1-2 minutes (step 5) to promote adhesion between the hBN and PMMA. Whilst still on the hotplate, I held down the sample firmly with a soft piece of cloth, and very slowly pulled the tape with tweezers parallel to the sample surface until it fully separated from the PMMA as depicted in step 6. This ensured a low detachment angle between the tape and PMMA, thus increasing yield of thin hBN. I was able to exfoliate 2-3 large (> 50 µm lateral size) flakes of ~ 5 nm thickness or less per exfoliation, along with many hundreds of bulk flakes > 10 nm thickness.

3.2.3 Flake Searching

After exfoliation, all flake searching was done with a Nikon Eclipse LV150N microscope. By raster scanning the sample below, I was able to identify the rough thickness of different flakes based on their colour to within ~ 10 nm. The colour would change slightly depending on flake and substrate materials, and so accurate measurements of thickness were subsequently performed on selected flakes using atomic force microscopy (AFM). I used this method to identify ideal bulk WS_2 and few-layer hBN candidates, as in Figures 3.2 (a) and (b) respectively, for fabrication of inverted gratings and grating heterostructures in Chapter 5. The hBN flakes were significantly more transparent when ~ 5 nm or less in thickness as seen in Figure 3.2 (b), so great care was taken not to miss any. Changing the colour contrast in the microscope software NIS Elements also helped. I only selected uniform colour, and thus uniform thickness flakes at least 50 µm in lateral size, for transfer over as many gratings as possible. For identifying WSe_2 monolayers, I searched for only the most transparent flakes, and further confirmed the number of layers by switching the microscope into photoluminescence mode as in Figure 3.2 (d). This applied a short pass filter to the excitation path and a long pass filter to the collection path, thus only monolayers and bilayers would show signal from their excitonic emission. Monolayer PL was significantly brighter than bilayer owing to the direct band gap transition, making them easy to distinguish.

3.2.4 Electron Beam Lithography Patterning

Patterning of the samples fabricated in this thesis was done via electron beam lithography (EBL) in collaboration with Dr Yue (Christina) Wang from the University of York, and Dr Xuerong Hu within my research group at The University of Sheffield. For the nanoantennas, Dr Wang first spin-

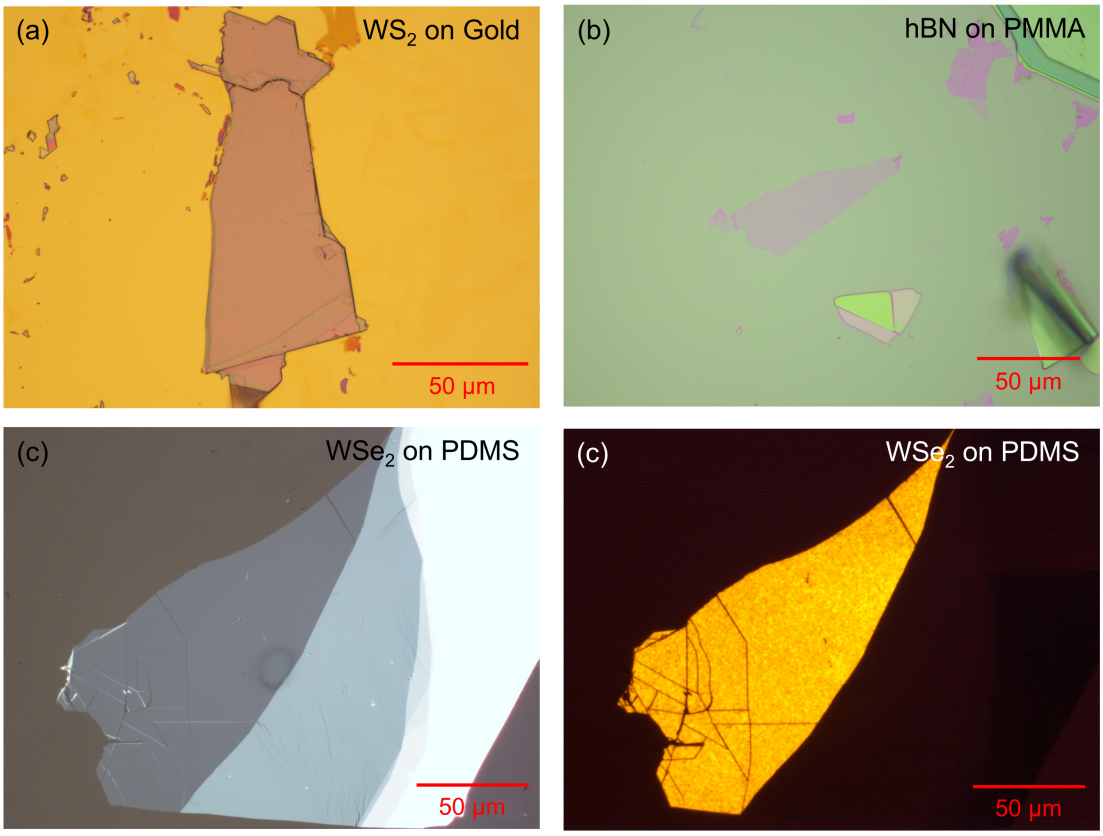


Figure 3.2: **Microscope images of exfoliated van der Waals materials on different substrates.** **(a)** Multi-layer WS_2 on gold in standard bright field microscopy mode. **(b)** Few-layer hBN on PMMA-coated Si substrate in bright field mode. Contrast between flake and substrate is weaker than with multi-layer. **(c)** Bright field image of WSe_2 on PDMS with a large monolayer region indicated by the most transparent section. **(d)** Photoluminescence image of the WSe_2 flake from **(c)**, showing bright direct band gap emission corresponding to the monolayer region.

coated a positive resist (CSAR 62 ARP-9 AllResist GmbH) onto the gold substrates containing WS_2 flakes at 3500 rpm for 60 s, before heating for 2 minutes at 180°C, as shown in Figure 3.3 (b). EBL was then performed using a Raith GmbH Voyager system at 50 kV accelerating voltage and 560 pA beam current, causing the regions of resist exposed to the electron beam to break down into smaller polymer chains. This was followed by development in o-Xylene to remove the irradiated resist, forming a pattern of repeating circles with varying radii in $\sim$ 10 nm steps, covering the majority of WS_2 flakes as in Figure 3.3 (c).

For the WS_2 double gratings, Dr Hu performed the same resist-spinning, patterning, and development procedure in Sheffield. However, since high precision was needed for the filling factor (FF) of the gratings, I designed a repeating double grating pattern with a different electron beam dosage for each column as depicted in Figure 3.3 (e). A higher dosage resulted in narrower WS_2 wires for the same period, therefore a lower filling factor, and vice versa. The columns were then repeated side by side with the period changed across each row, so that at least one pair of gratings would have the correct parameters to produce a topological Jackiw-Rebbi edge state for any thickness flake between 30-70 nm. Here the grating axis (i.e. parallel to the grooves) is along the

horizontal direction, with repeating interfaces between the high and low filling factor gratings (dark and light blue rectangles respectively) where Jackiw-Rebbi edge states are expected to exist. To also account for etching of the side walls during the next step, an additional 10% width was added to each wire compared to the desired value during patterning.

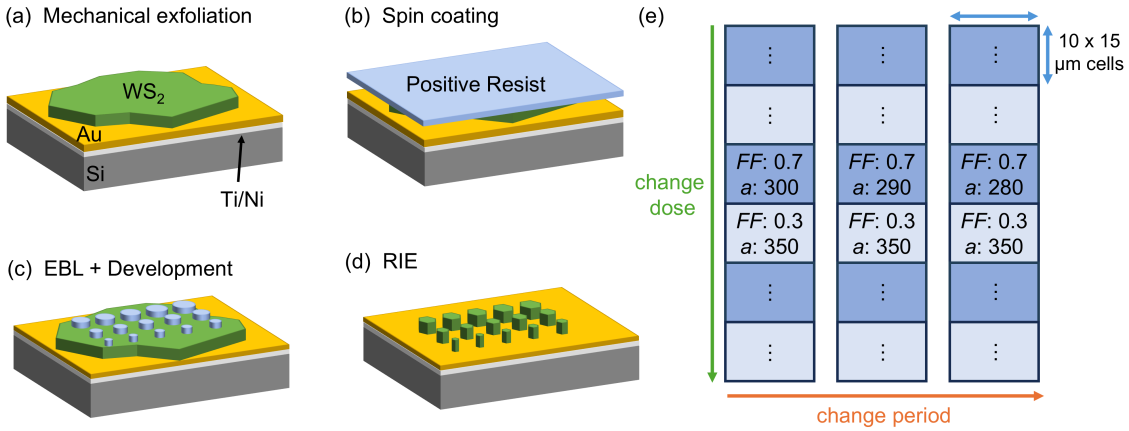


Figure 3.3: **Schematic of TMD nanostructure fabrication process. (a)** Mechanical exfoliation of TMD flakes onto electron-beam evaporated gold substrate. **(b)** Spin coating of positive resist (CSAR 62). **(c)** Electron-beam lithography and development of resist into pattern of circles of varying radii. **(d)** Chemical reactive ion etching into hexagonal nanoantennas. **(e)** Example EBL patterning for double grating structures. Dark and light blue rectangles correspond to the high and low filling factor gratings respectively, with the grooves of the gratings orientated along the horizontal axis. Electron beam dosage is varied down each column with constant alternating period and filling factor. Grating period is varied along the rows of the high filling factor regions to account for various flake thicknesses.

3.2.5 Reactive Ion Etching

The WS_2 nanoantennas were etched in York by Dr Wang via reactive ion etching (RIE). A chemical etching recipe was used to achieve hexagonal nanoantenna geometries as illustrated in Figure 3.3 (d). RIE was performed for 40 s with SF_6 gas at 0.13 mbar pressure with a DC bias of 50 V. This caused preferential etching of the armchair crystal axis of the bulk WS_2 faster than the zigzag axis, leading to 120° angles between them, and thus forming pillars with hexagonal cross-sections [254]. The gold substrate was etched much slower than the WS_2, and so acted as a natural etch stop, leaving nanoantennas on a flat gold surface, rather than on a pedestal of substrate material. The leftover resist was then removed using warm 1165 resist remover for 1 hour, before bathing in acetone for another hour, followed by an IPA rinse for 5 minutes. A final UV-ozone treatment of 20 min removed any residual organic debris.

The WS_2 double gratings were also etched using RIE, but with a more physical etching recipe consisting of SF_6 and CHF_3. This was performed in York by Dr Hu, and ensured that the edges of the grating wires were straight and parallel, rather than being etched in a zig-zag pattern as with purely chemical etching.

When fabricating completely new structures, e.g. when beginning the gratings project, there would typically be ~ 5 or more iterations of samples where the electron beam dosage and etching

parameters were optimised through trial-and-error, before true-to-design structures were realised. Once a good recipe was established, reliable turnaround of grating samples could be completed within a week. When parameters such as the grating period or filling factor were changed, 1-2 additional sample iterations were often required to achieve accurate structures. This could be avoided by patterning multiple

3.2.6 Flake Transfer

One of the key advantages of van der Waals materials over conventional semiconductors, is their ability to be easily transferred from one material to another, allowing the realisation of complex stacked structures. To perform such transfers, I used a metallic arm attached to a Scientifica PatchStar Micromanipulator. This motorised stage was able to move in all three directions, with a precision of 20 nm steps. The transfer arm was situated beside a Nikon Eclipse LV150N microscope, both within a nitrogen-environment glovebox to reduce the contamination between stacked layers. The arm was fitted with a vacuum tip, allowing samples to be attached for transfer. In this thesis I used two main methods during fabrication of the WS_2 double inverted gratings and double grating heterostructures, one using a PDMS stamp on glass, and the other with a suspended PMMA membrane as detailed below.

PDMS Stamp

The simplest of the two types of transfer I performed involved material exfoliated on a PDMS stamp situated on a glass slide, as described previously in Section 3.2.2. This all-dry technique involved attaching the glass slide to the transfer arm with the PDMS stamp facing down, and positioning under the microscope objective. By focusing on the PDMS, I drew an outline of the WSe_2 monolayer, allowing precise positioning of the sample beneath. The transfer arm was then slowly lowered until the PDMS was roughly 1 mm above the target sample. I then switched to the minimum magnification objective of $5\times$, and lowered the transfer arm very slowly until contact was made between the PDMS and the gold sample, as shown in Figure 3.4 (a). At this point a clear line interface was visible, separating the contacted and non-contacted regions. By further lowering the transfer arm, the contacted region expanded and vice versa. To ensure the fragile monolayer was not damaged, as the interface approached the monolayer and target region, I stopped lowering the transfer arm and let the interface move slowly of its own accord. If the interface stopped moving, I lowered the arm gently until the contacted region began expanding again. If the interface suddenly advanced rapidly, i.e. around a thick flake, piece of contamination, or uneven PDMS, I quickly but smoothly raised the arm to reduce the contact speed. As the monolayer began to contact the target region below, I constantly tuned the speed of the interface with the transfer arm height to go as slow as physically possible. Once the monolayer was in full contact with the target sample as in Figure 3.4 (b), I heated the stage to 65°C and left for $\sim$ 2-3 minutes to promote adhesion to the sample. For the best quality PDMS transfer, I found that simply decreasing the temperature back to 20°C was often enough to cause the PDMS to contract and begin reducing the size of the contacted region. This was also much smoother than manually controlling the height of the transfer arm, hence leading to better transfers with lower likelihood of cracking the monolayer. If the interface did not

fully pass back over the monolayer region, I raised the transfer arm as slow as possible until the interface began moving again. Once the contacted region was no longer close to the monolayer, I then raised the transfer arm completely to detach the PDMS stamp, leaving the monolayer on the target sample as imaged in Figure 3.4 (c). Owing to the viscoelastic properties of PDMS, as long as the peel-off was done very slowly, the adhesion between the monolayer and PDMS would be lower than between the monolayer and target sample. Thus transfer of monolayer TMDs using this method was quite reliable, even on uneven surfaces or pre-fabricated devices. Note that cracking of the monolayer during this step is common, however this is usually isolated to a few lines, and so using a large monolayer > 50 µm reduces the chances of the cracks being over the target regions.

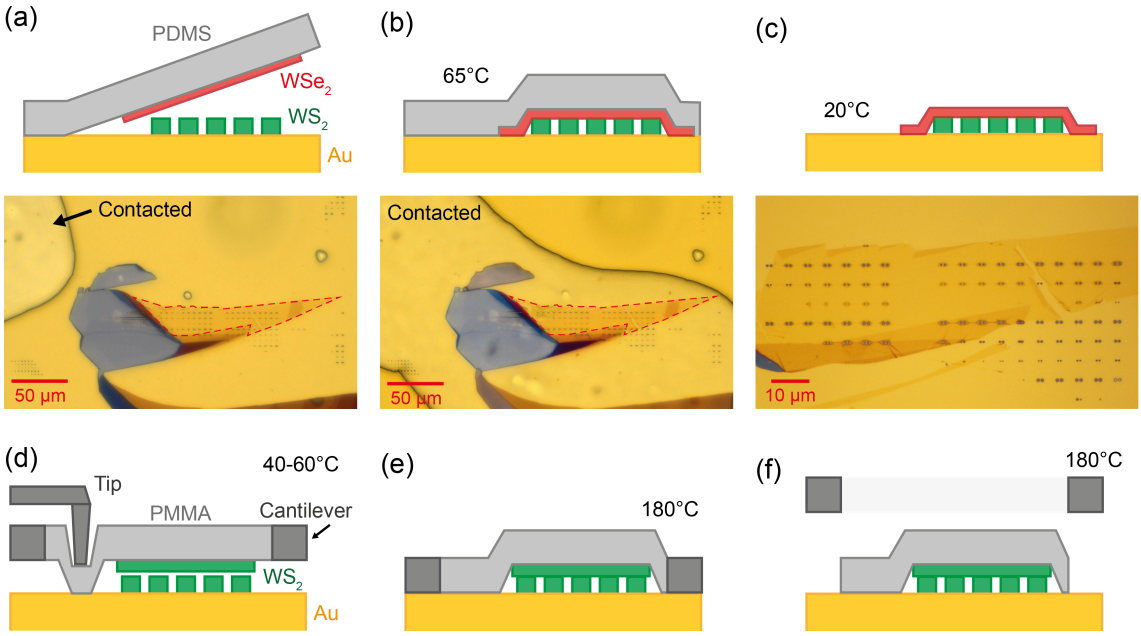


Figure 3.4: **Illustration of PDMS stamp and PMMA membrane transfer methods. (a)-(c)** Steps for transfer of monolayer WSe_2 via PDMS stamp. Example substrate is WS_2 nanoantennas on gold. Images below each schematic taken during the transfer process and show the interface between contacted and non-contacted regions. Monolayer outlined with red dashed line. **(d)-(f)** Process for transfer of multi-layer van der Waals materials via PMMA membrane. Sharp tip is used to initiate contact, before membrane is melted onto target WS_2 gratings on gold and cantilever removed. PMMA can then be washed away via solvent and O_2-plasma cleaning.

PMMA Membrane

To transfer flakes of WS_2 and hBN of specific thicknesses onto the previously fabricated WS_2 gratings, I used a suspended PMMA membrane attached to a metal ring cantilever. The spin-coated PMMA on Si substrates described previously in Section 3.2.2 were used owing to their flat top surface, enabling accurate AFM measurement of exfoliated flake thicknesses required for fabricating the inverted gratings and grating heterostructures of Chapter 5. In contrast, the surface of the PDMS stamps was too uneven to accurately measure the thickness of exfoliated flakes via AFM. I processed the PMMA substrates in a cleanroom, first using the sharp tip of a pair of metal tweezers to scribe a circle around the target flake for transfer, ensuring to cut through the top PMMA and middle sacrificial layer. Since the PVA sacrificial layer is water soluble, I then placed small

droplets of deionised (DI) water around one half of the circumference of the circle. The water then flowed into the scribed regions, gradually dissolving the sacrificial layer under the PMMA. After around 10 minutes, the sacrificial layer was completely dissolved, leaving the PMMA floating on a bed of water. I then carefully dipped the sample into a full beaker of DI water at a 45° angle, allowing the circular PMMA membrane to float in the beaker. The next step in preparing the suspended membranes was to use a ring-shaped metal cantilever to fish the PMMA out of the DI water from underneath. The fishing was done as slowly and smoothly as possible to achieve a flat membrane without wrinkles. This step was the most difficult in producing the PMMA membranes, requiring a steady hand and patience to ensure that the membrane sat central to the ring. Often the surface tension of the water would shift the membrane as the cantilever came into contact, leaving one side of the membrane unattached and thus not usable for transfer. With practice, ~ 3 suspended membranes could be fabricated per hour. The successful cantilevers were then placed on the edge of a hotplate at 180°C with the membrane section overhanging the edge to avoid damage. The conducted heat through the cantilever then dried the membrane, making it taught and ready for transfer after cooling.

To transfer the WS_2 and hBN from the suspended PMMA membrane onto a target sample, I began in the same way as Section 3.2.6, by attaching the cantilever to the transfer arm, and lowering it slowly until close to the sample beneath. I found that often the PMMA membrane would not contact the target sample, no matter how far down the transfer arm was moved. I therefore used a secondary x, y, z stage with a downwards pointed tip attached. As illustrated in Figure 3.4 (d), this was used to gently push the membrane into contact with the sample at a position away from the target region. For the contact to remain after removal of the tip, a temperature of between 40-60°C was applied. I then slowly increased the temperature of the stage in 5°C increments, monitoring the movement of the interface between the contacted and non-contacted regions. As with the PDMS transfer, any significant change in speed was compensated by moving the transfer arm up or down. I continually increased the temperature until the transfer flake and sample were in full contact as in Figure 3.4 (e), ensuring that the interface moved as slowly as possible over the target region. Once done, I then increased the temperature to 180°C to fully melt the PMMA membrane onto the target sample with the transfer flake in the desired position. I then lifted the transfer arm in small increments, before moving side to side in x and y to weaken the edges of the membrane where it joined the metal ring. I repeated this process until the edges eventually ripped, leaving the transfer arm free and the majority of the PMMA membrane stuck to the target sample as in Figure 3.4 (f). After being left to cool, the PMMA was simply washed with acetone and IPA, followed by O_2-plasma cleaning, leaving a clean sample with a transferred flake. Using this PMMA transfer technique it was always possible to transfer bulk van der Waals materials onto a target sample. The main difficulties arose from the lateral positioning of the flake over the gratings below. The PMMA had to be heated to a much higher temperature than PDMS and so expanded more. This meant that the flake would often shift by several microns relative to the target sample, making perfect alignment of layers challenging as the shift had to be predicted and taken into account.

3.3 FDTD Simulations

For all the FDTD simulations performed in this thesis, I used the commercial software package Lumerical, in tandem with The University of Sheffield's High Performance Computing (HPC) cluster. As previously described in Section 2.7.1, FDTD works by simulating finite-difference versions of Maxwell's equations on a discretised grid in space, iterated over over small time steps. Through Lumerical, I was able to design and visualise arbitrary-shaped nanostructures such as nanoantennas and gratings clearly through its graphical user interface. Furthermore, experimental refractive index data (e.g. from Figure 2.7) was uploaded and modelled for accurate simulation of real materials. The general approach I took to simulating different structures was to first start with a test design, in order to iron out any errors or instabilities that arose. All FDTD simulations require three main components: a light source, a structure, and light detection monitors, which will be explained in more detail in the following sections. Once I was satisfied that the simulation was producing accurate results via comparison to theory and previous literature, I then optimised the accuracy and efficiency by tuning the mesh size, and adding appropriate symmetry conditions. Only then did I begin various parameter sweeps for comprehensive characterisation of each device. I will begin this section by detailing the method behind obtaining far-field scattering spectra from WS_2 nanoantennas of various heights and radii on different substrates. Following this, I will explain how the near-field profiles of electric field intensity were measured for different resonances. Next, Purcell factor calculations for a dipole placed in various positions in and around the nanoantennas will be covered, along with the respective directivity profiles of the emission. Finally, I will move on to WS_2 gratings on gold, where I explain how I performed angle-resolved reflectance contrast simulations in two-dimensional wave vector space. These methods form the basis of the majority of simulations completed in this thesis, owing to the versatility of FDTD.

3.3.1 Scattering Spectra

The scattering cross-sections in Chapter 4 were calculated by simulating WS_2 nanoantennas of varying geometries on a semi-infinite gold substrate. The setup is illustrated in Figures 3.5 (a) and (b) for the x, y and x, z perspectives respectively. To emulate dark field experiments as closely as possible, a total-field scattered-field (TFSF) plane wave source was used, which formed a closed box around the nanoantennas and part of the substrate. The TFSF source works by injecting a plane wave in the box along a chosen axis, and then subtracting the incident wave outside of its area of effect. This way, only light scattered from structures within the box can escape to the far-field, not reflected or transmitted light. To capture the scattered light, a box of 2D frequency-domain field and power monitors was placed outside the TFSF source box, and above the nanoantenna as depicted by the grey boxes in Figure 3.5. These monitors were set to record the total power flux through their surface. The scattering cross-section was then calculated by dividing the vertically scattered power by the source intensity, which corresponds to the injected power of the TFSF source over its injection plane size. The incident wave was set to propagate normal to the substrate, and was polarised along the x axis. I also incorporated rounded edges of the nanoantennas to more accurately model real fabricated structures. I used a radius of curvature of 22 nm for each vertex, which

was the lowest measured in scanning electron microscopy images of previously fabricated WS_2 nanoantennas on SiO_2. Owing to the symmetry of the hexagonal nanoantennas and the chosen polarisation direction of the incident light along x in Figure 3.5 (a), anti-symmetric and symmetric boundary conditions were used along the $x = 0$ and $y = 0$ planes respectively, thus reducing simulation time and memory requirements. Stabilised PML (perfectly-matched layer) boundary conditions were used to reduce the likelihood of simulation instabilities caused by fields reflected back into the simulation, as illustrated by the red regions in Figure 3.5. The PML region is designed to absorb all fields leaving the simulation region, however with too few layers, the fields are not always absorbed completely, resulting in erroneous oscillations in the resulting scattering spectra. Stabilised PML therefore increases the number of layers to improve accuracy, at the cost of additional simulation time. With the simulation set up, I then performed sweeps over nanoantenna parameters such as height and radius, allowing the evolution of the scattering spectra to be visualised from structure to structure.

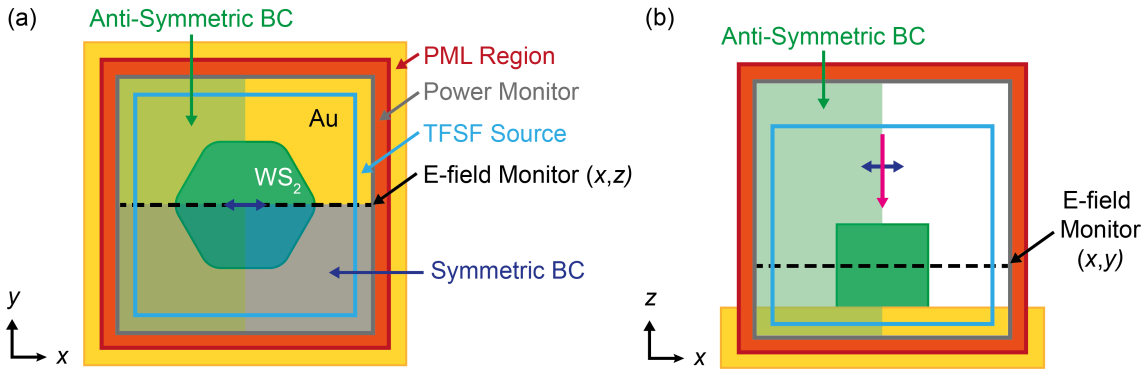


Figure 3.5: **FDTD simulation setup for calculation of scattering spectra and electric field distributions in WS_2 nanoantennas on gold. (a)** x, y perspective of the simulation from the top down. Hexagonal nanoantenna with rounded edges is first surrounded by the TFSF source box in light blue, then a box of power monitors at the edge of the simulation region in grey. Dashed black line corresponds to the position of a 2D frequency-domain field monitor in the x, z plane, and the outer red region depicts the PML layers for light absorption at the simulation boundaries. Incident light is polarised along x as depicted by the dark blue double-headed arrow. Transparent blue and green squares correspond to the symmetric and anti-symmetric boundary conditions imposed by the incident light respectively, meaning only the top right quarter needs to be simulated. **(b)** x, z perspective highlighting the incident light propagation direction with the pink arrow. Dashed black line corresponds to another 2D field monitor but in the x, y plane.

3.3.2 Near-Field Distributions

To visualise the electric and magnetic field distributions within and around WS_2 nanoantennas and gratings, I also used frequency-domain field and power monitors. However, here I set the monitors to record $E_{x,y,z}$ and $H_{x,y,z}$ at each point, rather than integrating the overall fields through the monitor to measure power. I positioned 2D monitor surfaces cutting through the middle of the nanoantennas in both the x, z and x, y planes, as in Figures 3.5 (a) and (b) respectively, to visualise the field distribution of different resonances. The recorded electric and magnetic field intensities were automatically normalised to that of the incident vacuum wave, thus giving a value for the

field confinement throughout the simulated structure. The same method was used for visualising the near-fields within WS_2 gratings on gold.

3.3.3 Purcell Factor and Radiative Rate Enhancement

As previously described by Equation 2.27, the Purcell factor can be calculated by dividing the power emitted by a dipole within some arbitrary photonic environment, by that of the same dipole in a homogeneous dielectric medium. To achieve this in simulation, I therefore removed any far-field sources such as plane waves, and added a dipole emitter as the primary source. Depending on the structure and resonances in question, the dipole was placed in different locations. For the WS_2 nanoantennas, I simulated a dipole within an hBN spacer between the nanoantennas and a gold substrate, for wavelengths between 550-850 nm, in order to emulate an hBN single photon emitter. I also rotated the orientation of the dipole in the x, z plane to consider different polarisations, as shown in Figure 3.6 (a). The Purcell factor was then spatially mapped throughout the hBN layer in x and y, calculated as the total emitted power from the dipole at each point, divided by the total emitted power of the same dipole in vacuum. I chose to use vacuum as the dielectric in the nanoantenna Purcell factor simulations to provide a consistent and ideal case for the reference dipole measurement. I kept all other parameters the same between the nanoantenna and vacuum simulations, only disabling the structures.

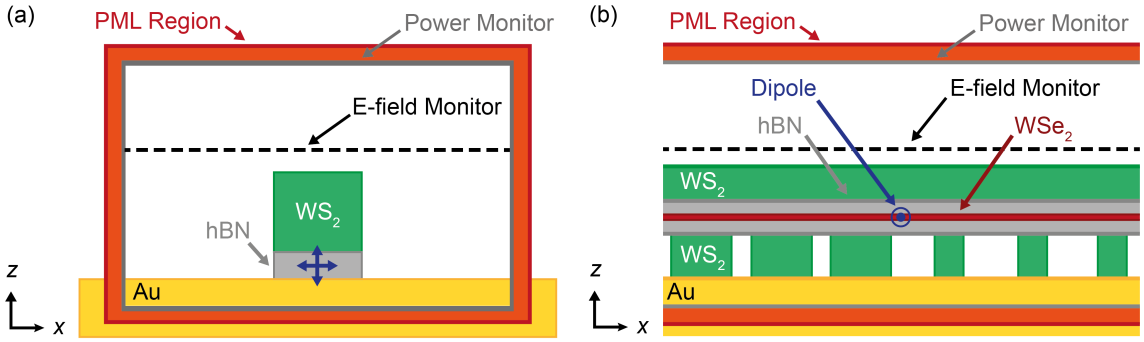


Figure 3.6: **FDTD simulation setup for calculation of Purcell factor and directivity of a dipole within WS_2 nanostructures on gold.** **(a)** x, z perspective of WS_2 nanoantenna on 5 nm thick hBN on gold. Dipole depicted by the blue double-headed arrows with two polarisation orientations considered, parallel and perpendicular to the substrate plane. Box of power monitors in grey collect the total emission from the system for calculation of Purcell factor at different dipole positions in x and y. Black dashed line corresponds to the electric field monitor used to capture all vertically scattered light for calculation of the far-field directivity. **(b)** x, z perspective of the interface section of a WS_2 double grating heterostructure on gold. Full structure continues in positive and negative x direction for 20 periods each way, ending with PML boundary conditions. Dipole placed within the monolayer WSe_2 polarised parallel to the grating axis (i.e. along y), and moved along x, calculating Purcell factor and directivity at each point.

A different method was used for calculating the radiative rate enhancement for a dipole within the grating heterostructures in Chapter 5. Here the structure was composed of two adjacent WS_2 gratings of different period and filling factor, followed by an hBN-encapsulated monolayer WSe_2, topped with a bulk WS_2 flake to make a five-layer structure. Shown in Figure 3.6 (b), the dipole location was set within the WSe_2 monolayer to emulate the photoluminescence from a direct band

gap exciton recombination event. Only a small section of the double grating interface is illustrated schematically in Figure 3.6 (b) for clarity, however the structure continues for 20 periods in each direction for the real simulation, also capped with PML boundary conditions in the x direction. Rather than comparing the total emitted intensity from a dipole within this heterostructure to the same dipole in vacuum, the heterostructure measurement was compared against a reference structure. This refrence structure was similar to the heterostructure in Figure 3.6 (b), however with the grating layer replaced by bulk WS_2 of the same thickness. Since the reference structure is not expected to host any grating modes, this allows for direct characterisation of the photoluminescence enhancement owing to coupling with the Jackiw-Rebbi edge state. Whilst the radiative rate enhancement here is due to the Purcell effect, I do not use the term 'Purcell factor' since the dipole in the reference structure does not experience a homogeneous dielectric environment. The radiative rate enhancement with respect to the reference structure was then calculated for different dipole positions moving along the x direction, perpendicular to the grating axis.

3.3.4 Directivity

I calculated the directivity of light emitted by dipoles in the same positions as for the Purcell factor. To do this I used an additional frequency-domain field and power monitor set to record all the field components directly above both the nanoantenna and grating structures in the x, y plane. The size of the monitor was set to be several times larger than the structure under investigation as in Figure 3.6 (a), in order to capture as much light emitted vertically into the positive z direction as possible. Note that for the gratings shown in Figure 3.6 (b), the field monitor continues in x beyond the region shown, reaching both ends of the simulation region encompassing 20 periods in each direction. The fields on the surface of the monitor were then extrapolated to the far-field by considering propagating plane waves from each point onto a hemisphere above the structure 1 meter away. This enabled clear visualisation of the angle-resolved emission in 3D. The far-field Poynting vector was then integrated over a solid angle characteristic of an objective lens with numerical aperture (NA) 0.64 for the nanoantennas, and 0.7 for the grating heterostructure, representative of those used in experiment. This value was then divided by the total power emitted in all directions to give a percentage of light emitted vertically from the dipole within each nanostructure. As in Chapters 4 and 5, the directivity, Purcell factor, and electric field confinement at each point were then combined to yield an overall enhancement factor of the structures for different dipole positions.

3.3.5 Band Structure

Implemented briefly in Section 5.2.1, simulations of the photonic band structure provide a useful tool for characterising all of the bands within devices composed of a periodically modulating refractive index profile, i.e. single 1D gratings. To set up this simulation, I used a dipole cloud object as the illumination source in Lumerical. This object was composed of many dipoles placed in random locations throughout the unit cell of a single grating structure, in order to excite all available resonances of the system. I then set the polarisation of each dipole to be along the grating axis to only consider TE excitation, along with Bloch boundary conditions in the x direction to define the repeating unit cell. To record the hosted resonances, I used a group of randomly placed point

time-domain monitors throughout the unit cell. These monitors record the electric and magnetic field components $E_{x,y,z}$ and $H_{x,y,z}$ for each time step of the simulation, with apodisation applied to ignore start and end effects of the simulation, thus collecting only the sustained resonances. The fields from each point monitor were then Fourier transformed into the frequency domain and added together, before using a peak finding function to identify the frequency of each resonance. This process was repeated for different Bloch vectors in k_x to calculate the dispersion of each photonic band across k-space. As mentioned in Section 5.2.1, whilst this simulation technique is the most rigorous for visualising the full band structure of photonic crystals in k-space, it is difficult to reproduce experimentally, and does not give reliable information on relative mode linewidths and amplitudes. The following sections will therefore focus on the setup of reflectance contrast simulations with both FDTD and RCWA, which will be used heavily throughout Chapter 5 for more complete characterisation of TMD grating structures, that can easily be compared to experiment.

3.3.6 Angle-Resolved Reflectance Contrast

Since the double grating structures cannot be defined in terms of a single repeating unit cell, I chose FDTD to simulate the angle-resolved reflectance contrast (RC) over RCWA. In contrast, for the individual gratings which repeat infinitely, RCWA is much more efficient as it only has to simulate a single unit cell, and will be covered later in Section 3.4.1. For the double grating structures, I simulated a minimum of 20 periods of both gratings. This gave accurate results in agreement with simulations of 50 periods of each grating or more, whilst not requiring too much time or computational power. As illustrated in Figure 3.7 (a), I used a plane wave source for the incident light, polarised parallel to the grating axis, and injected along the negative z direction towards the structure. This was accompanied by a frequency-domain field and power monitor in the x, y plane placed behind the source to measure the power of the reflected light. To measure the angle-resolved reflectance, I varied the angle of the source in the x, z plane between $\pm 50°$ (pink arrow), and recorded a power spectrum for each. To calculate the reflectance contrast, I simulated the same sweep but with only a gold substrate, and used Equation 5.1. The main difficulty with this type of simulation was ensuring that inaccuracies did not manifest owing to the change in source angle. The PML regions work best with light entering perpendicular to the boundary, and so at high source angles, instabilities began to occur as oscillations in the reflectance spectra due to PML reflections. I therefore used a custom PML profile to reduce the chance of these errors. This profile was the same as the "steep angle" preset, with increased number of layers to 42, thus reducing reflections to a negligible level. Furthermore, it was also important to allow the fields of the simulations to fully decay to at least 10^{-5} of the intensity of the injected wave, so that the frequency-domain results obtained via discrete Fourier transforms are accurate. I found a minimum simulation time of around 2000 fs to be adequate.

Owing to the lack of symmetry of the double grating structures, the full 40 periods had to be simulated without symmetry conditions, and so use of the HPC was necessary. For simulations of the reflectance contrast with respect to k_x, this was less of a problem as a 2D simulation region could be used owing to the uniformity along the y direction, thus significantly reducing required computational power. However, to calculate the dispersion of RC in k_y, a 3D simulation had to

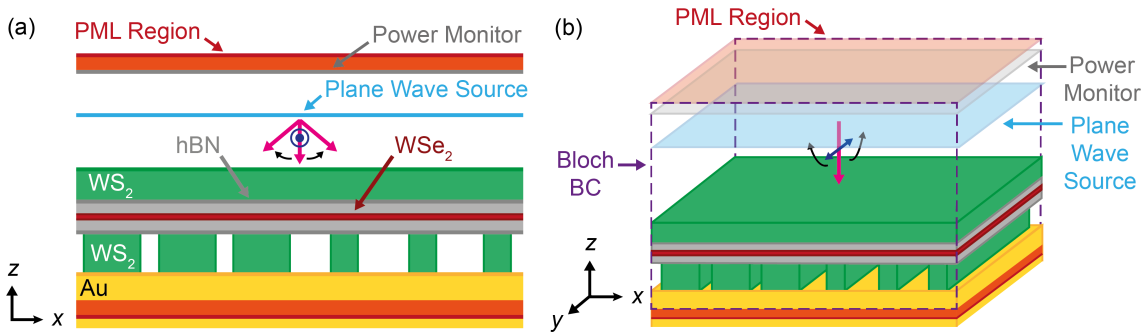


Figure 3.7: **FDTD simulation setup for angle-resolved reflectance contrast from WS_2 double grating structures.** **(a)** 2D angle-resolved simulation for dispersion in k_x shown in x, z perspective. Range of source angles in the x, z plane highlighted by the direction of the pink arrows. Plane wave source used with polarisation direction out-of-plane, parallel to the grating axis. Power of reflected light recorded through the frequency-domain power monitor at the top edge of the simulation region, behind the source. **(b)** 3D angle-resolved simulation for dispersion in k_y shown in isometric perspective. Setup is fundamentally the same as in **(a)**, however with the third spatial dimension considered, and with the source angle changing through the y, z plane. Bloch boundary conditions cap the simulation in the positive and negative y directions as depicted by the 2D purple dashed boxes, thus ensuring the wires run infinitely along y. PML boundaries are used for the x and z directions for both simulations, and full simulations consider 20 periods in each direction.

be performed, as shown schematically in Figure 3.7 (b). Not only was this more computationally expensive, but additional problems with the PML boundary conditions arose, giving spectra that did not look as expected. The solution was to use Bloch boundary conditions in the y direction, to account for the infinitely long grating wires, and keep custom-profile PML boundaries in all other directions. I then performed angle sweeps of the source along the y direction, recording the reflected power for each. These two techniques therefore enabled full k-space modelling of the dispersions of complex, non-periodic, topological grating structures, with excellent agreement to experimental results.

3.4 RCWA Simulations

When simulating infinitely periodic structures such as single gratings, I chose RCWA owing to its greater efficiency compared to FDTD in this regard. I used an open source Python implementation of the technique named S^4 [252], to calculate the reflectance contrast and electric field distributions of WS_2 inverted gratings. This allowed quick and easy optimisation of the grating parameters for realisation of a Jackiw-Rebbi edge state when combining two structures adjacently. Unlike Lumerical however, S^4 does not come with a built in graphical user interface, and so great care had to be taken to ensure the desired structure was correctly simulated. Also, rather than having a library of simple geometric objects to choose from and combine, the inverted gratings had to be manually coded layer by layer, with a repeating pattern imprinted to form the grating. As an advantage, S^4 does not require optimisation of boundary conditions, mesh discretisation, or time steps. Only the Fourier series truncation length affected the accuracy of the results, with the resolution in energy and wave vector set by the user. For reference, I found a truncation of 7 terms produced accurate

results for 1D gratings, producing full dispersions in k_x or k_y within a few seconds. Depending on whether the simulation was for optimisation or use in a figure, I chose resolutions of 100 or 200 points in both energy and wave vector respectively.

3.4.1 Angle-Resolved Reflectance Contrast

Using a simple Python code, I first defined all the grating structural parameters such as period, filling factor, and flake thicknesses. I then imported experimentally measured refractive indices for each material and defined the order of the layers, starting with the air superstrate, through the grating structure, and to the gold substrate. The pattern for the grating layer was then implemented by cutting out an air section in the middle of the unit cell of width $a(1 - F)$, where a and F are the grating period and filling factors respectively. Next, I set the Fourier series truncation length, polarisation direction of the incident light, as well as the plane of incidence. I then implemented the RCWA solver on the structure to calculate the reflectance coefficients over a chosen range of incident wavelengths, iterated over each wave vector. I also performed a variety of sweeps over different structural parameters for optimisation of the resulting band structures. For each simulation, I calculated the reflectance contrast compared to reflectance from just the substrate material through Equation 5.1, followed by saving and plotting each set of dispersions.

3.4.2 Near-Field Distributions

Once I had found the spectral positions of specific resonances such as the BIC and lossy mode through angle-resolved RC calculations, I then performed simulations of the electric fields at specific energies and wave vectors corresponding to each mode. I used the same structural and simulation parameters as for the reflectance contrast simulations, however used a different function included with S^4 to instead calculate the near-fields. These simulations were even faster than those for reflectance contrast, owing to the single wavelength and wave vector considered. As with Lumerical, S^4 returned $E_{x,y,z}$ and $H_{x,y,z}$ for each point within the simulation, allowing clear visualisation of the resonance characteristics in the near-field.

3.5 Far-Field Spectroscopy

In the following section I will detail the experimental far-field spectroscopy methods used to characterise both WS_2 nanoantennas and gratings on gold. Firstly, I will explain the premise behind dark field spectroscopy, providing a diagram of the setup and associated components used. I will then explain how angle-resolved measurements of both reflectance contrast and photoluminescence were taken using a home-built Fourier spectroscopy setup. The system was designed to include a range of changeable optics on flip mounts to switch between different measurement modes, hence standard micro-photoluminescence was also possible. With just these four techniques, I was able to comprehensively characterise the photonic resonances and excitonic coupling within van der Waals nanostructures in the far-field.

3.5.1 Dark Field

Fundamentally, dark field spectroscopy involves illuminating a sample at high angle to the surface normal and collecting only the vertically scattered signal, thus providing information about the various photonic resonances of a system. I performed dark field measurements on the WS_2 nanoantennas on gold discussed in Chapter 4, as the main characterisation technique in the far-field. This was done by illuminating the nanoantennas through the objective of a Nikon LV150N microscope fitted with an annular mirror between the illumination source (tungsten halogen lamp), and the $50\times$ magnification objective lens with high numerical aperture (NA) of 0.8. As in Figure 3.8 (a), the hole of the annular mirror was slightly smaller than the diameter of the beam, so that the central part was discarded and only the outer ring of light entered the objective. Due to the high numerical aperture, the sample was illuminated at a high oblique angle, causing light to resonate within, and be scattered from the nanoantennas. The vertically scattered light was then collected by the same objective and passed back through the hole in the annular mirror towards a 50 µm pinhole, before entering a fibre coupler. The pinhole ensured that only light scattered at a low angle to the substrate normal could propagate into the 100 µm diameter core of the multi-mode (MM) fibre. Another fibre coupler at the opposite end then collimated the beam and sent it onto a free space path, as in Figure 3.8 (b), where two convex achromatic lenses were used to minimise beam diversion of the multi-mode signal on its way to the spectrometer. Finally, a single achromatic lens was used to focus the beam onto the slit of a Princeton Instruments spectrometer, where the wavelength components were separated by a 750 nm blaze wavelength grating with 300 grooves per mm, followed by detection using a nitrogen-cooled charge-coupled device (CCD).

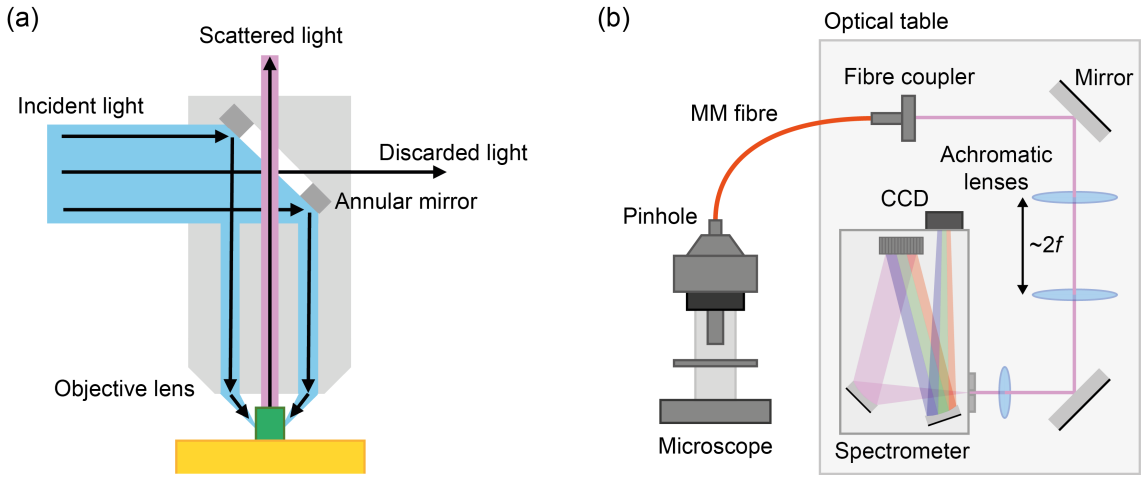


Figure 3.8: **Schematic of home-built dark field spectroscopy setup. (a)** Close-up diagram of objective lens and annular mirror. Centre profile of light from tungsten lamp is blocked, leading to high excitation angle of nanoantenna sample relative to normal incidence. Scattered light passes through the hole in the annular mirror, guided towards a pinhole and fibre coupler. **(b)** Illustration of collection path on an optical table. Multi-mode (MM) fibre connects to a fibre out-coupler before passing through two identical convex achromatic lenses to minimise beam diversion. f corresponds to the focal length of the lenses. Final achromatic lens focuses light onto the spectrometer slit, which is subsequently split into component wavelengths by a grating, before detection via a CCD.

3.5.2 Angle-Resolved Reflectance Contrast

To measure reflectance contrast over a range of wave vector space, I used Fourier spectroscopy techniques to separate the angular dispersions of signal from the grating structures presented in Chapter 5. The principle behind Fourier spectroscopy is to image the plane where light emitted or reflected from a sample is focused so that each point corresponds to the intensity of photons emitted with a particular wave vector. This plane is referred to as the Fourier plane, and so when imaged onto the spectrometer CCD, directly shows angle-resolved dispersions from a given sample. This technique differs from conventional reflectance spectroscopy, where the intensity at each point on the chosen focal plane corresponds to that of a real-space image of the sample.

Figure 3.9 illustrates the home-built Fourier spectroscopy setup that I was involved in assembling. The setup was designed to be versatile, able to operate in Fourier reflectance contrast and photoluminescence modes, as well as conventional real-space spectroscopy such as micro-RC and micro-PL. This was achieved by using a variety of optics on flip mounts. For typical Fourier spectroscopy, only a single lens placed to image the Fourier plane of the sample is needed, as indicated by the 250 mm focal length lens in Figure 3.9. However, to increase resolution in k-space, an additional two lens telescope system was added (600 and 200 mm lenses), thus increasing the size of the collection spot on the spectrometer CCD. To operate in Fourier-space imaging mode, the 200 mm lens was flipped into the beam path, and flipped out for real-space imaging.

For angle-resolved reflectance contrast measurements, a Thorlabs SLS201/M white light source was used for excitation, coupled onto the raised optical table via a multi-mode fibre as illustrated by the dark orange waveform in Figure 3.9. The beam then reflected from a mirror on a flip mount, through a linear polariser and half-wave plate to align the incident polarisation parallel to the grating axes (i.e. along the grooves). Before the 50:50 beam splitter (Thorlabs CCM1-BS013), a 150 mm focal length lens was used to ensure uniform Köhler illumination of the sample through the $100\times$ Mitutoyo M Plan Apo objective lens. The objective was mounted on an automated z stage for easy control of the focus, with the sample on an x, y stage on the lower optical table for precise positioning. The reflected light then travelled back up through the beam splitter and through a 250 mm lens (i.e. the first Fourier lens). This collimated the Fourier plane of the objective, whilst focusing the real-space plane at a rectangular variable aperture (Coherent 53-1137). Here, the signal from particular gratings could easily be isolated in real-space by changing the size and aspect ratio of the aperture. A periscope then guided the reflected signal down onto the lower optical table, before passing through a 600 mm lens followed by a second Fourier lens (200 mm) to increase the spot size by 3 times compared to using a single Fourier lens. A Thorlabs BP108 pellicle beam splitter redirected 8% of the signal to a Thorlabs DCC1645C-HQ camera for visualisation of the sample, focused via a 150 mm lens. If required, neutral density (ND) filters of different strengths were then flipped into the beam path to protect the spectrometer CCD. A final 150 mm lens focused the reflected Fourier plane onto the slit of a Princeton Instruments spectrometer, fitted with a 300 grooves per mm diffraction grating with blaze wavelength 860 nm. Importantly, the 700 nm long-pass filter was flipped out of the beam path for Fourier RC. A nitrogen-cooled CCD with 1340×400 pixels was then used for detection, with wavelength components separated along the long axis, and wave vector space dispersed along the short axis.

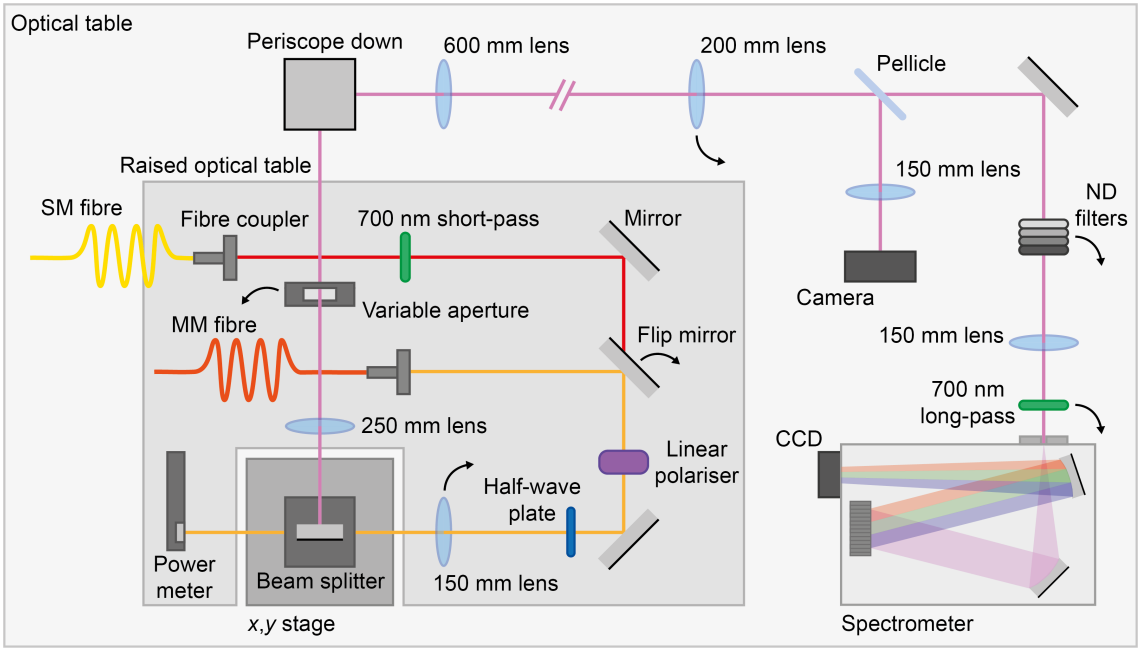


Figure 3.9: **Schematic of home-built Fourier spectroscopy setup.** Angle-resolved reflectance contrast measurements possible using white light excitation (orange beam) of sample through the multi-mode (MM) fibre. Linear polariser and half-wave plate allow choice of polarisation direction, and 150 mm lens before 50:50 beam splitter ensures uniform Köhler illumination. Below the beam splitter are the 100× objective mounted on a z stage, with sample on an x, y stage below. Reflected signal travels back through the beam splitter to a mirror and through a 250 mm lens to collimate the Fourier plane of the objective. Variable rectangular aperture then used in the real-space plane to determine the spatial region for signal collection. Further two 600 and 200 mm lenses act as a telescope to increase image size. 200 mm lens on flip mount used to switch between real-space and Fourier plane imaging modes. Pellicle allows visualisation of sample surface via a camera for positioning. Neutral density (ND) filters enable tuning of light intensity on the spectrometer CCD. Final lens before spectrometer focuses the signal on the slit for detection, with long-pass filter flipped out of the beam path. For angle-resolved photoluminescence, the single-mode (SM) fibre injects a 637 nm laser (red beam) onto the same excitation path as the white light with the central flip mirror and first 150 mm lens moved out of the path. 700 nm short-pass filter used in the collection path along with 700 nm long-pass in the collection path for removal of all signal except from sample PL emission. Micro-RC and micro-PL possible by flipping the 200 mm lens out of the beam path. All optics on flip mounts denoted by curved black arrows.

3.5.3 Angle-Resolved Photoluminescence

For Fourier photoluminescence measurements, the white light source was swapped for a Vortran Stradus 637 nm diode laser coupled onto the raised optical table via a single-mode (SM) fibre, as illustrated by the yellow waveform in Figure 3.9. The out-coupled beam (in red) subsequently passed through a 700 nm short-pass filter, before joining the same excitation path as the white light source upon flipping out the central mirror. The linear polariser and half-wave plate were again set to align the incident polarisation along the grating axes. Importantly, for Fourier-PL the 150 mm lens before the beam splitter was flipped out of the beam path, ensuring a tight focus of the laser to a 2 micron diameter spot on the sample. The variable aperture was also flipped out of the beam path, before continuing through the 600 and 200 mm lenses. ND filters were used during

alignment of the laser to protect the CCD. Finally, the 700 nm long-pass filter was flipped into the beam path to remove any laser and background signal in conjunction with the earlier-used 700 nm short-pass. In this way, angle- and wavelength-resolved photoluminescence emission was directly recorded by the spectrometer CCD.

3.6 Near-Field Spectroscopy

Whilst conventional far-field characterisation techniques can give great insight into the optical properties of materials and devices, the resolution is often limited to micron-sized collection regions, with fundamentally different properties to the near-field. Scanning probe methods can strongly improve spatial resolution down to tens of nanometers, with the ability to map samples over tens of microns within minutes. In addition, the nature of a scattering tip means that local fields can be directly probed, rather than indirectly determining their character from far-field spectroscopy. Therefore, in this final section of the methods chapter I will discuss the principles behind scattering-type scanning near-field optical microscopy (s-SNOM), and how I implemented this technique to probe the local resonant responses of van der Waals nanostructures.

3.6.1 Scattering-Type Scanning Near-Field Optical Microscopy

Fundamentally, s-SNOM is a form of atomic force microscopy combined with an illumination source incident on the tip. As well as the AFM topography, this allows probing of the optical properties of a sample on the nanoscale. I used a commercial neaspec modular s-SNOM system in conjunction with a tunable Coherent Chameleon + Compact OPO laser, to excite both the WS_2 nanoantennas and gratings on gold studied in Chapters 4 and 5 respectively. The tunable laser was aligned onto a Platinum-Iridium (PtIr) coated cantilever tip (NanoWorld Arrow NCPt), with radius of curvature less than 25 nm, using a parabolic mirror within the s-SNOM system as illustrated in Figure 3.10. The beam made a 60° angle with the tip, and was polarised parallel to the plane of incidence (p-polarised), in order to maximise the field component along the tip axis. This led to strong near-field confinement of the incident light at the tip, which then interacted with the samples below. Once well-aligned, the sample was raster scanned beneath the tip to map the near-fields, rather than moving the tip itself, in order to retain good alignment. Since the spot size was considerably larger than the tip (order of a few microns), the signal was dominated by background scattering from the sample and tip shaft as is common with s-SNOM. In order to remove the overwhelming background signal, a pseudoheterodyne (PsHet) interferometric detection configuration was used.

Before explaining PsHet, I will first detail how most of the background signal can be removed simply by considering how the background has a different dependence on tip height compared to the near-field signal of interest. The background signal varies almost negligibly upon oscillation of the tip over tens of nanometers tapping amplitude, however in contrast, the near-field signal from the tip-sample region is strongly influenced by the distance between the tip and sample. This means that by locking in the detector at harmonics of the tapping frequency Ω, much of the background can already be filtered out. Equation 3.1 defines the intensity of the scattered light from the tip

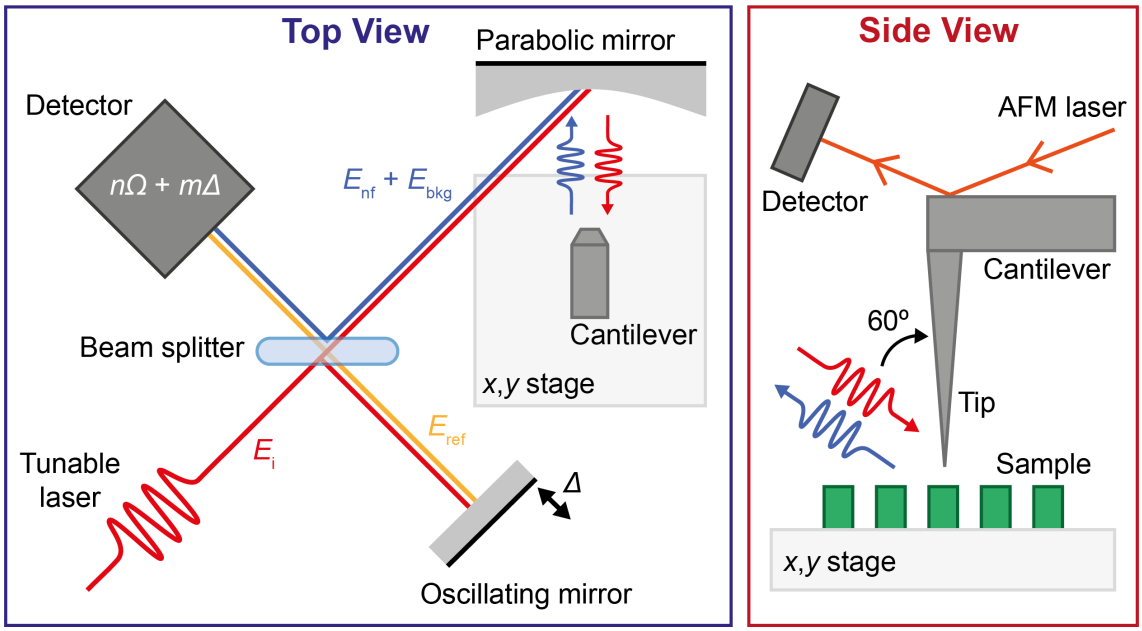


Figure 3.10: **Schematic of commercial neaspec s-SNOM setup.** Top down view illustrated within the blue box containing a tunable laser with electric field strength E_i incident on a $50:50$ beam splitter as shown in red. Half the light reflects to a mirror oscillating at frequency Δ to produce a reference beam with a phase modulation described by E_ref as shown in yellow. Remaining half passes through to a parabolic mirror for focusing onto the tip apex. Back-scattered light from the tip-sample interaction region is collected by the same parabolic mirror, containing a small near field signal and a large background contribution $E_\mathrm{nf} + E_\mathrm{bkg}$, as shown by the blue line. This recombines with the reference beam at the beam splitter, before reaching the detector. To remove the background, the detector locks in at sideband frequencies of the tapping and reference mirror frequencies $n\Omega + m\Delta$. Red box illustrates the side view of the tip-sample region, where the red and blue waveforms correspond to the incident and scattered signal propagating at $60°$ to the tip axis. Laser incident on the back of the cantilever in orange is used for AFM topographical measurements. During scanning, only the sample moves beneath the tip via an x, y stage to retain good alignment.

$$\begin{aligned} I &= (E_\mathrm{bkg} + E_\mathrm{nf})^2, \\ &= E_\mathrm{bkg}^2 + E_\mathrm{nf}^2 + 2E_\mathrm{bkg}E_\mathrm{nf}, \end{aligned} \tag{3.1}$$

where the measured scattering intensity I contains two contributions. E_bkg corresponds to the background signal, and E_nf corresponds to the near-field signal of interest. By locking in at harmonics $n\Omega$, the detector measures the cross-term $2E_\mathrm{bkg}E_\mathrm{nf}$, thus removing the strong E_bkg^2 dependence, however the signal still contains a multiplicative E_bkg factor. Here, pseudoheterodyne detection needs to be used in order to remove the unwanted background signal completely, and focus purely on the near-field signal. PsHet works by using a beam splitter to direct half of the incident light to the tip, and half to an oscillating reference mirror as in Figure 3.10, which induces a phase modulation. The reference beam is then recombined with the scattered signal at the detector. Equation 3.1 therefore gains an additional term, E_ref, as follows

$$
\begin{aligned}
I &= (E_{\text{bkg}} + E_{\text{ref}} + E_{\text{nf}})^2, \\
&= E_{\text{bkg}}^2 + E_{\text{ref}}^2 + E_{\text{nf}}^2 + 2E_{\text{bkg}}E_{\text{ref}} + 2E_{\text{bkg}}E_{\text{nf}} + 2E_{\text{ref}}E_{\text{nf}}.
\end{aligned} \tag{3.2}
$$

The interference between the total scattered signal and the reference beam produces sidebands of frequencies $f_{n,m} = n\Omega + m\Delta$ [255], where Δ is the reference arm modulation frequency. By locking onto a sideband frequency, the detector measures only the final term from equation 3.2, where the pure near-field signal E_{nf} can be calculated by dividing through by the electric field of the reference beam, hence removing all background contributions.

By modelling the tip-sample interaction as a point dipole in the apex of the tip that induces a mirror dipole in the sample, the effective polarisability of the system α_{eff} can be extracted through the proportionality $E_{\text{nf}} \propto \alpha_{\text{eff}} E_{\text{i}}$ [256], where E_{i} corresponds to the electric field of the incident illumination. Since both E_{i} and E_{nf} are complex numbers, dividing the two yields another complex number $\alpha_{\text{eff}} = se^{i\phi}$, where s is the amplitude and ϕ is the phase of the scattered near-field signal. This means that through PsHet detection, simultaneous measurement of the near-field scattering amplitude and phase is possible, which relate to the real and imaginary parts of the dielectric function of the sample respectively. Along with complete background suppression and enhanced signal owing to the reference beam, PsHet is an effective technique for reliable, high signal-to-noise ratio s-SNOM measurements.

4

Hybrid Mie-Plasmonic Resonances in WS_2 Nanoantennas on Gold

4.1 Introduction

In the last decade, transition metal dichalcogenide monolayers have attracted a large research effort owing to their direct band gap transition and useful opto-electronic properties [50], rendering the bulk material largely overlooked. More recently, nanoresonators utilising bulk TMDs to host Mie resonances have gained interest, however these studies primarily focus on fabricating such structures on low refractive index dielectric substrates such as SiO_2 [102–104, 147, 257–259]. A hybrid TMD-nanoantenna-on-metal system has not been thoroughly explored experimentally, with previous work being focused on different structures such as TMD gratings on gold [260], metallic nanoparticle-on-TMD monolayer systems [261, 262], or hybrid silicon-metal-based structures [171, 172, 174, 263–266]. One of the first hybrid devices to be numerically characterised was a dielectric nanowire above a metallic substrate by Rupert Oulton *et al.* [175], which led to the prediction of hybrid dielectric-plasmonic modes. Since then, a variety of other dielectric-metallic nanostructures have been considered. For example, Yi Yang *et al.* numerically analysed dielectric nanoantennas situated several nanometers above a silver substrate [171]. Their work demonstrated hybrid dielectric-plasmonic modes [171, 175] with quality factors up to $\sim 10^3$ and Purcell enhancements of > 5000, along with strong electric field confinement in the nanoantenna-substrate gap. Shiyu Shen *et al.* [263] built on this by simulating an hBN-WSe_2 heterostructure placed within the gap, achieving strong light-matter coupling. Experimental work has so far been focused around silicon-based nanoresonators on metallic substrates. In 2018, Lei Xu *et al.* fabricated silicon nanodisks on a gold substrate, realising an anapole mode [267]. The anapole was used to enhance third harmonic generation by two orders of magnitude compared to the same nanodisk

on an insulating substrate. Aili Maimaiti *et al.* fabricated a similar device composed of polycrystalline silicon nanodisks on a gold substrate, but with the introduction of an Al_2O_3 spacer layer between the nanodisk and substrate [172]. This led to an electric field enhancement in the spacer of over 40, and a Purcell factor of 300 for a vertically oriented dipole in simulation. In experiment, they demonstrated fluorescence enhancement, and surface-enhanced Raman spectroscopy of coupled molecules with a more stable signal than solely plasmonic nanodisks. More recently, Pavel Dmitriev *et al.* fabricated silicon nanorings on gold with a layer of embedded quantum emitters between them [174]. They observed Mie resonances from the nanoring in dark field spectroscopy, along with strong directionality of the coupled emitters normal to the substrate, with a fluorescence enhancement of over 650. Finally, in our recent work by Panaiot Zotev *et al.* [21], WS_2 nanoantennas were fabricated on gold as proof of concept, showing initial evidence of a drastic change in the mode structure in nanoantennas on a gold substrate compared to on SiO_2 in dark field spectra. However, a thorough investigation into the physics and applications of such a different mode structure in hybrid TMD nanoantennas-on-metal is yet to be performed, which is the main focus of this experimental chapter.

TMDs present an attractive alternative to silicon-based nanophotonics [268] for generating strong mode confinement owing to their higher refractive indices [269], whilst also having negligible absorption over large parts of the visible wavelength range [80]. Additionally, one can achieve high crystalline quality of thin films (from monolayer up to $\sim$ 500 nm) required for fabrication of nanoantennas, through simple exfoliation from bulk TMDs [2]. Furthermore, they can be exfoliated onto a range of other materials owing to their inherent van der Waals attractive forces [50]. This avoids difficulties with materials bonding as well as lattice matching requirements [22] and growth in molecular beam epitaxy chambers, which are associated with fabricating nanostructures from other conventional dielectrics such as GaAs and GaP [23]. Use of TMDs thus opens exciting additional possibilities in the design and fabrication of hybrid dielectric-metallic structures of a variety of thicknesses, enabling advanced control of photonic and plasmonic resonances on the nanoscale.

In this study, I provide detailed insight into the physics of hybrid dielectric-metallic nanophotonic systems that host high quality factor modes not seen in purely dielectric Mie resonators. To do this, I first simulate a WS_2 nanoantenna suspended in vacuum using the finite-difference time-domain method, and obtain scattering spectra containing a range of features. I then identify constituent Mie resonances and anapole conditions in the spectra by performing rigorous multipole expansions, and plotting the associated electric field distributions. To characterise the effect of adding a metallic substrate, I gradually move the nanoantenna closer to an infinite gold plane until Fano-lineshape, hybrid Mie-plasmonic modes [270] appear in the scattering spectra. These hybrid modes show strongly enhanced quality factors compared to the Lorentzian-lineshape Mie modes in WS_2 nanoantennas on SiO_2, with strong near-field localisation to the gold-TMD boundary. Further simulations upon changing nanoantenna radii for gold, SiO_2, and vacuum substrates confirm the plasmonic nature of the MP mode, which only exists when the gold substrate is present.

Following the simulations, I then fabricate WS_2 nanoantennas on a gold substrate and characterise their optical response with experimental dark field spectroscopy. The results agree well with

my previous simulations and other work [21], exhibiting strong tunability with changing height and radius. In particular, the hybridised Mie-plasmonic modes exhibit experimental Q factors up to 165, a factor of 33 times higher than Mie modes previously measured in nanoantennas on silica [21], highlighting potential applications in switching and sensing [271–274]. Additional Fabry–Perot, and Fabry–Perot-plasmonic modes are also identified in taller nanoantennas of height 180 nm, via comparison to theory and simulations of their electric field distributions.

Next, I explore strong mode coupling between a Fabry–Perot-plasmonic mode and a Mie resonance in the vicinity of the higher-order anapole condition in both experiment and simulation. Such resonances can be tuned to realise an anti-crossing in the scattering spectra, with an experimental Rabi splitting of 48 ± 5 meV. At the point of minimum energy splitting, signatures of a highly confined supercavity mode [130] (i.e. BIC) with an experimental Q factor of 263 ± 28 are observed, resulting from destructive interference of the two modes outside of the nanoantenna structure. This offers a simple-to-fabricate solution for realising a supercavity mode in finite-sized nanophotonic devices with applications in enhancing non-linear effects [275].

Finally, I highlight potential applications of the hybrid dielectric-metallic nanophotonics platform under study, by modelling WS_2 nanoantennas on top of 5 nm thick layers of hBN attached to a gold substrate. With this device, I numerically achieve strong electric field enhancement exceeding 2600 in the hBN spacer between the nanoantenna and gold. From this, I calculate Purcell enhancements of over 700 for a dipole polarised normal to the substrate within the hBN, and light extraction efficiencies as high as 50% through a numerical aperture of 0.64. These factors combined yield an overall enhancement factor of over 10^7, highlighting the potential for strongly enhancing the emission of coupled single photon emitters (SPEs), or interlayer and moiré excitons [276, 277] in TMD heterostructures placed within the gap via standard van der Waals material transfer techniques.

4.2 Simulations of WS_2 Nanoantenna Resonances

I begin my study into WS_2 nanoantennas by performing a comprehensive characterisation of Mie modes, anapoles, and hybridised plasmonic resonances in simulation. To do this, I first consider a nanoantenna suspended in vacuum as a basis. By performing multipole expansions, I identify all Mie resonances and anapoles present in the structure, before progressing to gradually introducing a gold substrate. Each mode is then tracked in spectral position and quality factor to directly visualise how the presence of gold changes the mode structure. Electric field distributions of all the modes in suspended nanoantennas and nanoantennas on gold will also be compared, thus highlighting the hybridisation with plasmons that occurs owing to the metallic substrate. I then finish this section by varying the nanoantenna radii for different substrates, clearly highlighting the advantages of using gold, and the tunability of each resonance. These simulations will subsequently form the basis for the design and fabrication of WS_2 nanoantennas on gold in experiment.

4.2.1 Multipole Expansion of Mie Resonances in Suspended Nanoantennas

In order to assign the contributions of individual Mie modes to peaks in the overall scattering spectra of WS_2 nanoantennas on gold, we must first understand the decomposition of the modes for the

simpler case of a nanoantenna suspended in vacuum. Here I used the open source software MENP [88] in order to perform rigorous multipole expansions of the electric and magnetic fields within and around a WS_2 nanoantenna simulated with FDTD. The MENP package uses theory detailed previously in Sections 2.4.2 and 2.4.3, to numerically calculate the partial scattering cross-sections associated with each Mie resonance for any finite-sized nanostructure. Firstly, I performed an exact multipole expansion using Equation 2.13 [89], which enabled identification of the base Mie modes such as the electric dipole (ED), magnetic dipole (MD), electric quadrupole (EQ), and magnetic quadrupole (MQ) moments. The total and partial scattering cross-sections for each mode are shown in Figures 4.1(a) and (d) for two different sizes of nanoantennas. It is immediately evident that the predominant contribution to the scattering spectra of both the smaller and larger nanoantennas is from the ED mode. This is likely owing to the small size of the structures compared to the incident wavelength. In Figure 4.1 (a), there is also a small magnetic quadrupole contribution at $\sim$ 700 nm wavelength, whilst the MD and EQ modes are negligible. As the size of the nanoantenna increases in Figure 4.1 (d), smaller partial scattering cross-sections for all the multipole moments become visible, however mostly below 800 nm wavelength. These results indicate that the main resonance peaks for such WS_2 nanoantennas can confidently be attributed to the electric dipole mode, however this does not explain the cause of the dips in scattering intensity.

The first dip at around 625 nm for both of the spectra in Figures 4.1 (a) and (d) can be attributed to absorption losses owing to the WS_2 exciton. To identify the cause of subsequent scattering minima, I performed an additional multipole expansion for both structures using the long-wavelength approximation associated with Equation 2.19. With this technique, the partial scattering intensity associated with the electric dipole mode from Figures 4.1 (a) and (d) can be decomposed into two terms, $C_p = \left|\boldsymbol{p}^{\mathrm{Car}} + ik\boldsymbol{T}^{\mathrm{Car}}\right|^2$, as detailed in Section 2.4.3. Here, $\boldsymbol{p}^{\mathrm{Car}}$ and $\boldsymbol{T}^{\mathrm{Car}}$ refer to the Cartesian electric and toroidal dipole components respectively [95], and k is the wavenumber. The partial scattering cross-sections associated with these two terms, denoted $\left|\boldsymbol{p}^{\mathrm{Car}}\right|^2$ and $k^2\left|\boldsymbol{T}^{\mathrm{Car}}\right|^2$ are plotted in Figures 4.1 (b) and (e) for the two nanoantennas of different sizes. From the previous expression for C_p, a scattering minimum can be achieved when $\boldsymbol{p}^{\mathrm{Car}} = -ik\boldsymbol{T}^{\mathrm{Car}}$, also known as the anapole condition [88, 93, 96]. Whilst the anapole condition is not an eigenstate of the system itself [92] like the Mie modes are, it can be visualised as a destructive interference of the Cartesian electric and toroidal components [93, 95, 96], thus causing suppression of the scattering in the far-field [94]. By plotting the partial scattering cross-sections for $\left|\boldsymbol{p}^{\mathrm{Car}}\right|^2$ and $k^2\left|\boldsymbol{T}^{\mathrm{Car}}\right|^2$ as in Figure 4.1 (b), one can see that the two curves intersect at around 700 nm wavelength. This indicates that the magnitude of the partial scattering cross-sections are equal, however to prove that the anapole condition is met, the two contributions must also be of opposite phase. I therefore plotted the phase of the Cartesian electric p_x^{Car} and Cartesian toroidal $-ikT_x^{\mathrm{Car}}$ components for the smaller nanoantenna in Figure 4.1 (c), demonstrating cancellation of the two phase components at 700 nm. I repeated the same process for the larger nanoantenna and plotted the approximate multipole expansion and phase in Figures 4.1 (e) and (f) respectively. In both plots, a crossing of the Cartesian electric and toroidal components occurs twice, at around 720 nm and 1040 nm, hence unveiling an additional higher-order anapole (HOAP) at lower wavelength. These results therefore confirm the existence of an anapole and higher-order anapole condition in suspended WS_2 nanoantennas in simulation.

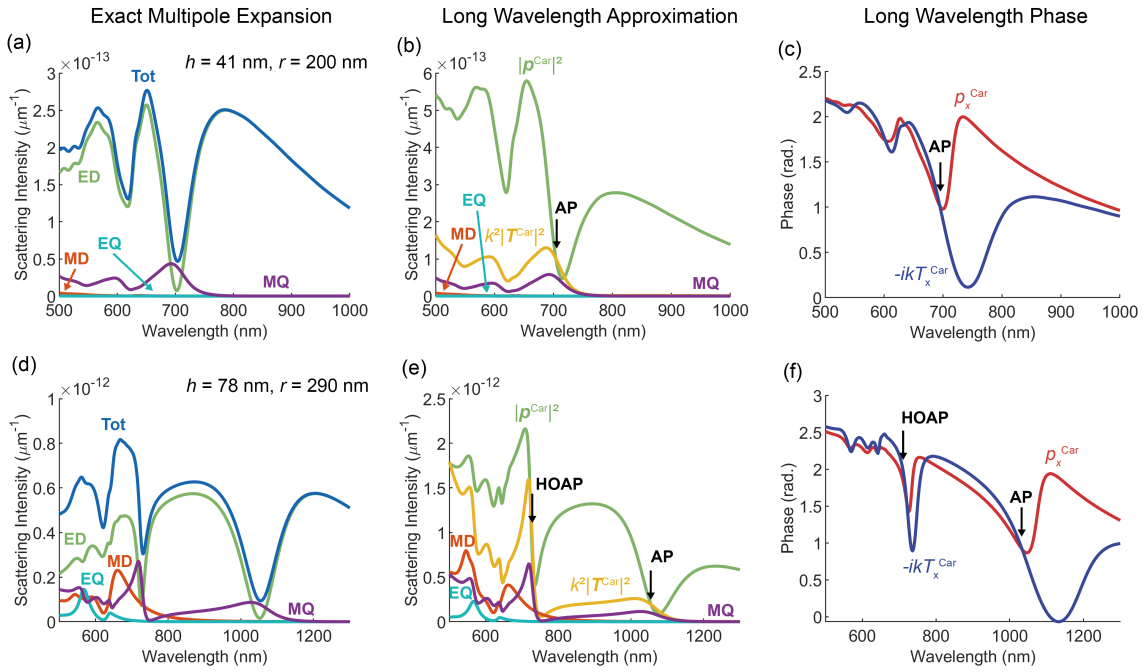


Figure 4.1: **Rigorous multipole expansion of Mie modes within WS_2 hexagonal nanoantennas suspended in vacuum.** **(a)** Exact multipole expansion of Mie modes for a WS_2 nanoantenna of height 41 nm and radius 200 nm in vacuum. ED, MD, EQ, MQ, and Tot correspond to the scattering from the electric and magnetic dipoles, the electric and magnetic quadrupoles, and the sum of all contributions respectively. **(b)** Approximate multipole expansion where the ED mode has been decomposed into partial scattering cross-sections from the Cartesian electric dipole component, $\left|\boldsymbol{p}^{\mathrm{Car}}\right|^2$, and toroidal electric dipole component, $k^2\left|\boldsymbol{T}^{\mathrm{Car}}\right|^2$ where k is the wavenumber. AP corresponds to the anapole condition. **(c)** Phase calculation of the Cartesian electric (p_x^{Car}) and toroidal ($-ikT_x^{\mathrm{Car}}$) dipole components. **(d)**, **(e)**, and **(f)** show results for a nanoantenna of height 78 nm and radius 290 nm in vacuum for the exact multipole expansion, approximate expansion, and approximate expansion phase respectively. HOAP corresponds to the higher-order anapole.

4.2.2 Electric Field Distributions in Suspended WS_2 Nanoantennas

To further characterise the resonances in WS_2 nanoantennas suspended in vacuum, I performed electric field simulations of the electric dipole mode, anapole, and higher-order anapole. The results are presented in Figure 4.2, and give further insight into the characteristic near-field distributions of each resonance. Firstly, I observed that the electric dipole mode is confined most strongly at and around the nanoantenna vertices [145], along the polarisation direction of the incoming light, as shown in Figures 4.2 (a) and (d). A central lobe is present within the nanoantenna, however the electric field intensity is an order of magnitude weaker than at the vertices. In contrast, Figures 4.2 (b) and (e) show that the anapole resonance is strongly confined to within the nanoantenna boundaries, with little leakage to the environment. This is also true for the HOAP presented in Figures 4.2 (c) and (f), which demonstrates stronger maximum field intensity of 26 compared to 9 for the AP. Here, the electric field intensity in each case is normalised to that of the incident plane wave for fair comparison. Both the AP and HOAP show very characteristic field distributions for the anapole condition, consisting of a central maximum surrounded by two symmetric lobes along the direction perpendicular to the incoming polarisation, which is well-documented in literature [92,

94, 105, 120, 267, 278]. The number of outer lobes simply increases for each additional order, with the central maximum becoming more and more confined. Since there is no substrate for any of the simulated structures, the electric field lobes are mostly symmetric about the $z = 0$ plane, extending near equally out of the top and bottom of the nanoantennas. These field distributions serve as a comparison to further simulations that I will present in Section 4.2.4 for WS_2 nanoantennas on a gold substrate, as well as providing additional understanding behind the behaviour of each mode.

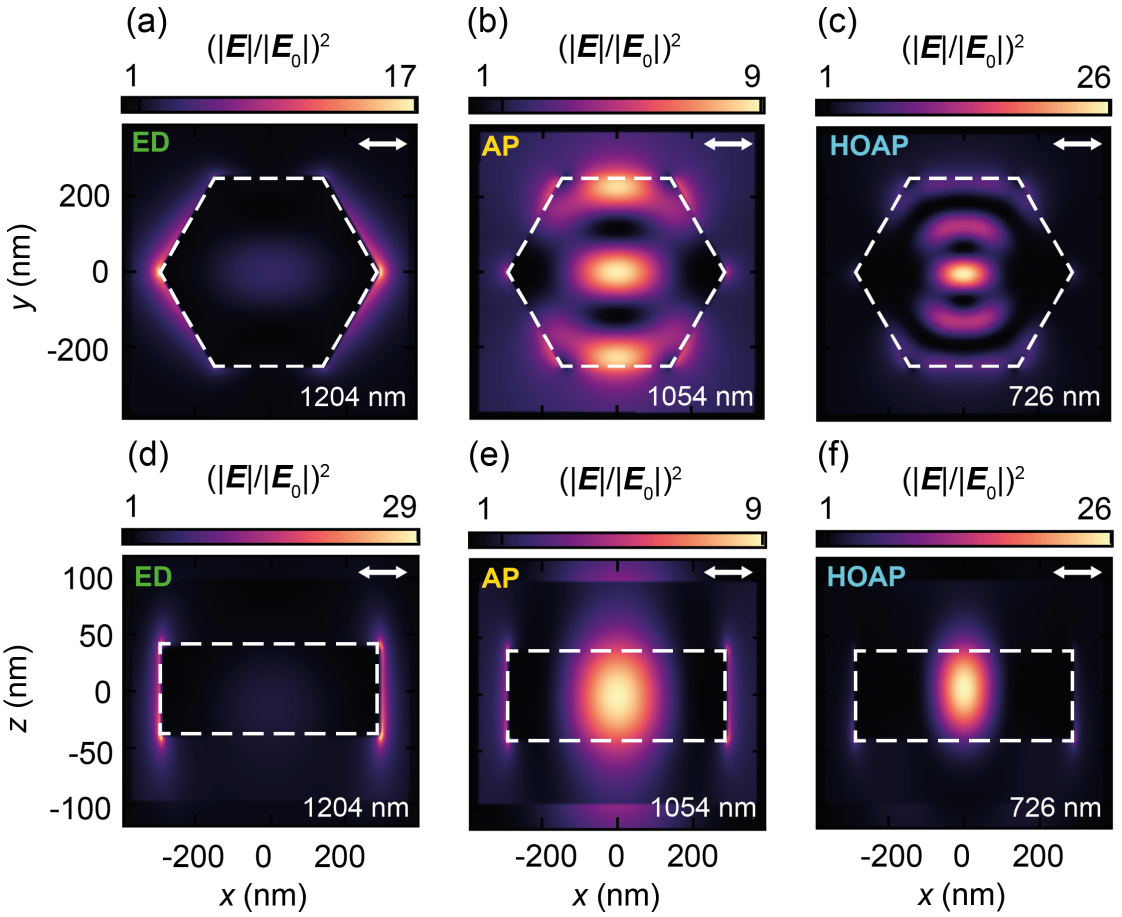


Figure 4.2: **Simulated electric field intensity within a WS_2 nanoantenna of height 78 nm and radius 290 nm in vacuum for different resonances.** **(a)**, **(b)**, and **(c)**, correspond to the electric field distributions of the electric dipole mode, anapole, and higher-order anapole in a cross-section through the middle of the nanoantenna in the x, y plane respectively. **(d)**, **(e)**, and **(f)** correspond to the same modes in the x, z plane. Incident plane wave is polarised along the x axis. Bottom right value in each panel denotes incident wavelength. White dashed boxes indicate the nanoantenna edges. ED mode shows greater leakage outside the structure than the more confined AP and HOAP.

4.2.3 Introducing the Gold Substrate

With the constituent Mie modes and anapoles all identified for a WS_2 hexagonal nanoantenna in vacuum, I will now progress to investigating the effects of using a gold substrate on each individual mode, rather than a dielectric. By considering an all-dielectric, hexagonal WS_2 nanoantenna on SiO_2 system as illustrated in Figure 4.3 (a), and a hybrid dielectric-metallic WS_2 nanoantenna on gold system as in Figure 4.3 (b), one could suggest three important differences. The first being

that incident light will be reflected much more strongly from a metallic substrate than a dielectric. Therefore, it is reasonable to expect that any resonances present in the nanoantennas would increase in quality factor owing to the gold. Secondly, the reflection at the gold-TMD boundary will introduce a π phase shift of the light, hence doubling the effective mode volume. For a closed cavity hosting a standing wave, there must be nodes at the two end faces to satisfy the boundary conditions. However with the π phase shift at the TMD-gold face, there can exist an antinode at this boundary. This means that resonances of larger vacuum wavelength can be confined to the same volume compared to nanoantennas with a dielectric substrate. Finally, there is likely to be a plasmonic resonance effect owing to the free electrons in the gold and sub-wavelength confinement of light from the nanoantennas.

I first strived to understand exactly how the metallic substrate changes the mode structure of the nanoantenna system, by simulating a WS_2 nanoantenna of fixed geometry moving towards a gold substrate in 1 nm steps. With each step, I calculated the scattering spectrum from the whole system to incrementally visualise how the modes shift, and how additional modes form during the transition between an all-dielectric, and hybrid dielectric-metallic regime. A schematic of the structure is illustrated in Figure 4.3 (c), where the distance between the nanoantenna and gold substrate s is reduced from 20 nm to 0 nm. This method was necessary owing to restrictions of Equations 2.13 and 2.19, which require a homogeneous environment around the nanoantenna to perform accurate multipole expansions. I used the FDTD method to calculate the scattering cross-sections shown in Figures 4.3 (d) and (e), which correspond to single hexagonal nanoantennas (monomers) of heights 41 nm and 78 nm, and radii 200 nm and 290 nm respectively, the same as in Figure 4.1. The anisotropy of WS_2 was taken into account by using experimentally measured in- and out-of-plane refractive indices as a function of wavelength [21], as presented previously in Figure 2.7 (c). From the rigorous multipole expansions I performed previously, I was able to assign individual Mie resonances and anapoles to their respective peaks in the overall scattering spectra of the suspended nanoantennas case. These are plotted at the top of Figures 4.3 (d) and (e), labelled $s = \infty$, and serve as the reference for investigating how each mode changes due to the presence of gold.

I then tracked the spectral positions of the resonances as the nanoantennas were incrementally moved towards a gold substrate, as shown by the dashed lines in Figures 4.3 (d) and (e). The green dashed lines follow the peak scattering of the ED mode as the distance between the nanoantenna and gold s is decreased from 20 to 0 nm. The peak red-shifts by 140 nm, indicating weaker confinement due to the gold substrate, and narrows for the nanoantennas in Figure 4.3 (d) ($h = 41$ nm, $r = 200$ nm), leading to an increased quality factor. In contrast to the ED peak, the AP exhibits a small blue-shift with decreasing s, thus indicating increasing confinement due to the gold. More detailed analysis of the electric field distributions of such modes will be considered later in Section 4.2.4, to aid in explaining their opposite shifting behaviour. Interestingly, a resonance peak not seen in purely dielectric systems emerges in the spectra when s is reduced to the order of 10 nm. I label this mode Mie-plasmonic (MP) [279], as it occurs due to a hybridisation of Mie modes within the nanoantenna and plasmons in the gold, getting stronger as s decreases. Its origin will become more clear later in Section 4.2.4, where I investigate the electric field distribution of the mode. Notably,

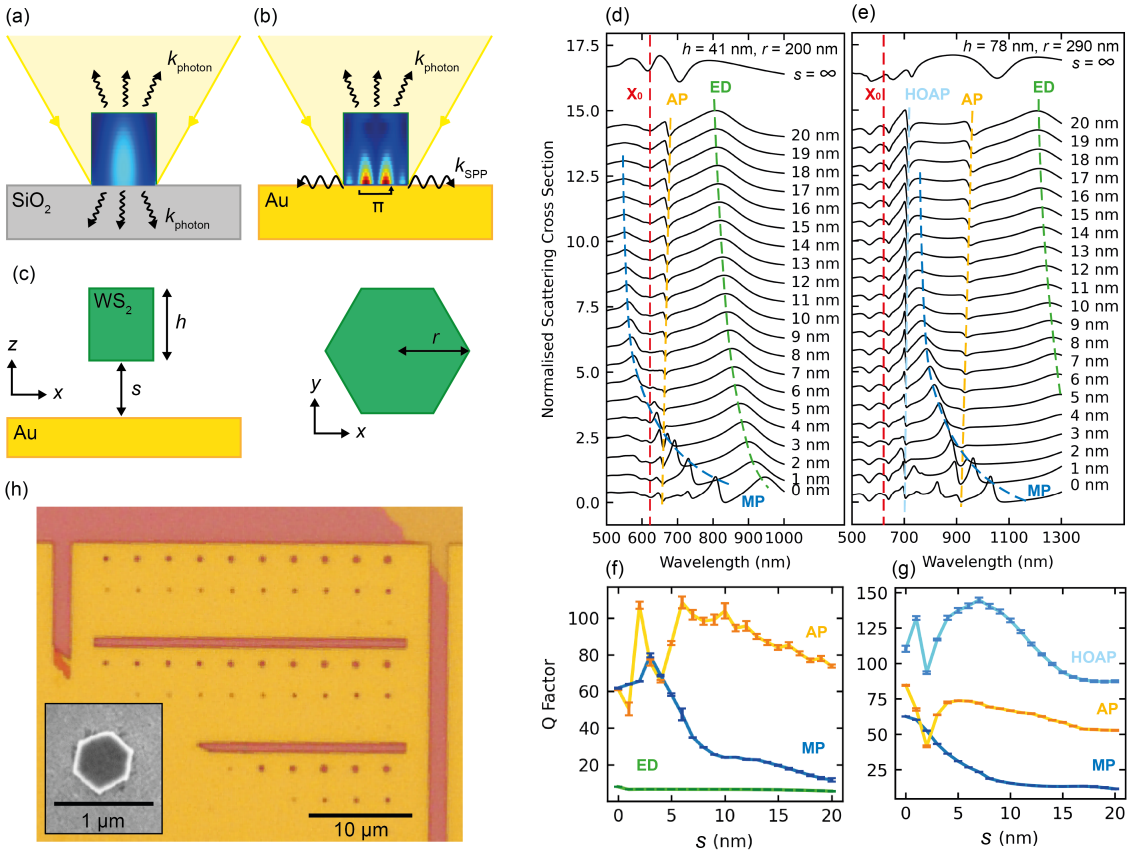


Figure 4.3: **WS_2 nanoantennas from vacuum to gold simulations.** **(a)**, **(b)** Illustrations of WS_2 nanoantennas on SiO_2 and gold substrates respectively. Inside the nanoantennas are example electric field distributions for both cases. k_{photon} and k_{SPP} correspond to the wave vector of scattered photons and guided surface plasmon-polaritons respectively. **(c)** Schematic of the structure considered in the mode tracking simulations. h and r correspond to nanoantenna height and radius respectively. s corresponds to the distance between the bottom surface of the nanoantenna and top surface of the gold substrate. **(d)**, **(e)** Simulated normalised scattering cross-section of WS_2 nanoantennas with increasing distance from a gold substrate. Geometries are $h = 41$ nm, $r = 200$ nm, and $h = 78$ nm, $r = 290$ nm respectively. X_0 corresponds to the WS_2 exciton, ED corresponds to the electric dipole mode, MP corresponds to the Mie-plasmonic mode, AP and HOAP correspond to the anapole, and higher-order anapole respectively. **(f)** and **(g)** show the Q factors of each simulated resonance as a function of s. AP, MP and HOAP are fitted with a Fano curve, and ED mode fitted with a Lorentzian. Error bars correspond to error in the fitting. **(h)** Optical image of fabricated nanoantennas arranged into arrays of 30 with increasing radii. Smaller nanoantennas not visible. Inset shows scanning electron microscopy image illustrating the hexagonal shape of the nanoantennas.

this peak is much sharper than the ED mode, and red-shifts more strongly by 159 nm from $s = 4$ nm to $s = 0$ nm for the $h = 41$ nm nanoantenna in Figure 4.3 (d). Similar behaviour is also seen in Figure 4.3 (e) for the MP mode of the $h = 78$ nm nanoantenna.

For each spectrum in Figures 4.3 (d) and (e), I fitted the various peaks using a Fano curve for the AP, HOAP, and MP mode, and a Lorentzian for the ED mode. I then extracted quality factors for each resonance by dividing the peak position by its respective linewidth as shown in Figures 4.3 (f) and (g). For the hybrid MP mode at $s = 0$ nm, I calculated a quality factor of 60, an order

of magnitude higher than that of the ED mode in Figure 4.3 (f). Furthermore, one can observe from Figure 4.3 (g) that the AP and HOAP both increase in Q factor by approximately 1.5 times as the nanoantennas are moved closer to the gold substrate, highlighting the immediate advantage of using a metallic substrate over a dielectric. The Q factors show apparent dips and discontinuities at smaller values of s, which can be explained by the spectral proximity of the AP and HOAP to the WS_2 exciton, where we expect to observe polaritonic light-matter interactions. Additional photonic modes can also couple to the AP and HOAP, which will be explored in more detail later in Section 4.3.3.

Enlarged plots of the MP mode's evolution under changing s for both the small and large nanoantennas are shown in Figures 4.4 (a) and (b) respectively. Here, I present a smaller range of spectra for $s = 0$-10 nm, with a reduced wavelength range to illustrate the behaviour of the MP mode in more detail. An anti-crossing of the MP mode and the WS_2 exciton can be observed in Figure 4.4 (a), which suggests that there could be strong coupling with the potential for polaritons. This behaviour has been reported previously in studies of Mie modes or anapoles coupling with TMD excitons [102, 120]. In addition, I note further avoided crossings with the anapole for both nanoantenna geometries in Figures 4.4 (a) and (b), which is a potential indication of additional hybridisation between multiple resonances. For the purpose of this chapter, I will focus only on hybridisation between the MP mode and anapoles, with additional optimised structures presented later in Section 4.3.3 to explore this coupling in more depth. Furthermore, when s is reduced to ~ 3 nm, another Fano-shaped peak emerges in Figure 4.4 (b) at around 690 nm wavelength. This mode exhibits a strong red-shift to 825 nm at $s = 0$ nm, suggesting that higher-order MP modes can exist within WS_2 nanoantennas on a gold substrate, hence the naming MP_1 and MP_2.

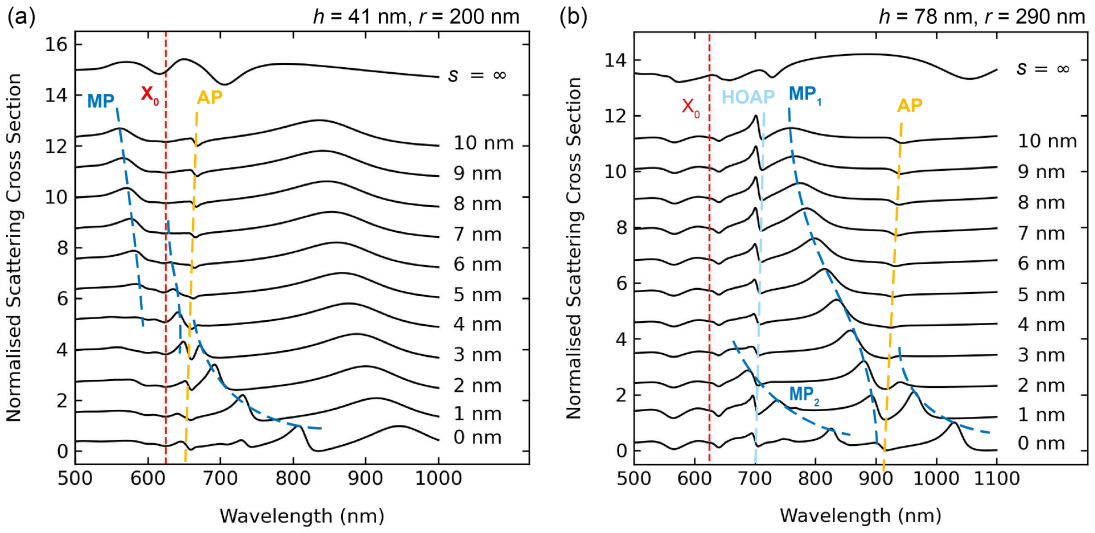


Figure 4.4: **Simulated scattering spectra with changing distance between a WS_2 nanoantenna and gold substrate s. (a), (b)** Enlarged scattering spectra from Figures 4.3 (d) and (e) corresponding to nanoantennas of $h = 41$ nm, $r = 200$ nm and $h = 78$ nm, $r = 290$ nm respectively, for clearer visualisation of the mode evolution with the introduction of a gold substrate. MP, AP and HOAP correspond to the Mie-plasmonic mode, anapole, and higher-order anapole respectively. X_0 corresponds to the WS_2 exciton. In **(d)**, an additional, higher order MP mode emerges. For both sets of spectra, a variety of anti-crossing are visible suggesting mode hybridisation.

4.2.4 Electric Field Distributions in WS_2 Nanoantennas on Gold

In order to gain further insight into the origin of the modes observed in WS_2 nanoantennas on gold, specifically the Mie-plasmonic mode, I performed electric field simulations through a cross-section of the same WS_2 nanoantenna as simulated in Figure 4.2, but on a gold substrate. The results are presented in Figure 4.5, for slices through the middle of the structure in both the x, y and x, z planes. It is immediately apparent that the field distributions of resonances within WS_2 nanoantennas on gold is very different compared to those in nanoantennas in vacuum or on low-index substrates. By first considering the ED mode in the x, y plane (Figure 4.5 (a)), a single prominent symmetrical field maximum exists in the centre of the nanoantenna. This is similar to the case of the ED mode in a nanoantenna in vacuum, however the field is less confined at the nanoantenna vertices. Nevertheless, the relative field strength for the gold substrate and vacuum cases are of the same order of magnitude. Next, by changing perspective to the x, z plane as in Figure 4.5 (d), one can observe that the central lobe protrudes upwards and out of the top of the nanoantenna with the introduction of the gold substrate, making the mode volume larger compared to in vacuum (see Figure 4.2 (d)). I therefore attribute the red-shift of the ED mode with decreasing s from Figures 4.3 (d) and (e) to this increased mode volume, stemming from the interaction of the mode with its mirror image due to the gold.

By considering the electric field profile of the anapole shown in Figure 4.5 (b), a characteristic field distribution in the x, y plane is observed [94], as with the suspended nanoantenna case. However, in the x, z plane (Figure 4.5 (e)), the central field maximum extends slightly less out the bottom of the nanoantenna compared to the case of a nanoantenna in vacuum (see Figure 4.2 (e)) owing to the gold substrate, and remains localised mostly within the structure. This is in contrast with the ED mode in Figure 4.5 (d), which becomes less confined owing to the gold. The AP likely has a different coupling strength to its mirror image compared to the ED mode, and thus becomes more strongly confined with the gold present, hence causing the blue-shift with decreasing s shown in Figures 4.3 (d) and (e). Interestingly, there appears to be field enhancement at the nanoantenna-gold interface for the anapole, which is around 4 times stronger than the intensity in the suspended nanoantenna simulations. This effect will be discussed in more depth in the following paragraphs, and is likely due to hybridisation with plasmons.

Lastly, I simulated the field distribution of the MP mode as in Figures 4.5 (c) and (f). I observed a pattern not seen in previously all-dielectric nanoantenna systems, where the electric field in the x, z plane is very strongly localised to the gold-TMD boundary. Two central maxima can be seen in both the x, y and x, z planes along the polarisation axis of the incident light, with an order of magnitude stronger field confinement at the gold surface than the previously measured ED mode and anapole. This suggests that there is a contribution from plasmons in the gold, hence the naming Mie-plasmonic. In addition, the MP mode takes a Fano lineshape in the scattering spectra as opposed to a Lorentzian, which suggests an interference between a discrete state (a Mie mode within the nanoantennas) and a continuum of states (plasmons) [273, 274, 280], hence giving further evidence for hybridisation. Both the AP and HOAP also exhibit Fano lineshapes, whereas they can be described by a more symmetric Lorentzian function for the case of nanoantennas on a dielectric substrate or surrounded by vacuum. This can be seen more clearly in Figures 4.4 (a) and (b), by

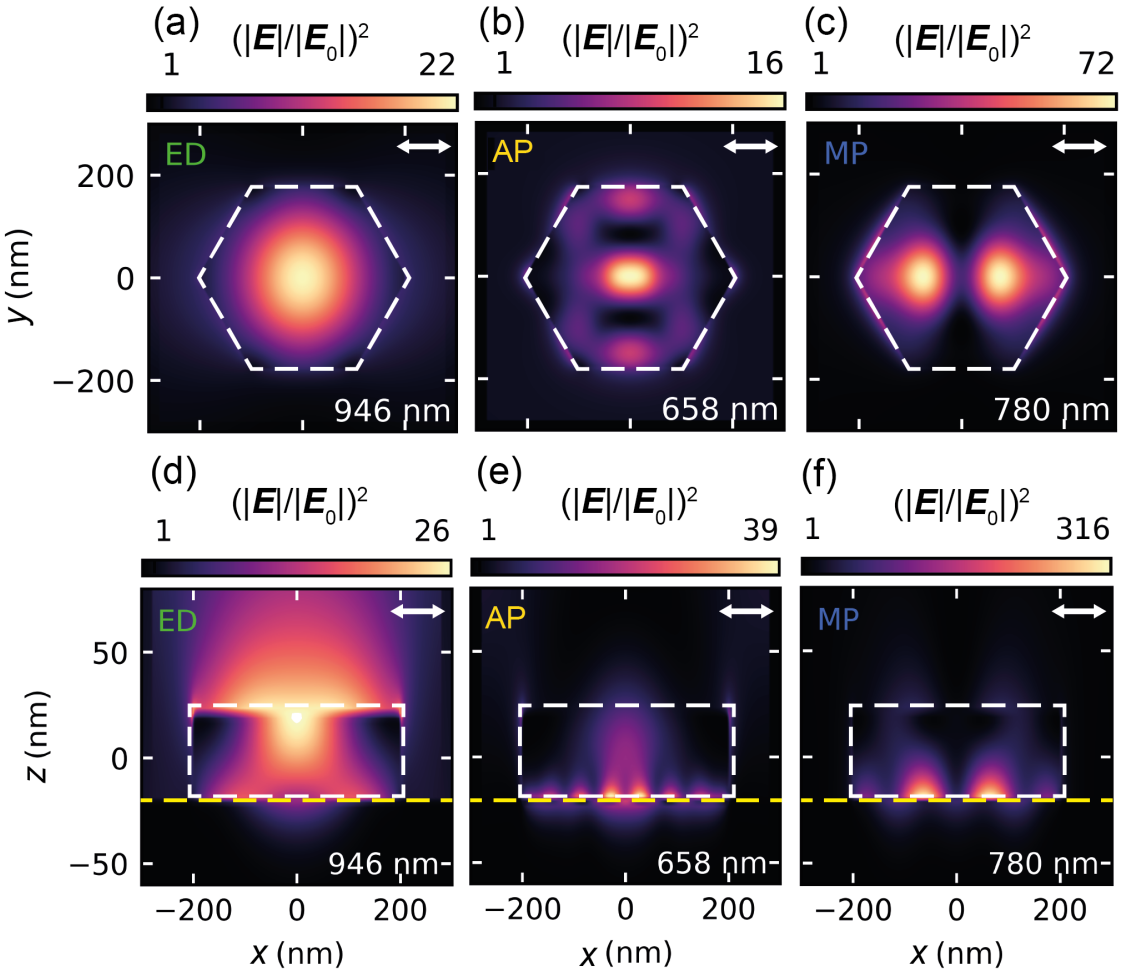


Figure 4.5: **Simulated electric field intensity within a WS_2 nanoantenna of height 78 nm and radius 290 nm on gold for different resonances. (a)-(c)** Electric field distributions for the electric dipole mode, anapole, and Mie-plasmonic mode within a nanoantenna of height 41 nm and radius 200 nm for s = 0 nm respectively. Slice is through the middle of the nanoantenna in the x, y plane, with incident light polarised along x denoted by the white double arrow. White dashed lines represent the edges of the nanoantennas. Bottom right value corresponds to the incident wavelength. **(d)-(f)** Electric field distributions for the same modes through a slice in the x, z plane. Yellow dashed lines represent the surface of the gold substrate. Clear hybridisation with plasmons at the nanoantenna-gold interface can be seen for each mode.

comparing the $s = \infty$ spectra with those as s decreases. The Fano lineshapes and electric field localisation of the anapole in Figure 4.5 (e) therefore indicate some hybridisation with plasmons, albeit much weaker than for the MP mode. The gold-TMD interface field localisation can also be observed to a lesser extent for the ED mode. This suggests that both the ED and AP also hybridise with plasmons in the gold along with the MP mode, but not as strongly.

4.2.5 Scattering Radius Dependence for Different Substrates

After characterising the modes within WS_2 nanoantennas in vacuum and on gold for fixed nanoantenna geometries, I then tuned the radius r in 10 nm steps in simulation to investigate the effects upon each resonance. I performed the radius sweeps for three substrates: vacuum, low index SiO_2,

and gold, to clearly illustrate the differences in mode structure. The resulting scattering spectra are presented in Figure 4.6, for nanoantennas of height 78 nm and radii ranging from 50-300 nm. The modes are each labelled, with coloured dashed lines tracking their peak positions as the radius is tuned. On inspection, the spectra for nanoantennas in vacuum and on SiO_2 are near identical, hosting the same modes with only a slight shift in energy between substrates. The ED mode, AP and HOAP all red-shift with increasing radius as expected, each showing hybridisation with the WS_2 exciton present at 625 nm wavelength. The linewidths of each mode also increase slightly with increasing r. I present the SiO_2 substrate results to show a feasible structure that could be fabricated on commercial SiO_2/Si wafers. When switching to a gold substrate as in Figure 4.6 (a), a narrowing of the ED mode, AP and HOAP is clearly observed as with previous simulations. Most importantly however, one can see that the MP mode is only observed with the gold substrate, and not in the cases with nanoantennas on SiO_2 or in vacuum, no matter the size of the structure. Furthermore, the MP mode is not documented in previous experimental or numerical dark field studies of all-dielectric nanoantenna structures [102, 103, 147, 257, 258]. Also note that the Fano lineshape of the MP mode, AP and HOAP is preserved upon changing radius for the case of nanoantennas on gold. This can be seen in Figure 4.6 (a) by the asymmetric resonance peaks that increase then decrease in intensity as the wavelength is increased. In contrast, the AP and HOAP exhibit Lorentzian lineshapes for dielectric substrates. The above evidence further supports that there is a hybridisation of both Mie and plasmonic modes present in the TMD nanoantenna-on-gold system.

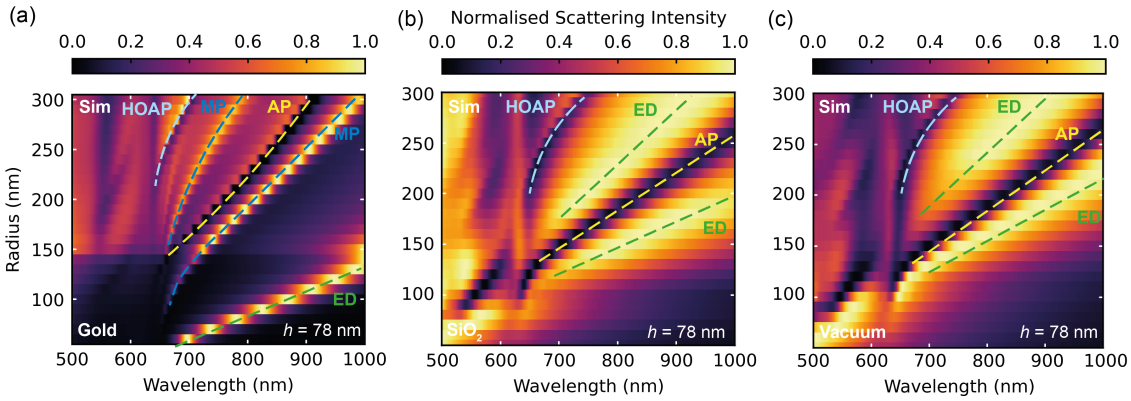


Figure 4.6: **Simulated normalised scattering intensity of WS_2 hexagonal nanoantennas of height 78 nm with varying radii compared with different substrates.** **(a)**, **(b)**, and **(c)** correspond to gold, SiO_2 and vacuum substrates respectively, for the same range of radii. Electric dipole mode, anapole and higher-order anapole present for nanoantennas on all three substrates. MP mode only emerges with metallic substrate.

4.3 Experimental Characterisation of WS_2 Nanoantennas on Gold

After identifying the constituent Mie modes, anapoles, and Mie plasmonic modes in WS_2 nanoantennas on gold in simulation, I now fabricate and characterise such structures in experiment. This section will begin with a recipe for nanoantenna fabrication, which can be utilised for different types of TMDs. I then perform dark field spectroscopy to carefully analyse the far-field scattering

spectra of the nanoantennas, providing comparison to simulation for each structure. Additional to the modes discussed so far, Fabry–Perot and Fabry–Perot-plasmonic modes will also be investigated, only observed in taller nanoantennas of $\sim$ 100 nm or greater in height. The Fabry–Perot plasmonic mode will then be tuned into resonance with a Mie mode in the vicinity of the high-order anapole condition. I further characterise the interaction between the two, fitting the anti-crossing to a coupled oscillator model, and subsequently proving strong mode coupling with a high quality factor. This result is well reproduced in additional simulations, which prove the highly confined nature of a Friedrich-Wintgen BIC at the point of minimum energy splitting, highlighting potential uses in local emitter enhancement, lasing, non-linear effect boosting and more.

4.3.1 Fabrication of Nanoantennas on Gold

I realised WS_2 nanoantennas on a gold substrate using well-established nanofabrication techniques as detailed in Section 3.2. This included mechanical exfoliation of bulk WS_2 onto gold substrates, spinning of a positive resist, electron beam lithography patterning, and reactive ion etching. A circular pattern was used with 30 nanoantennas in each block. The blocks were then repeated in both the x and y directions across an entire sample to pattern every flake. Due to etching of the sides of the nanoantennas during RIE, the radius of each individual nanoantenna mask was increased by 10% to achieve the desired radii with greater accuracy. An isotropic etching recipe with SF_6 gas then yielded nanoantennas of specified radii with hexagonal cross-sections, owing to a faster etching of the armchair axis of the crystal compared to the zigzag axis [147, 254, 269]. I found that nanoantennas of $\sim$ 50 nm radius or less did not etch well, sometimes becoming completely detached and washing away during the etching process. Larger nanoantennas of several hundred nanometers in diameter began to lose their well-define hexagonal cross-section, resulting in more rounded edges as seen in previous studies [21]. The gold substrate acted as a natural etch stop, thus producing nanoantennas flat to the gold substrate, rather than on a pedestal of substrate material like with SiO_2, which is also etched by the SF_6. Figure 4.3 (h) shows both optical and scanning electron microscopy (SEM) images of the finalised nanoantennas for reference. Overall, the fabrication process was very precise and repeatable, with a large range of nanoantennas with radii starting from $\sim$ 50 nm able to be etched into a single TMD flake.

4.3.2 Dark Field Scattering Spectra

In order to optically characterise the fabricated samples, I performed dark field spectroscopy on individual WS_2 nanoantennas on gold. I measured three different heights of nanoantennas (41, 78, 180 nm as measured by atomic force microscopy) with radii between $\sim$ 50-300 nm in roughly 10 nm steps for each, and plotted the normalised scattering intensities in Figures 4.7 (a)-(c). Panels (d)-(f) show the simulated scattering cross-sections for the same range of heights and radii using the FDTD method, exhibiting very good agreement. I attribute any slight discrepancies between the calculated and measured spectra to fabrication imperfections, and error in the experimentally measured refractive index data [21] used for simulation. Note that panels (c) and (f) correspond to double nanoantennas (dimers), with a gap between them on the order of half a micron. I did not see

a significant change in the normalised scattering intensity profiles between monomers and dimers for such large gap sizes [147].

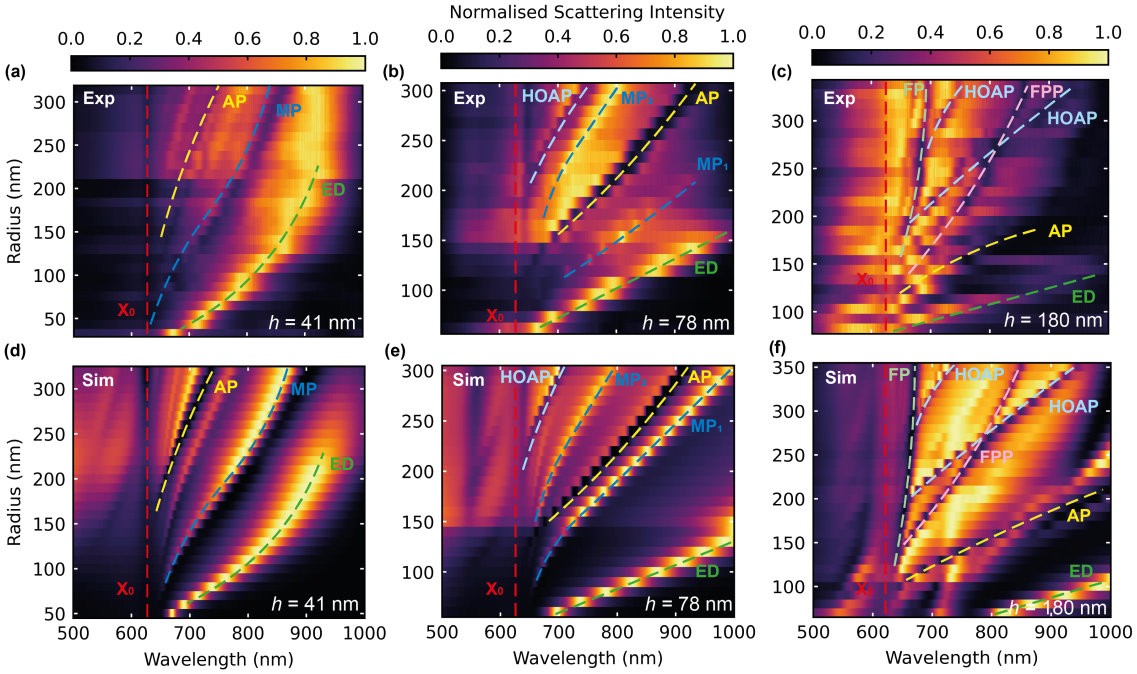


Figure 4.7: **Optical far-field characterisation of WS_2 nanoantennas on gold.** **(a)-(c)** Normalised scattering cross-section from experimental dark field spectroscopy of nanoantennas on gold of heights 41, 78, and 180 nm respectively, with increasing radii in $\sim$ 10 nm steps. **(d)-(f)** Simulated normalised scattering cross-section of WS_2 nanoantennas for the same geometries as in experiment, with refractive index data from Zotev *et al* [21]. Excellent agreement is observed. Left and central columns show data corresponding to single pillars (monomers), whilst right column corresponds to double pillars (dimers) with a separation of 475 nm. ED corresponds to the electric dipole mode, and AP and HOAP correspond to the anapole and higher-order anapole respectively. MP, FP, and FPP correspond to Mie-plasmonic, Fabry–Perot, and Fabry–Perot-plasmonic modes respectively. X_0 represents the WS_2 exciton.

The mode structure becomes increasingly complex as the nanoantenna height is increased. In the simplest case of monomers with height 41 nm (Figures 4.7 (a) and (d)), I observed a variety of maxima and minima in the scattering spectra that red-shift with increasing radius corresponding to the ED, AP, and MP modes. The dip in scattering at a constant wavelength of 625 nm is due to absorption from the WS_2 exciton, where I observed avoided crossings with the Mie modes as seen in previous simulations (Figure 4.6) and literature [102]. As the height of the nanoantennas was increased to 78 nm (Figures 4.7 (b) and (e)), the HOAP and an additional MP mode emerged, hence I denote these MP_1 and MP_2. I then extracted the quality factor of the ED and MP modes in experiment for WS_2 nanoantennas on gold of height 78 nm from Figure 4.7 (b). A Lorentzian function was fitted to the ED mode, and a Fano curve for the MP modes to calculate the maximum Q factors as with previous simulated results. In order to avoid any strong light-matter interaction which could impact measured linewidths, I only considered modes $>$ 100 nm from the WS_2 exciton wavelength, far from any Rabi splitting. I measured a maximum experimental Q factor of 13 for the ED mode and 72 for the MP_2 mode. The MP_1 mode reaches a significantly higher maximum

Q factor of 165. I then compared these Q factors to those previously measured in experiment for Mie resonances in WS_2 nanoantennas of similar sizes but on a SiO_2 substrate, which reach a maximum Q factor of 5 for the ED mode [21]. This yields a 33-fold increase in the maximum achievable Q factor when switching to a metallic substrate, demonstrating the strong confinement that can be achieved through the hybrid nanoantenna-on-metal system compared to purely dielectric nanoantennas.

The quality factors of the simulated scattering spectra agree well with experiment for the ED and MP_2 modes. Only the MP_1 is not well-reproduced in simulation, yielding a lower Q factor and shifted wavelength compared to the experimental results. I attribute this to discrepancies in the refractive index data used, simulation mesh size constraints, and imperfections in the fabricated nanoantennas.

When the nanoantenna height is increased to 180 nm as in Figures 4.7 (c) and (f), the mode structure becomes much more complex. Not only are anapole and higher-order anapole states visible, but similar to previous simulations [111, 130, 281–283] and experiments [284–287] of various dielectric nanostructures, a Fabry–Perot (FP) mode trapped between the TMD-gold interface at the bottom of the nanoantenna, and the TMD-air interface at the top can be observed. This mode shifts very little with changing radius, as would be expected from a vertically propagating FP mode. In order to host a Fabry–Perot resonance within a cavity, the round-trip phase accumulation of a wave within it must equal an integer number of 2π radians, as described by Equation 2.21. By changing the cavity length L, i.e. the height of the nanoantenna, the wavelength of allowed Fabry–Perot modes can be calculated for different orders. I assumed the gold to be a perfect electrical conductor, and hence the reflection phase change at the gold-WS_2 boundary is π. In contrast, $\phi_t = 0$ for the top of the nanoantenna, as the wave reflects from a boundary where the outside (i.e. vacuum) is of a lower refractive index than within the nanoantenna. I used the experimentally measured refractive index n of WS_2 from Munkhbat *et al.* [80], with wavenumber $k = 2\pi/\lambda$. The predicted Fabry–Perot modes are presented in Figure 4.8, overlaid on top of simulated scattering spectra for a nanoantenna of fixed radius 200 nm, and varying height. In Figure 4.8 (a) the experimental refractive index of WS_2 is used for both the simulations and theoretical FP mode model, whereas in Figure 4.8 (b), a constant refractive index of $n = 4.1$ is used for both.

Good agreement is observed between the simple FP mode models (dashed green lines in Figure 4.8) and the dark modes in the FDTD simulations for both WS_2, and constant refractive index monomers on gold. For the $n = 4.1$ monomers, the FP modes red-shift linearly with height in the scattering spectra, in agreement with theory. When WS_2 is considered in Figure 4.8 (a), the exciton at 625 nm causes many of the modes to become unresolvable around this wavelength. However, at larger wavelengths the mode also red-shifts linearly with increasing nanoantenna height. This is predicted by theory well, where we see an asymmetric feature around the excitonic absorption, followed by a linear increase in wavelength with nanoantenna height. Notably, the modes in the scattering spectra are blue-shifted compared to the theory, and have slightly different gradients. This can likely be attributed to the lateral confinement of the FP mode owing to the finite size of the nanoantennas. The FP mode model used considers an infinite plane dielectric, and so does not take into account lateral confinement or edge effects introduced by the nanoantennas. The

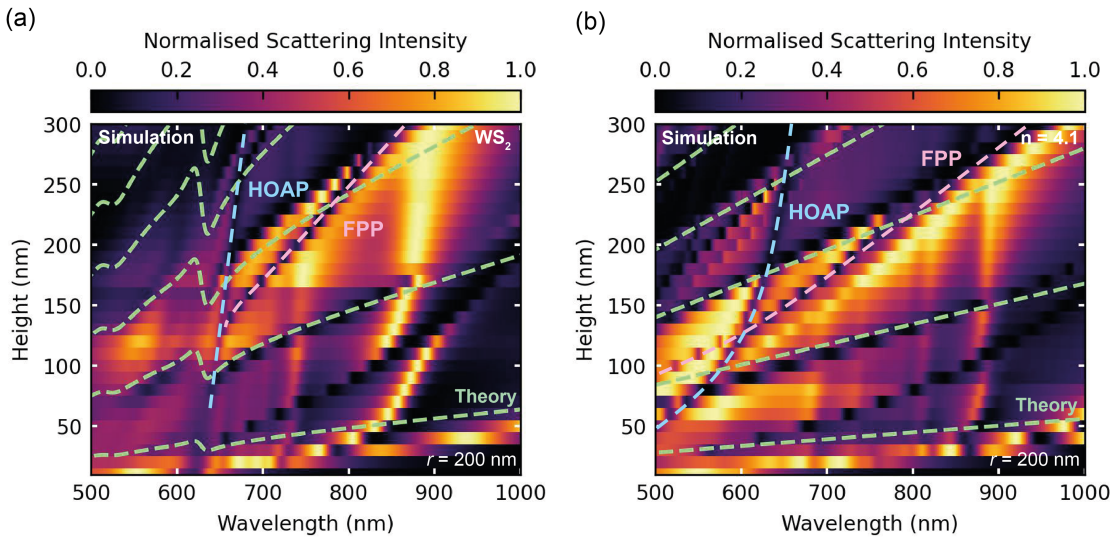


Figure 4.8: **Comparison of Fabry–Perot mode theory with FDTD simulations of high index hexagonal monomers with varying height on a gold substrate. (a), (b)** correspond to monomers using the refractive index of WS_2, and a constant refractive index of $n = 4.1$ respectively. All radii are fixed at 200 nm. Light green dashed lines correspond to predicted FP mode positions from theory, agreeing well with the dark modes from simulation. HOAP and FPP correspond to the higher-order anapole and Fabry–Perot-plasmonic modes respectively.

simulated electric field distribution of the FP mode is presented in Figure 4.9 (a) and (d) for slices through the x, y and x, z planes respectively. In Figure 4.9 (a), the mode resembles that of the electric dipole with a single, central maximum. However, upon considering the distribution in the x, z plane as in Figure 4.9 (d), the vertically propagating nature of the Fabry–Perot mode is evident. Three vertically-arranged maxima are present with minima between them, characteristic of the anti-nodes and nodes of a standing wave. Furthermore, since there is an additional π phase shift at the gold-TMD boundary, the effective mode volume is doubled and thus larger wavelengths of light can be confined within the same sized structure compared to a nanoantenna on a low index substrate such as SiO_2.

In the $h = 180$ nm nanoantennas on gold from Figures 4.7 (c) and (f), I also observed a dark resonance similar to that of a Fabry–Perot mode, but with more of a dependence on radius, marked by the light pink dashed line labelled Fabry–Perot-plasmonic (FPP). This mode was reproduced in both simulation and experiment, and so I simulated its electric field distribution to investigate its origin. The results are presented in Figures 4.9 (b) and (e), in the x, y and x, z planes respectively. Here, the gold-TMD boundary enables the necessary k-space matching required for the formation of plasmons at certain wavelengths of incident light. In Figure 4.9 (e), there are two vertically-stacked maxima, similar to the FP mode in Figure 4.9 (d), albeit with weaker contrast owing to the colour limits used. The main difference between the FP and FPP modes is the strong field confinement at the gold-TMD boundary. I therefore consider this no-longer a pure FP mode, but a hybridisation of an FP cavity and the plasmon continuum similar to the MP mode, hence the naming Fabry–Perot-plasmonic. The FPP mode also takes a Fano lineshape in the scattering spectra as opposed to the Lorentzian lineshape of the FP mode, and is not observed in simula-

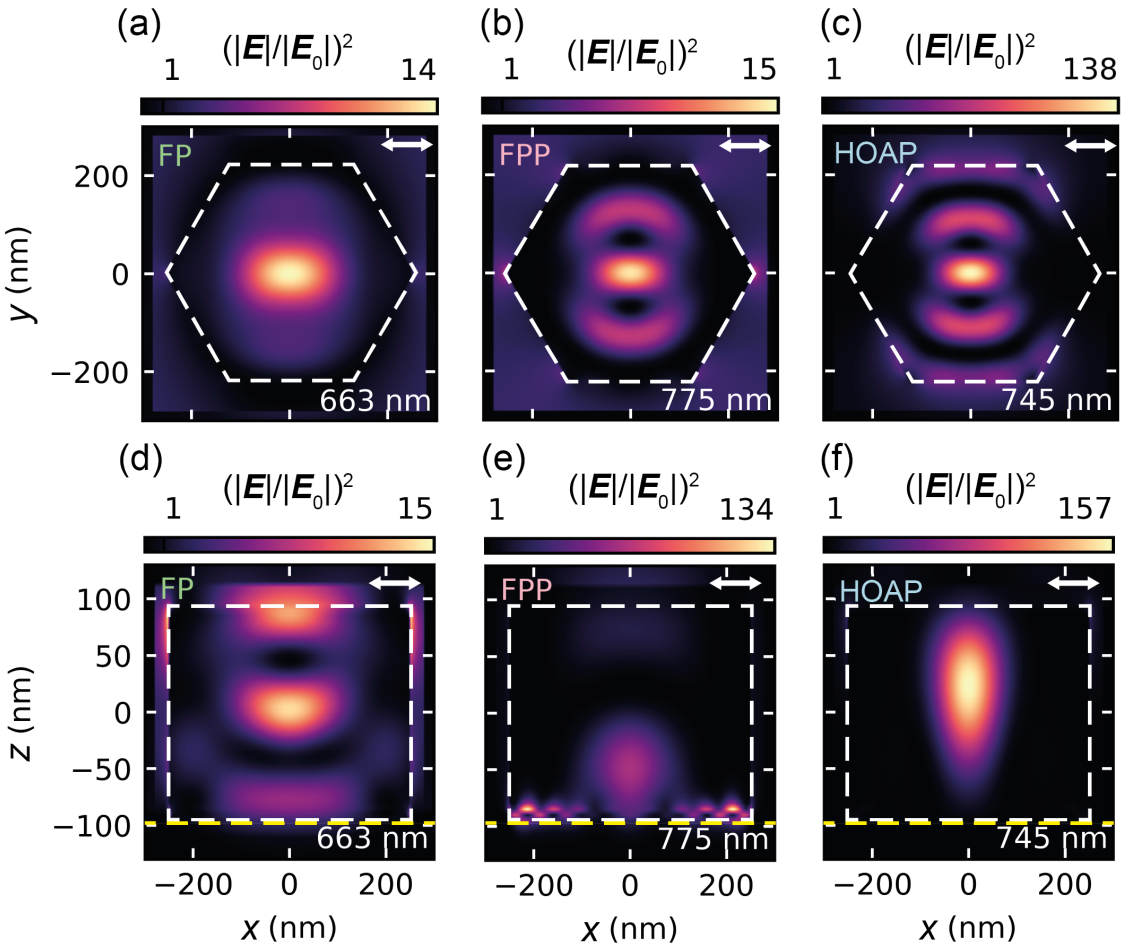


Figure 4.9: **Simulated electric field intensity within a WS_2 nanoantenna of height** 180 **nm and radius** 250 **nm on a gold substrate for different hybrid resonances. (a)**, **(b)**, and **(c)**, correspond to the electric fields for the Fabry–Perot mode, Fabry–Perot-plasmonic mode, and higher-order anapole in a cross-section through the middle of the nanoantenna in the x, y plane respectively. **(d)**, **(e)**, and **(f)** correspond to the same modes in the x, z plane. Incident light is polarised along the x axis, with wavelength denoted by the bottom right value in each panel. White dashed boxes indicate the nanoantenna edges, and yellow dashed lines represents the position of the gold substrate.

tions of WS_2 nanoantennas on dielectric substrates, thus further indicating a hybridisation with plasmons. For completeness, I plotted the electric field distribution of the higher-order anapole in WS_2 nanoantennas on gold in Figures 4.9 (c) and (f). The HOAP possesses a very similar field distribution to that within a nanoantenna suspended in vacuum (Figure 4.2 (c) and (f)) as expected. The main differences are the order of magnitude higher intensity owing to the confinement from the gold substrate, and the asymmetry of the field maximum about the z axis, likely owing to the interaction of the mode with its mirror image. Note that the field distribution in the x, y plane for the FPP mode in Figure 4.9 (b) appears similar to that of the HOAP in Figure 4.9 (c). However, the intensity of the FPP field is an order of magnitude lower than that of the HOAP, and the field distribution within the x, z plane in Figure 4.9 (e) is significantly different to that of the HOAP in Figure 4.9 (f). This similarity in the x, y plane is therefore likely due to the spectral proximity of this FPP mode to the HOAP ($\sim$ 30 nm), thus causing some preliminary hybridisation. Both modes can be tuned to fully hybridise by varying the nanoantenna radius as seen by the intersection of the

dashed lines in Figures 4.7 (c) and (f), which will be explored in more detail later in Section 4.3.3.

4.3.3 Strong Coupling and Supercavity Mode

In addition to the plasmon hybridisation discussed previously, I observed signatures of a highly-confined, non-radiating supercavity mode in both experiment and simulation, by tuning the radii of the $h = 180$ nm WS_2 nanoantennas on gold. This occurs as a result of the destructive interference of two different photonic modes, thus forming an extremely confined state with a Q factor that, in theory, increases to infinity [130]. The supercavity mode is analogous to a Friedrich-Wintgen bound state in the continuum [125] as discussed in Section 2.4.6, able to exist within a finite-sized structure such as a nanoantenna. Experimentally and in simulations, I discovered signs of this supercavity mode in the form of an anti-crossing between the FPP mode [287, 288], and the minimum in scattering identified as the HOAP condition as seen in Figures 4.7 (c) and (f). I chose to tune the HOAP into resonance with the FPP mode over the lowest-order anapole condition owing to its closer spectral proximity to the FPP mode. However, I expect that strong coupling with the lowest-order anapole is also possible in further tuned versions of such structures, with similar observations in previous studies [102, 120, 288]. The anti-crossing can be seen in the scattering spectra of dimer nanoantennas plotted in Figures 4.7 (c) and (f), for radii between 270 and 280 nm, at a wavelength of around 800 nm. This behaviour suggests that there is a strong exchange of energy between the FPP mode and HOAP, however as mentioned previously, anapoles are merely a destructive interference condition of component Mie modes, and thus not an eigenstate of the system itself [92]. This means that technically the coupling occurs between the FPP mode and a Mie mode, however for the sake of describing the results as-seen, I will describe this anti-crossing phenomenologically as strong coupling between the FPP and HOAP for the remainder of this chapter.

To characterise this coupling in greater depth, I then fitted the peak positions of the FPP mode and HOAP to a coupled oscillator model. To do this, I first fitted the HOAP and FPP peaks with a double Fano formula to account for the hybridisation of the individual modes with plasmons. I used the formula

$$y = mx + y_0 - |A_l| \frac{(q_\mathrm{l} + \epsilon_\mathrm{l})^2}{1 + \epsilon_\mathrm{l}^2} - |A_u| \frac{(q_\mathrm{u} + \epsilon_\mathrm{u})^2}{1 + \epsilon_\mathrm{u}^2}, \tag{4.1}$$

where

$$\epsilon_\mathrm{l} = \frac{x - x_\mathrm{lc}}{\Gamma_\mathrm{l}}, \quad \epsilon_\mathrm{u} = \frac{x - x_\mathrm{uc}}{\Gamma_\mathrm{u}} \tag{4.2}$$

for the lower (l) and upper (u) energy modes respectively. $A_{\mathrm{l,u}}$, $q_{\mathrm{l,u}}$, $x_{\mathrm{lc,uc}}$, $\Gamma_{\mathrm{l,u}}$ are the relative amplitudes, asymmetry parameters, peak centre positions, and full-width-at-half-maxima of the lower and upper wavelength peaks respectively. Example double Fano fits are presented in Figures 4.10 (a) and (b) in black, for the experimental and simulated scattering spectra respectively, both showing good agreement with each other and the fits. I then repeated this fitting process for all of the fabricated nanoantennas of height 180 nm with radii ranging from 220 to 330 nm in, on average, 10 nm increments. The peak centre positions were then plotted in terms of energy against nanoantenna radius as shown in Figure 4.10 (c). The error bars represent the uncertainty in the

measured radii of each nanoantenna, with one data point at $r = 293$ nm showing a notably large error. I attribute this uncertainty to fabrication imperfections of this particular nanoantenna, which had a more irregular hexagonal cross-section than others when imaged with SEM, thus making the determination of its radius less reliable. The error in the fitted peak energy was negligible for each point. I then fitted the peak centre positions to a coupled oscillator model, yielding upper and lower energy branches shown as red and blue lines respectively. I subsequently refer to these as the high and low Q factor modes respectively, since the individual FPP mode and HOAP become indistinguishable due to the hybridisation. The green dotted lines represent the uncoupled HOAP and FPP mode as obtained from the model. From this fitting, I extracted a minimum energy splitting of 48 ± 5 meV. This is greater than the sum of the half linewidths of the uncoupled modes (34 ± 1 meV), therefore confirming the existence of strong mode coupling [111] between the HOAP and an FPP mode [288].

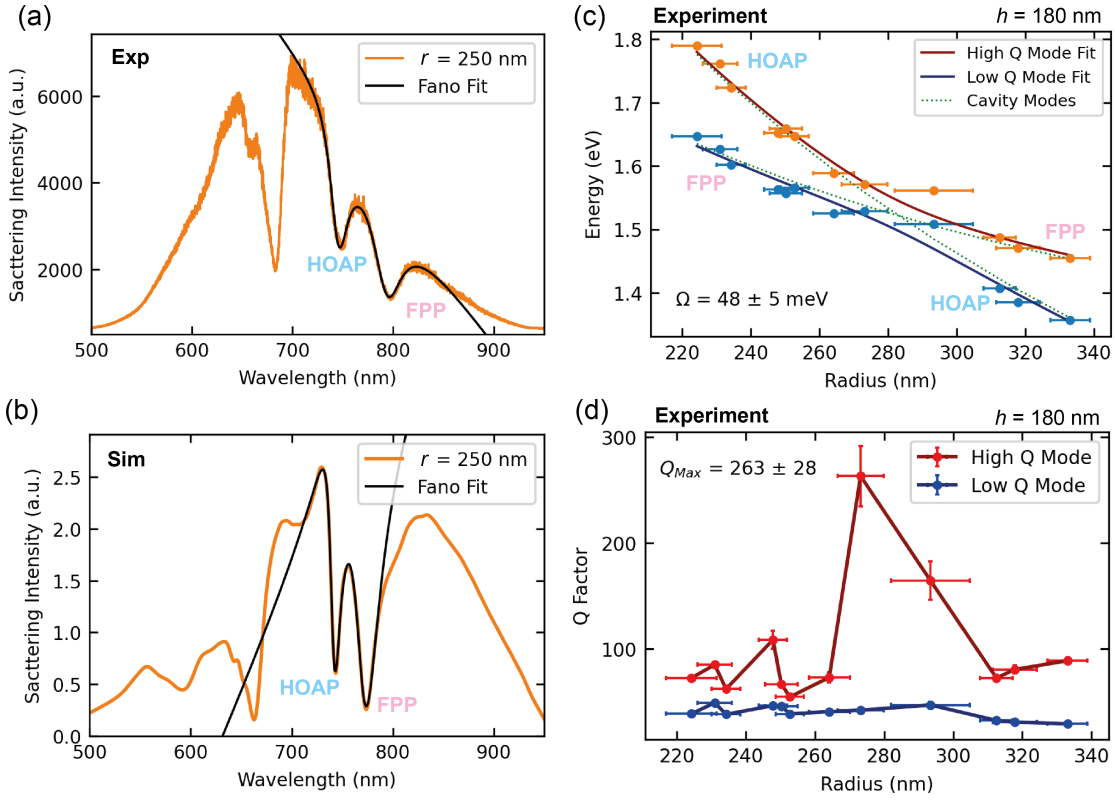


Figure 4.10: **Coupled oscillator model fit to experimental FPP mode and HOAP scattering spectra from WS_2 nanoantennas on a gold substrate.** **(a)** and **(b)** correspond to individual scattering spectra from dimer nanoantennas of height 180 nm and radius 250 nm from experiment and simulation respectively (orange lines). Black lines show double Fano curve fits to the higher-order anapole (HOAP) and Fabry–Perot-plasmonic (FPP) mode. **(c)** Experimental peak centre positions of the anti-crossed HOAP and FPP mode fitted to a coupled oscillator model, yielding a minimum energy splitting of 48 ± 5 meV. Error bars represent uncertainty in the measured radii of the nanoantennas. Nanoantenna height is 180 nm and separation 475 nm. Green dotted lines correspond to the uncoupled HOAP and FPP mode as obtained from the model. **(d)** Quality factor of the two modes with respect to radius. Error bars represent both uncertainty in the measured radii (horizontal), and error in the fits (vertical). Q factor calculated as the central wavelength of each peak divided by its respective full-width-at-half-maximum.

In addition to extracting the FPP mode and HOAP spectral positions, I calculated the Q factor of each peak and plotted against nanoantenna radius as in Figure 4.10 (d). Whilst the low Q factor mode remains mostly constant, the high Q factor mode increases significantly at a radius of 273 nm. This radius corresponds to the point of minimum energy splitting between the two anti-crossed modes in Figure 4.10 (c). I subsequently calculated a maximum Q factor of 263 ± 28, an order of magnitude larger than for the ED mode reported earlier in this study. This sharp increase in Q factor along with the observation of strong mode coupling are both signatures of a Friedrich-Wintgen BIC, similar to other experimental results documented for Si nanowires [289] and AlGaAs nanoantennas [131]. However, owing to the confinement introduced from the gold substrate and the interaction with plasmons in the hybrid WS_2 nanoantenna-on-metal structure, I demonstrated this BIC hosted within a volume 40 times smaller than in previous dielectric nanoantennas on a SiO_2/ITO/SiO_2 substrate [131].

In order to better understand the mode behaviour around the anti-crossing, I performed FDTD simulations of WS_2 nanoantennas of height 200 nm on gold for a range of radii between 250-350 nm, with a much finer step in radius of 1 nm. The greater height compared to the nanoantennas measured in experiment was chosen in order to red-shift the anti-crossing away from other modes in the scattering spectra, thus aiding with fitting. The anti-crossing between the FPP mode and HOAP is clearly reproduced in the simulated spectra, with the coupled oscillator fits presented in Figure 4.11 (a). From this I extracted a minimum energy splitting of 37.5 ± 0.3 meV, which is of the same order as the experimental observations. Furthermore, upon plotting the Q factors of each of the branches against nanoantenna radius as in Figure 4.11 (b), it is clear that the low Q factor mode remains approximately constant, whereas the high Q factor mode peaks significantly for a radius of 302 nm. I calculated a maximum Q factor of 602 ± 82 at this radius, with the high error owing to suppression of the peak in the scattering spectra, thus making it difficult to fit. The simulation results support the experimental data from Figures 4.10 (c) and (d) very well, both exhibiting strong mode coupling between the FPP mode and HOAP, and displaying sharply increasing Q factors of similar order of magnitude at the closest point to the anti-crossing, despite the differences in nanoantenna size. This behaviour therefore gives compelling evidence for the existence of a highly-confined, Friedrich-Wintgen quasi-BIC in WS_2 nanoantennas on gold. In previous literature, this type of mode in non-periodic nanostructures is often referred to as a supercavity mode [111, 130, 131, 290–292].

I also simulated the electric field distribution within a single nanoantenna of the same dimensions as the dimer considered in Figures 4.11 (a) and (b). I found no significant differences between the scattering spectra and electric field distributions of monomer and dimer nanoantennas with such large gaps on the order of 500 nm, hence the single nanoantenna electric fields are shown as insets for clarity. Profiles through the centre of the nanoantennas in the x, z plane are presented for the points along each mode marked by the coloured circles in Figure 4.11 (c). Away from the point of anti-crossing, the FPP mode displays electric field maxima and minima in the x, z plane as would be expected from a Fabry–Perot mode confined vertically within the nanoantenna [111], as well as hybridisation with plasmonic modes at the gold-WS_2 boundary, as described previously in Section 4.3.2. For smaller radii the FPP mode appears mostly plasmonic, with a field maximum near

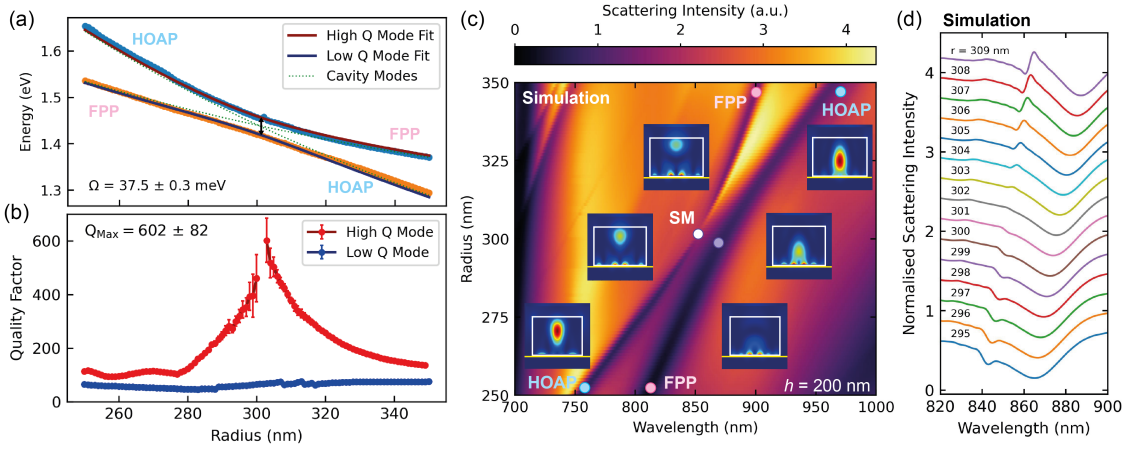


Figure 4.11: **Supercavity mode characterisation for WS_2 dimer nanoantennas on a gold substrate in simulation.** **(a)** Simulated peak positions of the HOAP and FPP mode fitted to a coupled oscillator model, from optimised nanoantennas of 200 nm height and varying radii between 250-350 nm. Ω denotes the minimum energy splitting between the modes. **(b)** Extracted quality factor for all peaks fitted in **(a)**. **(c)** Simulated scattering spectra of optimised nanoantennas on gold with a normally incident plane wave excitation source over a range of radii increasing in steps of 1 nm on a gold substrate. Pink and blue circles correspond to the FPP mode and HOAP respectively. White central circle denotes the position of the high Q factor supercavity mode (SM), and the purple circle corresponds to the low Q factor lossy mode. Remaining insets show electric field distributions through the centre of a single nanoantenna in the x, z plane at the corresponding circles in the scattering spectra for reference. White boxes highlight the edges of the nanoantennas, and yellow lines correspond to the position of the gold substrate. **(d)** Waterfall of normalised simulated scattering spectra from **(c)** for different radii, showing suppression of the high Q factor mode for the nanoantenna radius corresponding to the minimum wavelength splitting between the two modes ($r = 302$ nm).

the bottom of the nanoantenna. In contrast, the HOAP field distribution is strongly localised at the centre of the nanoantenna, exhibiting little hybridisation with plasmons. As the radius is increased, the electric field profile of the FPP mode hybridises with that of the HOAP to form a well-confined supercavity mode labelled SM, and a lossy mode as marked by the purple circle. Upon increasing the nanoantenna radius further, the HOAP returns to a similar field distribution as before the anti-crossing, with the central field maximum localised closer to the gold interface. The FPP mode field maximum is pushed up towards the top of the nanoantenna after the anti-crossing, whilst retaining the characteristic plasmon field distribution at the bottom.

To confirm the BIC-like nature of the supercavity mode, I further investigated the suppression of the high Q factor mode as the nanoantenna radius was tuned. Figure 4.11 (d) shows individual simulated scattering spectra from Figure 4.11 (c) for a range of radii close to the anti-crossing. Whilst the low Q factor mode (higher wavelength) retains mostly the same form, the high Q factor mode (lower wavelength) becomes almost invisible when the radius is tuned to 302 nm. This suppression of scattering corresponds to the point where the HOAP and FPP mode destructively interfere near perfectly, forming a highly confined resonance within the nanoantenna, confirmed by the rapidly increasing Q factor as it tends to infinity. These simulations thus provide additional evidence to support the observation of a supercavity mode in hybrid WS_2-on-gold nanoantennas in experiment.

One can envisage applications of such high-Q factor modes in boosting non-linear effects on the nanoscale, such as second harmonic generation (SHG) enhancement of a TMD monolayer [275] coupled to WS_2 nanoantennas on gold, or further enhancement of SHG efficiency in quasi-bulk TMD pillars containing a low symmetry interface [21]. Other applications include quasi-BIC-enabled lasing [132] and directionality control when considering a metasurface of nanoantennas [220], highlighting the potential for using TMD nanoantennas on gold within complex integrated optical circuits.

4.4 Mie-Plasmonic Resonances for Emitter Enhancement

In this final section on WS_2 nanoantennas on gold, I will provide simulations pushing the structures towards potential applications. I consider how the Mie-plasmonic mode can be utilised to enhance both the emission and directivity of coupled emitters within an ultra-thin hBN layer. The results will therefore highlight the versatility of TMDs for nanophotonics, potentially aiding with future integration amongst more established silicon-based chips.

The strong localisation of electric field strength at the TMD-metal boundary, depicted in Figure 4.5 (f), prompted further study into Purcell enhancement of emitters at this position. I therefore simulated the electric field distribution within an hBN layer of 5 nm thickness, placed between a WS_2 nanoantenna and a gold substrate as shown schematically in Figure 4.12 (a). hBN was chosen owing to its transparency throughout the visible wavelength range [293], low refractive index of $\sim$ 2.2 [294], and the presence of single photon-emitting defects, radiating at a variety of wavelengths from around 550-850 nm [295–298]. Such a system bears similarities to other work on gold nanoparticle-on-mirror (NPoM) structures [261], however boasts several advantages. Dielectric materials offer lower losses than the solely plasmonic resonances of the gold nanoparticles, therefore one can achieve higher Q factor modes and thus stronger Purcell enhancement. Furthermore, WS_2 nanoantennas can be fabricated experimentally with precise size, geometry, and positioning, unlike the random nature of gold nanoparticle deposition. This allows wider control over the resonances, and overall greater functionality.

The electric field simulation results are displayed in Figures 4.12 (b) and (c) for a nanoantenna of height 60 nm and radius 210 nm, showing field distributions of similar shape to those for silicon nanoantennas above gold with a SiO_2 spacer [264] in literature. I optimised the geometry of the WS_2-nanoantenna-above-gold system for the maximum possible Purcell factor within the hBN layer over the wavelengths previously reported for hBN SPEs. I calculated a maximum electric field enhancement of 2647 within the hBN spacer at 773 nm wavelength (the MP mode as discussed previously), two orders of magnitude higher than the maximum field within the nanoantennas for the ED mode (Figure 4.5 (d)), and one order of magnitude higher than that of the MP mode inside a nanoantenna directly on a gold substrate (Figure 4.5 (f)). I further spatially mapped the Purcell factor of a dipole emitter placed within the hBN (see Figure 4.12 (a) for dipole location), mimicking a single photon emitter. This mapping is shown in Figures 4.12 (d) and (e), where the dipole was oriented perpendicular (along z), and parallel (along x) to the substrate respectively, showing a strong variation in Purcell enhancement depending on both position and polarisation.

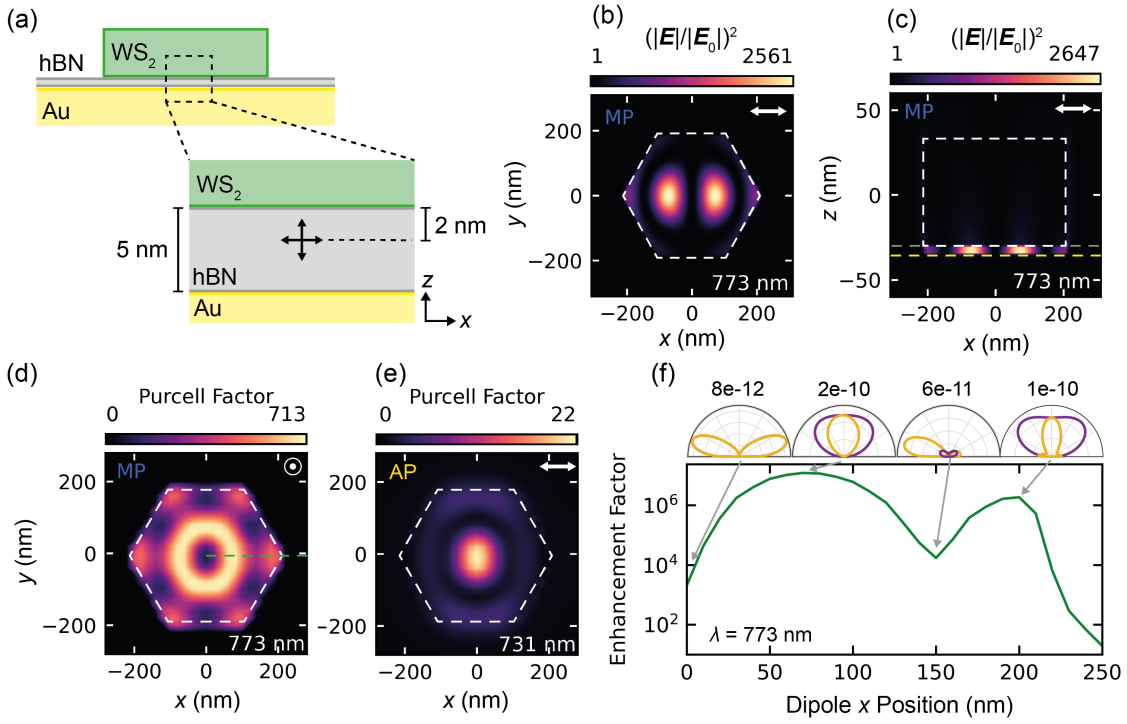


Figure 4.12: **Simulated electric field and light extraction enhancement throughout an hBN layer between a WS_2 nanoantenna and gold substrate.** **(a)** Schematic of the structure showing the z position at which the dipole was placed to simulate the Purcell factor and directivity. Crossed arrows represent the two polarisations considered. Nanoantenna modelled with height 60 nm and radius 210 nm. **(b)**, **(c)** correspond to electric field distributions in the x, y plane within the nanoantenna-substrate gap, and the x, z plane through the centre of the nanoantenna respectively, when illuminated by a 773 nm plane wave. Dashed white lines represent the edges of the nanoantenna, yellow denotes the gold-hBN boundary, and grey corresponds to the top surface of the hBN. **(d)**, **(e)** Maps of the maximum Purcell factor for a dipole within the hBN oriented perpendicular (polarised along z), and parallel (polarised along x) to the substrate respectively, in the same plane as **(b)**. Dipole wavelength set to 773 nm and 731 nm respectively, corresponding to the MP mode and the AP. **(f)** Total enhancement of a dipole within the hBN layer with respect to position along the dashed green line in **(d)** at a wavelength 773 nm. Polar plots show the far-field radiation patterns of a dipole at the marked x positions. Purple and yellow curves correspond to slices through the $x = 0$ and $y = 0$ planes respectively. Values above the plots indicate the respective intensities for comparison.

From Figure 4.12 (d), I calculated a maximum Purcell factor of 713 for a dipole polarised perpendicular to the substrate at an emission wavelength of 773 nm (the MP mode), over two times greater than previously reported for silicon nanoantennas above gold for the same gap size [172]. Comparing to a dipole polarised parallel to the substrate in Figure 4.12 (e), I observed a much lower maximum Purcell factor of 22 at 731 nm (the AP). I further integrated the total emitted intensity of the dipole in all directions over a range of wavelengths from 550 nm to 850 nm for varying polarisations in the x, z plane (not shown). This displayed the same strong sensitivity to dipole orientation within the hBN layer, suggesting that particular enhancement is expected in systems where the dipole is oriented vertically, irrespective of wavelength. Example structures with vertical dipoles are hetero- and homobilayer TMDs, where interlayer excitons can be observed with

electrons and holes in adjacent layers [299].

I also considered how the directivity of a dipole at different x positions within the hBN layer will change, thus affecting the light collection efficiency through an objective lens. I defined the directivity as the fraction of light captured in the far-field through a numerical aperture of 0.64 directly above the nanoantenna-hBN-gold structure, compared to the total light emitted in all directions. This forms part of the overall enhancement factor

$$\langle EF \rangle = \frac{\gamma_{exc}(\lambda)}{\gamma^0_{exc}(\lambda)} \cdot \frac{q(\lambda)}{q^0(\lambda)} \cdot \frac{\eta(\lambda)}{\eta_0(\lambda)}, \tag{4.3}$$

similar to previous work considering excitonic emission from monolayer WSe_2 coupled to GaP dimer nanoantennas [153]. Equation 4.3 represents the ratio of the collected light from a dipole within the hBN spacer at a given wavelength, to that of a dipole in free space. The first term of Equation 4.3, $\gamma_{exc}/\gamma^0_{exc}$, is the ratio of the excitation rate at wavelength λ within the hBN spacer, compared to free space. This is proportional to the electric field intensity, $(|\boldsymbol{E}|/|\boldsymbol{E}_0|)^2$, within the spacer as displayed in Figure 4.12 (b). The second term, q/q^0, represents the quantum efficiency enhancement of the dipole at wavelength λ. Under the assumption of a low quantum yield, this is equivalent to the Purcell factor as given by Equation 2.27. The final term, η/η_0, accounts for the directivity enhancement, which is the ratio of the directivity of a dipole within the hBN spacer to a dipole in vacuum, both at wavelength λ.

For an ideal hBN single photon emitter placed within the nanoantenna-gold gap, the enhancement factor therefore defines the potential increase in signal that would be collected by an objective lens in experiment, compared to that of the same emitter in free space. This figure of merit differs from the Purcell factor since it takes into account the excitation rate enhancement and directivity of emission. In an experimental measurement, the Purcell factor can be calculated by comparing the radiative lifetimes of the emitter within the nanoantenna and free space cases, whereas the overall enhancement factor relates to a comparison of emission intensities.

The simulated enhancement factor is presented in Figure 4.12 (f), where the wavelength is fixed at 773 nm for consideration of only the MP mode, and the dipole position in x is varied along the dashed green line in Figure 4.12 (d), with polarisation perpendicular to the substrate. Above the enhancement factor plot are slices of the far-field radiation patterns in the $x = 0$ and $y = 0$ planes (purple and yellow curves) for dipole positions of particular interest. When the dipole in the hBN layer is positioned directly underneath the centre of the nanoantenna ($x = 0$ nm), the Purcell factor is low as seen in Figure 4.12 (d), and most of the light is directed towards the sides of the structure as shown in the top left inset of Figure 4.12 (f). Therefore, very little light would be collected by an objective lens directly above the structure, and thus the overall enhancement factor is low. Note that in this case, owing to the symmetry about the centre of the structure, the $x = 0$ and $y = 0$ far-field slices are identical, so overlap completely. I calculated a maximum directivity of $\sim 50\%$ at $x = 70$ nm, corresponding to a very high enhancement factor of 1.2×10^7. As seen by the far-field radiation pattern, the dipole emits near perfectly vertically for this x position, and combined with a high Purcell factor and well-confined electric field, a strong overall light extraction enhancement is achieved. The far-field patterns, electric field distributions, and Purcell factors explain the enhancement factors calculated at $x = 150$ and 200 nm in the same way. These results

show that not only can the Purcell factor be strongly tailored depending on dipole polarisation and position within the hBN layer, but so can the directivity of the emitted light. By placing emitters with vertically orientated dipoles such as TMD heterostructures with interlayer excitons within the nanoantenna-gold gap, one could achieve up to 10^7 times enhancement of the extracted emission compared to the emitter outside of the cavity. Such large enhancement of emission has potential applications in quantum information processing, or boosting non-liner interactions. Furthermore, by changing the nanoantenna height and radius, the maximum enhancement factor can be tuned for emitters operating at different wavelengths, thus making the TMD nanoantenna-gold gap an ideal system for studying a range of low intensity dipolar sources including SPEs, excitons and more.

4.5 Conclusion

In this study, I significantly built on previous work concerning WS_2 nanoantennas on gold [21] by providing an in-depth analysis of the mode structure, and the reasons behind why the resonances differ greatly compared to that of all-dielectric nanoantenna systems, before highlighting real applications of such devices. By simulating WS_2 nanoantennas moving towards a gold substrate, I was able to gain insight into how the mode structure transitions from a purely dielectric, to dielectric-metallic regime, thus predicting the behaviour and properties of hybrid Mie-plasmonic modes before fabrication. Compared to conventional III-V materials requiring complex molecular beam epitaxy to fabricate, the TMD-based nanoantennas were simple to realise on gold substrates using mechanical exfoliation and standard nanofabrication techniques. Here, no lattice matching was required owing to the inherent van der Waals forces, with the added benefit of gold providing a natural etch stop during RIE. Once fabricated, I investigated resonant Mie modes within the nanoantennas through experimental dark field spectroscopy, and observed excellent agreement with simulation. I demonstrated that all the resonances identified can be tuned to different wavelengths simply by changing the nanoantenna radii, and that additional, higher-order modes can be introduced by increasing the nanoantenna height. The Fano-lineshape Mie-plasmonic resonances exhibited high quality factors, up to 33 times higher than Mie modes in nanoantennas placed on a low-index SiO_2 substrate in experiment [21], hence enabling applications in switching and sensing [271–274].

I further demonstrated strong mode coupling of Mie and Fabry–Perot-plasmonic modes within WS_2 nanoantennas on a gold substrate in experiment and simulation. I calculated a minimum energy splitting of 48 ± 5 meV, and with careful tuning of the nanoantenna geometry, I discovered signatures of a quasi-BIC supercavity mode at the point of anti-crossing. The supercavity mode yielded a significantly increased experimental Q factor compared to other modes of over 260, and near complete suppression of scattering in simulation. Here, the use of a gold substrate reveals a simple-to-fabricate method of confining a visible wavelength supercavity mode to nanometer-scale structures in experiment, with potential applications ranging from second harmonic generation and other non-linear effect enhancement [275], to directional lasing [132, 220].

Finally, I observed in simulations that very strong electric field enhancement of over 2600 occurs in a nanometer scale gap between the studied WS_2 nanoantennas and gold substrate. For a

gap filled with 5 nm of hBN, I measured light extraction efficiencies of up to 50%, and a maximum Purcell factor of 713 for an emitter within the hBN polarised perpendicular to the substrate, 32 times greater than for parallel polarisation. From these values, I calculated a maximum overall enhancement of the collected light from emitters within such structures to exceed 10^7. Hybrid WS_2 nanoantennas on gold therefore introduce opportunities for strongly enhancing emitters placed within the nanoscale gap, such as SPEs in TMDs [24, 300–310] and hBN [295–298], as well as interlayer excitons in TMD bilayers [299] and van der Waals heterostructures [311–316]. Coupling of this system to other photonic devices such as waveguides, photonic crystals, and gratings, offers near limitless combinations for using TMDs and metals together to fabricate nano-optical circuits with strong field confinement and low losses.

5

Topological Edge States in 1D WS_2 Double Gratings

5.1 Introduction

With 0D TMD-based nanoresonators on gold thoroughly investigated, I will now turn my focus towards periodic, quasi-infinite structures to explore how symmetry and topology can give rise to additional exotic resonance phenomena, not seen in finite-sized structures. One of the earliest theoretical considerations of the behaviour of waves in a periodic medium was by Lord Rayleigh in 1887, who derived equations for mechanical waves on a periodically weighted string [317]. He mathematically discovered the presence of a range of frequencies with near-unity reflection, i.e. a band gap, owing to perfect constructive interference of waves propagating in one direction along the string, and destructive interference for waves in the opposite direction. Lord Rayleigh also suggested the application of this theory to light in laminated thin films, and so with the development of nanofabrication techniques in the 1970s, early 1D photonic crystals such as DBRs could be realised in experiment via molecular beam epitaxy [318]. The working principles of these structures form the foundation of the work I will discuss in this chapter.

Fast-forward to more recent years, research effort into 1D dielectric gratings saw a decline in favour of more complex 2D and 3D photonic crystals with additional degrees of freedom. However, with the birth of topological photonics in the late 2000s [33, 34, 36], renewed interest in exploiting topological phenomena in a wide variety of photonic structures has arisen. A prominent example is the bound state in the continuum, which was predicted to be an intrinsically topological effect by Bo Zhen *et al.* in 2014 [129]. Their work proposed that BICs are the centre of a polarisation vortex in k-space, with an associated integer winding number which is robust to small local changes or defects in the host structure as described in Section 2.6.4. This was later proved through experi-

mental measurements of the polarisation vortex of a BIC in 1D SiN gratings by Hugo Doeleman *et al.* in 2018 [218]. Topological BICs in dielectric gratings have since been explored in a variety of contexts, for example, it was demonstrated that coupling to quantum well emission could achieve polariton Bose-Einstein condensates [189], thus allowing macroscopic quantum states to be manipulated by topological effects. Furthermore, in 2021 Ki Young Lee *et al.* published theoretical work detailing the possibility of combining two BIC-hosting systems of different topological invariants to achieve a Jackiw-Rebbi edge state [37, 232]. As described in Section 2.6.5, they modelled two adjacent 1D dielectric gratings with different refractive indices and filling factors, thus producing photonic modes with BICs on opposite energy branches. Therefore, at the interface between the two gratings the associated topological invariant of the bands was forced to change, giving rise to an edge localised, topological Jackiw-Rebbi state. A year later, Lee *et al.* furthered this work by characterising the directivity of emitters coupled to the Jackiw-Rebbi edge state in simulation, producing highly directional beam-shaping [242]. To the best of my knowledge, so far the only published experimental work on Jackiw-Rebbi edge states in 1D gratings (in contrast to 1D resonator chains [236] and binary waveguide devices [237, 238]) has been in metallic gratings by Lorenzo Orsini *et al.* in 2024 [319]. They successfully imaged the enhanced near-field of the edge state at the interface between two gratings of different topologies through s-SNOM, achieving a confinement four orders of magnitude smaller than the free space wavelength in the infrared regime. A very recent study was published during the writing of this thesis by Yu Sung Choi *et al.*, who demonstrated a proof-of-concept double SiN grating design, hosting a Jackiw-Rebbi edge state in the near-infrared range as measured by angle-resolved transmission spectroscopy [320]. In terms of high refractive index, TMD-based gratings, recent work by Paul Bouteyre and myself sets the scene for characterising the non-topological grating resonances [321]. We fabricated WS_2 single gratings on both gold and SiO_2 substrates, and measured various forms of polaritons between the bulk WS_2 exciton and grating photonic modes. Furthermore, joint first authors Tommi Isoniemi and Paul Bouteyre simulated and experimentally measured topological edge states in 2D TMD-based hexagonal photonic crystals [229]. As with the 1D case, they placed photonic crystals with different topological invariants adjacent to each other, and observed a highly localised and unidirectional edge state at the boundary between the two. For 1D systems this unidirectionality has not been observed, however potential applications of the Jackiw-Rebbi edge states could lie in lasing, non-linear effect boosting, waveguiding, and more.

The lack of in-depth experimental study on Jackiw-Rebbi edge states in high index 1D gratings, prompted my research into the realisation and characterisation of such structures. Specifically, I chose to work with high refractive index dielectrics such as WS_2, in order to achieve stronger light confinement than previous works, within the visible wavelength range as opposed to infrared. Furthermore, the published structures so far have been purely passive devices, whereas I will push towards using the Jackiw-Rebbi edge state in application, for enhancing the photoluminescence emission and directivity of coupled excitonic emitters. My aim in this experimental chapter will therefore be to bring together the versatility of van der Waals materials for producing multi-layer grating devices, with the topological phenomena of BICs, to produce robust, high quality factor, strongly localised, and highly directional Jackiw-Rebbi edge states, for advanced nanophotonic

control.

I will begin this chapter by introducing the choice of substrate for my grating devices, and the reasons behind why I chose to use gold. I will then present condensed results from a large range of grating parameter sweeps, to clearly show how the resulting mode structure can be manipulated through structural tuning. Next, I explain why the transfer of a top WS_2 slab onto the gratings is required in order to achieve photonic band inversion, and thus change the band topology. By bringing together two gratings of different topology in simulation, I will demonstrate the ability to achieve Jackiw-Rebbi edge states in double inverted WS_2 gratings. Subsequent detailing of the fabrication process of the designed gratings will follow, along with comparison of the experimentally measured angle-resolved modes with simulation. I will then fully characterise the far-field reflectance contrast of the fabricated structures in 2D k-space, proving the existence of a highly localised Jackiw-Rebbi edge state in experiment. After investigating the far-field response, I will simulate the near-fields of the all of the grating modes, aiding further understanding of the nanoscale behaviour of the lossy mode, BIC, and edge state. To finish this chapter, I design and fabricate an optically active double grating heterostructure, comprising an hBN-encapsulated monolayer WSe_2 placed between the WS_2 grating and top flake. I first simulate the five layer heterostructure, confirming that Jackiw-Rebbi edge states can still be reliably produced in this more complex device. I then present simulated angle-resolved emission from the monolayer coupled to the edge state in the far-field, along with a maximum predicted enhancement factor of over 1000 compared to uncoupled monolayer PL. To prove the coupling in experiment, I fabricate the heterostructure using multiple transfers, before measuring the angle-resolved PL. Clear edge state coupling of the monolayer PL is observed, with an experimental enhancement of over 16. These results prove that robust emitter enhancement and beam-shaping can be achieved with on-chip, micron-scale devices supporting exotic topological Jackiw-Rebbi edge states, whilst promoting the multi-layer stacking ability of van der Waals materials.

5.2 WS_2 Inverted Gratings on Gold

In this section, I will first discuss the motivation behind my choice to use a gold substrate beneath the WS_2 gratings. I will then spend the bulk of this section focusing on RCWA simulations with changing grating parameters such as period, thickness, and filling factor. The mode structures in k-space will be compared to find the ideal parameters to achieve band inversion of the BIC, for later producing a topological Jackiw-Rebbi edge state. I then discuss why an additional WS_2 slab is required on top of the gratings to achieve this band inversion in high index gratings. Finally, I design a double inverted grating structure and simulate the angle-resolved reflectance, predicting the presence of a Jackiw-Rebbi edge state at the centre of the band gap. These simulations will serve as the blueprints for fabricating such devices in experiment in the following section.

5.2.1 Choice of Substrate

The first step in designing and simulating WS_2 gratings was to understand how the photonic band structure changes upon varying the geometrical parameters, i.e. thickness t, filling factor FF, and

period a, as well as investigating how the choice of substrate can impact the photonic response. I began by fixing the grating geometry to $t = 80$ nm, $FF = 0.85$, and $a = 300$ nm, and calculated the band structure for the gratings on a 300 nm SiO_2 on Si substrate, and gold substrate using the FDTD method as described in Section 3.3.5. The results are shown in Figures 5.1 (a) and (c) respectively, and show a number of differences. By first concentrating on the guided modes (solid blue curves), it is evident that the grating on SiO_2 has a steeper gradient, and thus larger group velocity, compared to the case on a gold substrate. This can be explained by considering the effective permittivities of the two systems. For the grating on transparent SiO_2, the modes partially leak into the substrate, and thus the overall effective refractive index that the modal photons experience is reduced compared to pure WS_2. For the gold substrate, the electric fields cannot penetrate into the gold, and so the effective refractive index is closer to that of pure WS_2. Relating this back to Equation 2.45, one can see that a smaller effective refractive index will therefore lead to a steeper gradient of the guided modes in k-space and vice versa. Another difference is that the modes for the SiO_2 substrate structure are red-shifted compared to those on gold. I also attribute this to stronger confinement of the modes within the grating with reflective gold beneath. The overall mode volume is decreased with a gold substrate compared to SiO_2, and so shorter wavelengths can be confined within the structure. This is the same rationale as with the additional confinement provided by gold beneath the TMD nanoantennas studied in Chapter 4. The final difference is in the light cones as marked by the light blue squares in Figures 5.1 (a) and (c). For the SiO_2 substrate case there are two light cones, the inner cone corresponds to vacuum photons that can leave through the top of the grating, and the outer cone represents the dispersion of photons exiting through the SiO_2 substrate. Here the SiO_2 is modelled with a refractive index of 2.12, i.e. greater than that of air, and so leads to a broader light cone. For the grating on a gold substrate there exists only the vacuum light cone as the photons cannot escape through the gold and are simply reflected.

To link the photonic band structure to a more experimentally measurable result, I then simulated the reflectance from the WS_2 grating on both SiO_2 and gold as in Figures 5.1 (b) and (d) respectively. This was done using an open source Python-implementation of the RCWA method, as explained in Sections 2.7.2 and 3.4.1, using experimentally measured refractive indices. It is clear that the FDTD and RCWA results agree extremely well for both substrate cases. Furthermore, the reflectance calculations give additional information about the character of the guided modes, such as lineshapes, linewidths, and relative amplitudes. Therefore, I will focus on simulations and experiments of reflectance for the bulk of this chapter. From these, the photonic band structure is revealed through dips in the reflectance, where incident light becomes trapped within in-plane guided modes. The most notable difference between the reflectance simulations for WS_2 gratings on SiO_2 and gold substrates in Figures 5.1 (b) and (d), is the difference in contrast between the guided modes and the reflection from the background substrate. For the SiO_2 substrate case the contrast is poor, and the modes are more difficult to distinguish from those with the gold substrate, which exhibits effectively unity reflection everywhere except the guided modes. This is especially important for the BIC at the Γ point, which is much more clear with gold. In addition, there is a broad Fabry–Perot resonance present in Figure 5.1 (b) which further complicates the mode structure, and reduces visibility of the BIC and guided modes that I am interested in. This Fabry–Perot

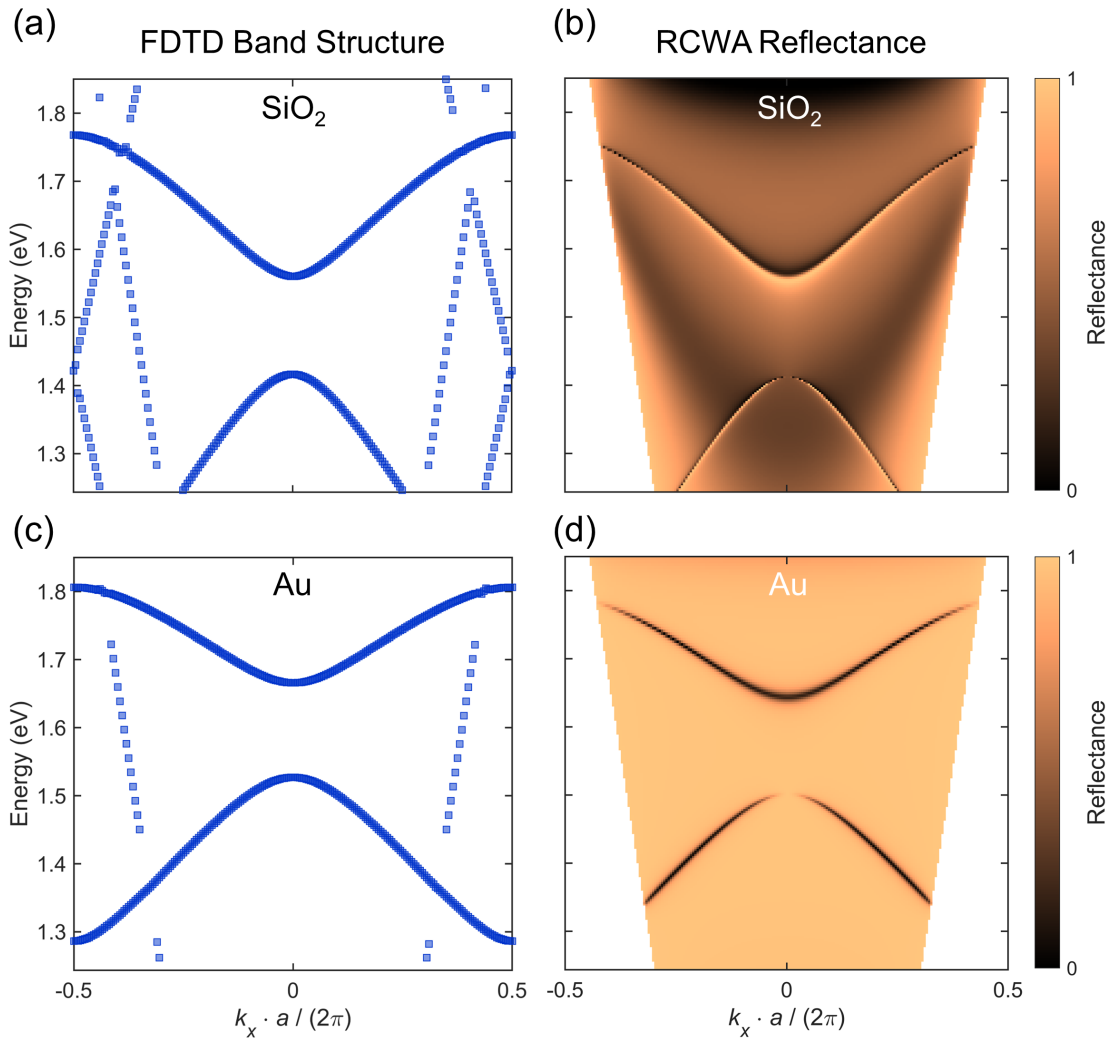


Figure 5.1: **Simulated band structure and reflectance of a WS_2 grating on silica and gold substrates. (a)** Band structure simulated using the FDTD method by exciting all available modes of a WS_2 grating on SiO_2 substrate for TE polarisation. Grating period, thickness, and filling factor are 300 nm, 80 nm, and 0.85 respectively. x axis corresponds to wave vector k_x perpendicular to the grating axis, normalised to the grating period a. Inner and outer diagonal lines represent the edges of the vacuum and SiO_2 light cones respectively. **(b)** Reflectance contrast simulated using the RCWA method showing perfect agreement with the band structure calculations. Guided modes yield an asymmetric Fano lineshape with weak contrast to the background. **(c)** Simulated band structure for a WS_2 grating of the same parameters but on a gold substrate. Modes are blue-shifted compared to SiO_2 substrate case, and have a shallower gradient. Only the vacuum light cone is present as expected. **(d)** Simulated reflectance contrast of WS_2 grating on gold again showing perfect agreement with the calculated band structure. Guided modes show symmetric Lorentzian lineshapes with strong contrast to the background, therefore BIC can be easily observed.

mode exists within the 300 nm SiO_2 layer on top of the silicon substrate, which was simulated to mimic commercially available wafers, and so this mode would also be present in experiment. The final difference lies in the lineshapes of the modes. For the SiO_2 substrate the mode takes a Fano lineshape in the reflectance spectra, whereas for the gold substrate it is Lorentzian. The asymmetric Fano form is not possible with a gold substrate since the reflectance is already unity, and so the

resonance forms a symmetric Lorentzian dip which is simple to fit.

As well as all of the above complications associated with a SiO_2 substrate, from a fabrication perspective, the substrate would also be etched into a grating along with the TMD. In practice this turns out to make very little difference to the reflectance measurements, however, to make as-designed structures, gold is again the clear choice as it provides a natural chemical etch stop, and thus gratings on top of a flat substrate. Also from a technical standpoint, fabricating TMD nanogratings on metal further proves the versatility of van der Waals materials, with their inherent ability to adhere to and stack on any surface to make complex 3D heterostructures and devices. To this end, the WS_2 gratings explored in this chapter will all be situated on gold substrates.

5.2.2 Grating Parameter Tuning

After deciding on a substrate, I then varied the grating geometrical parameters and simulated the resulting reflectance contrast (RC) as in Figure 5.2. Here the reflectance contrast refers to

$$RC = \frac{R - R_{\text{ref}}}{R_{\text{ref}}}, \tag{5.1}$$

where R is the reflectance from the entire structure, and R_{ref} is a reference measurement of reflectance, in this case from the gold substrate alone. Reflectance contrast thus removes any background effects and normalises the result to a reference point. Whilst this is less important for simulated data as the reference point will always be the same, in experiment the reference may change from sample to sample. Also note that since the gold has effectively unity reflectivity, Equation 5.1 will naturally give results between 0 and -1. However, for clarity I always renormalise the results I present in this thesis so that the minimum and maximum values correspond to 0 and 1 respectively.

The simplest tuning parameter to understand is the grating period a. By increasing a and keeping the thickness and filling factor constant, the unit cell simply increases in size in the x direction (i.e. perpendicular to the grating axis), with the width of each grating segment w increasing proportionally. The larger cavity volume therefore leads to a red-shift in energy as can be seen in Figure 5.2 (a). The thickness of the grating t also has a similar effect in increasing the mode volume and therefore red-shifting the mode [322] as in Figure 5.2 (b). However, more subtly, increasing t also increases the gradient (or curvature) of the guided modes. This can be understood by considering Equation 2.45, which describes the dispersion of waveguide modes. For the gratings simulated with RCWA, their length l in the y direction is infinite, and so the second term in the square root goes to zero. Then, by keeping all other variables constant and changing the thickness t, the energy bands will approach that of the fundamental mode, which is linear with k_x as plotted in Figure 2.15 (b). This has the effect of making the gradient appear steeper as t is increased, even though the effective refractive index of the structure is not changing. Another feature to note is the broad resonance that appears in the rightmost panel of Figure 5.2 (b) for $t = 100$ nm. This is a Fabry–Perot mode trapped between the top surface of the grating and the gold substrate, akin to those discussed in Sections 2.4.4 and 4.3.2. Increasing the grating thickness too much thus introduces additional modes to the system which are not of interest for the work in this thesis, and so I will focus on gratings with $t < 100$ nm.

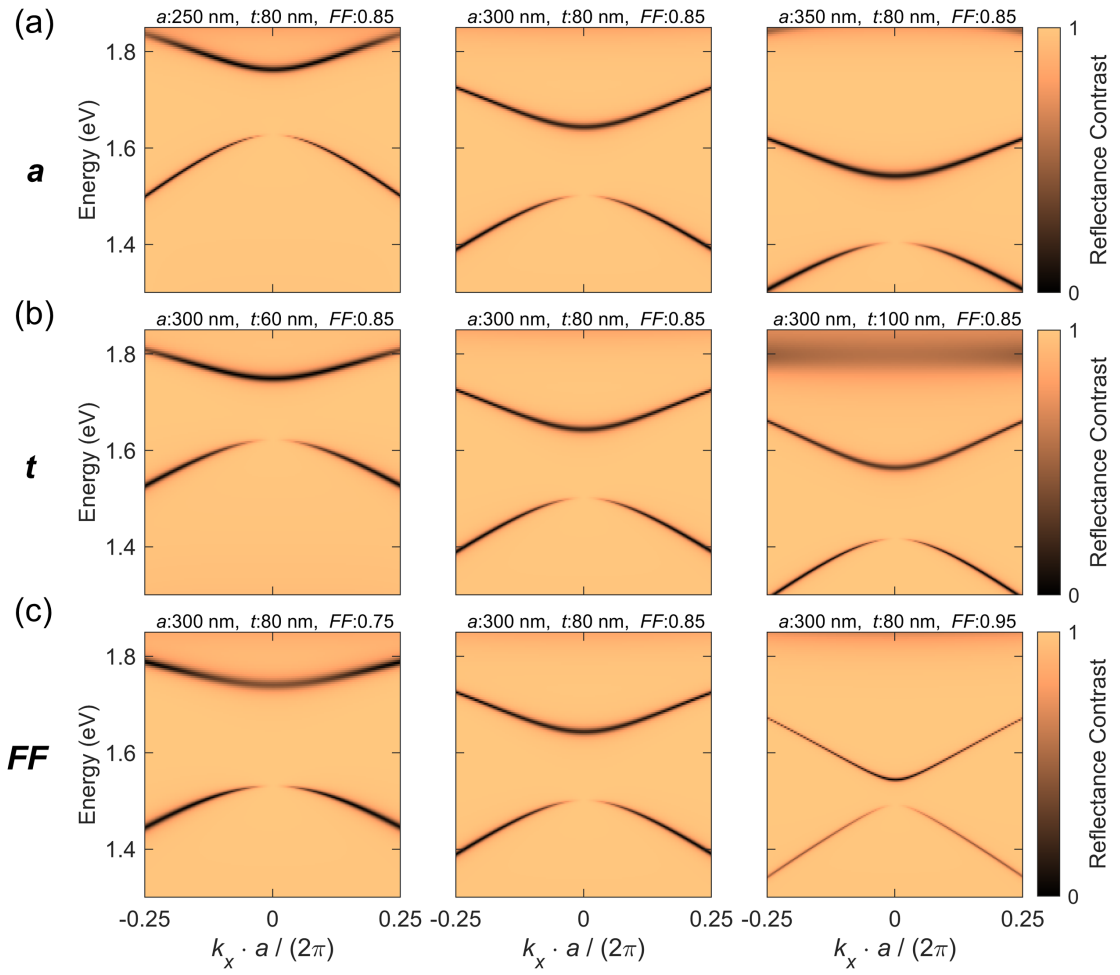


Figure 5.2: **Simulated reflectance contrast of a WS_2 grating on gold upon varying geometrical parameters.** **(a)** Mode structure upon increasing grating period a showing red-shift of modes. From left to right: $a = 250$, 300, and 350 nm respectively. **(b)** Mode structure upon increasing grating thickness t showing red-shift and increase in curvature of modes. From left to right: $t = 60$, 80, and 100 nm respectively. **(c)** Mode structure upon increasing grating filling factor FF showing small red-shift, increased mode curvature, and decrease of photonic band gap. From left to right: $FF = 0.75$, 0.85, and 0.95 respectively.

The final geometrical parameter than can be tuned is the filling factor FF. In the simulations I present in Figure 5.2 (c), varying the FF leads to multiple effects on the mode structure, the most obvious being a change in the size of the photonic band gap [323, 324]. To understand why this happens, we must first recall that the band gap is created owing to diffractive coupling between the forwards and backwards propagating modes as detailed in Section 2.5.3. These modes can exchange energy owing to the perturbation introduced by the alternating refractive indices along the grating. Changing the filling factor fundamentally alters the in-plane coupling between the two modes [242, 325], which is represented by U in the Hamiltonian from Equation 2.46. The real part of the eigenvalues at $k_x = 0$ differ by $2U$ (Equations 2.48 and 2.49), and thus the band gap can be directly tuned through changing FF. In addition, similar to the period and thickness, increasing the filling factor also causes a red-shift of the modes, although the effect is less pronounced. Whilst the overall size of the unit cell does not increase in x or y when increasing FF, the effective mode volume

does increase. This is because the electric field tends to be more localised to the higher index parts of the unit cell, i.e. the WS_2 wires, for the fundamental grating mode. Note that higher order modes may display different behaviour owing to different electric field distributions. A higher FF thus spreads the mode profile out more in the x direction within each unit cell hence causing a red-shift. More about the electric field distributions will be covered later in Section 5.3.3. The filling factor also affects the curvature of the modes since it directly impacts the effective refractive index experienced by the guided modes within the structure [326]. The final difference upon increasing FF is a reduction in the mode linewidths, observable in Figure 5.2 (c). This suggests that the modes are more strongly confined with a higher quality factor. The smaller proportion of low index material in each unit cell likely leads to less leakage of the mode into the environment [322], as there is more opportunity for total internal reflection within the high index segments.

5.2.3 Photonic Band Inversion

Whilst the three parameters explored in the previous section allow for significant tunability of the modes, I found that it was not possible to fully close the band gap with any combination of a, t, and FF. This is important as the main goal of this experimental chapter is to realise photonic band inversion, so that the BIC flips to the opposite energy band and changes topological phase. From this, a topologically protected Jackiw-Rebbi state can be formed and characterised, as described theoretically in Section 2.6.5. In Figure 5.2 (c) I tuned the filling factor up to 0.95 in simulation, however, even pushing FF further to 0.99 and higher, I found that the band gap could never fully close. Besides, such a high FF would not be achievable in reality with the current nanofabrication techniques available. To overcome this, I simulated a WS_2 grating on gold with an additional unpatterned WS_2 slab placed on top as illustrated in Figure 5.3 (a), which I term an inverted grating. I then varied the ratio of the grating thickness t_{gr} to the slab thickness t_{slab}, whilst keeping the overall thickness of the structure constant so that the resulting modes had minimal shift in energy. The period and filling factor were also kept constant at 300 nm and 0.85 respectively. The angle-resolved reflectance contrast results are shown in Figure 5.3 (c), and a clear decrease in the band gap can be observed with an increase in the relative slab thickness. This can be explained by considering the whole structure as a grating, with high and low index segments both of thickness $t_{\text{gr}} + t_{\text{slab}}$. However, in this case the low index segments now have an increased effective refractive index as they are part air and part WS_2. This means that the overall refractive index contrast is reduced compared to a WS_2 grating alone, and in analogy to a DBR [185, 327], the band gap therefore reduces.

With the inherently reduced band gap of the inverted grating structure, I was then able to tune the filling factor to both close, and reopen the band gap as shown in Figure 5.3 (d). Here t_{gr} and t_{slab} were set to 35 and 45 nm respectively. The first panel from the left shows the characteristic band structure discussed previously with a BIC on the lower energy branch. By then decreasing FF and compensating for the energy shift by tuning the grating period, the band gap can be completely closed to form a Dirac point [194] as in the centre-left panel. Further decreasing FF then reopens the band gap with the BIC on the upper energy branch, suggesting that the topological phase of the band structure has changed. The inverted grating structure thus adds an additional degree of

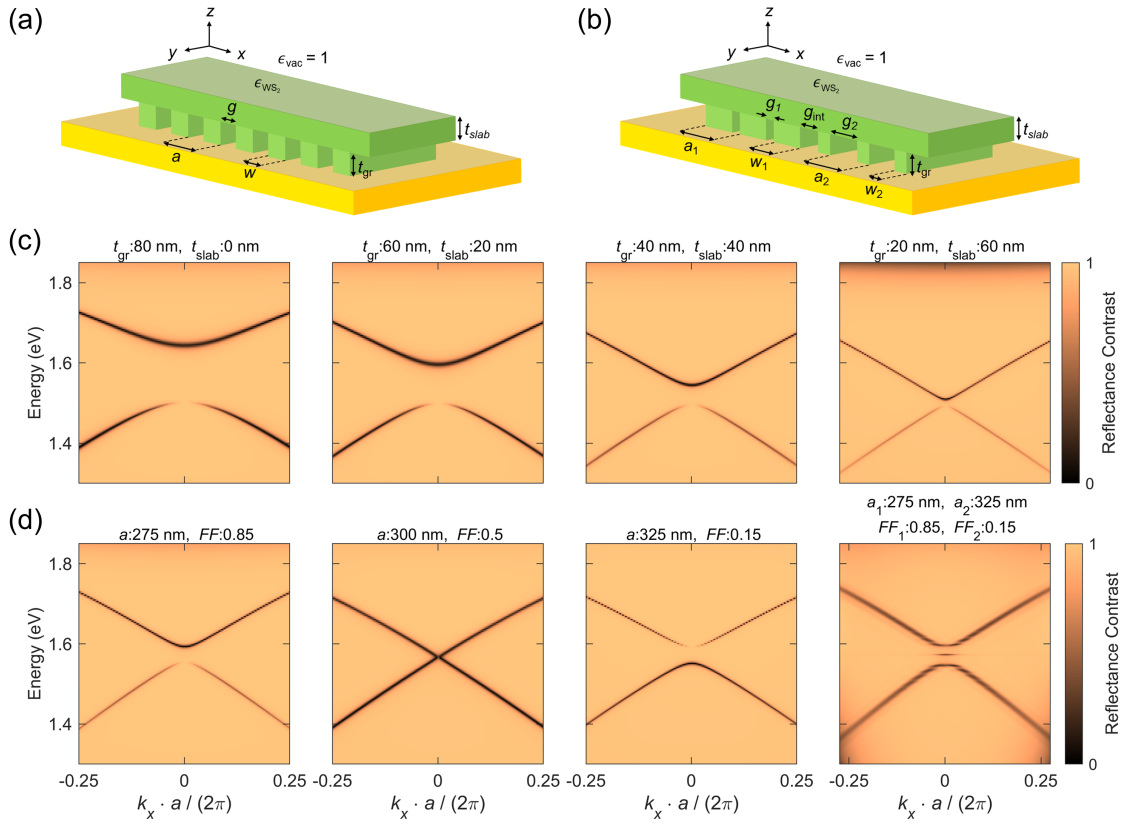


Figure 5.3: **Simulated photonic band inversion via a WS_2 grating on gold with a WS_2 slab placed on top.** **(a)** Schematic of single inverted grating structure where the permittivity of the grating and top slab is the same ϵ_{WS_2}. a, w, and g correspond to the grating period, high index segment width, and low index segment (gap) width respectively. t_{gr} and t_{slab} correspond to the thicknesses of the grating and top WS_2 respectively. **(b)** Schematic of double inverted grating structure composed of two single inverted gratings joined together in the x direction. $a_{1,2}$, $w_{1,2}$, and $g_{1,2}$ correspond to the period, high index segment width, and low index segment width of the left and right gratings respectively. g_{int} corresponds to the central gap width at the interface between the high and low FF gratings. **(c)** Simulated normalised reflectance contrast for a plane wave incident upon a single WS_2 grating on gold with increasing thicknesses of t_{slab} from left to right. Grating period and filling factor are $a = 300$ nm, and $FF = 0.85$ respectively. The total thickness of the structure is kept constant for each simulation to keep the modes at roughly the same energy. As the ratio of t_{slab} to t_{gr} is increased, the mode curvature increases and the band gap is reduced. **(d)** Simulated tuning of the grating filling factor to achieve photonic band inversion. Period is also tuned to shift each mid-gap to the same energy, with $t_{gr} = 35$ nm and $t_{slab} = 45$ nm. First three panels correspond to the reflectance contrast of single inverted gratings. Left panel shows BIC on the lower energy branch for a high FF. Centre-left panel exhibits a Dirac point where the modes cross for $FF = 0.5$. Centre-right panel shows BIC flipped to the upper energy branch for low FF. Right panel corresponds to simulated reflectance contrast of a double inverted grating structure combining the high and low FF gratings. A topologically protected Jackiw-Rebbi edge state can be observed at the mid-gap energy as a result.

freedom in the form of band inversion, as well as having the tunability offered by a, t, and FF of a standard grating. I then combined the two inverted grating structures with high and low energy BICs along the x axis as illustrated schematically in Figure 5.3 (b), and calculated the resulting RC spectra through FDTD simulations. Here the width of the gap between the adjacent gratings at the

interface is set to be $g_{\text{int}} = (g_1 + g_2)/2$, where $g_{1,2} = a_{1,2}(1 - FF_{1,2})$. The results are shown in the rightmost panel of Figure 5.3 (d), where a clear Jackiw-Rebbi edge state is observable at the mid-gap energy, not present in the two gratings alone. These simulations therefore provide the basis for designing and fabricating double inverted grating structures, to realise exotic topologically protected states in experiment.

The inverted grating structure may seem an unconventional choice at first given that equally, band inversion would also be possible in a grating partially etched into a WS_2 flake on gold, i.e. taking the entire WS_2 structure and rotating it $180°$ about the x or y axes. Initially, this structure seemed the natural choice to fabricate, however, I found that the chemical etching of these materials was not as controllable as would be required. During the RIE process, the plasma takes several seconds to initiate, and has an unstable etch rate for the first ~ 10 s. I calculated an average etch speed of 6 nm s^{-1} for WS_2 using the recipe from Section 3.2.5, meaning that achieving nanometer depth resolution for structures needing to be etched by only tens of nanometers was not viable. Preliminary tests showed that structures came out either completely etched, or by non-repeatable amounts with different etch depths for different grating parameters. Fabricating an inverted grating removed the difficulty in etching as the gratings simply needed to be fully etched each time. At this mid-point in fabrication before transfer of the top flake, I measured angle-resolved RC using the Fourier setup detailed in Section 3.5.2. This acted as a quality check, along with AFM and SEM imaging, to measure the fabricated parameters and compare to the initial designs. From then, most small errors in fabrication could be compensated by choosing a top flake of a tailored thickness, calculated by further RCWA simulations of the measured structures. This would not be possible with a partially-etched grating, as any fabrication imperfections would be permanent, with the only solution to make another sample. The inverted grating structure therefore turned out to be the more versatile, accurate and repeatable option, enabled owing to the inherent interlayer adhesion of van der Waals materials.

5.3 WS_2 Double Inverted Gratings for Edge States

After demonstrating the rich tunability of inverted gratings in simulation, and their ability to host topologically protected edge states in the previous section, I will now turn my focus towards realising these states in experiment. I will begin with an overview of the fabrication process of double inverted gratings, covering the measured geometrical parameters, and top flake thickness calculations. Next, I will discuss angle-resolved reflectance contrast results measured via Fourier spectroscopy in 2D k-space, to fully characterise the modes of the system in TE polarisation. Finally, electric field simulations of the lossy mode, BIC, and Jackiw-Rebbi edge state will be presented and compared, thus unveiling more information about the nature of each mode. This section serves as a demonstration of the ability to create Jackiw-Rebbi edge states in passive WS_2 grating structures, with the view to couple emitters to this state in Section 5.4.

5.3.1 Fabrication of Double Inverted Gratings

The fabrication of double inverted grating structures began with mechanical exfoliation of bulk WS_2 flakes from HQ Graphene directly onto an electron beam evaporated gold substrate on silicon as detailed in Section 3.2.2. The substrates were of the same parameters as those used for the nanoantennas on gold from Chapter 4, with 150 nm gold atop 10 nm nickel to promote adhesion to the commercial silicon wafer below. The samples were then spin-coated with a positive resist, before being patterned with alternating high and low filling factor gratings across the entire substrate using EBL. Following the patterning, RIE was performed with a hybrid chemical and physical etching recipe using a mixture of SF_6 and CHF_3 gases, to fully etch the WS_2 into parallel gratings as seen from the SEM image in Figure 5.4 (a). As with the nanoantennas project, the gold acted as a natural etch stop as it is chemically inert, and thus only a small physical etch of several nanometers was observed. This can bee seen in the AFM measurements in Figure 5.4 (b), which were also used to calculate the grating thicknesses. However, the AFM images were less suitable for lateral measurements such as the grating filling factor, as the tip has a finite width which is not known precisely. Furthermore, the tip width can change during scans as it accumulates soft materials, or if part of the tip breaks off. Therefore, I took high resolution SEM images and used an ImageJ macro named InteredgeDistance [328] to calculate grating periods and filling factors.

Figure 5.4 (c) shows an optical microscope image of an example patterned and etched flake of WS_2. The blue dashed box indicates the pattern that is repeated across the whole sample in the horizontal and vertical directions, in order to cover as many flakes as possible. Within each repeated pattern, there are various grating sub-patterns with varied parameters as illustrated previously in Figure 3.3 (e). The grating axis (i.e. parallel to the grooves) is oriented horizontally in Figure 5.4 (c), and alternating high and low FF gratings are arranged in pairs vertically, with dosage of the electron beam during EBL increasing with each pair down the columns. A higher dose means that the resist is exposed to more electrons and thus the pattern is made smaller. In the case of gratings, this means that the resulting wires have a lower filling factor after etching, and so a range of filling factors are achieved by varying the dose. This increases the likelihood of fabricating structures with the correct parameters for the realisation of a Jackiw-Rebbi edge state, which requires very precise tuning down to the nanometer as discussed in Section 5.2.3. Varying the dosage also accounts for any fluctuations in the power of the electron beam, as this can change from use to use. Across the rows of the pattern, the grating sub-pattern pairs repeat, but with a varying period. I did this since mechanical exfoliation leads to many flakes, but all with random thicknesses. Therefore, using the same grating period for every flake would cause the modes to be shifted to different energies depending on thickness, and may not always have the same mid-gap energy as adjacent gratings required to form an edge state. This happens because changing the thickness of a low FF grating leads to a smaller overall change in mode volume compared to a high FF grating, and thus the shift in energy of the modes is different. To combat this problem, I designed pairs of grating sub-patterns with periods that would produce an edge state for specific thicknesses in the range of 30-70 nm in 10 nm increments. As mentioned in Section 5.2.2, this is because the total thickness should be < 100 nm to avoid Fabry–Perot resonances. Therefore, for the majority of exfoliated flakes of ~ 100 µm in lateral size or greater, this pattern should yield at least one good edge state. Furthermore, the

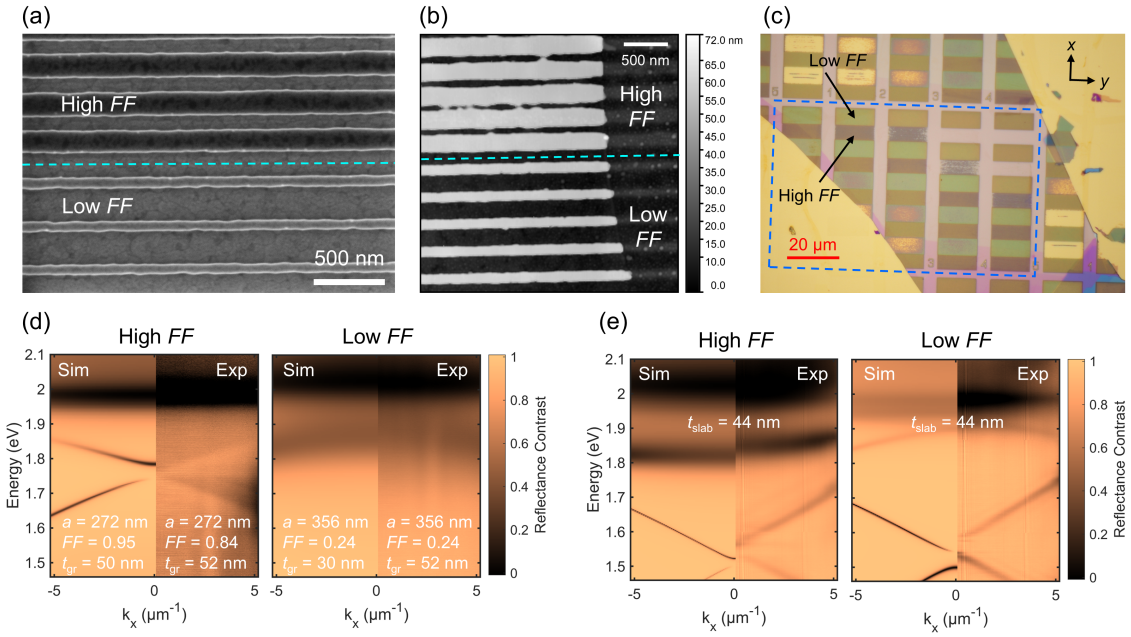


Figure 5.4: **Fabricated gratings parameter check and top flake thickness calibration.** **(a)** Example SEM image of the interface between gratings of different period and filling factor etched into the same WS_2 flake. Top grating has high FF and bottom grating low FF with gold substrate seen between wires. Interface region denoted by the light blue dashed line. **(b)** Example AFM image of an interface between gratings at the edge of the flake used to measure grating thickness of $t_{gr} = 47$ nm. The slight gold etch of ~ 8 nm is also visible. **(c)** Optical microscope image of a patterned WS_2 flake before top flake transfer showing repeating pairs of high and low FF gratings down each column. Grating axis and interfaces are in the horizontal direction along the y axis as with **(a)** and **(b)**. Blue dashed region outlines the repeated pattern used over the entire sample. Electron beam dosage is varied down each column, and grating period varied across rows. **(d)** Simulated and experimental angle-resolved RC for single WS_2 gratings before transfer. Each half-panel details the corresponding parameters used in simulation and calculated from experiment for comparison. Left and right panels correspond to high and low FF gratings respectively. **(e)** Simulated and experimental angle-resolved RC for the same WS_2 gratings in **(d)** after transfer of a 44 nm thick top WS_2.

mid-gap energy of the modes can then be tuned for both adjacent gratings by changing the thickness of the top WS_2 flake. This will become more important in Section 5.4, when coupling emitters to the edge state.

As mentioned in Section 5.2.3, before transferring the top WS_2, I performed a quality check by measuring the angle-resolved RC of the single gratings in experiment using the home-built Fourier spectroscopy setup detailed in Section 3.5.2. I then compared the resulting spectra from each grating to RCWA simulations using the parameters obtained from analysis of respective AFM and SEM images. However, owing to small errors in the measured parameters, and potential discrepancies between the refractive index data used in simulation [80] and that of the physical structure, the simulated and experimental mode structures did not always agree perfectly. This meant that predicting the top flake thickness to produce modes at the same mid-gap energy for both adjacent gratings in experiment was quite unreliable. To increase the chances of achieving an edge state, I tuned simulated parameters such as the filling factor and thickness until the modes resembled

those of experiment as in Figure 5.4 (d). For the high FF grating, I had to increase FF from 0.84 to 0.95 in simulation, along with a small decrease in thickness from 52 to 50 nm to reproduce the experimental results. For the low FF grating, only the thickness had to be decreased from 52 to 30 nm to see good agreement. Note the change in t_{gr} needed for the low FF grating is larger since changing thickness has a smaller effect on lower FF gratings as mentioned previously in this section. I then performed further RCWA simulations with the addition of a top WS_2 flake over a range of thicknesses t_{slab}. This served both as a check that modes of adjacent gratings would be at the same mid-gap energy to form an edge state, but also as a tuning parameter to shift the mid-gap to a desired energy. As shown in Figure 5.4 (e), I found a top flake thickness of 44 nm produced modes at the same mid-gap energy for the high and low FF inverted gratings in simulation. Here the band gap is larger for the low FF gratings, however I found that the size of the gap does not need to be identical to produce a Jackiw-Rebbi edge state.

After finding an ideal top flake thickness, I then mechanically exfoliated more WS_2, this time on a silicon substrate spin coated with several hundred nanometers of PMMA. I searched for flakes of roughly the correct thickness via colour, and then performed AFM to measured the exact thicknesses. Once a flake of $t_{\text{slab}} = 44$ nm was found, I then transferred it onto as many calibrated gratings as possible, using the method from Section 3.2.6, ensuring that each individual grating from a pair and the interface between the two were maximally covered. I then measured angle-resolved RC again and compared the results to the simulated prediction in Figure 5.4 (e). Whilst the modes are shifted by ~ 50 meV compared to simulation, the experimental results have perfectly aligned mid-gap energies and BICs on opposite energy branches, therefore achieving both criteria for realisation of a Jackiw-Rebbi edge state. Again, the differences here between simulation and experiment are likely owing to discrepancies in the measured parameters and refractive indices, but also the additional transfer step adds further error. Whilst every effort was made to keep the grating and top flake as clean as possible, and the transfer was carried out in a nitrogen environment, there could still be some contamination between the top layer and grating. For example, any moisture or hydrocarbons could become trapped in the gaps between grating wires, thus decreasing the refractive index contrast and increasing the mode volume, which would red-shift the modes slightly. In addition, since the top flake is very thin, I observed a slight bending of the flake of $\sim$ 2-3 nm into the air gaps between grating wires in post-transfer AFM measurements. Again, this would fundamentally affect the mode structure in a similar way causing an energy shift and slight reduction in the band gap. Whilst this t_{slab} calibration method alone is not perfect, combined with the versatility offered by the varied patterning, I was able to repeatably fabricate adjacent gratings with near-identical mid-gap energies to within ~ 20 meV.

5.3.2 Jackiw-Rebbi Edge States

To confirm the existence of Jackiw-Rebbi edge states in the fabricated double grating structures in experiment, I performed further angle-resolved RC using the previously mentioned Fourier spectroscopy setup, taking signal from both a high and low FF grating together using a variable rectangular aperture. An optical microscope image of the structure is shown in Figure 5.5 (c), with the patterned WS_2 outlined by the blue dashed line, and the top WS_2 slab outlined in red. Here

the grating axis is in the horizontal direction, as is the interface between the adjacent gratings of alternating parameters, and the scanned wave vector is perpendicular to the grating axis, k_x. The spectra in the left and centre panels of Figure 5.5 (a) were taken from the yellow and green measurement regions of Figure 5.5 (c) respectively, in order to isolate the signal from each independent grating. The measured grating parameters were $a = 319$ nm, $FF = 0.41$ for the left panel, and $a = 279$ nm, $FF = 0.81$ for the centre panel, as calculated from SEM images. I also measured the grating and slab thickness via AFM as $t_{\text{gr}} = 47$ nm and $t_{\text{slab}} = 41$ nm. The experimental RC results show very good agreement with theory (Section 2.5.3) and simulation (Section 5.2.3), with the low filling factor grating hosting a BIC on the high energy branch, and the high filling factor grating hosting a quasi-BIC on the low energy branch. The reason for the poorer quality spectra and quasi-BIC of the high FF grating in the centre panel of Figure 5.5 (a), is due to the smaller size of the measurement region, since the top WS_2 slab was not wide enough to fully cover both gratings. This means that the number of grating periods measured was less than for the low FF grating, and so the mode linewidths were broader. Furthermore, the blurred region for negative k_x is likely owing to light scattered from the edge of the top flake at high angles away from the collection angle of the objective. This is also visible for the low FF grating (left panel of Figure 5.5 (a)) but for positive k_x, as the top flake edge is on the opposite side as depicted by the yellow dotted box in Figure 5.5 (c). The effect is less pronounced than for the high FF grating however, as the available measurement area was larger than the green region, and so the signal to edge noise ratio was higher.

After characterising the high and low FF gratings individually, I measured the grating interface across the yellow and green regions as in the rightmost panel of Figure 5.5 (a). Here the signal improved owing to the larger measurement region, and most importantly, a new resonance was observed at the mid-gap energy. This mode was not present in RC measurements of either of the gratings alone, and so was direct evidence of a highly confined, topologically protected Jackiw-Rebbi state present in the double inverted WS_2 gratings on gold. Topologically protected phenomena are inherently robust to defects, and thus require large global changes to the system to change or remove them as explained in Section 2.6. This robustness was already evident from the measured Jackiw-Rebbi edge state presented in Figure 5.5 (a). The high FF grating only hosts a quasi-BIC owing to the reduced number of covered grating periods, and has an obscured mode structure, yet still yields a topological edge state when combined with the appropriate low FF grating with a BIC on the opposite energy branch. In addition to the high physical robustness, the edge state is very well localised in energy at 1.64 eV, with a narrow average linewidth of just 6 meV. This is less than half that of the guided modes within individual gratings, at 14 and 16 meV for the upper and lower energy branches respectively. Note that I took the average of the guided mode branches away from $k_x = 0$ to avoid effects of the BICs. Furthermore, the Jackiw-Rebbi edge state is also strongly localised in k_x, with a linewidth of $\Delta k_x = 1.1$ μm^{-1} for $k_y = 0$. Using the following equation,

$$\Delta\theta = \arcsin\left(\frac{\Delta k_x \lambda_0}{2\pi}\right), \tag{5.2}$$

I calculated an angular bandwidth $\Delta\theta$ of 7.3°, where λ_0 is the free space wavelength of 755 nm.

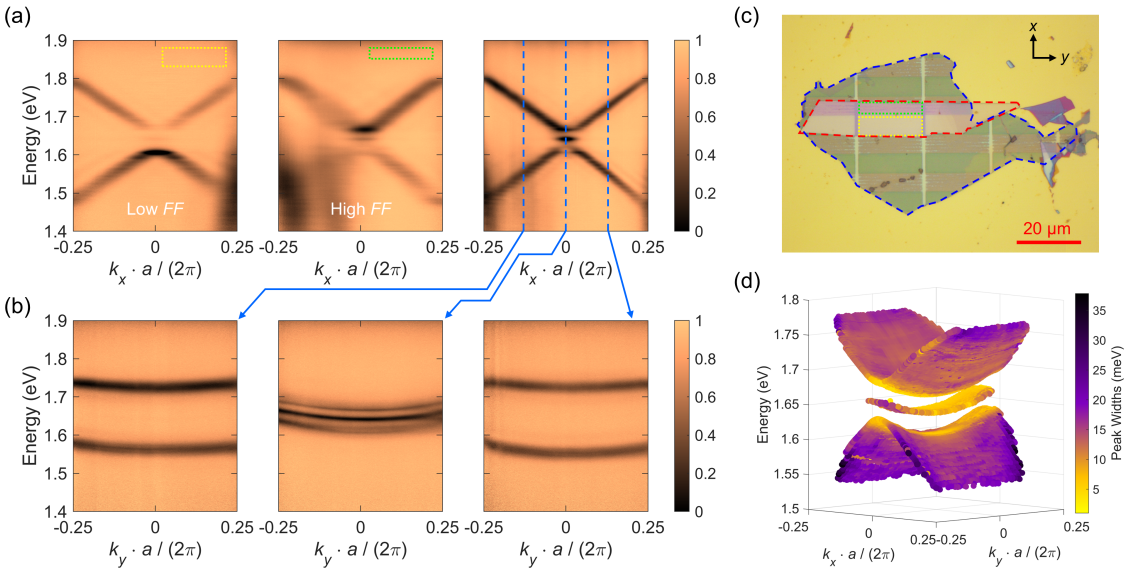


Figure 5.5: **Experimental normalised angle-resolved reflectance contrast of WS_2 double inverted gratings on gold substrate showing Jackiw-Rebbi edge state. (a)** Reflectance contrast with respect to wave vector k_x at $k_y = 0$, normalised to the grating period a. Left and centre panels correspond to measurements of single inverted gratings taken from the yellow and green dotted regions of **(c)** either side of the interface. The grating parameters are $a_{1,2} = 319$ and 279 nm, $FF_{1,2} = 0.41$ and 0.81 respectively. Both have thicknesses $t_{gr} = 47$ nm and $t_{slab} = 41$ nm. BIC visible on the upper energy branch for the low FF grating, and quasi-BIC on the lower energy branch of the high FF grating. Right panel corresponds to RC from the double inverted grating interface (i.e. both yellow and green dotted regions), showing a clear Jackiw-Rebbi edge state localised at the mid-gap energy. **(b)** Reflectance contrast at the edge state with respect to wave vector k_y for three different values of k_x, represented by the dashed blue lines in the right panel of **(a)**. Left and right panels show identical dispersions of lossy modes owing to the symmetry of the structure along k_y. Centre panel shows dispersion of Jackiw-Rebbi edge state at $k_x = 0$, which shifts parabolically in energy with k_y as with the lossy modes. **(c)** Microscope image of the double inverted grating structure. Blue dashed curve outlines the patterned bottom flake with alternating grating parameters as seen by the brown and green regions. Grating axes and interfaces are along the y axis. Top transferred WS_2 is outlined in red, and covers multiple interfaces between the alternating single gratings. Presence of the top flake changes the perceived colour of the gratings beneath. Yellow and green dotted boxes outline the measurement regions of the single gratings. Edge state measurement was taken over both combined. **(d)** Extracted mode energies plotted in 2D k-space (k_x and k_y) with colour corresponding to mode linewidths. Upper energy band forms a 2D parabola with a positive curvature, whilst the lower energy band is saddle-shaped with a negative curvature. The edge state has a finite linewidth in k_x and always exists at the mid-gap energy throughout k_y.

This highlights the highly directional nature of the Jackiw-Rebbi edge state, with potential applications in beam-shaping, lasing, and waveguiding.

After measuring the angle-resolved RC with respect to wave vector k_x, I then rotated the sample by 90° and repeated the measurements of the edge state to obtain spectra as a function of k_y, i.e. parallel to the grating axis. I did this for three different values of k_x represented by the dashed blue lines in the right panel of Figure 5.5 (a). At values of k_x far from zero, only two lossy modes are visible, one from each of the single gratings as in the left and right panels of Figure 5.5 (b).

This is expected as the edge state has a finite linewidth in k_x as discussed previously, and so is not visible for high k_x. The structure is symmetric along the y direction, and so the dispersions displayed in the left and right panels with equal magnitude of k_x are identical. The band edges simply shift parabolically in k_y, akin to a waveguide mode as in Figure 2.15 (b). Measuring at $k_x = 0$, the edge state is clearly visible and extends throughout the full range of measured k_y as seen in the centre panel of Figure 5.5 (b). Since the edge state must always exist at the mid-gap, it too disperses parabolically in k_y. Another observation is that the linewidths of the guided modes and edge states change negligibly with k_y. This means that these high quality factor resonances can still be accessed for a range of angles parallel to the grating axis, whilst being highly confined in the perpendicular direction. The angle-selective directivity thus could offer additional degrees of freedom and versatility for on-chip light manipulation.

To envisage the full dispersion of all the modes in 2D k-space, I measured many more planes in k_x and fitted each resonance with a Lorentzian curve, before extracting the peak positions for all k_x and k_y. The results are plotted in Figure 5.5 (d), where the colour corresponds to the fitted linewidths of each mode. The upper energy band forms a 2D parabola with a positive curvature, whereas the lower energy band is saddle-shaped, thus being described by a negative curvature. The Jackiw-Rebbi edge state extends parabolically in k_y, always at the mid-gap energy, whilst showing strong localisation in k_x. This means that the edge state can be in- and out-coupled for a broad range of angles parallel to the grating axis, but only a very narrow range of angles perpendicular. Furthermore, it is clear that throughout the measured range of k_y, the edge state and band edges around $k_x = 0$ have much narrower linewidths than the lossy guided modes at higher $|k_x|$. This is opposite to increasing $|k_y|$, where the linewidths remain the same. Therefore, large excitation angles parallel to the grating axis do not affect the edge state quality factor, making them robust options for on-chip waveguiding and light confinement. These angle-resolved measurements thus prove the highly directional nature of Jackiw-Rebbi edge states, with selective localisation in wave vector, and strong confinement in energy.

5.3.3 Electric Field Simulations

The next step in characterising the resonances of WS_2 inverted gratings on gold was to investigate the near-field responses. I began by simulating the electric field distribution through a cross-section of a single inverted grating with the same parameters as from the optimised gratings of Figure 5.3 (d). In Figure 5.6 (a), I present the electric field component E_y parallel to the grating axis for a slice in the x, z plane. The inverted grating structure is outlined by the solid black lines towards the bottom of the plot, with the substrate at $z = 0$. The unit cell is represented by the dashed black lines, and is repeated once either side of the central unit cell. I chose an incident wavelength of $\lambda = 800$ nm to selectively excite the lossy grating mode for normal incidence, i.e. $k_{x,y} = 0$, as predicted via the reflectance contrast simulations of Figure 5.3 (d). The results show a symmetric field profile about each unit cell, in agreement with theory from Section 2.6.4. The symmetric pattern therefore allows coupling to the radiative continuum, as seen by the propagating plane waves in the z direction. I then simulated the same structure for an incident wavelength of $\lambda = 773$ nm, where the BIC was expected to exist. This produced an asymmetric field pattern about each

unit cell, thus cancelling out radiative coupling to the far-field as predicted. Note that very weak plane waves can still be observed in Figure 5.6 (b). This is because the angle of incidence needed to be increased slightly in order to observe the BIC at all. For $k_x = 0$, symmetry-protected BICs are fully decoupled from the continuum and thus cannot be visualised via the RCWA method as it involves injecting light into the system, which would not 'see' the BIC. By further increasing the incident angle along x, the state would couple more to radiating plane waves, thus becoming more visible in the far-field. The plot in Figure 5.6 (b) is therefore technically a quasi-BIC, but still demonstrates the characteristic asymmetric field pattern required to completely suppress far-field radiation. These simulations therefore confirm the existence of symmetry-protected BICs in WS_2 inverted gratings on gold.

After demonstrating the electric field symmetries of the lossy mode and BIC in single gratings, I simulated a double grating structure, again using the same parameters as from Figure 5.3 (d). I used the FDTD method this time as the whole structure is finite, and considered 20 grating periods each side of the boundary in the full simulation. In Figure 5.6 (c) I present the electric field intensity normalised to the incident wave, i.e. $(|\boldsymbol{E}|/|\boldsymbol{E}_0|)^2$, for an illumination wavelength of $\lambda = 789$ nm, used to excite the Jackiw-Rebbi edge state. The plot focuses on a region of the x, z plane around the edge state, where clear localisation to the boundary between the two gratings can be seen in real space, with a maximum confinement of 663 times that of the incident wave. The cross-section of the double inverted grating structure is highlighted in white for comparison with the field intensity, and the gold substrate highlighted in yellow. It is evident that the majority of the field is actually confined more within the top WS_2 flake than in the grating itself. This is because the effective refractive index of the slab is higher than the grating beneath, and so can confine light to smaller mode volumes. In Figure 5.6 (d), I averaged the edge state field profile from 5.6 (c) over all z. This is plotted in green, with each peak marked by a yellow or purple circle corresponding to field maxima within the high or low FF gratings respectively. The central peak corresponding to the edge state at $x = 0$ is marked in red for reference. I then fitted each side to an exponential curve as depicted by the yellow and purple dotted lines, and extracted decay lengths of 0.71 and 0.74 µm respectively. The reason behind the difference is again due to a change in effective refractive index between the two gratings. The high FF grating has a higher effective refractive index and so confines light more strongly, therefore the edge state decays quicker in that direction, and vice versa. As a figure of merit, the total confinement in the x direction is $\Delta x = 1.45$ µm, or less than five grating periods. By then comparing to the experimental linewidth in wave vector measured previously in Section 5.3.2, $\Delta x \Delta k_x = 1.6 \geq 1/2$. Since the real-space confinement is a simulated result I expect Δx to be a lower bound, meaning that the experimental far-field characterisation of the Jackiw-Rebbi edge state in k_x is not too far from the minimal uncertainty imposed by the Heisenberg uncertainty principle [329]. These simulated results suggest that in addition to strong confinement in energy and wave vector as measured from angle-resolved RC, the photonic Jackiw-Rebbi edge state also boasts highly localised real-space confinement in the direction perpendicular to the grating axis. This suggests potential applications of such states in deep sub-wavelength waveguiding and Purcell enhancement of quantum emitters. In Chapter 6, I will present experimental near-field probing of the edge state using scattering-SNOM, to prove the real-space confinement in fabricated structures.

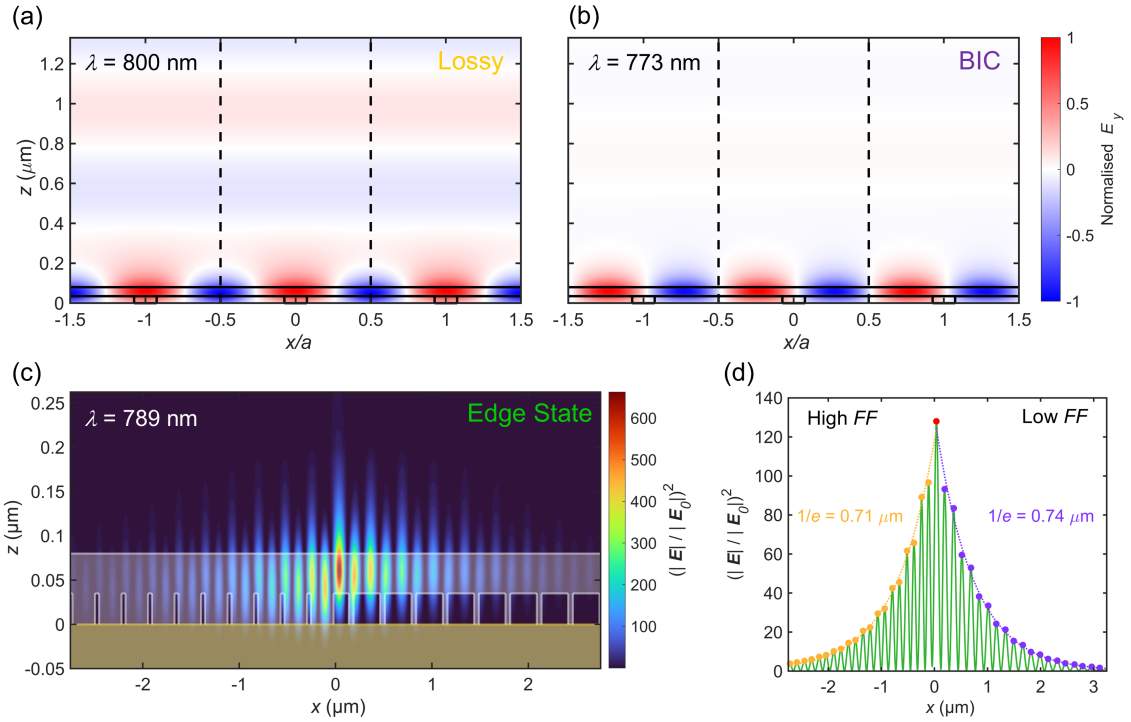


Figure 5.6: **Simulated electric field distributions within WS_2 single and double inverted gratings on gold for different photonic modes.** **(a)** y component of the electric field E_y in the x, z plane through a single inverted grating on gold. Incident wavelength of 800 nm corresponds to the lossy mode at $k_x = 0$. Parameters are $a = 325$ nm, $FF = 0.15$, $t_{gr} = 35$ nm, and $t_{slab} = 45$ nm. Field pattern is symmetric about the unit cell (outlined by the black dashed lines) and thus couples to the continuum of plane waves. Solid black lines outline the inverted grating cross-section. **(b)** E_y in the x, z plane through the same inverted grating structure but with incident wavelength 773 nm, corresponding to the BIC around $k_x = 0$. Field pattern is asymmetric about the unit cell, therefore cancelling out in the far-field. **(c)** Total electric field intensity normalised to the incident wave in the x, z plane through a double inverted grating on gold. Right grating has same parameters as in **(a)** and **(b)**. Left grating has parameters $a = 275$ nm and $FF = 0.85$, with same thicknesses as the right grating. Interface between gratings is at $x = 0$. Incident wavelength is 789 nm corresponding to excitation of the Jackiw-Rebbi edge state. Field pattern is strongly confined at the interface between the two gratings, localised mostly within the high index top slab. Double inverted grating structure highlighted in white for reference, along with the substrate in yellow. **(d)** Normalised electric field intensity averaged over z at the edge state energy plotted in green. Peaks in intensity for the high and low filling factor gratings are marked in yellow and purple respectively. Red marker corresponds to the intensity at the boundary between the two gratings ($x = 0$ nm), where the edge state is most strongly localised. Dotted lines correspond to exponential fits either side of the grating boundary, showing slightly different decay lengths depending on period and filling factor.

5.4 Active WSe_2 Monolayer-Coupled Double Grating Heterostructure

In the following section, I will move towards using the Jackiw-Rebbi edge state in WS_2 double inverted gratings on gold, to enhance the photoluminescence emission of a coupled monolayer WSe_2. I will begin with simulations of a proposed structure, incorporating an insulated WSe_2 monolayer

between the double grating and top WS_2 slab considered previously. The grating parameters will then be tuned until the edge state is in resonance with the monolayer photoluminescence, after which I shall calculate the potential emission enhancement in simulation. Next, I will demonstrate the feasibility of fabricating such a double grating heterostructure, using similar techniques to building the inverted gratings. The angle-resolved reflectance contrast will be measured to observe the resulting mode structure and edge state, with comparison to simulation. I will then explore the enhancement of WSe_2 direct-gap emission via angle-resolved photoluminescence measurements, using the home-built Fourier setup with some adjustments. Measurements will be taken on both the high and low filling factor gratings individually, as well as at the interface between the two to clearly show the change in photoluminescence for each different photonic mode. These results will therefore prove the utility of Jackiw-Rebbi edge states for both Purcell, and directivity enhancement of coupled emitters.

5.4.1 Photoluminescence Enhancement Simulations

To push the previously considered passive structures towards application, I began to explore incorporating an active TMD monolayer into the double inverted gratings. The rationale behind using monolayer TMDs was that they possess very bright, direct band gap emission as discussed in Section 2.3.2, with purely in-plane polarisation owing to the out-of-plane confinement of the excitons. This means that the majority of excitons will have at least some component of their electric field parallel to the grating axis, and thus couple well to the TE grating modes. Note that good coupling would also be observed for TM modes, however these do not produce the topological Jackiw-Rebbi edge states of interest. Furthermore, since TMD monolayers are, by nature, extremely thin, they will have a negligible impact on the mode structure of the overall grating structure. Other emitting structures such as quantum dots or wells require many layers of material, adding up to hundreds of nanometers total. This would shift the grating modes beyond recognition, with a separate study required to determine if parameter tuning could still realise an edge state with such structures. Using monolayer TMDs also further proves the versatility of this family of van der Waals materials, with their inherent ability to stick to any surface or device, which has not been well-investigated for other materials.

I chose WSe_2 for the active layer owing to its strong excitonic emission at room temperature, and its ideal band gap energy centred at 1.65 eV ($\sim$ 750 nm). This is far from the absorption region of the WS_2, which is significant below ~ 625 nm, and well within the range of wavelengths I was previously able to produce Jackiw-Rebbi edge states. From electric field simulations of the edge state as in Figure 5.6 (c), I found the ideal place for the monolayer was between the grating and top flake, in order to maximise the field confinement. This is predicted to boost the excitation rate of the excitons, thus leading to more recombination, and hence emission due to the Purcell effect [140]. However, simply placing a monolayer TMD in this position in real gratings would lead to significant charge transfer between the monolayer WSe_2 and bulk WS_2, hence almost completely quenching any photoluminescence emission. To overcome this, I proposed to insulate the monolayer by encapsulation in hBN as illustrated schematically in Figure 5.7 (a). Since the structure consists of five layers, I now refer to it as a double grating heterostructure. Whilst the hBN

spacers solve the issue of charge transfer, they presented a new problem of fundamentally altering the mode structure depending on their thicknesses. hBN has a significantly lower refractive index ($\sim$ 2.2 [294]) compared to WS_2 (4.46 [80]), and so adds additional reflections at each boundary with high index WS_2 or WSe_2. If the hBN spacers become thick enough ($>$ 10 nm each), Fabry–Perot modes emerge and interfere with the guided modes, similar to Figure 5.2 (b) where the grating thickness is increased. In addition, by considering the entire structure as a grating with high and low index sections like in Section 5.2.3, the effective refractive index contrast between the high and low index regions is reduced further by addition of more hBN. This is because the effective refractive index of the high index regions is reduced more by the presence of low index hBN than the low refractive index regions. The reduction in effective refractive index contrast therefore reduces the size of the band gap further, and so too much hBN causes additional complications with gap size, as well as mid-gap energy alignment, which are necessary for realisation of the Jackiw-Rebbi edge state. A single layer of hBN either side of the WSe_2 would work very well with negligible effect on the mode structure, however in practice, monolayer hBN is very difficult to find as it is almost completely transparent. From RCWA simulations of the reflectance contrast of grating heterostructures with different thicknesses of hBN spacers, I found $\sim$ 5 nm each or less to work for grating designs similar to those in Figure 5.5, without being too difficult to obtain in fabrication.

To demonstrate that the Jackiw-Rebbi edge state is still obtainable in an active double grating heterostructure, I simulated the angle-resolved RC of the system as presented in Figure 5.7 (b). An edge state at the mid-gap energy is visible, and in further simulations (not shown) of each single grating heterostructure alone, I do not observe such a state. The main difference between the edge state in the active structure compared to the passive structure, is the clarity of the resonance peak. Since the monolayer WSe_2 introduces excitonic absorption at 1.65 eV, there are noticeable additional losses which manifest as a blurring around the edge state and lower contrast. However, the main result is coupling of monolayer photoluminescence to the edge state, and so the RC measurements serve simply as a way of determining that the edge state exists in double grating heterostructures, and that it resonates at the intended energy. To explore potential PL coupling, I performed FDTD simulations of the double grating heterostructure with a dipole source placed at the interface between the two gratings, with peak emission energy centred at 1.65 eV. The dipole z position was set to be embedded within the WSe_2 monolayer, with polarisation parallel to the grating axis (TE) to mimic an ideal exciton. No external plane wave source was used for this simulation. I measured the emitted near-fields on a plane above the structure, before performing a far-field transform via decomposition of each point into a radiating plane wave. From this, I calculated the angle-resolved intensity in the far-field where a set of collection optics would be, in order to mimic a PL measurement. The results are shown in Figure 5.7 (c), where coupling of the emission to the edge state is immediately visible at just over 1.65 eV. The emission therefore takes on the characteristics of the edge state, with strong localisation in energy, real space, and wave vector k_x, hence confirming highly directional beaming. Since the dipole source in this simulation emits with a relatively broad linewidth of 110 meV, coupling to the other grating modes can be observed across the considered energy range, albeit with $\sim$ 5 times weaker output intensity. This further proves the advantages of Jackiw-Rebbi edge states over standard diffractive grating modes.

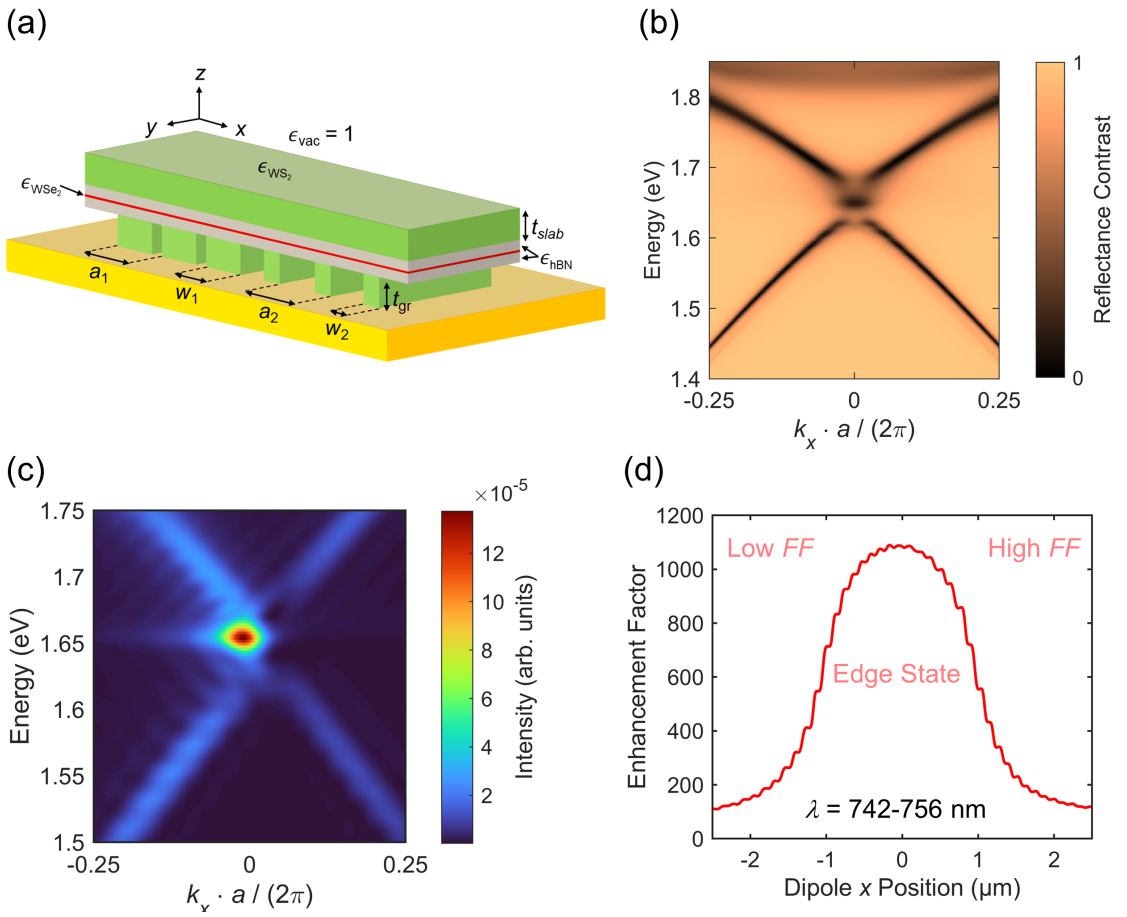


Figure 5.7: **Simulations of an active WSe_2 monolayer-integrated double grating heterostructure.** **(a)** Schematic of double grating heterostructure comprised of an hBN-encapsulated monolayer WSe_2 between a WS_2 double grating and bulk flake, all on a gold substrate. **(b)** Simulated reflectance contrast of structure from **(a)** with grating parameters $t_{gr} = 47$ nm, $a_{1,2} = 245$ and 269 nm respectively, and $FF_{1,2} = 0.81$ and 0.41 respectively. $t_{slab} = 41$ nm, with both hBN spacers of thickness 5 nm each, and WSe_2 modelled as 1 nm thick. Edge state still observable but with less prominence than in the passive double inverted grating structures. **(c)** Angle-resolved emission intensity of a dipole placed at the interface between the two gratings within the monolayer in simulation. Clear coupling to the edge state is observed with strong enhancement of directivity around 1.65 eV. Emission is also coupled to the grating guided modes but with five times weaker output intensity. **(d)** Calculated overall enhancement factor of emission from a 2 μm diameter measurement spot on the grating heterostructure, compared to the same structure but with bulk WS_2 replacing both gratings as a reference. Signal also integrated over the edge state energy between 742-756 nm, predicting a potential enhancement of over 1000.

The final set of simulations involved calculating an overall enhancement factor of the dipolar emission depending on its position along the direction perpendicular to the grating axis, as presented in Figure 5.7 (d). Here, $x = 0$ represents the interface between the high and low FF gratings, and corresponds to the highest enhancement of 1090. The enhancement is calculated in a similar way to in Section 4.4 for nanoantennas, by taking into account three factors

$$EF(x) = \int_{\lambda_1}^{\lambda_2} \left[\frac{\sum_{x'=x-r}^{x+r} |\boldsymbol{E}(\lambda, x')|^2 \cdot P_{\text{hs}}(\lambda, x') \cdot \eta_{\text{hs}}(\lambda, x')}{\sum_{x'=x-r}^{x+r} |\boldsymbol{E}_0(\lambda, x')|^2 \cdot P_{\text{ref}}(\lambda, x') \cdot \eta_{\text{ref}}(\lambda, x')} \right] \mathrm{d}\lambda. \tag{5.3}$$

The first factor is the electric field intensity $|\boldsymbol{E}(\lambda, x')|^2$ compared to that of the incident illumination $|\boldsymbol{E}_0(\lambda, x')|^2$, at the z position of the monolayer with respect to both wavelength and x position. This is the same calculation as presented in Figure 5.6 (c), and accounts for the excitation rate enhancement an emitter will experience at each point owing to the field confinement. The next factor is composed of the total power emitted in all directions of a dipole within the monolayer of the double grating heterostructure $P_{\text{hs}}(\lambda, x')$, over the total power of a dipole within a reference structure $P_{\text{ref}}(\lambda, x')$. The reference structure is the same as the grating heterostructure, but with the two gratings replaced by bulk WS_2. This gives a reference measurement for emission from the monolayer without any effects of the grating modes, and is the same as for the experimental results I will present later, where sections of WS_2 were left unetched for this purpose. This second term of Equation 5.3 therefore measures the radiative rate enhancement of the emitter due to the grating modes at each point in x over a range of λ. This can be attributed to the Purcell effect, where the local photonic environment around the emitter has an effect on its radiative rate. The final term takes into account the directivity of the emission. This is composed of the directivity of an emitter at a given x position within the grating heterostructure $\eta_{\text{hs}}(\lambda, x')$, compared to a dipole in the reference structure $\eta_{\text{ref}}(\lambda, x')$. To calculate each $\eta(\lambda, x')$, I integrated angle-resolved intensities, as from Figure 5.7 (c), over a range of wave vectors corresponding to a half-angle of $\theta = 44°$, in order to mimic the numerical aperture of our Fourier setup objective lens ($NA = 0.7$). This was repeated for each dipole x position. To further recreate what would be measured in experiment, I took a moving sum over x of the numerator and denominator of Equation 5.3 separately, thus mimicking the signal acquired from a finite-sized collection spot. I considered a spot diameter of $d = 2$ µm as would be used experimentally in the Fourier PL setup detailed in Section 3.5.3, and therefore summed the signal from the grating heterostructure between $x - r$ and $x + r$, where $r = d/2$ is the spot radius, before dividing by the same moving sum for the reference structure. This process leads to the smoothing of oscillations seen in Figure 5.7 (d), as the three factors of Equation 5.3 vary significantly with x across a single grating period. Finally, I integrated over a range of wavelengths $\lambda_{1,2} = 742$ and 756 nm respectively, to obtain an overall enhancement factor focusing only on emission coupled to the edge state. This figure of merit is similar to that of the nanoantennas calculated via Equation 4.3, however here the reference dipole is situated within an experimentally measurable structure, rather than the ideal case of being isolated in vacuum. The results presented in Figure 5.7 (d) therefore show a potential three orders of magnitude increase in measured WSe_2 photoluminescence from the heterostructure directly owing to coupling with a Jackiw-Rebbi state.

5.4.2 Fabrication of Double Grating Heterostructure

Fabrication of the double grating heterostructure was the main obstacle of achieving coupling of monolayer PL to the Jackiw-Rebbi edge state, owing to the complexity of the structure. I began

in the same way as detailed previously in Section 5.3.1, by patterning and etching a range of bulk WS_2 flakes on gold into alternating high and low filling factor gratings. Note that the patterns were adjusted in filling factor and period to produce an edge state at the WSe_2 emission energy of 1.65 eV, whilst also accounting for the band gap reduction induced by the addition of 10 nm of hBN total. As with the previous double inverted grating structures, I performed a quality check by measuring the angle-resolved RC of the single etched gratings using the Fourier setup from Section 3.5.2, and comparing to simulation using measured parameters from AFM and SEM. This enabled me to decide on the gratings most likely able to produce a Jackiw-Rebbi edge state after transfer of the top layers. I then performed a top flake thickness calibration, this time also taking into account the effects of a 1 nm monolayer WSe_2 with 5 nm hBN on either side, between the grating and top flake in simulation. I decided to use an etched flake of thickness $t_{gr} = 69$ nm, as this is still below 100 nm and so will not be affected by Fabry–Perot modes, but also because the flake was very large in lateral size, at $\sim 100 \times 200$ µm. This meant that the full grating pattern from Section 5.3.1 could be etched around two and a half times into a single flake, therefore greatly increasing the chance of achieving an edge state by transferring the top layers across multiple pairs of gratings with varied parameters. This etched flake can be seen in Figure 5.8 (b), with the electron beam patterning dose increasing down each column (i.e. decreasing filling factor), and the grating period varied along each row.

To build the heterostructure, I first exfoliated hBN onto PMMA-coated silicon substrates using the technique explained in Section 3.2.2, thus producing a variety of hBN flakes with different thicknesses and lateral sizes. I searched only for very thin flakes based on their transparency, and discounted any that were smaller than $\sim$ 50 µm in lateral size. I then scanned the selected flakes using AFM and calculated precise thicknesses, keeping those of $\sim$ 5 nm or less. I found a cluster of three large hBN flakes covering a total area of $\sim$ 100 $\times$ 50 µm, as shown in Figure 5.8 (a), which was the largest area coverage I found throughout my exfoliations. The large lateral size combined with a 6 nm thickness made it ideal as a bottom hBN spacer, so that as many grating pairs as possible could be covered from the beginning. During the transfer, I found the hBN tended to adhere very strongly to the PMMA, thus presenting difficulties in detaching the flake from the PMMA onto to the gratings. This is likely due to the fact that the gratings have less surface area for the hBN to adhere to, compared to full contact with the PMMA. I therefore chose to melt the PMMA membrane onto the substrate as described in Section 3.2.6, with the hBN flake positioned across as many ideal gratings as possible. After cooling, the PMMA was then dissolved with acetone, before an IPA rinse then O_2-plasma cleaning of the sample to remove any stubborn debris. The result was a clean transfer of all three flakes as shown in Figure 5.8 (b), where the hBN is outlined in purple and is almost completely transparent.

For the next layer, I exfoliated WSe_2 onto PDMS until I found a monolayer large enough to cover several grating pairs. Here, PDMS was used owing to its favourable viscoelastic properties, leading to reliable, large monolayer exfoliation of $\sim$ 50 µm in lateral size. In addition, chemical solvents like acetone and IPA should not be used in direct contact with monolayer TMDs as they cause significant charge transfer, thus quenching PL emission. Since PDMS is less strongly adhesive than PMMA, I was able to perform an all-dry transfer, as detailed in Section 3.2.6, stacking the

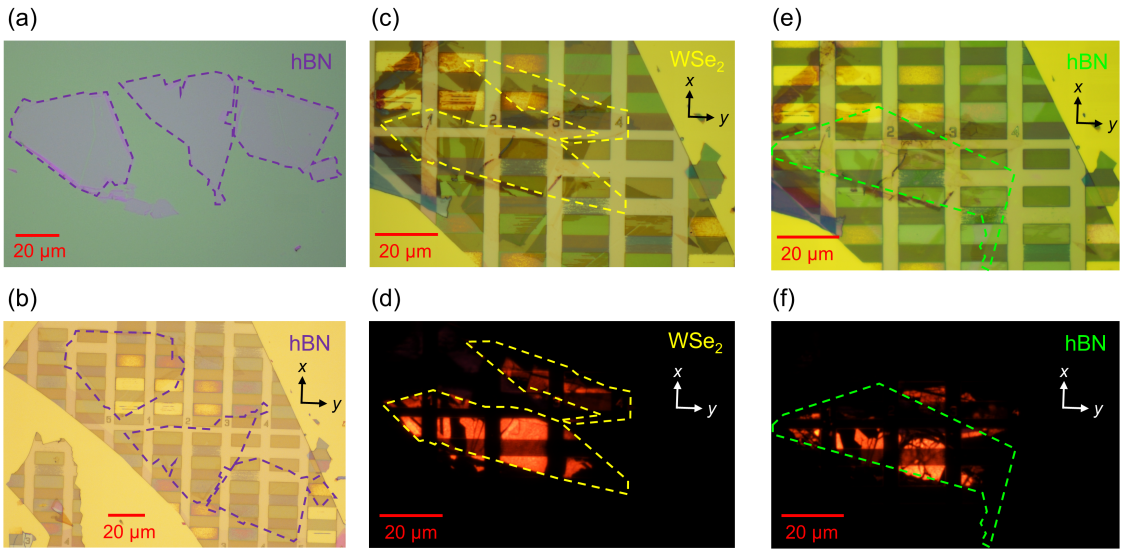


Figure 5.8: **Images of grating heterostructure fabrication after transfer of encapsulated monolayer WSe_2. (a)** Optical microscope image of hBN flakes of thickness 6 nm on PMMA-coated silicon substrate. Flakes outlined with purple dashed line are used as the bottom hBN spacer. **(b)** Resulting transfer of bottom hBN spacer onto double grating-patterned WS_2 of thickness 69 nm. Thin hBN is almost completely transparent when transferred onto the gratings so is again outlined in purple. **(c)** Resulting transfer of WSe_2 monolayer as outlined by the dashed yellow lines. Some cracks occurred during transfer, and thicker parts of the flake attached to the monolayer were also transferred, visible to the left of the monolayer outlines. **(d)** Photoluminescence image taken with an optical microscope of the now grating-hBN-monolayer structure from **(c)**. Emission mostly uniform, with dark areas corresponding to the cracked regions. **(e)** Resulting transfer of top hBN spacer as outlined by the green dashed line. **(f)** Photoluminescence image of the grating-hBN-monolayer-hBN structure from **(e)**. Additional cracks formed as a result of difficulties during transfer, however PL is still bright with regions large enough to measure.

monolayer onto the grating-hBN structure without any quenching of PL due to solvents. The resulting structure is shown in Figure 5.8 (c), with the monolayer outlined in yellow. Some additional multilayer WSe_2 attached to the monolayer was also transferred, visible outside to the left of the dashed yellow line. Also, several cracks can be seen in the monolayer, which is common for this kind of lift-off transfer, caused by random changes in the speed of PDMS detachment during lift-off. This occurs due to the arbitrary shape and size of the materials beneath the PDMS, especially thick flakes or contamination in the vicinity of the gratings which cause the polymer stamp to not sit completely flat to the substrate. The resulting PL microscope image is presented in Figure 5.8 (d), and shows bright, mostly uniform emission across multiple gratings. This proves that the hBN between the monolayer and grating is adequately insulating the WSe_2 from any charge transfer.

The next step was to encapsulate the monolayer with a top hBN spacer as outlined in green in Figure 5.8 (e). This time I used a thinner hBN flake of 3 nm with a lateral size slightly larger than the monolayer WSe_2 for complete encapsulation. After placing down the PMMA membrane with the hBN positioned over the desired grating, I attempted to lift off the PMMA to leave behind the hBN. Unfortunately, the strong adhesion to the PMMA meant that the hBN did not transfer, and actively picked up the monolayer and some of the bottom hBN spacer below. I then continued by using the same method as for the bottom hBN, by melting the PMMA followed by solvent washing,

thus placing all three layers of encapsulated WSe_2 back onto the gratings. However, during the failed lift-off process the monolayer WSe_2, and likely some of the hBN, cracked further. When placing the layers back down, the substrate had shifted by a small amount (< 1 µm), and so the transferred layers did not sit completely flat as they were previously, thus leading to the formation of wrinkles. This is visible in the photoluminescence image presented in Figure 5.8 (f), where the PL is significantly more fragmented than before the top hBN transfer in Figure 5.8 (d). However, despite the cracks and wrinkles, there were still uniform areas large enough for measurement with a spot size of 2 µm as used in the home-built Fourier PL setup.

The final step in fabricating the double grating heterostructure was to cap the grating-hBN-monolayer-hBN structure with bulk WS_2 of the correct thickness. I exfoliated bulk WS_2 on PMMA-coated silicon, and chose a flake of thickness 32 nm, as calculated from thickness calibration RC simulations. I then performed the final transfer using the PMMA melt and wash technique with the results shown in Figure 5.9 (a). Here the top WS_2 is outlined in blue, and the monolayer in yellow for reference. Since the top flake is still very thin compared to the lateral size, the wrinkles beneath can be clearly seen causing bulges in the WS_2. A photoluminescence image is shown in Figure 5.9 (b), where PL is still visible from within the heterostructure. The emission is dimmer than before the transfer, as can be seen via comparison to the brighter PL region near the top of the image that is not covered by the transferred WS_2. Previous to this sample, I fabricated a grating heterostructure with monolayer WSe_2 between a WS_2 grating and top flake without hBN encapsulation. In the microscope PL image there was no discernible emission, even on the maximum exposure setting of 60 s, owing to strong charge transfer between the monolayer and bulk WS_2, thus causing complete quenching of the PL. For reference, the PL image in Figure 5.9 (b) was taken using 10 s exposure, therefore confirming that the WSe_2 monolayer is well encapsulated. Importantly, the PL is observed to be brighter along a horizontal line in the centre of the white dotted box. This coincides exactly with the interface between the high and low FF gratings as denoted by the light blue arrow, thus giving an early indication of the presence of edge state-coupling even in this simple microscope image.

5.4.3 Fourier Photoluminescence

To first prove the existence of a Jackiw-Rebbi edge state in the fabricated double grating heterostructure, I performed angle-resolved reflectance contrast measurements as done on all previous samples. I measured each grating covered by the top WS_2 (blue dotted line) and encapsulated monolayer WSe_2 (yellow dotted line) shown in Figure 5.9 (a), with the best result (i.e. most closely aligned band gaps of the high and low FF gratings) presented in Figure 5.9 (c). This data was acquired from the white dotted region from Figure 5.9 (b), covering a pair of high and low FF gratings and the interface between the two. The corresponding periods and filling factors were $a_{1,2} = 271$ and 310 nm, and $FF_{1,2} = 0.61$ and 0.22 respectively, as extracted from SEM images. A clear resonance is visible within the band gap, in agreement with previous angle-resolved RC results of the double inverted gratings, therefore proving that Jackiw-Rebbi edge states can still exist in the modified double grating heterostructure system. In addition, the edge state lies at the required WSe_2 emission energy of ~ 1.65 eV, hence I observed some slight blurring of the resonance peak

owing to weak coupling with the WSe_2 direct exciton in agreement with the simulations presented in Figure 5.7 (b). This coupling is also likely the reason why the edge state is not positioned exactly in the centre of the band gap in energy, as was the case for previous structures without an active layer.

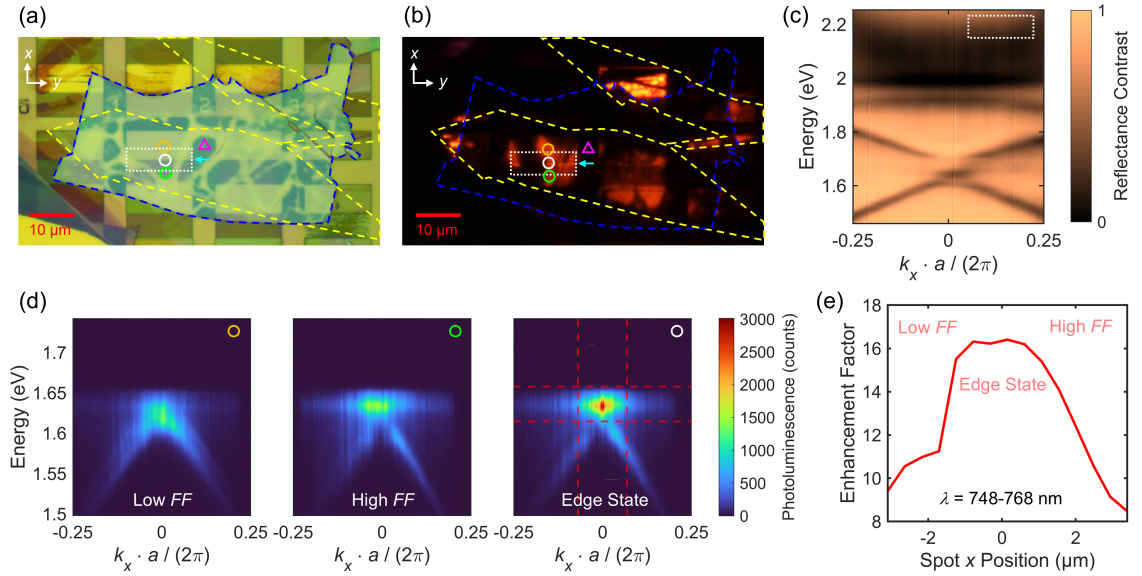


Figure 5.9: **Experimental angle-resolved characterisation of active WSe_2-coupled double grating heterostructure.** **(a)** Optical microscope image of the grating heterostructure in standard bright field mode. Blue dashed line indicates the edge of the top WS_2 flake with thickness 32 nm. Monolayer WSe_2 position outlined in yellow, encapsulated in hBN between the grating and top flake. Alternating high and low FF gratings with thickness 69 nm can be seen through the heterostructure as the base layer, with grating axis along the horizontal direction. Grating parameters: $a_{1,2} = 271$ and 310 nm, $FF_{1,2} = 0.61$ and 0.22 respectively. Wrinkles can be seen owing to the multiple transfers performed. White dotted box outlines the Fourier RC measurement region with high and low FF grating interface denoted by the light blue arrow. Orange and green circles mark the Fourier PL measurement spots for the low and high FF gratings respectively. White circle marks the grating interface PL measurement spot. Pink triangle marks reference PL measurement spot on area of heterostructure with unetched WS_2 beneath the monolayer. **(b)** Photoluminescence image taken through an optical microscope for the same region as in **(a)**. Cracks in the monolayer that occurred during the transfer process can be seen as the dips in PL intensity. PL enhancement observed within the white dotted box horizontally across the grating boundary as denoted by the light blue arrow. **(c)** Angle-resolved reflectance contrast taken from the white measurement region of **(b)**, confirming the presence of a Jackiw-Rebbi edge state within the band gap. **(d)** Angle-resolved photoluminescence measurements taken from the circle regions of corresponding colour. Left and centre panels taken from the low and high FF gratings individually, and show coupling to grating modes with moderate enhancement. Right panel corresponds to PL taken from the interface between the two gratings, showing the strongest enhancement owing to coupling to the edge state. Red dashed lines correspond to integration region for enhancement factor calculations. **(e)** Overall PL enhancement factor due to coupling with the edge state as a function of position perpendicular to the grating axis. Signal integrated over wavelengths 748-768 nm to consider only the edge state. Enhancement peaks at 16 around $x = 0$, corresponding to the interface between the high and low FF gratings.

I then modified the home-built Fourier setup to use a continuous wave 637 nm laser for excitation of the WSe_2 monolayer exciton. Using a 700 nm short-pass filter in the excitation path, and

700 nm long-pass filter in the collection path (setup described in more detail in Section 3.5.3), I measured the angle-resolved photoluminescence from different regions of the double grating heterostructure as shown in Figure 5.9 (d). The left and centre panels correspond to data collected from the low and high FF gratings respectively, as indicated by the orange and green circles in Figure 5.9 (a). The PL is clearly enhanced by the resonances of each grating, showing dispersions in k-space following the mode structures measured through angle-resolved RC. This time however, rather than measuring a dip in signal as the modes propagate light away in-plane as is done with RC, the PL measurements show peaks in intensity associated with the WSe_2 monolayer exciton emitting into the grating modes, and coupling out to the objective lens. In the left panel, the low FF grating has a lossy mode on the lower energy branch, and so the monolayer emission couples into that channel, following the parabolic dispersion. Moderate enhancement of the PL is observed around $k_x = 0$ with a peak of 1491 counts, indicating that the emission from the low FF grating is more directional perpendicular to the substrate plane. In the centre panel, the high FF grating has a BIC on the lower energy branch. This is apparent in the angle-resolved PL, where a dip is clearly observed at $k_x = 0$, in contrast to the low FF grating. Here, the light emitted from the WSe_2 monolayer couples directly into the (quasi) BIC, and hence very little light can escape to the far-field. PL enhancement is also observed at the WSe_2 exciton energy of 1.65 eV. I attribute this to contributions from the edge state, which was in close spatial proximity and thus difficult to filter out. In the rightmost panel there is strong enhancement of the PL at 1.65 eV and $k_x = 0$, showing very good agreement with the previous angle-resolved FDTD simulation from Figure 5.7 (c). In addition, since this measurement was taken at the interface between the high and low FF gratings (white circle region), and shows a peak at the same energy as the edge state measured in angle-resolved RC from Figure 5.9 (c), I attribute this enhancement directly to coupling with the Jackiw-Rebbi edge state. I measured a maximum of 3008 counts, twice that of the lossy mode, therefore proving that topological Jackiw-Rebbi edge states can enhance coupled emitters more strongly than standard lossy grating modes alone, whilst also steering such emission into a highly directional beam.

As with the emission enhancement simulations from Figure 5.7 (d), I calculated an experimental photoluminescence enhancement factor at points along a line between the orange and green circles in Figures 5.9 (a) and (b), crossing the high and low FF grating interface. To do this, I took Fourier PL spectra at each point, as well as a reference measurement marked by the pink triangle. Note that the spot size was the same for both the grating and reference measurements, the triangle is used for easy distinction. The reference region contains unetched WS_2 as a base, with the top layers of hBN-encapsulated monolayer WSe_2 and bulk WS_2 top slab remaining the same. This served as a reference point since there is no effect of grating modes on the monolayer emission, and so the Fourier PL signal was uniform across k_x. For each measurement spot across the gratings, I integrated the PL over the region surrounding the edge state in both normalised wave vector (± 0.07) and energy (1.61-1.66 eV), as depicted by the red dashed lines in the rightmost panel of Figure 5.9 (d). I then did the same for the reference measurement, before dividing the integrated PL at each spot position by the integrated reference PL to get an overall enhancement factor. The results are presented in Figure 5.9 (e), showing a clear peak around $x = 0$ corresponding to the inter-

face between the high and low FF gratings. The form of the enhancement factor curve agrees well with previous simulations from Figure 5.7 (d), albeit with lower magnitude as is expected from any non-perfect experimental system. This result shows that the Jackiw-Rebbi edge state in this double grating heterostructure can enhance monolayer WSe_2 PL emission by over 16 times in experiment, therefore highlighting potential applications in increasing output from quantum emitter systems.

5.5 Conclusion

In this chapter I investigated photonic resonances and topological phenomena within 1D periodic grating nanostructures made from layered van der Waals materials. I began by setting the context behind this work in the broader scheme of advancing control of light-matter interactions at the nanoscale, ultimately pushing towards on-chip photonic computing. To explore this field, I started from the ground up, first considering the optimal choice of substrate for the grating devices in question. Gold was the natural choice owing to its high reflectivity, thus giving clear, strong signal from fabricated nanostructures whilst avoiding any interference from substrate modes, such as Fabry–Perot resonances present in SiO_2/Si substrates. I confirmed this by performing simulations of a WS_2 grating structure on gold and SiO_2/Si, calculating both the photonic band structure and reflectance contrast using FDTD and RCWA respectively, showing perfect agreement between the two. Good agreement with theory was also found, with the grating diffractive modes showing typical parabolic dispersions in k-space, as well as strong coupling and thus an energy gap at $k_x = 0$, with a lossy mode and symmetry-protected BIC on the upper and lower energy branches respectively.

After deciding on the gold substrate, I then ran large parameter sweeps over the grating period, thickness, and filling factor in RCWA simulations, to visualise their effects on the mode structure for TE polarisation. All three parameters cause shifting of the photonic modes in energy, however more importantly, the filling factor controls the size of the energy gap via tuning of the mode coupling strength. I found that no combination of grating parameters could fully close the band gap since the refractive index of WS_2 is so high. Closing and reopening of the band gap was needed in order to change the fundamental topology of the energy bands, thus leading to the possibility of creating exotic topological edge states. To overcome this problem, I reduced the effective refractive index contrast between the high and low index sections of the grating by adding a bulk WS_2 slab on top in simulation. This inverted grating structure immediately reduced the size of the band gap, meaning that I was able to close and reopen the gap through tuning of the filling factor. I then simulated two gratings placed adjacent to each other along the direction perpendicular to the grating axis, i.e. the x axis. Crucially, one grating hosted a BIC on the upper energy branch (low FF), whilst the other showed a BIC on the lower energy branch (high FF). This yielded a topological photonic Jackiw-Rebbi edge state as predicted by theory. The edge state manifested at the centre of the band gap, and was highly localised in both energy and wave vector, indicating a high quality factor resonance with inherent strongly directional emission.

Following my previous simulations suggesting the potential existence of a Jackiw-Rebbi edge state in double inverted gratings on gold, I began to fabricate such structures through standard

nanofabrication techniques, including mechanical exfoliation, EBL patterning, RIE etching, and flake transfer. By varying the EBL dosage and period of the pattern, I was able to obtain multiple pairs of gratings with different parameters on each WS_2 base flake. This way, at least one pair would have aligned band gaps and thus be able to produce an edge state for any flake thickness between 30-70 nm. After fabrication of the grating layer with a reliable etching recipe, I comprehensively characterised each grating through AFM, SEM, and angle-resolved RC. This enabled me to compare the fabricated gratings to simulation, and perform a top flake thickness calibration for the best chance of achieving an edge state. I then exfoliated and transferred an unpatterned WS_2 flake of the calibrated thickness onto as many grating pairs as possible to finish the structure. This three-step fabrication process of grating production, calibration, then top layer transfer, proved to be crucial for the repeatability of realising structures hosting Jackiw-Rebbi edge states, where as long as the high and low FF band gaps were aligned in energy, an edge state would always be observed. I proved the existence of the edge state in double inverted gratings in experiment through subsequent Fourier RC measurement, with excellent agreement to previous simulations. By first measuring each grating separately using a variable rectangular aperture to only take signal from one region, I demonstrated the ability to achieve photonic band inversion through tuning of the filling factor. I then measured across the interface of both gratings, yielding a clear new resonance in the centre of the band gap, not visible when measuring gratings individually. This is one of the first experimental realisations of the photonic Jackiw-Rebbi edge state in such structures, offering a highly versatile platform for the characterisation of exotic topological phenomena. The edge state was strongly localised in energy with a 6 meV linewidth, whilst also exhibiting an angular bandwidth of 7° with respect to k_x, therefore proving the highly directional nature of the Jackiw-Rebbi edge state in experiment. To fully characterise the dispersion of the edge state in reciprocal space, I also measured the angle-resolved RC with respect to k_y, i.e. parallel to the grating axis. I fitted each mode (lossy, BIC, and edge state) with a Lorentzian, and plotted the peak positions in energy against $k_{x,y}$ on a 3D plot, with colour corresponding to the mode linewidths. Whilst I observed strong localisation of the edge state in k_x, along k_y the mode linewidth remained unchanged across the whole measurement range ($\pm 44°$), and simply shifted parabolically owing to the constant refractive index parallel to the grating axis. This allows for highly selective angles of in- and out-coupling, with a large range in k_y but a very narrow range in k_x.

After characterising the far-field response of the inverted gratings, I investigated the spatial distribution of the lossy mode, BIC, and edge state in the near-field through simulations of the electric field intensity. I observed characteristic symmetric and anti-symmetric field distributions about the grating unit cell for the lossy mode and BIC respectively in single inverted gratings. The symmetric lossy mode was able to couple to the continuum and plane waves can be seen radiating away from the structure in the simulations. The BIC shows the opposite behaviour owing to the field anti-symmetry, where the mode remains completely localised within and around the structure, hence leading to an infinite quality factor. The field distribution of the edge state, however, was highly localised to the boundary between the adjacent high and low FF gratings. I also calculated an order of magnitude stronger electric field confinement of the edge state compared to the lossy mode and BIC, at over 600 times that of the incident wave, indicating possible uses in Purcell

enhancement of weak quantum emitters. By fitting an exponential to the average electric field profile for each side of the grating interface, I extracted a total spatial confinement of the edge state of 1.45 μm in the x direction. As with the dispersions in $k_{x,y}$, the edge state extends along the full length of the grating interface in the y direction, but shows strong confinement in x. In the following chapter, I will investigate the near-field of the Jackiw-Rebbi edge state in experiment through scattering-type SNOM.

The final periodic structure I considered included the addition of an hBN-encapsulated WSe_2 monolayer sandwiched between the WS_2 grating layer and top flake, in order to turn the previous passive devices into active emitters. I named the new device a double grating heterostructure, and began by simulating the corresponding reflectance contrast spectrum, whilst tuning the grating parameters to achieve a Jackiw-Rebbi edge state at the same energy as the WSe_2 direct band gap emission, i.e. 1.65 eV. With both hBN spacers ~ 5 nm or less, I was able to reproduce the edge state in simulation, which already showed some weak coupling with the WSe_2 exciton. From this, I simulated a dipole emitter embedded within the monolayer WSe_2 in TE polarisation, in order to mimic photoluminescence emission. I then measured the angle-resolved far-field intensity, and observed clear enhancement of the emission around 1.65 eV and $k_x = 0$ corresponding to edge state-coupled emission. To quantify this enhancement, I simulated the dipole moving in small steps from the low FF grating, across the boundary, and into the high FF grating region. At each point, I extracted the electric field confinement and Purcell enhancement, along with the far-field directivity as a percentage of light that would be collected by the objective lens of our home-built Fourier setup with NA $= 0.7$. I then multiplied these factors together and summed over a 2 μm spot size as in experiment, before integrating over a small wavelength range around the edge state. Dividing this value at each dipole x position by the same measurement for a dipole in a reference heterostructure with unetched bottom WS_2, I calculated the overall PL enhancement factor as a figure of merit. Both the high and low FF gratings alone showed a potential PL enhancement of ~ 100, whereas at the boundary between the gratings where the Jackiw-Rebbi edge state is localised, the enhancement could reach an order of magnitude higher at over 1000.

The main difficulty was to then fabricate such a complex structure. I used the same fabrication techniques as with the passive double inverted gratings, ensuring that the monolayer transfer step involved no solvents to avoid any charge transfer. After the four transfers, the monolayer PL was fragmented due to cracking and wrinkles between layers, however there were still bright regions large enough to measure in experiment. Before this however, I first measured angle-resolved RC spectra to prove the existence of an edge state in the double grating heterostructure, which showed good agreement with simulation. I then measured the angle-resolved PL from each individual grating, and subsequently at the grating interface. Clear coupling to the grating modes was observed for the individual gratings, with PL enhancement observed from the lossy mode at $k_x = 0$, and a dip in emission around the BIC as expected. The PL measurement at the grating interface showed strongly localised emission in both energy and wave vector at the wavelength where the edge state was measured in RC. To measure the overall PL enhancement, I then took measurements in a line across the grating interface as with the previous simulations. I integrated over a range of energies and wave vector encompassing the edge state for each x position, before dividing by a reference PL

measurement showing no coupling to any grating modes. From this, I calculated a maximum experimental PL enhancement of over 16 when coupled to the edge state, compared to 9 for coupling to the lossy grating mode. These results prove the viability of using the Jackiw-Rebbi edge state to couple to quantum emitters, thereby increasing light output, as well as forcing highly directional emission, not attainable with standard diffractive grating modes.

As a result of this investigation into exotic topological resonances in 1D van der Waals grating devices, I have shown that robust, high Q factor, strongly confined Jackiw-Rebbi edge states can be achieved in these structures, with a high level of precision and repeatability through the three-step fabrication process. These results also further support theoretical works on symmetry-protected BICs being topological phenomena [124, 129], showing the rich degrees of freedom and controllability possible in simple 1D systems. Furthermore, I hope to have promoted the versatility of van der Waals materials, especially TMDs, in general through this work. With other conventional semiconductors used for nanophotonics such as silicon or III-V materials, unlocking modulation in the third dimension requires intense fabrication effort. For van der Waals materials, stacking is in their nature. The inverted grating structures I presented show the ease with which these materials can be built up together, to precisely and reliably create tailored light-matter interactions for a range of applications. With future improvements in scalability, I believe van der Waals materials to be crucial for future on-chip photonic device design, with the potential of limitless combinations of stacked materials, all hosting a vast range of different optoelectronic properties and degrees of freedom.

6

Near-Field Imaging of WS_2 Nanophotonic Structures

6.1 Introduction

Scanning near-field optical microscopy (SNOM) is a powerful technique that allows circumvention of the Abbe diffraction limit [330, 331] through utilising sub-wavelength apertures. The idea was first proposed by Edward Hutchinson Synge in 1928 [332, 333], who suggested to illuminate a metal film with a 100 nm cutout, and scan the aperture over a sample at a height of 100 nm whilst collecting the scattered light. Ash and Nicholls subsequently proved this technique in experiment in 1972, achieving resolution down to 60 times smaller than the incident microwave illumination wavelength [334]. Later in 1984, Dieter Pohl *et al.* pushed near-field imaging into the visible light range, presenting the first results of a tip-based aperture-type SNOM (a-SNOM), achieving lateral resolution down to 25 nm [335]. A-SNOM works by utilising a hollow metallic tip, with light incident down the tip axis towards its aperture. The light then becomes highly confined at the aperture, and can be used to excite local near-fields that are often detected by optics in a transmission configuration. Another method is known as scattering-type SNOM (s-SNOM), and uses a solid metal tip. In this configuration, the illumination source is incident at high oblique angle to the tip axis, focused at the apex. The scattered near-fields are then detected on either side of the tip to the source, thus allowing opaque materials to be measured. S-SNOM also has the advantage of theoretically finer resolution than a-SNOM [256], along with simpler tip fabrication, therefore reducing costs and improving reliability in manufacturing. For the results presented in this chapter, I used a commercial scattering-type SNOM from neaspec. One of the main obstacles with any form of near-field probe, is isolating the small tip-sample interaction signal from the large background signal [256]. With the neaspec system, this problem is greatly reduced by interfering

the scattered signal with a reference beam reflected from an oscillating mirror. The detected signal is then demodulated at harmonics of the reference mirror oscillation frequency, and the tapping frequency of the tip, in a process known as pseudoheterodyne detection [255]. This process is described in more depth and mathematical rigour in Section 3.6.1, however the effect is to remove the overwhelming background signal that varies much less upon tip oscillation compared to the near-field signal of interest. PsHet detection also enables the phase of the scattered light from the tip-sample interaction region, with respect to the reference beam, to be measured simultaneously with the amplitude.

Owing to the strong tip-sample interaction enabled by incident illumination during s-SNOM, the scattered light inherently carries information about both the tip and the sample. A common modelling technique is to consider the apex of the tip as a point dipole, which then induces a mirror dipole in the sample below [256, 336]. The strength of this interaction, and the subsequent scattering from it, is governed by the effective polarisability of the system in the weakly interacting regime [337]. This assumes that no electric fields from other sources interact with the tip-sample region, e.g. from nanophotonic resonances. Therefore, since the material parameters of the tip are known, the polarisability, and thus the electric permittivity of the sample can be calculated at each point. By using PsHet detection to measure the relative phase of the scattered light, the sample's absorption characteristics can also be probed. S-SNOM is therefore a powerful tool for mapping complex refractive indices of samples down to $\sim$ 20 nm lateral resolution [338]. Furthermore, the tip-sample interaction region is strongly influenced by local electric fields [339]. This enables direct probing of a variety of nanoscale resonances for high-resolution characterisation of photonic devices.

For the work presented in this chapter, probing of local electric fields within and around nanophotonic resonators will be the main motivation behind using scattering SNOM. In previous literature, this technique has been used to interact with, and directly visualise phonon-polaritons in few-layer hBN [340–343], as well as surface plasmon-polaritons in graphene [344–347]. In addition, various sub-wavelength devices have been characterised through s-SNOM, including metallic nanoantennas [348, 349], topological 1D gratings [319], and chiral resonators [350], thus emphasising the versatility of near-field-probing techniques.

The first section of this chapter will be dedicated to characterising the near-field plasmonic response of hybrid modes within WS_2 nanoantennas on gold, as previously measured in the far-field in Chapter 4. I demonstrate clear SPP interference patterns, with SPPs being launched radially from each nanoantenna along the gold surface. By changing the radius and incident wavelength, I show that the nanoantenna-launched SPPs change in intensity, corresponding to the excitation of different hybrid Mie modes, as measured via dark field spectroscopy. These results give further evidence supporting the existence of highly-tunable, hybrid Mie-plasmonic modes in WS_2 nanoantennas on gold. I will then move towards measuring the near-field response of the double inverted WS_2 gratings on gold, as discussed in Chapter 5. With careful optimisation of the sample angle with respect to the incident illumination, I demonstrate the ability to simultaneously excite and probe the topological Jackiw-Rebbi edge state. The results directly prove the highly spatially localised nature of the edge state, existing only along the boundary between two gratings of opposite topologies.

The near-field maps from both nanophotonic structures therefore provide additional insight into the nature of a variety of exotic resonances, unable to be resolved via conventional far-field techniques.

6.2 Near-Field Imaging of WS_2 Nanoantennas on Gold

In this section, I will explore the near-field properties of plasmon-hybridised resonances in WS_2 nanoantennas on a gold substrate through scattering-type SNOM. I will begin with an overview of how the measurements were carried out, detailing two main methods in which surface plasmon-polaritons can be simultaneously launched and probed via a scanning tip. Following this, experimental scattering maps of several nanoantennas with different radii will be presented, highlighting the different near-field responses from each. I will then tune the incident wavelength and compare the results to previously measured far-field spectroscopy, thus demonstrating how different resonances can enhance the plasmons launched from the nanoantennas. Finally, I will prove the validity of these results by imaging low index pillars, which show significantly reduced plasmon patterns compared to high index WS_2. These results therefore complement those from Chapter 4, showing direct experimental evidence of plasmon hybridisation.

For the measurements in this section, I used a commercial neaspec s-SNOM with a tunable visible laser source as detailed in Section 3.6.1. Since the nanoantennas were symmetric, the orientation of the sample with respect to the tip and incident light had little effect on the results. I performed scans of 8×30 μm in size to cover a full array of 30 nanoantennas with different radii, each with height 41 nm, corresponding to those measured previously with dark field spectroscopy in Figure 4.7 (a). As the tip was scanned across the sample, the amplitude of the scattered light from the tip-sample interaction at each point was measured using the PsHet detection method, simultaneously allowing the phase of the signal relative to the incident light to be extracted. The near-field scattering amplitude and phase maps of three nanoantennas with different radii are presented in Figures 6.1 (a) and (b) respectively, both exhibiting circular ripples in the signal around each nanoantenna. To understand why this happens, I must first explain the different mechanisms of SPP formation and propagation in the system. In short, s-SNOM enables probing of both material optical properties and localised electric fields, such as those from SPPs [167, 351]. The ripple patterns emerge due to an interference between light incident on the probe region, and electric field contributions from tip- and nanoantenna-launched SPPs, amongst other mechanisms [167, 351–356]. As the tip is moved across the sample, the contributions to the s-SNOM signal either interfere constructively or destructively. This produces a pattern of bright and dark fringes in the amplitude and phase of the scattered light, which is observed as ripples. There are several methods by which sample-scattered light and SPPs can interact with the incident light at the tip, and each produce different interference patterns [167, 352, 354]. For the case of WS_2 nanoantennas on gold however, I consider two prominent mechanisms, the first being tip-launched SPPs. As the incident light reaches the tip (left dark blue arrow in Figure 6.1 (c)), it becomes strongly localised at the tip's apex. This strong near-field enhancement, and matching of the photon and plasmon wavevectors, causes tip-launched plasmons that emanate radially into the gold [357]. Such SPPs can then reflect from nearby structures and interfere with the incident light back at the tip as depicted by

the double-headed cyan arrow in Figure 6.1 (c). The second mechanism involves SPPs launched from the nanoantennas [357]. The right dark blue arrow in Figure 6.1 (c) represents light incident on the nanoantenna, which causes subsequent excitation of a hybrid resonance, and launching of SPPs which travel to the tip and interfere with the incoming light (cyan arrow). A combination of these two effects is thus observed in the ripple patterns in Figures 6.1 (a) and (b).

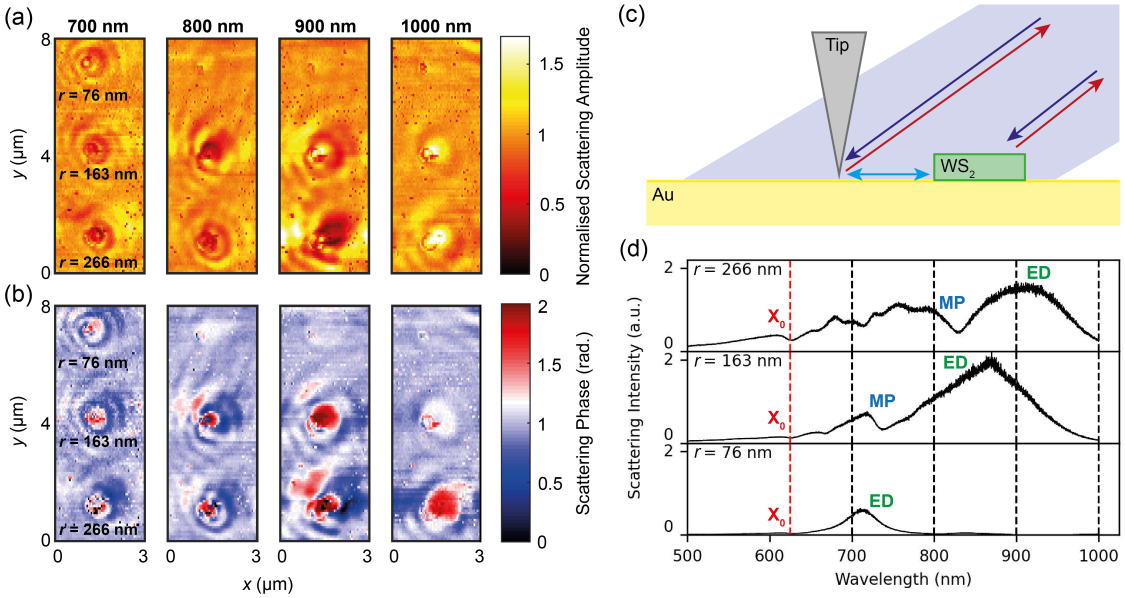


Figure 6.1: **Experimental near-field characterisation of SPPs launched from WS_2 nanoantennas on gold.** **(a)** S-SNOM scattering amplitude data for three WS_2 nanoantennas on a gold substrate for varying incident wavelengths as labelled above each panel. All data normalised to the scattering amplitude from an area of gold free from SPP effects. Nanoantenna heights are all 41 nm, with radii 76 nm (top), 163 nm (middle), and 266 nm (bottom) for comparison. **(b)** Scattering phase of same nanoantennas from **(a)** relative to the incident beam, showing the same SPP ripple patterns. **(c)** Schematic of the tip-nanoantenna interaction region during an s-SNOM measurement. Blue shaded region depicts the excitation spot. Dark blue arrows correspond to photons incident on the tip and WS_2 nanoantenna. Red arrows correspond to photons scattered from the tip and nanoantenna. Cyan double-headed arrow represents the plasmonic interaction between the nanoantenna and tip. **(d)** Normalised experimental dark field scattering intensity for the three WS_2 nanoantennas on gold from **(a)** and **(b)**. Black vertical dashed lines correspond to excitation wavelengths used in the s-SNOM measurements. Red dashed line represents the WS_2 exciton (X_0). MP and ED correspond to the Mie-plasmonic and electric dipole modes respectively.

To de-convolute the signal into contributions from individual mechanisms is beyond the scope of this thesis. However, with additional Fourier analysis of the ripples, it is possible to discern between tip- and nanoantenna-launched SPPs based on the differences in interference patterns, and thus the resulting wave vector [358]. This will be a topic for further study.

From Figures 6.1 (a) and (b), I observed that the amplitude of the SPP ripples corresponds strongly to the nanoantenna size and incident wavelength. By comparing the s-SNOM amplitude data in Figure 6.1 (a) to the dark field spectra of the same nanoantennas as in Figure 6.1 (d), there is a clear correlation between the amplitude of the SPP ripples and peaks in the respective dark field spectra. Here, I expect minimal shift in the resonances between s-SNOM and dark field

measurements since the excitation angles are comparable at 60° and 53° respectively. At shorter wavelengths, such as 700 nm, I observed the highest amplitude ripples from the smallest nanoantenna ($r = 76$ nm), followed by the $r = 163$ nm nanoantenna. This observation matches with the experimental dark field data, where a strong resonant ED mode exists at around 700 nm wavelength for the $r = 76$ nm nanoantenna, and an MP mode for the $r = 163$ nm nanoantenna. As the incident wavelength is increased to 800 nm, the $r = 76$ nm nanoantenna begins to resonate less in the s-SNOM amplitude and phase images, in agreement with the decreasing dark field response shown in Figure 6.1 (d). In contrast, the $r = 163$ nm nanoantenna shows a stronger SPP interference pattern, correlating to excitation of the ED mode. At 900 nm illumination, both the $r = 163$ and 266 nm nanoantennas exhibit strong SPP ripples, following the red-shift of the ED mode in the dark field data. Finally, at 1000 nm illumination wavelength, the amplitude of the SPP interference patterns around all of the nanoantennas is much lower, corresponding to the dip in overall scattering in the dark field spectra. These observations suggest that TMD nanoantennas on gold can both scatter light to the far-field, and couple light to SPPs detectable in the near-field. Furthermore, the launched SPPs are strongly correlated in intensity with the excitation of various Mie resonances within the nanoantennas, such as the ED and MP modes, hence providing direct evidence for the coupling between Mie and plasmonic modes.

The relative phase maps in Figure 6.1 (b) tell much the same story as the amplitude data from Figure 6.1 (a). This is because the local electric fields from the interfering SPPs dominate the near-field signal. With a non-resonant, weakly interacting sample, the amplitude and phase maps would be proportional to the real and imaginary parts of the local dielectric function respectively, hence giving information about the reflectivity and absorption at each point.

As a reference, I repeated the same s-SNOM measurements for an area of gold without nanoantennas, as well as for low index resist (CSAR 62) pillars on gold. Figures 6.2 (a) and (b) show the respective AFM and near-field scattering maps of just the gold substrate, yielding no SPP ripple patterns as expected. Small lumps and pits $\sim$ 10-20 nm in height/depth are present on the surface of the gold. The lumps show lower scattering amplitude than the surface of the gold in 6.2 (b), suggesting that the refractive index differs from the gold, and hence are likely a form of contamination. The pits have the same refractive index as the gold and are likely fabrication imperfections. During the measurement, tip-launched plasmons are still present, however they have no edges or large structures nearby to reflect back from. This means that the SPPs cannot interfere with the tip-incident light, and thus no interference patterns are seen. Upon introducing low index pillars of comparable height to the WS_2 nanoantennas measured in Figure 6.1 (a), no strong SPP patterns are observed in the near-field scattering amplitude image (Figure 6.2 (d)). The resist pillars do not support well-confined photonic modes at visible wavelengths owing to their low refractive indices ($\sim$ 1.6 [359, 360]), and so coupling to plasmons is weak. Furthermore, tip-launched plasmons are expected to transmit through such structures with very little reflection back to the tip. In Figure 6.2 (f), I present s-SNOM results for an array of low index pillars with a single high index WS_2 nanoantenna in the middle. Strong SPP ripples are observed around the nanoantenna, unlike the low index pillars. In addition, the SPP pattern is not circular, but more of a stretched ellipse. This is due to interference between the incident plane wave source, and radially-launched plasmons from

the nanoantennas, both interacting at the tip [167]. For solely tip-launched plasmon patterns, the ripple pattern would be perfectly circular. This observation therefore further supports my previous results, suggesting that only the high refractive index WS_2 nanoantennas can launch SPPs through coupling with strongly-confined, hybridised Mie resonances.

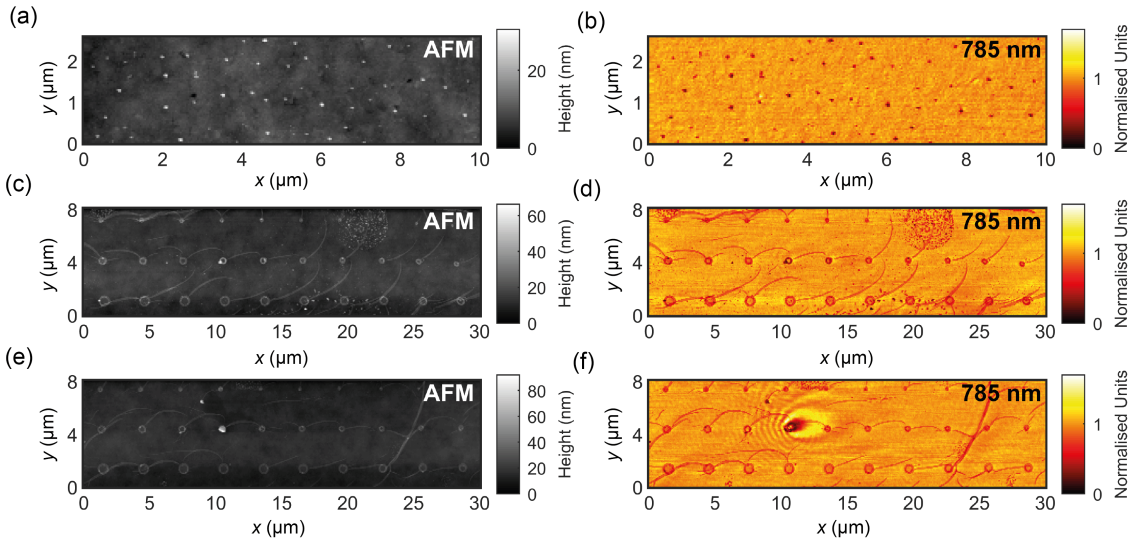


Figure 6.2: **AFM and s-SNOM amplitude images of a bare gold substrate and low index pillars on a gold substrate at** 785 **nm excitation. (a)** and **(b)** correspond to AFM and s-SNOM images of the gold substrate away from any WS_2 nanoantennas respectively. **(c)** and **(d)** correspond to AFM and s-SNOM images of low index pillars on gold of comparable height to the WS_2 nanoantennas measured in Figure 6.1 (a) respectively. **(e)** and **(f)** correspond to AFM and s-SNOM images respectively of additional low index pillars on gold with a single WS_2 nanoantenna in the middle, surrounded by a nanoantenna-launched SPP interference pattern.

It is important to note that there are several further mechanisms that may contribute to the observed SPP interference patterns, such as photon scatter from the nanoantenna edges, s-SNOM tip, and sample substrate, as well as a host of second- and higher-order mechanisms. However, given the correlation between the amplitude of the s-SNOM interference ripples and the dark field scattering data, alongside the data presented in Figure 6.2 of low-index materials on gold, it is likely that the tip- and nanoantenna-launched SPP mechanisms discussed above describe the data wholly and appropriately.

6.3 Near-Field Imaging of Jackiw-Rebbi Edge States in WS_2 Gratings on Gold

Moving on from nanoantennas now, I will switch focus to near-field imaging of WS_2 double inverted gratings on gold, specifically with the aim of probing the topological Jackiw-Rebbi edge state. I will begin with a brief overview of the s-SNOM setup, including the limitations which imposed very strict configurations for which I was able to couple to and observe the edge state. Following this, I will present near-field simulations unveiling the expected electric field distributions along the top of the grating structure, where the s-SNOM tip would be located during scanning. I then sweep the simulated wavelength, showing the change in potential field confinement

with respect to position across the high and low filling factor grating interface. Leading on from the simulations, I demonstrate the near-field distribution of the edge state through experimental s-SNOM scattering maps at a variety of incident wavelengths. These results serve to accompany the far-field characterisations presented previously in Chapter 5, giving direct evidence of the highly spatially localised nature of the Jackiw-Rebbi edge state in 1D gratings in experiment.

The same commercial neaspec s-SNOM system detailed in Section 3.6.1 was used for near-field mapping of the previously measured double inverted WS_2 gratings on gold from Figure 5.5. However, unlike with the scans of WS_2 nanoantennas, great care had to be taken with the sample orientation with respect to the incoming light. From the far-field measurements in Figure 5.5, I established that the Jackiw-Rebbi edge state has a very narrow angular bandwidth in the direction perpendicular to the grating axis (x), however can be excited throughout the full measured range of k_y. Our s-SNOM system has incident light fixed at $\sim 60°$ to the sample normal (i.e. tip axis), as shown in the top schematic of Figure 6.3 (a). This meant that the only way to directly excite the edge state with the incident light, was to orientate the sample so that the beam travelled parallel to the grating axis, i.e. along the y direction. I used the tip as a reference for this orientation, as the incoming light was known to be incident on the tip at an azimuthal angle of $\sim 45°$, as depicted in the bottom schematic of Figure 6.3 (a). To find the correct excitation wavelength for the grating sample from Figure 5.5, I had to take into account the angular dispersion in k_y that would occur due to an incident angle of $60°$ to the sample normal. I therefore fitted and extrapolated the edge state from the middle panel of Figure 5.5 (b) up to $k_y = \pm 8.5$ μm^{-1}, which corresponds to a $60°$ excitation angle from comparison to FDTD simulations. This process is shown in Figure 6.3 (b) using a quadratic fit, and yielded an estimated excitation energy of 1.68 eV, or 736 nm wavelength.

After calculating the required sample orientation and excitation wavelength, I ran FDTD simulations of the system to predict the electric field strength that would be experienced by the tip during a real s-SNOM measurement. I used a plane wave source with $60°$ excitation angle relative to normal incidence, directed along k_y (i.e. $k_x = 0$) for a range of wavelengths around 736 nm. I then extracted the electric field enhancement ($|\boldsymbol{E}^2|/|\boldsymbol{E}_0^2|$) along the top surface of the WS_2 slab, perpendicular to the grating axis. This was done to mimic the near-fields that would leak from the top surface of the structure and be probed by the scanning s-SNOM tip in this configuration, with the results plotted in Figure 6.3 (c). I observed a clear enhancement of the electric field strength, localised at the high and low FF grating interface at 737 nm incident wavelength, almost exactly as predicted by the angle-resolved RC extrapolation, thus indicative of the Jackiw-Rebbi edge state. The maximum field enhancement of the edge state was over 30, therefore an order of magnitude smaller than calculated for the fields at the same z position but with light incident $0°$ to the surface normal, as from previous simulations of the edge state in optimised structures presented in Figure 5.6 (c). This shows that whilst it is still possible to couple in and out of the edge state at very high angles parallel to the grating axis, the confinement of the mode does eventually significantly reduce, leading to more losses and hence less light output should be expected. In addition to the electric field enhancement of the edge state at $x = 0$, there is also a lesser field enhancement associated with the lossy grating modes and BICs. This is most evident looking towards the top of Figure 6.3 (c) at 755 nm incident wavelength. Here the average field strength is higher for negative

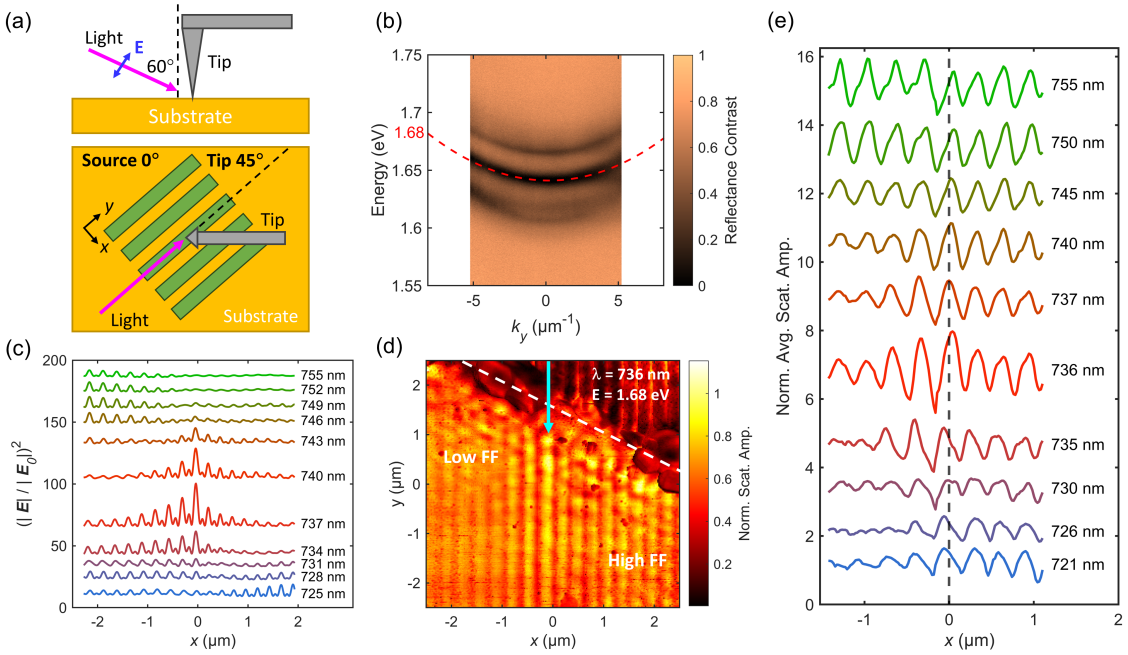


Figure 6.3: **Near-field characterisation of a topological Jackiw-Rebbi edge state in WS_2 double inverted gratings on gold. (a)** Top schematic shows side view of the s-SNOM setup with incident light depicted by the pink arrow propagating at 60° to the tip axis. Blue arrow shows polarisation direction (p-polarised) to ensure a component along the tip axis for efficient near-field excitation. Bottom schematic shows top-down view of the system with orientation of the grating parallel to the incident light to excite along the k_y direction. **(b)** Experimentally measured angle-resolved reflectance contrast with respect to k_y, as previously plotted in the middle panel of Figure 5.5 (b). Edge state fitted and extrapolated up to values of k_y corresponding to light incident at $\pm 60°$. This gives an estimated excitation energy of 1.68 eV. **(c)** Simulated electric field along the direction perpendicular to the grating axis (x direction), for z height corresponding to the top surface of the double inverted grating structure, thus mimicking the near-field enhancement experienced by a scanning tip. Incident light propagates at 60° to the surface normal to recreate the experimental setup. As wavelength is varied, clear enhancement can be seen for 737 nm wavelength (1.68 eV) at $x = 0$, i.e. the interface between the high and low FF gratings, corresponding to the edge state. A smaller enhancement is also present at higher wavelengths for negative x values (i.e. the low FF grating side) owing to the lossy grating mode. This switches to the positive x side (high FF grating) as the wavelength tunes through the edge state to lower wavelengths and excites the BIC. **(d)** Normalised experimental near-field scattering map of the double inverted gratings on gold from previous Figure 5.5 for incident wavelength 736 nm. Low and high FF gratings are to the left and right of the light blue arrow respectively, with grating axis along the y direction. Edge of the top WS_2 flake denoted by the white dashed line. Enhanced scattering from the grating modes is observed through the top flake, with the strongest scattering along the vertical line between the two gratings, indicative of the Jackiw-Rebbi edge state. **(e)**. Near-field scattering profiles averaged over y for a range of incident wavelengths. Increased scattering is observed at $x = 0$ only for 736 nm wavelength, corresponding exactly to the edge state excitation wavelength. At higher wavelengths more scattering is observed from the low FF grating (negative x) and vice versa, hence corresponding to the electric field simulations from **(c)**. The regions of lower scattering are thus linked to light trapped within a BIC.

x values than positive. The simulation was set up to have the low FF grating on the negative x side and the high FF grating on the positive x side. From previous simulations and experiments

shown in Figures 5.3 (d) and 5.5 (a), the low FF gratings host a BIC on the high energy branch and lossy mode on the low energy branch, whereas the high FF gratings show the opposite trend. This means that the larger electric field strength for negative x at 755 nm wavelength in Figure 6.3 (c) corresponds to the lossy mode of the low FF grating, and the lower electric field strength at positive x is associated with the BIC of the high FF grating. This behaviour switches when sweeping the wavelength through the edge state as the bands and associated topology inverts, leaving higher enhancement on the positive x side associated with the lossy mode of the high FF grating, and lower field strength for the BIC of the low FF grating. This may seem counter-intuitive at first since the BIC is inherently perfectly confined to the structure, however for light incident at $k_x = 0$, little to no light can actually couple into this state owing to its symmetry restrictions, thus leading to a minimum in field strength.

To characterise the double inverted gratings experimentally with s-SNOM, I inserted the sample (same as from Figure 5.5) with grating axis as close to $45°$ to the cantilever back as possible by eye. I then performed scans at 736 nm incident wavelength, making with small adjustments to the sample angle until signal from the high and low FF grating interface was maximised. After optimising the angle, I then performed a wavelength sweep in roughly 5 nm increments, increasing resolution to 1 nm steps when closer to the edge state wavelength. The full scan for 736 nm incident wavelength is presented in Figure 6.3 (d), which shows the normalised scattering intensity from the tip at each point along the sample. Here, the data is first normalised to the signal averaged over the top right corner of the image beyond the white dashed line. This corresponds to a region where no top WS_2 flake is present, and thus no grating modes are expected to be active. This normalisation will be important for comparing scans of different wavelengths, where the laser power can fluctuate. I then performed another normalisation which accounted for the two different grating structures present. Since s-SNOM works via measuring tip-sample interactions, the scattered signal is dependent upon the refractive index of the material beneath the tip at any one time. This means that the high and low FF gratings will have different baseline scattering intensities owing to different effective refractive indices. I therefore median levelled the left and right sides of the image separately, with the light blue arrow in Figure 6.3 (d) depicting the boundary between the two gratings. The s-SNOM tip also probes the local electric fields of samples. In the previous near-field characterisation of WS_2 nanoantennas on gold from Section 6.2, the s-SNOM tip acted as both an excitation source and near-field probe of surface plasmon-polaritons. However, in this case the tip acts almost entirely as a probe, directly interacting with the near-field distribution of the edge state as excited by the incident laser, and scattering such signal to the far-field for measurement. This is evident from Figure 6.3 (d), where electric field minima and maxima can be seen through the top WS_2 flake corresponding to photonic modes within the structure beneath. Most importantly, there is clear enhancement of the scattered signal at the interface between the high and low FF gratings, at exactly the wavelength predicted by previous simulations and angle-resolved reflectance contrast extrapolation for the Jackiw-Rebbi edge state.

To concisely show the wavelength dependence of the edge state, I averaged the normalised s-SNOM amplitude scans for a range of wavelengths over many rows in y, ensuring to only take rows far from the edge of the top WS_2 flake to avoid any interference effects. This interference can be

seen as weak fringes parallel to the white dashed line travelling normal to the edge for $\sim$ 1 µm, and are likely a result of edge-scattered photons interacting with the tip. Whilst interesting in its own right and important to mention, this effect is not within the scope of this study, and simply increases/decreases the scattering from the edge state due to constructive/destructive interference. After averaging the normalised signal over many rows for each wavelength, I plotted the results in Figure 6.3 (e), with the grating interface at $x = 0$. The enhancement from the Jackiw-Rebbi edge state is only visible at 736 nm incident wavelength, and dies away when changing the wavelength by just 1 nm either side. In addition, there is slight enhancement of the scattered signal from the low FF gratings (negative x) at 755 nm wavelength, which switches to the high FF side (positive x) when the wavelength is reduced to 721 nm. In contrast, there is decreased signal from the high FF grating at 755 nm wavelength, which switches to the low FF side at 721 nm wavelength. The near-field scattering maps thus agree well with the electric field simulations from Figure 6.3 (c), proving that the s-SNOM tip can successfully probe the grating lossy mode, BIC, and topological edge state. These results further confirm the highly localised nature of the Jackiw-Rebbi edge state in both energy and real space, as well as demonstrating the power of near-field mapping techniques that can see well beyond the diffraction limit compared to standard far-field spectroscopy.

6.4 Conclusion

In this final experimental chapter, I investigated the near-field properties of exotic photonic resonances in both WS_2 nanoantennas, and double inverted gratings on gold, using cutting edge s-SNOM techniques. This enabled me to probe the optical response of each structure beyond the diffraction limit and into the deep sub-wavelength range, thus providing new insight not attainable with conventional far-field spectroscopy as considered in the previous two chapters. I began by outlining the basic working principles of s-SNOM, followed by seminal work using this technique to probe and image nanophotonic devices. I then presented near-field scattering maps of the fabricated WS_2 nanoantennas on gold from Chapter 4, exploring the change in signal upon varying nanoantenna radius and tuning incident wavelength. I discovered that the nanoantenna-launched SPP intensities were strongly correlated to resonances within the nanoantenna, following the redshift of the modes upon increasing nanoantenna radii in far-field scattering spectroscopy. The hybrid Mie modes can therefore couple to the far-field as measured with dark field spectroscopy, and produce SPPs detectable in the near-field with s-SNOM imaging. I verified this by mapping low index pillars on gold without confined Mie resonances as a comparison, which exhibited negligible plasmonic response as opposed to the WS_2 nanoantennas. These results complement the far-field analysis well, providing further evidence for coupling between Mie and plasmonic modes, whilst also highlighting the power of s-SNOM in probing the optical performance of devices on the nanoscale.

I then switched focus to near-field mapping of double inverted WS_2 gratings on gold, with the aim to specifically probe the Jackiw-Rebbi edge state. I first explained the s-SNOM configuration needed for this type of structure, with the incident light propagating parallel to the grating axis. This enabled coupling to the edge state at high angle to the surface normal, whilst also having the

required polarisation along the grating axis. I then extrapolated previous angle-resolved reflectance contrast data to estimate the wavelength needed to excite the edge state at high angle of incidence. Further FDTD simulations of the electric field intensity at the tip position under high angle of incidence excitation, showed strong confinement at the high and low filling factor grating interface at the predicted wavelength, indicative of the edge state. Following this, I performed experimental s-SNOM scans of a fabricated structure at the predicted edge state wavelength of 736 nm, and observed clear enhancement of the scattering along the boundary between the two gratings. Finally, by sweeping the incident wavelength, I showing that this spatially localised enhancement was only present at 736 nm, thus proving its origin as the topological Jackiw-Rebbi edge state. These results not only supported the previous observations of Jackiw-Rebbi edge states in double inverted gratings in far-field spectroscopy, but also provided direct evidence of the highly spatially localised nature of the state, hosted only along the interface between the two gratings of opposite topologies.

The results in this chapter primarily serve to accompany the characterisations performed in Chapters 4 and 5, by improving the understanding of the near-field response of different photonic resonances beyond the diffraction limit in experiment. As such, the applications of the WS_2 nanoantennas and gratings remain the same as discussed previously, broadly contributing to the advanced control of light-matter interactions for easily integrable on-chip photonics. This chapter also establishes the utility of near-field imaging techniques for nanophotonics, where one could see applications in probing nanoscale phenomena, not resolvable with conventional far-field spectroscopy. Combine this with the ever-expanding list of other scanning probe techniques such as conductive AFM, AFM-IR, and kelvin probe force microscopy, and comprehensive characterisation of almost any device is possible down to tens of nanometers resolution.

7

Conclusion

In this thesis, I have comprehensively characterised the resonant responses of several different van der Waals material-based nanostructures, with the view of integration towards versatile, robust, hybrid electro-photonic circuitry. I took an extensive approach, beginning with mathematical theory of a variety of resonances within WS_2 nanoantennas and grating structures in order to aid with design. I subsequently performed rigorous simulations over large parameter sweeps for precise optimisation of each device, before utilising the inherent attractive forces of van der Waals materials to build complex structures on metallic substrates. This was done with relative ease compared to fabrication of other conventional dielectrics such as III-V materials, which require advanced molecular beam epitaxy with careful lattice matching. I then used a range of experimental far- and near-field characterisation techniques, yielding excellent agreement of all the fabricated structures with both theory and simulation. I believe the key results summarised below raise the profile of van der Waals nanophotonics, highlighting clear advantages over conventional dielectric systems such as silicon photonics, with huge potential for advanced, on-chip light control.

7.1 Summary of Research

I began this work with a thorough description of the theory behind transition metal dichalcogenides in Chapter 2, covering their distinct optoelectronic properties arising from the layered nature of such crystals. This allows TMDs to be integrable onto almost any substrate or device, creating near limitless combinations for realisation of complex heterostructure. High refractive indices combined with low losses throughout much of the visible wavelength range, make TMDs ideal candidates for deep sub-wavelength light confinement in multi-layer structures. Furthermore, simple conversion into active devices is possible through the addition of monolayers, yielding strong direct band gap emission from high oscillator strength excitons. In order to provide a basis for un-

derstanding optical resonances within such structures, I then covered the fundamental Maxwell's equations governing light propagation within different media. From this, analytical solutions to Maxwell's equations were discussed in the form of Mie resonances for waves on the surface of a conducting metal nanosphere, also applicable to dielectrics. The different multipolar contributions can then produce more complex phenomena such as scattering suppression under the destructive interference effect of the anapole condition. I further provided mathematical descriptions of simple Fabry–Perot modes, as well as the possibility of coupling photonic resonances to excitons, thus yielding exciton-polaritons. Optically inaccessible modes in non-periodic structures named Friedrich-Wintgen bound states in the continuum were then introduced, which are true eigenstates of a given system hence differentiating them from anapoles. Through matrix eigenvalue equations, I showed that BICs are not able to couple light in or out, hence yielding a theoretically infinite quality factor with no losses. Such high quality factor states were then discussed in terms of increasing the Purcell factor of coupled emitters, leading to an increased spontaneous emission rate compared to the same emitter in vacuum. I then outlined the theory behind plasmonic resonances using the Drude-Lorentz model, including explanation of the formation of surface plasmon-polaritons in metallic nanostructures.

Following the overview of resonances in non-periodic nanostructures, I then focused on providing the necessary background for understanding photonic modes in 1D periodic photonic crystals such as gratings. Simple treatment of two counter-propagating waveguide modes in a slab was first considered, before introducing a periodic modulation of the refractive index, resulting in a band folding of the modes into the first Brillouin zone. Through use of an appropriate Hamiltonian, diffractive coupling was then added between the two modes, resulting in an anti-crossing at zero wave vector. By solving the corresponding matrix eigenvalue problem, I showed how symmetry-protected BICs can exist within the gratings, possessing inherent topological properties. To fully describe this phenomenon, I began with an introduction to topology in its most basic form, describing global invariant geometrical parameters such as the number of holes, or genus, of an object. Then, applying similar logic, I detailed the discovery of topological insulators, able to host highly robust conducting edge states at boundaries between materials of different topologies. As with the correlation between electronic and photonic band structures, photonic crystals can also be described by topological invariants, hence the birth of topological photonics. Focusing back on symmetry-protected BICs, I then explained the process of changing band topologies through closing and re-opening of the photonic band gap. By then combining two photonic crystals of differing topologies, a robust Jackiw-Rebbi edge state must exist along the boundary between the two structures. Finishing the theory chapter, I described the principles behind two different simulations techniques used extensively throughout this thesis, finite-difference time-domain, and rigorous coupled-wave analysis.

In Chapter 3, I provided a detailed account of all the fabrication, simulation, and experimental characterisation methods used throughout my research projects. In terms of fabrication, I first described the substrate preparation and subsequent mechanical exfoliation process for a range of van der Waals materials on different substrates. This included WS_2 on gold, hBN on PMMA, and WSe_2 on PDMS. I gave a brief overview of flake searching and selection, before detailing the procedure

for patterning and etching of chosen flakes into nanostructures of arbitrary shapes, using electron beam lithography and reactive ion etching respectively. The transfer process of layered materials was then reported, where I used two different techniques depending on the material. A suspended PMMA membrane facilitated the transfer of bulk WS_2 and few-layer hBN, whereas a PDMS stamp on glass was used for transfer of monolayer WSe_2. I then explained the setup behind each different type of simulation performed for the work in this thesis. I began with simple scattering simulations from nanoantennas using the FDTD method, outlining the type of source used and monitor parameters required to collect only the scattered light, for identification of different resonances over a range of wavelengths. Electric field monitors were also used to give further insight into the nature of modes within both nanoantennas and grating structures. I then switched the plane wave source to a dipole for calculation of the Purcell factor and associated directivity at different points within and around both structures, giving an overall expected enhancement factor. Focusing solely on grating simulations, I then detailed the setup behind band structure and reflectance contrast calculations over a range of wave vector space perpendicular to the grating axis. This enabled full modal characterisation of both periodic single gratings, and non-periodic double adjacent grating structures. I also explained how I implemented RCWA techniques through an open-source Python module S^4, for more efficient modelling of the reflectance contrast from single grating structures, thus enabling quick optimisation sweeps. After describing the simulation methods, I then outlined the experimental far-field spectroscopy setups I used for characterisation of the fabricated nanostructures. This included dark field spectroscopy for measuring the light scattered from WS_2 nanoantenna resonances, along with angle-resolved reflectance contrast and photoluminescence of WS_2 gratings and grating heterostructures via Fourier spectroscopy. I then finished with a description of the near-field probing technique s-SNOM, including details of background signal removal through a pseudoheterodyne interferometric detection regime.

I began discussion of my experimental work in Chapter 4, focusing on fully characterising the plethora of resonances hosted within hexagonal WS_2 nanoantennas on a gold substrate. By performing rigorous multipole expansions of the fields associated with an illuminated nanoantenna suspended in vacuum, I was able to assign individual Mie modes to corresponding peaks in the scattering spectra. Then, using a long wavelength approximation, I identified anapole conditions leading to suppression of scattering. With the dielectric resonances all accounted for, I subsequently moved the nanoantenna incrementally towards a gold substrate in simulation. This enabled clear and systematic visualisation of the dramatic effect of a metal substrate on the mode structure. The existing Mie resonances became sharper in linewidth, whilst new Fano-shaped features appeared in the spectra when the nanoantenna was positioned ~ 5 nm away from the gold, identified as hybrid Mie-plasmonic modes. By studying the electric field profiles of each mode, clear hybridisation with the plasmon continuum at the nanoantenna-gold interface was seen for the MP mode. Following the simulations, I then fabricated WS_2 nanoantennas on gold with a range of heights and radii. The structures yielded excellent agreement via dark field scattering spectroscopy measurements, hosting MP modes with quality factors 33 times higher than for Mie modes in purely dielectric WS_2 nanoantennas on SiO_2 [21]. By increasing the nanoantenna height, additional Fabry–Perot resonances were unveiled, also showing coupling to plasmons in the gold. I

then tuned these Fabry–Perot-plasmonic modes into resonance with Mie modes around the higher-order anapole condition, where a clear anti-crossing between the two was observed. By fitting to a coupled oscillator model, I proved strong coupling with a Rabi splitting of 48 ± 5 meV. I also observed signatures of a highly confined supercavity mode, with a measured experimental quality factor of 263 ± 28 at the point of minimum energy splitting. I found clear agreement with simulation, and further calculated the electric field distribution of the supercavity mode and surrounding resonances. Finally, I simulated a WS_2 nanoantenna atop a 5 nm hBN spacer on gold, with a dipole source inside the hBN to model a single photon emitter. I calculated an electric field confinement of over 2600 within the spacer, a Purcell factor of 713 for polarisation normal to the substrate, and directivity up to 50%, leading to an overall potential emission enhancement of over 10^7. These results highlight applications of TMD nanoantenna-based structures in on-chip enhancement of weak single photon sources for quantum computing; as directional scattering and coupling elements; for optical cloaking through BICs; as well as being a basis for exploring a range of strong, exotic light-matter interactions.

In Chapter 5, I switched focus to periodic grating structures fabricated from WS_2 amongst other van der Waals materials. As with the nanoantennas work, I first began with rigorous simulations of WS_2 gratings on gold over a range of parameters using the RCWA method. I varied the thickness, grating period, and filling factor to clearly demonstrate the tunability of the band structure, exhibiting strong coupling at zero wave vector with a symmetry-protected BIC on one energy branch, and a lossy mode on the other as predicted by theory. I then tuned the gratings via the filling factor and period to achieve photonic band inversion, only made possible by the addition of a WS_2 slab on top of the gratings, owing to reduction of the overall effective refractive index contrast. Since the photonic band gap must close and re-open in order to invert the bands and switch the BIC from one energy branch to the other, the inherent topology of the high and low energy BICs must change through this transition. To prove the opposite topologies of the two different inverted gratings, I simulated the two structures placed adjacent to one another using FDTD, and observed a clear edge-localised state along the boundary between the two structures. This state manifested at the centre of the photonic band gap in the calculated reflectance contrast spectra at $k_x = 0$, existing only when the two gratings were brought together. I therefore attributed this phenomena to topological effects, agreeing strongly with theory and simulations in literature on Jackiw-Rebbi edge states [37, 232]. I further fabricated such WS_2 double inverted gratings on gold using a PMMA transfer technique for the top slab, and observed excellent agreement with my simulations. I measured the Jackiw-Rebbi edge state to be strongly localised in energy with an experimental linewidth of 6 meV, as well as being highly directional with a 7° angular emission bandwidth in k_x, i.e. the direction perpendicular to the grating axis. In addition, I characterised the reflectance contrast throughout k_y, showing a parabolic dispersion of the edge state and grating modes. The edge state was also reliable to produce in multiple structures, and highly robust to fabrication defects, further highlighting its topological nature. To illustrate the real space confinement of each mode present in the structure, I simulated the electric field profiles in a slice through the x, z plane for various incident wavelengths. I calculated a field confinement of over 600 times that of the incident wave for the Jackiw-Rebbi edge state at the grating boundary, with a spatial

profile extending just 1.45 μm along the direction perpendicular to the grating interface, hence highlighting the highly spatially localised nature of this topological state. To move towards applications, I then modelled an active device, composed of a double inverted grating structure with an hBN-encapsulated monolayer WSe_2 sandwiched between the grating and top WS_2 slab. Through simulation, I used a dipole emitter to mimic the photoluminescence emission of the monolayer, and observed coupling to the Jackiw-Rebbi edge state with highly directional emission, and up to 1000 times enhancement compared to monolayer PL without the grating. To prove the coupling in experiment, I first fabricated the five-layer double grating heterostructure using two different transfer methods, before measuring the angle-resolved reflectance contrast and photoluminescence. In agreement with the simulations, I observed coupling of the WSe_2 excitonic emission to the edge state, with enhanced directional emission at the boundary between the two gratings up to 16 times stronger than from uncoupled monolayer PL. These results further emphasize the versatility of van der Waals materials in building complex heterostructures via simple transfers, without the need for expensive and difficult fabrication methods such as molecular beam epitaxy. The topological nature of the Jackiw-Rebbi edge state also adds additional degrees of freedom for highly robust, advanced light manipulation in micron-scale optical circuits.

To conclude my experimental work, I presented near-field characterisations of both the WS_2 nanoantennas and double inverted gratings on gold in Chapter 6, using scattering-type scanning near-field optical microscopy. For the nanoantennas, I mapped three structures of the same height but different radii over several incident wavelengths, observing interference patterns characteristic of nanoantenna-launched surface plasmon-polaritons on the surface of the gold. These formed elliptical ripples around each nanoantenna in both the scattering amplitude and phase, with different intensities depending on the nanoantenna. By tuning the incident wavelength, the SPP intensities also changed, with strong correlation to resonances identified previously in dark field spectra. Further scans of low index pillars on gold revealed negligible SPP response, confirming that only the high index WS_2 nanoantennas can launch tailored SPPs coupled to the resonances excited within. I then performed s-SNOM scans of a WS_2 double inverted grating on gold, previously shown to host a Jackiw-Rebbi edge state in far-field measurements. By sweeping the incident wavelength and accounting for the energy shift owing to the inherent high excitation angle of the s-SNOM system, I observed enhancement of the scattered near-field amplitude along the boundary between the two adjacent gratings, at precisely the predicted edge state energy. These results provided direct evidence of the highly spatially localised nature of the Jackiw-Rebbi edge state, whilst highlighting the deep sub-wavelength lateral resolution possible through s-SNOM, also able to probe tens of nanometers into the surface of devices. Scanning probe techniques therefore provide additional characterisation potential simply not possible with conventional far-field spectroscopy, hence improving physical understanding of nanoscale interactions and devices, for pushing the leading edge of nanophotonic control.

7.2 Future Perspective

I hope that with the results presented in this thesis, I have convinced the reader of the extensive utility and versatility of the lesser known family of van der Waals materials for nanophotonics, not as rivals, but as accomplices to conventional silicon-based devices. Key advantages stem from their inherent attractive forces allowing construction of an arbitrary number of stacked layers using a simple metal arm on a movable stage. Furthermore, the diverse range of such layered materials with different optoelectronic properties further add to the library of structures that can be realised, from conducting graphene sheets, to isolating hBN; high index TMDs with a range of transparency windows and excitonic properties, to magnetic materials such as $MnPSe_3$; as well as 2D piezo- and ferroelectric materials, with the list ever-expanding. It would be extremely limiting to constrain photonic circuitry to a single material, and so to me, it seems clear that van der Waals materials can provide adaptable support when specific properties are required. One example for further research could be to realise the WS_2 nanoantennas on gold with an hBN spacer containing single photon emitting defects as explored in simulation as part of Chapter 4. Here, I envisage strong enhancement of the SPEs and directivity tailoring to be possible, thus improving the performance for use within quantum computing, without needing GaAs quantum dot or quantum well structures which require significant fabrication effort. Furthermore, nanoantennas could be grouped together in the hundreds to form complex metasurfaces, with a range of applications including nanoholography [361–365], on-chip micro spectrometry [137, 366], directional lasing [220, 367], and beam-shaping [362, 368] just to name a few.

Given additional time, a more rigorous analysis of the surface plasmon-polariton interference patterns as presented in Section 6.2 would aid in understanding the different mechanisms of plasmon interactions available with high index WS_2 nanoantennas on gold. Via two-dimensional Fourier transforms of the near-field scattering and phase maps around each nanoantenna, information on the SPP wave vector and energy can be extracted. From this, the individual contributions to the overall signal from various scattering mechanisms such as nanoantenna- and tip-launched SPPs, as well as edge-scattered photons could then be determined for a more comprehensive account of the near-field response.

For periodic structures such as gratings, one way in which the system could yield additional functionality is by stacking two gratings of different periods to form a moiré supercell. The larger unit cell would imprint macroscopic patterns in the optical response of the device, thus able to induce strongly correlated quantum states [369, 370]. Furthermore, the ability to manipulate photonic band structures to produce exotic zero group velocity flat bands [369, 371], presents potential applications in achieving structural slow light for advanced control over signal processing [372]. Additional degrees of freedom such as a twist angle between devices, or adding a periodic width perturbation between neighbouring grating wires could yield further controllability for realising both trivial and topological photonic states. By then fabricating such devices from non-linear van der Waals materials such as 3R-MoS_2 [373], the hosted resonances could be used directly to enhance second harmonic generation with potential for tunable lasing.

Complementary to conventional photonics, topological photonics is currently gaining a great

deal of traction owing to the inherent robustness to defects [37], as well as providing additional degrees of freedom for versatile light-matter control. Future direction in this field could consist of complex photonic waveguide networks, with built-in unidirectionality and thus increased efficiency due to back-reflection immunity [38, 229]. The field is still in its infancy and thus huge untapped potential may lay ahead, with current advancements already promising significant leaps forward for photonic computing. As the production of fully operational quantum computers grows nearer, the transition towards more efficient and adaptable all-photonic, or perhaps at least hybrid electro-photonic chips, is becoming more of a reality. As such, the work in this thesis serves to promote the potential of van der Waals nanophotonics, with far-reaching and diverse applications from simple-to-fabricate structures and devices.

References

[1] Novoselov, K.S., Geim, A.K., Morozov, S.V., Jiang, D., Zhang, Y., Dubonos, S.V., Grigorieva, I.V., and Firsov, A.A. Electric field effect in atomically thin carbon films. *Science*, **306**(5696):666–669, (2004).

[2] Novoselov, K.S., Jiang, D., Schedin, F., Booth, T.J., Khotkevich, V.V., Morozov, S.V., and Geim, A.K. Two-dimensional atomic crystals. *Proceedings of the National Academy of Sciences*, **102**(30):10451–10453, (2005).

[3] Qiu, D., Gong, C., Wang, S., Zhang, M., Yang, C., Wang, X., and Xiong, J. Recent advances in 2D superconductors. *Advanced Materials*, **33**(18):2006124, (2021).

[4] Novoselov, K.S., Mishchenko, A., Carvalho, A., and Castro Neto, A.H. 2D materials and van der Waals heterostructures. *Science*, **353**(6298):aac9439, (2016).

[5] Xia, F., Wang, H., Xiao, D., Dubey, M., and Ramasubramaniam, A. Two-dimensional material nanophotonics. *Nature Photonics*, **8**(12):899–907, (2014).

[6] Cui, C., Xue, F., Hu, W.J., and Li, L.J. Two-dimensional materials with piezoelectric and ferroelectric functionalities. *npj 2D Materials and Applications*, **2**(1):18, (2018).

[7] Khriachtchev, L. *Silicon Nanophotonics: Basic Principles, Present Status, and Perspectives*. CRC Press, (2016).

[8] Margalit, N., Xiang, C., Bowers, S.M., Bjorlin, A., Blum, R., and Bowers, J.E. Perspective on the future of silicon photonics and electronics. *Applied Physics Letters*, **118**(22):220501, (2021).

[9] Yang, K.Y., Shirpurkar, C., White, A.D., Zang, J., Chang, L., Ashtiani, F., Guidry, M.A., Lukin, D.M., Pericherla, S.V., Yang, J., *et al.* Multi-dimensional data transmission using inverse-designed silicon photonics and microcombs. *Nature Communications*, **13**(1):7862, (2022).

[10] Zhao, S., Lian, D., Chen, J., Dai, D., and Shi, Y. Polarization multiplexing silicon photonic optical phased array with a wide scanning range. *Optics Letters*, **48**(23):6092–6095, (2023).

[11] Su, Y., Zhang, Y., Qiu, C., Guo, X., and Sun, L. Silicon photonic platform for passive waveguide devices: materials, fabrication, and applications. *Advanced Materials Technologies*, **5**(8):1901153, (2020).

[12] Rahim, A., Hermans, A., Wohlfeil, B., Petousi, D., Kuyken, B., Van Thourhout, D., and Baets, R. Taking silicon photonics modulators to a higher performance level: state-of-the-art and a review of new technologies. *Advanced Photonics*, **3**(2):024003–024003, (2021).

[13] Mu, X., Wu, S., Cheng, L., and Fu, H. Edge couplers in silicon photonic integrated circuits: a review. *Applied Sciences*, **10**(4):1538, (2020).

[14] Cheng, L., Mao, S., Li, Z., Han, Y., and Fu, H. Grating couplers on silicon photonics: design principles, emerging trends and practical issues. *Micromachines*, **11**(7):666, (2020).

[15] Samusenko, A., Hamedan, V., Pucker, G., Ghulinyan, M., Ficorella, F., Guider, R., Gandolfi, D., and Pavesi, L. Integrated silicon photodetector for lab-on-chip sensor platform. In *2015 XVIII AISEM Annual Conference*, pages 1–4. IEEE, (2015).

[16] De Vita, C., Toso, F., Pruiti, N.G., Klitis, C., Ferrari, G., Sorel, M., Melloni, A., and Morichetti, F. Amorphous-silicon visible-light detector integrated on silicon nitride waveguides. *Optics Letters*, **47**(10):2598–2601, (2022).

[17] Siew, S.Y., Li, B., Gao, F., Zheng, H.Y., Zhang, W., Guo, P., Xie, S.W., Song, A., Dong, B., Luo, L.W., *et al.* Review of silicon photonics technology and platform development. *Journal of Lightwave Technology*, **39**(13):4374–4389, (2021).

[18] Pelucchi, E., Fagas, G., Aharonovich, I., Englund, D., Figueroa, E., Gong, Q., Hannes, H., Liu, J., Lu, C.Y., Matsuda, N., *et al.* The potential and global outlook of integrated photonics for quantum technologies. *Nature Reviews Physics*, **4**(3):194–208, (2022).

[19] Shekhar, S., Bogaerts, W., Chrostowski, L., Bowers, J.E., Hochberg, M., Soref, R., and Shastri, B.J. Roadmapping the next generation of silicon photonics. *Nature Communications*, **15**(1):751, (2024).

[20] Liu, C.h., Zheng, J., Chen, Y., Fryett, T., and Majumdar, A. Van der Waals materials integrated nanophotonic devices. *Optical Materials Express*, **9**(2):384–399, (2019).

[21] Zotev, P.G., Wang, Y., Andres-Penares, D., Severs-Millard, T., Randerson, S., Hu, X., Sortino, L., Louca, C., Brotons-Gisbert, M., Huq, T., *et al.* Van der Waals materials for applications in nanophotonics. *Laser & Photonics Reviews*, **17**(8):2200957, (2023).

[22] Raj, V., Haggren, T., Wong, W.W., Tan, H.H., and Jagadish, C. Topical review: pathways toward cost-effective single-junction III–V solar cells. *Journal of Physics D: Applied Physics*, **55**(14):143002, (2021).

[23] Vyas, K., Espinosa, D.H., Hutama, D., Jain, S.K., Mahjoub, R., Mobini, E., Awan, K.M., Lundeen, J., and Dolgaleva, K. Group III-V semiconductors as promising nonlinear integrated photonic platforms. *Advances in Physics: X*, **7**(1):2097020, (2022).

[24] Sortino, L., Zotev, P.G., Phillips, C.L., Brash, A.J., Cambiasso, J., Marensi, E., Fox, A.M., Maier, S.A., Sapienza, R., and Tartakovskii, A.I. Bright single photon emitters with enhanced quantum efficiency in a two-dimensional semiconductor coupled with dielectric nano-antennas. *Nature Communications*, **12**(1):1–9, (2021).

[25] Zotev, P.G., Randerson, S.A., Hu, X., Wang, Y., and Tartakovskii, A.I. Single photon emitters in monolayer semiconductors coupled to transition metal dichalcogenide nanoantennas on silica and gold substrates. *arXiv preprint, arXiv:2408.01070*, (2024).

[26] Ermolaev, G., Grudinin, D., Voronin, K., Vyshnevyy, A., Arsenin, A., and Volkov, V. Van der Waals materials for subdiffractional light guidance. *Photonics*, **9**(10):744, (2022).

[27] Vyshnevyy, A.A., Ermolaev, G.A., Grudinin, D.V., Voronin, K.V., Kharichkin, I., Mazitov, A., Kruglov, I.A., Yakubovsky, D.I., Mishra, P., Kirtaev, R.V., *et al.* Van der Waals materials for overcoming fundamental limitations in photonic integrated circuitry. *Nano Letters*, **23** (17):8057–8064, (2023).

[28] Gan, X., Englund, D., Van Thourhout, D., and Zhao, J. 2D materials-enabled optical modulators: from visible to terahertz spectral range. *Applied Physics Reviews*, **9**(2), (2022).

[29] Kang, J., Rakheja, S., and Zhu, W. Reconfigurable transistors based on van der Waals heterostructures. *MRS Advances*, **8**(14):773–779, (2023).

[30] Lopez-Sanchez, O., Lembke, D., Kayci, M., Radenovic, A., and Kis, A. Ultrasensitive photodetectors based on monolayer MoS_2. *Nature Nanotechnology*, **8**(7):497–501, (2013).

[31] Taffelli, A., Dirè, S., Quaranta, A., and Pancheri, L. MoS_2 based photodetectors: a review. *Sensors*, **21**(8):2758, (2021).

[32] Li, X., Aftab, S., Hussain, S., Kabir, F., Al-Sehemi, A.G., Aslam, M., Kim, J.H., and Goud, B.S. Progress in photodetector devices utilizing transition metal dichalcogenides. *Journal of Materials Chemistry C*, **12**(4):1211–1232, (2024).

[33] Haldane, F.D.M. and Raghu, S. Possible realization of directional optical waveguides in photonic crystals with broken time-reversal symmetry. *Physical Review Letters*, **100**(1): 013904, (2008).

[34] Raghu, S. and Haldane, F.D.M. Analogs of quantum-Hall-effect edge states in photonic crystals. *Physical Review A—Atomic, Molecular, and Optical Physics*, **78**(3):033834, (2008).

[35] Klitzing, K.V., Dorda, G., and Pepper, M. New method for high-accuracy determination of the fine-structure constant based on quantized Hall resistance. *Physical Review Letters*, **45** (6):494, (1980).

[36] Wang, Z., Chong, Y., Joannopoulos, J.D., and Soljačić, M. Observation of unidirectional backscattering-immune topological electromagnetic states. *Nature*, **461**(7265):772–775, (2009).

[37] Lee, K.Y., Yoo, K.W., Choi, Y., Kim, G., Cheon, S., Yoon, J.W., and Song, S.H. Topological guided-mode resonances at non-hermitian nanophotonic interfaces. *Nanophotonics*, **10**(7): 1853–1860, (2021).

[38] Lan, Z., Chen, M.L., Gao, F., Zhang, S., and Wei, E. A brief review of topological photonics in one, two, and three dimensions. *Reviews in Physics*, **9**:100076, (2022).

[39] Khanikaev, A.B. and Alù, A. Topological photonics: robustness and beyond. *Nature Communications*, **15**(1):931, (2024).

[40] Mansha, S. and Chong, Y.D. Robust edge states in amorphous gyromagnetic photonic lattices. *Physical Review B*, **96**(12):121405, (2017).

[41] Yang, B., Zhang, H., Shi, Q., Wu, T., Ma, Y., Lv, Z., Xiao, X., Dong, R., Yan, X., and Zhang, X. Details of the topological state transition induced by gradually increased disorder in photonic Chern insulators. *Optics Express*, **28**(21):31487–31498, (2020).

[42] Wong, S., Saba, M., Hess, O., and Oh, S.S. Gapless unidirectional photonic transport using all-dielectric kagome lattices. *Physical Review Research*, **2**(1):012011, (2020).

[43] Nussbaum, E., Sauer, E., and Hughes, S. Inverse design of broadband and lossless topological photonic crystal waveguide modes. *Optics Letters*, **46**(7):1732–1735, (2021).

[44] Huang, X., Liu, C., and Zhou, P. 2D semiconductors for specific electronic applications: from device to system. *npj 2D Materials and Applications*, **6**(1):51, (2022).

[45] Molaei, M.J., Younas, M., and Rezakazemi, M. A comprehensive review on recent advances in two-dimensional (2D) hexagonal boron nitride. *ACS Applied Electronic Materials*, **3**(12): 5165–5187, (2021).

[46] Wang, T., Park, M., Yu, Q., Zhang, J., and Yang, Y. Stability and synthesis of 2D metals and alloys: a review. *Materials Today Advances*, **8**:100092, (2020).

[47] Fox, M. *Optical Properties of Solids*, volume 3. Oxford university press, (2010).

[48] Böer, K.W. and Pohl, U.W. *Semiconductor Physics*. Springer, (2023).

[49] Bromley, R., Murray, R.B., and Yoffe, A.D. The band structures of some transition metal dichalcogenides. III. group VIA: trigonal prism materials. *Journal of Physics C: Solid State Physics*, **5**(7):759, (1972).

[50] Mak, K.F. and Shan, J. Photonics and optoelectronics of 2D semiconductor transition metal dichalcogenides. *Nature Photonics*, **10**(4):216–226, (2016).

[51] Choudhury, T.H., Zhang, X., Al Balushi, Z.Y., Chubarov, M., and Redwing, J.M. Epitaxial growth of two-dimensional layered transition metal dichalcogenides. *Annual Review of Materials Research*, **50**(1):155–177, (2020).

[52] Zhang, R., Koutsos, V., and Cheung, R. Elastic properties of suspended multilayer WSe_2. *Applied Physics Letters*, **108**(4), (2016).

[53] Sortino, L., Brooks, M., Zotev, P.G., Genco, A., Cambiasso, J., Mignuzzi, S., Maier, S.A., Burkard, G., Sapienza, R., and Tartakovskii, A.I. Dielectric nanoantennas for strain engineering in atomically thin two-dimensional semiconductors. *ACS Photonics*, **7**(9):2413–2422, (2020).

[54] Papageorgiou, D.G., Dong, M., Zhang, H., Liu, M., and Young, R.J. Mechanical properties of transition metal dichalcogenides: towards high-performance polymer nanocomposites. *2D Materials*, **12**(1):012002, (2024).

[55] Li, Y., Kuang, G., Jiao, Z., Yao, L., and Duan, R. Recent progress on the mechanical exfoliation of 2D transition metal dichalcogenides. *Materials Research Express*, **9**(12):122001, (2022).

[56] Wang, Q.H., Kalantar-Zadeh, K., Kis, A., Coleman, J.N., and Strano, M.S. Electronics and optoelectronics of two-dimensional transition metal dichalcogenides. *Nature Nanotechnology*, **7**(11):699–712, (2012).

[57] Van Baren, J., Ye, G., Yan, J.A., Ye, Z., Rezaie, P., Yu, P., Liu, Z., He, R., and Lui, C.H. Stacking-dependent interlayer phonons in 3R and 2H MoS_2. *2D Materials*, **6**(2):025022, (2019).

[58] Bloch, F. Über die quantenmechanik der elektronen in kristallgittern. *Zeitschrift für Physik*, **52**(7):555–600, (1929).

[59] Splendiani, A., Sun, L., Zhang, Y., Li, T., Kim, J., Chim, C.Y., Galli, G., and Wang, F. Emerging photoluminescence in monolayer MoS_2. *Nano Letters*, **10**(4):1271–1275, (2010).

[60] Mak, K.F., Lee, C., Hone, J., Shan, J., and Heinz, T.F. Atomically thin MoS_2: a new direct-gap semiconductor. *Physical Review Letters*, **105**(13):136805, (2010).

[61] Sun, Y., Wang, D., and Shuai, Z. Indirect-to-direct band gap crossover in few-layer transition metal dichalcogenides: a theoretical prediction. *The Journal of Physical Chemistry C*, **120**(38):21866–21870, (2016).

[62] Kormányos, A., Burkard, G., Gmitra, M., Fabian, J., Zólyomi, V., Drummond, N.D., and Fal'ko, V. k·p theory for two-dimensional transition metal dichalcogenide semiconductors. *2D Materials*, **2**(2):022001, (2015).

[63] Chang, C.H., Fan, X., Lin, S.H., and Kuo, J.L. Orbital analysis of electronic structure and phonon dispersion in MoS_2, $MoSe_2$, WS_2, and WSe_2 monolayers under strain. *Physical Review B—Condensed Matter and Materials Physics*, **88**(19):195420, (2013).

[64] Silva-Guillén, J.Á., San-Jose, P., and Roldán, R. Electronic band structure of transition metal dichalcogenides from ab initio and Slater–Koster tight-binding model. *Applied Sciences*, **6**(10):284, (2016).

[65] Wannier, G.H. The structure of electronic excitation levels in insulating crystals. *Physical Review*, **52**(3):191, (1937).

[66] Yu, H., Cui, X., Xu, X., and Yao, W. Valley excitons in two-dimensional semiconductors. *National Science Review*, **2**(1):57–70, (2015).

[67] Dziobek-Garrett, R. and Kempa, T.J. Excitons at the interface of 2D TMDs and molecular semiconductors. *The Journal of Chemical Physics*, **160**(20):200902, (2024).

[68] Frenkel, J. On the transformation of light into heat in solids. I. *Physical Review*, **37**(1):17, (1931).

[69] Hwang, J., Zhang, C., Kim, Y.S., Wallace, R.M., and Cho, K. Giant renormalization of dopant impurity levels in 2D semiconductor MoS_2. *Scientific Reports*, **10**(1):4938, (2020).

[70] Molina-Sánchez, A., Sangalli, D., Hummer, K., Marini, A., and Wirtz, L. Effect of spin-orbit interaction on the optical spectra of single-layer, double-layer, and bulk MoS_2. *Physical Review B—Condensed Matter and Materials Physics*, **88**(4):045412, (2013).

[71] Cheiwchanchamnangij, T. and Lambrecht, W.R. Quasiparticle band structure calculation of monolayer, bilayer, and bulk MoS_2. *Physical Review B—Condensed Matter and Materials Physics*, **85**(20):205302, (2012).

[72] Wang, G., Chernikov, A., Glazov, M.M., Heinz, T.F., Marie, X., Amand, T., and Urbaszek, B. Colloquium: excitons in atomically thin transition metal dichalcogenides. *Reviews of Modern Physics*, **90**(2):021001, (2018).

[73] Kośmider, K., González, J.W., and Fernández-Rossier, J. Large spin splitting in the conduction band of transition metal dichalcogenide monolayers. *Physical Review B*, **88**(24): 245436, (2013).

[74] Malic, E., Selig, M., Feierabend, M., Brem, S., Christiansen, D., Wendler, F., Knorr, A., and Berghäuser, G. Dark excitons in transition metal dichalcogenides. *Physical Review Materials*, **2**(1):014002, (2018).

[75] Wang, G., Robert, C., Glazov, M.M., Cadiz, F., Courtade, E., Amand, T., Lagarde, D., Taniguchi, T., Watanabe, K., Urbaszek, B., *et al.* In-plane propagation of light in transition metal dichalcogenide monolayers: optical selection rules. *Physical Review Letters*, **119**(4): 047401, (2017).

[76] Robert, C., Amand, T., Cadiz, F., Lagarde, D., Courtade, E., Manca, M., Taniguchi, T., Watanabe, K., Urbaszek, B., and Marie, X. Fine structure and lifetime of dark excitons in transition metal dichalcogenide monolayers. *Physical Review B*, **96**(15):155423, (2017).

[77] Feierabend, M., Brem, S., and Malic, E. Optical fingerprint of bright and dark localized excitonic states in atomically thin 2D materials. *Physical Chemistry Chemical Physics*, **21** (47):26077–26083, (2019).

[78] Xiao, D., Liu, G.B., Feng, W., Xu, X., and Yao, W. Coupled spin and valley physics in monolayers of MoS_2 and other group-VI dichalcogenides. *Physical Review Letters*, **108** (19):196802, (2012).

[79] Cao, T., Wang, G., Han, W., Ye, H., Zhu, C., Shi, J., Niu, Q., Tan, P., Wang, E., Liu, B., *et al.* Valley-selective circular dichroism of monolayer molybdenum disulphide. *Nature Communications*, **3**(1):887, (2012).

[80] Munkhbat, B., Wróbel, P., Antosiewicz, T.J., and Shegai, T.O. Optical constants of several multilayer transition metal dichalcogenides measured by spectroscopic ellipsometry in the 300–1700 nm range: high index, anisotropy, and hyperbolicity. *ACS Photonics*, **9**(7):2398–2407, (2022).

[81] Hopfield, J. Theory of the contribution of excitons to the complex dielectric constant of crystals. *Physical Review*, **112**(5):1555, (1958).

[82] Fano, U. Effects of configuration interaction on intensities and phase shifts. *Physical Review*, **124**(6):1866, (1961).

[83] Ling, H., Li, R., and Davoyan, A.R. All van der Waals integrated nanophotonics with bulk transition metal dichalcogenides. *ACS Photonics*, **8**(3):721–730, (2021).

[84] Drude, P. Zur elektronentheorie der metalle. *Annalen der Physik*, **306**(3):566–613, (1900).

[85] Drude, P. Zur elektronentheorie der metalle; II. Teil. galvanomagnetische und thermomagnetische effecte. *Annalen der Physik*, **308**(11):369–402, (1900).

[86] Feynman, R.P., Leighton, R.B., and Sands, M.L. *The Feynman Lectures on Physics. Vol. 1, Mainly Mechanics, Radiation, and Heat, Definitive Edition*. Pearson/Addison-Wesley, (2006).

[87] Mie, G. Beiträge zur Optik trüber medien, speziell kolloidaler Metallösungen. *Annalen der Physik*, **330**(3):377–445, (1908).

[88] Hinamoto, T. and Fujii, M. MENP: an open-source matlab implementation of multipole expansion for nanophotonics. *OSA Continuum*, **4**(5):1640–1648, (2021).

[89] Alaee, R., Rockstuhl, C., and Fernandez-Corbaton, I. An electromagnetic multipole expansion beyond the long-wavelength approximation. *Optics Communications*, **407**:17–21, (2018).

[90] Zhang, X.L., Wang, S., Lin, Z., Sun, H.B., and Chan, C.T. Optical force on toroidal nanostructures: toroidal dipole versus renormalized electric dipole. *Physical Review A*, **92**(4): 043804, (2015).

[91] Shafiei, F., Monticone, F., Le, K.Q., Liu, X.X., Hartsfield, T., Alù, A., and Li, X. A subwavelength plasmonic metamolecule exhibiting magnetic-based optical Fano resonance. *Nature Nanotechnology*, **8**(2):95–99, (2013).

[92] Monticone, F., Sounas, D., Krasnok, A., and Alù, A. Can a nonradiating mode be externally excited? nonscattering states versus embedded eigenstates. *ACS Photonics*, **6**(12):3108–3114, (2019).

[93] Afanasiev, G. and Stepanovsky, Y.P. The electromagnetic field of elementary time-dependent toroidal sources. *Journal of Physics A: Mathematical and General*, **28**(16):4565, (1995).

[94] Miroshnichenko, A.E., Evlyukhin, A.B., Yu, Y.F., Bakker, R.M., Chipouline, A., Kuznetsov, A.I., Luk'yanchuk, B., Chichkov, B.N., and Kivshar, Y.S. Nonradiating anapole modes in dielectric nanoparticles. *Nature Communications*, **6**(1):8069, (2015).

[95] Baryshnikova, K.V., Smirnova, D.A., Luk'yanchuk, B.S., and Kivshar, Y.S. Optical anapoles: concepts and applications. *Advanced Optical Materials*, **7**(14):1801350, (2019).

[96] Savinov, V., Papasimakis, N., Tsai, D., and Zheludev, N. Optical anapoles. *Communications Physics*, **2**(1):69, (2019).

[97] Svyakhovskiy, S.E., Ternovski, V.V., and Tribelsky, M.I. Anapole: its birth, life, and death. *Optics Express*, **27**(17):23894–23904, (2019).

[98] Fernandez-Corbaton, I., Nanz, S., Alaee, R., and Rockstuhl, C. Exact dipolar moments of a localized electric current distribution. *Optics Express*, **23**(26):33044–33064, (2015).

[99] Fernandez-Corbaton, I., Nanz, S., and Rockstuhl, C. On the dynamic toroidal multipoles from localized electric current distributions. *Scientific Reports*, **7**(1):7527, (2017).

[100] Jackson, J.D. *Classical Electrodynamics*. Wiley, (1998).

[101] Ospanova, A.K., Labate, G., Matekovits, L., and Basharin, A.A. Multipolar passive cloaking by nonradiating anapole excitation. *Scientific Reports*, **8**(1):12514, (2018).

[102] Verre, R., Baranov, D.G., Munkhbat, B., Cuadra, J., Käll, M., and Shegai, T. Transition metal dichalcogenide nanodisks as high-index dielectric Mie nanoresonators. *Nature Nanotechnology*, **14**(7):679–683, (2019).

[103] Green, T.D., Baranov, D.G., Munkhbat, B., Verre, R., Shegai, T., and Käll, M. Optical material anisotropy in high-index transition metal dichalcogenide Mie nanoresonators. *Optica*, **7**(6):680–686, (2020).

[104] Busschaert, S., Reimann, R., Cavigelli, M., Khelifa, R., Jain, A., and Novotny, L. Transition metal dichalcogenide resonators for second harmonic signal enhancement. *ACS Photonics*, **7**(9):2482–2488, (2020).

[105] Liu, S.D., Wang, Z.X., Wang, W.J., Chen, J.D., and Chen, Z.H. High q-factor with the excitation of anapole modes in dielectric split nanodisk arrays. *Optics Express*, **25**(19): 22375–22387, (2017).

[106] Gurvitz, E.A., Ladutenko, K.S., Dergachev, P.A., Evlyukhin, A.B., Miroshnichenko, A.E., and Shalin, A.S. The high-order toroidal moments and anapole states in all-dielectric photonics. *Laser & Photonics Reviews*, **13**(5):1800266, (2019).

[107] Zenin, V.A., Evlyukhin, A.B., Novikov, S.M., Yang, Y., Malureanu, R., Lavrinenko, A.V., Chichkov, B.N., and Bozhevolnyi, S.I. Direct amplitude-phase near-field observation of higher-order anapole states. *Nano Letters*, **17**(11):7152–7159, (2017).

[108] Díaz-Escobar, E., Barreda, Á.I., Griol, A., and Martínez, A. Experimental observation of higher-order anapoles in individual silicon disks under in-plane illumination. *Applied Physics Letters*, **121**(20), (2022).

[109] Fabry, C. and Perot, A. Sur les franges des lames minces argentées et leur application à la mesure de petites épaisseurs d'air. *Annales de Chimie et de Physique, 7. Série*, **12**(1): 459–501, (1896).

[110] Fabry, C. and Perot, A. Théorie et applications d'une nouvelle méthode de spectroscopie interférentielle. *Annales de Chimie et de Physique, 7. Série*, **16**(1):115–144, (1899).

[111] Bogdanov, A.A., Koshelev, K.L., Kapitanova, P.V., Rybin, M.V., Gladyshev, S.A., Sadrieva, Z.F., Samusev, K.B., Kivshar, Y.S., and Limonov, M.F. Bound states in the continuum and Fano resonances in the strong mode coupling regime. *Advanced Photonics*, **1**(1):016001–016001, (2019).

[112] Tolpygo, K. Physical properties of a rock salt lattice made up of deformable ions. *Zhurnal Eksperimental'noi i Teoreticheskoi Fiziki*, **20**(6):497–509, (1950).

[113] Hopfield, J. and Thomas, D. Polariton absorption lines. *Physical Review Letters*, **15**(1):22, (1965).

[114] Savona, V., Andreani, L., Schwendimann, P., and Quattropani, A. Quantum well excitons in semiconductor microcavities: unified treatment of weak and strong coupling regimes. *Solid State Communications*, **93**(9):733–739, (1995).

[115] Dufferwiel, S., Schwarz, S., Withers, F., Trichet, A., Li, F., Sich, M., Del Pozo-Zamudio, O., Clark, C., Nalitov, A., Solnyshkov, D., *et al.* Exciton–polaritons in van der Waals heterostructures embedded in tunable microcavities. *Nature Communications*, **6**(1):8579, (2015).

[116] Ghosh, S., Su, R., Zhao, J., Fieramosca, A., Wu, J., Li, T., Zhang, Q., Li, F., Chen, Z., Liew, T., *et al.* Microcavity exciton polaritons at room temperature. *Photonics Insights*, **1**(1):R04, (2022).

[117] Rodriguez, S.R.K. Classical and quantum distinctions between weak and strong coupling. *European Journal of Physics*, **37**(2):025802, (2016).

[118] Bajoni, D. Polariton lasers. hybrid light–matter lasers without inversion. *Journal of Physics D: Applied Physics*, **45**(31):313001, (2012).

[119] Beaumariage, J., Sun, Z., Alnatah, H., Yao, Q., Myers, D.M., Steger, M., West, K., Baldwin, K., Pfeiffer, L.N., Tam, M.C.A., *et al.* Measurement of exciton fraction of microcavity exciton-polaritons using transfer-matrix modeling. *arXiv preprint, arXiv:2406.12940*, (2024).

[120] As'ham, K., Al-Ani, I., Huang, L., Miroshnichenko, A.E., and Hattori, H.T. Boosting strong coupling in a hybrid WSe_2 monolayer–anapole–plasmon system. *ACS Photonics*, **8**(2):489–496, (2021).

[121] Kasprzak, J., Richard, M., Kundermann, S., Baas, A., Jeambrun, P., Keeling, J.M.J., Marchetti, F., Szymańska, M., André, R., Staehli, J., *et al.* Bose–einstein condensation of exciton polaritons. *Nature*, **443**(7110):409–414, (2006).

[122] Laussy, F.P., Taylor, T., Shelykh, I.A., and Kavokin, A.V. Superconductivity with excitons and polaritons: review and extension. *Journal of Nanophotonics*, **6**(1):064502–064502, (2012).

[123] von Neumann, J. and Wigner, E.P. *The Collected Works of Eugene Paul Wigner: Part A: The Scientific Papers*, chapter Über merkwürdige diskrete Eigenwerte, pages 291–293. Springer Berlin Heidelberg, (1993).

[124] Hsu, C.W., Zhen, B., Stone, A.D., Joannopoulos, J.D., and Soljačić, M. Bound states in the continuum. *Nature Reviews Materials*, **1**(9):1–13, (2016).

[125] Friedrich, H. and Wintgen, D. Interfering resonances and bound states in the continuum. *Physical Review A*, **32**(6):3231, (1985).

[126] Plotnik, Y., Peleg, O., Dreisow, F., Heinrich, M., Nolte, S., Szameit, A., and Segev, M. Experimental observation of optical bound states in the continuum. *Physical Review Letters*, **107**(18):183901, (2011).

[127] Bulgakov, E.N. and Sadreev, A.F. Bound states in the continuum in photonic waveguides inspired by defects. *Physical Review B—Condensed Matter and Materials Physics*, **78**(7): 075105, (2008).

[128] Hsu, C.W., Zhen, B., Lee, J., Chua, S.L., Johnson, S.G., Joannopoulos, J.D., and Soljačić, M. Observation of trapped light within the radiation continuum. *Nature*, **499**(7457):188–191, (2013).

[129] Zhen, B., Hsu, C.W., Lu, L., Stone, A.D., and Soljačić, M. Topological nature of optical bound states in the continuum. *Physical Review Letters*, **113**(25):257401, (2014).

[130] Rybin, M.V., Koshelev, K.L., Sadrieva, Z.F., Samusev, K.B., Bogdanov, A.A., Limonov, M.F., and Kivshar, Y.S. High-q supercavity modes in subwavelength dielectric resonators. *Physical Review Letters*, **119**(24):243901, (2017).

[131] Koshelev, K., Kruk, S., Melik-Gaykazyan, E., Choi, J.H., Bogdanov, A., Park, H.G., and Kivshar, Y. Subwavelength dielectric resonators for nonlinear nanophotonics. *Science*, **367** (6475):288–292, (2020).

[132] Mylnikov, V., Ha, S.T., Pan, Z., Valuckas, V., Paniagua-Domínguez, R., Demir, H.V., and Kuznetsov, A.I. Lasing action in single subwavelength particles supporting supercavity modes. *ACS Nano*, **14**(6):7338–7346, (2020).

[133] Muhammad, N., Chen, Y., Qiu, C.W., and Wang, G.P. Optical bound states in continuum in MoS_2-based metasurface for directional light emission. *Nano Letters*, **21**(2):967–972, (2021).

[134] Melik-Gaykazyan, E., Koshelev, K., Choi, J.H., Kruk, S.S., Bogdanov, A., Park, H.G., and Kivshar, Y. From Fano to quasi-BIC resonances in individual dielectric nanoantennas. *Nano Letters*, **21**(4):1765–1771, (2021).

[135] Colom, R., Binkowski, F., Betz, F., Kivshar, Y., and Burger, S. Enhanced purcell factor for nanoantennas supporting interfering resonances. *Physical Review Research*, **4**(2):023189, (2022).

[136] Wang, J., Li, P., Zhao, X., Qian, Z., Wang, X., Wang, F., Zhou, X., Han, D., Peng, C., Shi, L., *et al.* Optical bound states in the continuum in periodic structures: mechanisms, effects, and applications. *Photonics Insights*, **3**(1):R01, (2024).

[137] Tittl, A., Leitis, A., Liu, M., Yesilkoy, F., Choi, D.Y., Neshev, D.N., Kivshar, Y.S., and Altug, H. Imaging-based molecular barcoding with pixelated dielectric metasurfaces. *Science*, **360** (6393):1105–1109, (2018).

[138] Carletti, L., Koshelev, K., De Angelis, C., and Kivshar, Y. Giant nonlinear response at the nanoscale driven by bound states in the continuum. *Physical Review Letters*, **121**(3):033903, (2018).

[139] Carletti, L., Kruk, S.S., Bogdanov, A.A., De Angelis, C., and Kivshar, Y. High-harmonic generation at the nanoscale boosted by bound states in the continuum. *Physical Review Research*, **1**(2):023016, (2019).

[140] Purcell, E.M., Torrey, H.C., and Pound, R.V. Resonance absorption by nuclear magnetic moments in a solid. *Physical Review*, **69**(1-2):37, (1946).

[141] Haroche, S. and Kleppner, D. Cavity quantum electrodynamics. *Physics Today*, **42**(1): 24–30, (1989).

[142] Dirac, P.A.M. The quantum theory of the emission and absorption of radiation. *Proceedings of the Royal Society of London. Series A, Containing Papers of a Mathematical and Physical Character*, **114**(767):243–265, (1927).

[143] Fermi, E. *Nuclear Physics: A Course Given by Enrico Fermi at the University of Chicago*. University of Chicago press, (1950).

[144] Gerard, J.M. and Gayral, B. Strong purcell effect for InAs quantum boxes in three-dimensional solid-state microcavities. *Journal of Lightwave Technology*, **17**(11):2089, (1999).

[145] Choi, H., Heuck, M., and Englund, D. Self-similar nanocavity design with ultrasmall mode volume for single-photon nonlinearities. *Physical Review Letters*, **118**(22):223605, (2017).

[146] Robinson, J.T., Manolatou, C., Chen, L., and Lipson, M. Ultrasmall mode volumes in dielectric optical microcavities. *Physical Review Letters*, **95**(14):143901, (2005).

[147] Zotev, P.G., Wang, Y., Sortino, L., Severs Millard, T., Mullin, N., Conteduca, D., Shagar, M., Genco, A., Hobbs, J.K., Krauss, T.F., *et al.* Transition metal dichalcogenide dimer nanoantennas for tailored light–matter interactions. *ACS Nano*, **16**(4):6493–6505, (2022).

[148] Li, J., Zhong, Y., and Zhang, D. Excitons in monolayer transition metal dichalcogenides. *Journal of Physics: Condensed Matter*, **27**(31):315301, (2015).

[149] Müller, M., Bounouar, S., Jöns, K.D., Glässl, M., and Michler, P. On-demand generation of indistinguishable polarization-entangled photon pairs. *Nature Photonics*, **8**(3):224–228, (2014).

[150] Chen, Y., Zopf, M., Keil, R., Ding, F., and Schmidt, O.G. Highly-efficient extraction of entangled photons from quantum dots using a broadband optical antenna. *Nature Communications*, **9**(1):2994, (2018).

[151] Abudayyeh, H., Lubotzky, B., Blake, A., Wang, J., Majumder, S., Hu, Z., Kim, Y., Htoon, H., Bose, R., Malko, A.V., *et al.* Single photon sources with near unity collection efficiencies by deterministic placement of quantum dots in nanoantennas. *APL Photonics*, **6**(3), (2021).

[152] Amani, M., Lien, D.H., Kiriya, D., Xiao, J., Azcatl, A., Noh, J., Madhvapathy, S.R., Addou, R., K C, S., Dubey, M., *et al.* Near-unity photoluminescence quantum yield in MoS_2. *Science*, **350**(6264):1065–1068, (2015).

[153] Sortino, L., Zotev, P., Mignuzzi, S., Cambiasso, J., Schmidt, D., Genco, A., Aßmann, M., Bayer, M., Maier, S.A., Sapienza, R., *et al.* Enhanced light-matter interaction in an atomically thin semiconductor coupled with dielectric nano-antennas. *Nature Communications*, **10**(1):5119, (2019).

[154] Roy, S., Sharbirin, A.S., Lee, Y., Kim, W.B., Kim, T.S., Cho, K., Kang, K., Jung, H.S., and Kim, J. Measurement of quantum yields of monolayer TMDs using dye-dispersed PMMA thin films. *Nanomaterials*, **10**(6):1032, (2020).

[155] Lorentz, H. The motion of electrons in metallic bodies I. In *KNAW, proceedings*, volume 7, pages 438–453, (1905).

[156] Prandini, G., Rignanese, G.M., and Marzari, N. Photorealistic modelling of metals from first principles. *npj Computational Materials*, **5**(1):129, (2019).

[157] Pines, D. and Bohm, D. A collective description of electron interactions: II. collective vs individual particle aspects of the interactions. *Physical Review*, **85**(2):338, (1952).

[158] Koh, A.L., Bao, K., Khan, I., Smith, W.E., Kothleitner, G., Nordlander, P., Maier, S.A., and McComb, D.W. Electron energy-loss spectroscopy (EELS) of surface plasmons in single silver nanoparticles and dimers: influence of beam damage and mapping of dark modes. *ACS Nano*, **3**(10):3015–3022, (2009).

[159] Herzing, A.A., Guler, U., Zhou, X., Boltasseva, A., Shalaev, V., and Norris, T.B. Electron energy loss spectroscopy of plasmon resonances in titanium nitride thin films. *Applied Physics Letters*, **108**(17), (2016).

[160] Borja-Urby, R., Paredes-Carrera, S.P., Viltres-Cobas, H., Santiago-Jacinto, P., Paraguay-Delgado, F., Herrera-Pérez, G., Rendón-Vázquez, L., Sánchez-Ochoa, J.C., and Morales-Cruz, D. Confined volume plasmon spatial distribution by low-loss EELS on self-assemble bismuth nanoparticles. *Journal of Electron Spectroscopy and Related Phenomena*, **237**: 146891, (2019).

[161] Yang, A., Wang, D., Wang, W., and Odom, T.W. Coherent light sources at the nanoscale. *Annual Review of Physical Chemistry*, **68**(1):83–99, (2017).

[162] Aftab, M., Mansha, M.S., Iqbal, T., and Farooq, M. Surface plasmon excitation: theory, configurations, and applications. *Plasmonics*, **19**(4):1701–1719, (2024).

[163] Ritchie, R.H. Plasma losses by fast electrons in thin films. *Physical Review*, **106**(5):874, (1957).

[164] Heinz, R. *Surface Plasmons on Smooth and Rough Surfaces and on Gratings*, volume 111 of *Springer Tracts in Modern Physics*. Springer-Verlag, (1988).

[165] Kliewer, K. and Fuchs, R. Collective electronic motion in a metallic slab. *Physical Review*, **153**(2):498, (1967).

[166] Otto, A. Excitation of nonradiative surface plasma waves in silver by the method of frustrated total reflection. *Zeitschrift für Physik A Hadrons and Nuclei*, **216**(4):398–410, (1968).

[167] Chang, Y.C., Chu, J., Wang, T., Lin, M., Yeh, J., and Wang, J.K. Fourier analysis of surface plasmon waves launched from single nanohole and nanohole arrays: unraveling tip-induced effects. *Optics Express*, **16**(2):740–747, (2008).

[168] Yang, J., Xiao, X., Hu, C., Zhang, W., Zhou, S., and Zhang, J. Broadband surface plasmon polariton directional coupling via asymmetric optical slot nanoantenna pair. *Nano Letters*, **14**(2):704–709, (2014).

[169] Randerson, S.A., Zotev, P.G., Hu, X., Knight, A.J., Wang, Y., Nagarkar, S., Hensman, D., Wang, Y., and Tartakovskii, A.I. High q hybrid Mie–plasmonic resonances in van der Waals nanoantennas on gold substrate. *ACS Nano*, **18**(25):16208–16221, (2024).

[170] Vesseur, E.J.R., de Abajo, F.J.G., and Polman, A. Broadband purcell enhancement in plasmonic ring cavities. *Physical Review B—Condensed Matter and Materials Physics*, **82**(16): 165419, (2010).

[171] Yang, Y., Miller, O.D., Christensen, T., Joannopoulos, J.D., and Soljacic, M. Low-loss plasmonic dielectric nanoresonators. *Nano Letters*, **17**(5):3238–3245, (2017).

[172] Maimaiti, A., Patra, P.P., Jones, S., Antosiewicz, T.J., and Verre, R. Low-loss hybrid high-index dielectric particles on a mirror for extreme light confinement. *Advanced Optical Materials*, **8**(6):1901820, (2020).

[173] Yang, S., Bao, W., Liu, X., Kim, J., Zhao, R., Ma, R., Wang, Y., and Zhang, X. Subwavelength-scale lasing perovskite with ultrahigh purcell enhancement. *Matter*, **4**(12): 4042–4050, (2021).

[174] Dmitriev, P.A., Lassalle, E., Ding, L., Pan, Z., Neo, D.C., Valuckas, V., Paniagua-Dominguez, R., Yang, J.K., Demir, H.V., and Kuznetsov, A.I. Hybrid dielectric-plasmonic nanoantenna with multiresonances for subwavelength photon sources. *ACS Photonics*, **10** (3):582–594, (2023).

[175] Oulton, R.F., Sorger, V.J., Genov, D., Pile, D., and Zhang, X. A hybrid plasmonic waveguide for subwavelength confinement and long-range propagation. *Nature Photonics*, **2**(8):496–500, (2008).

[176] Fang, Y. and Sun, M. Nanoplasmonic waveguides: towards applications in integrated nanophotonic circuits. *Light: Science & Applications*, **4**(6):e294, (2015).

[177] Kim, S.J., Yun, H., Park, K., Hong, J., Yun, J.G., Lee, K., Kim, J., Jeong, S.J., Mun, S.E., Sung, J., *et al.* Active directional switching of surface plasmon polaritons using a phase transition material. *Scientific Reports*, **7**(1):43723, (2017).

[178] Cao, L. and Zhang, Y. Light controlled surface plasmon polaritons switch based on a gradient metal grating. *Optics Communications*, **424**:103–106, (2018).

[179] Zhang, J., Zhang, L., and Xu, W. Surface plasmon polaritons: physics and applications. *Journal of Physics D: Applied Physics*, **45**(11):113001, (2012).

[180] Divya, J., Selvendran, S., Raja, A.S., and Sivasubramanian, A. Surface plasmon based plasmonic sensors: a review on their past, present and future. *Biosensors and Bioelectronics: X*, **11**:100175, (2022).

[181] Dutta, H.S., Goyal, A.K., Srivastava, V., and Pal, S. Coupling light in photonic crystal waveguides: a review. *Photonics and Nanostructures-Fundamentals and Applications*, **20**: 41–58, (2016).

[182] Meng, Y., Chen, Y., Lu, L., Ding, Y., Cusano, A., Fan, J.A., Hu, Q., Wang, K., Xie, Z., Liu, Z., *et al.* Optical meta-waveguides for integrated photonics and beyond. *Light: Science & Applications*, **10**(1):1–44, (2021).

[183] Jannesari, R., Dubois, F., Pühringer, G., Stocker, G., Tortschanoff, A., Grille, T., and Jakoby, B. Vertical coupling into a photonic crystal waveguide using band folding design. In *2021 IEEE Sensors*, pages 1–4. IEEE, (2021).

[184] Sun, K., Cai, Y., Levy, U., and Han, Z. Quasi-guided modes resulting from the band folding effect in a photonic crystal slab for enhanced interactions of matters with free-space radiations. *Beilstein Journal of Nanotechnology*, **14**(1):322–328, (2023).

[185] Bragg, W., Thomson, J., and Friedrich, H. Diffraction of short electromagnetic waves by a crystal. In *Proceedings of the Cambridge philosophical society: mathematical and physical sciences*, volume 17, page 43, (1914).

[186] Sheppard, C. Approximate calculation of the reflection coefficient from a stratified medium. *Pure and Applied Optics: Journal of the European Optical Society Part A*, **4**(5):665, (1995).

[187] Henry, C., Kazarinov, R., Logan, R., and Yen, R. Observation of destructive interference in the radiation loss of second-order distributed feedback lasers. *IEEE Journal of Quantum Electronics*, **21**(2):151–154, (1985).

[188] Li, S., Zhou, C., Liu, T., and Xiao, S. Symmetry-protected bound states in the continuum supported by all-dielectric metasurfaces. *Physical Review A*, **100**(6):063803, (2019).

[189] Ardizzone, V., Riminucci, F., Zanotti, S., Gianfrate, A., Efthymiou-Tsironi, M., Suàrez-Forero, D., Todisco, F., De Giorgi, M., Trypogeorgos, D., Gigli, G., *et al.* Polariton bose–einstein condensate from a bound state in the continuum. *Nature*, **605**(7910):447–452, (2022).

[190] Djemaiai, L., Hamidi, M., Mezeghrane, A., Belkhir, A., and Baida, F.I. Infinite versus finite 1D-dielectric gratings supporting SP-BIC modes for sensing applications. *Physica Scripta*, **99**(2):025520, (2024).

[191] Bhowmik, B.K., Rohith, K., John, S., Prabhu, S., and Kumar, G. High-quality factor quasi-BIC mode via selective symmetry-breaking approach in a terahertz metasurface. *New Journal of Physics*, **26**(6):063024, (2024).

[192] Lu, L., Joannopoulos, J.D., and Soljačić, M. Topological photonics. *Nature Photonics*, **8** (11):821–829, (2014).

[193] Hall, E.H. *et al.* On a new action of the magnet on electric currents. *American Journal of Mathematics*, **2**(3):287–292, (1879).

[194] Hasan, M.Z. and Kane, C.L. Colloquium: topological insulators. *Reviews of Modern Physics*, **82**(4):3045–3067, (2010).

[195] Berry, M.V. Quantal phase factors accompanying adiabatic changes. *Proceedings of the Royal Society of London. A. Mathematical and Physical Sciences*, **392**(1802):45–57, (1984).

[196] Born, M. and Fock, V. Beweis des adiabatensatzes. *Zeitschrift für Physik*, **51**(3):165–180, (1928).

[197] Pancharatnam, S. Generalized theory of interference, and its applications: part I. coherent pencils. In *Proceedings of the Indian Academy of Sciences-Section A*, volume 44, pages 247–262. Springer, (1956).

[198] Foucault, M.L. Physical demonstration of the rotation of the earth by means of the pendulum. *Journal of the Franklin Institute*, **21**(5):350, (1851).

[199] Thouless, D.J., Kohmoto, M., Nightingale, M.P., and den Nijs, M. Quantized Hall conductance in a two-dimensional periodic potential. *Physical Review Letters*, **49**(6):405, (1982).

[200] Haldane, F.D.M. Model for a quantum Hall effect without landau levels: condensed-matter realization of the "parity anomaly". *Physical Review Letters*, **61**(18):2015, (1988).

[201] Murakami, S., Nagaosa, N., and Zhang, S.C. Spin-hall insulator. *Physical Review Letters*, **93**(15):156804, (2004).

[202] Kane, C.L. and Mele, E.J. Quantum spin Hall effect in graphene. *Physical Review Letters*, **95**(22):226801, (2005).

[203] Bernevig, B.A., Hughes, T.L., and Zhang, S.C. Quantum spin Hall effect and topological phase transition in HgTe quantum wells. *Science*, **314**(5806):1757–1761, (2006).

[204] Konig, M., Wiedmann, S., Brune, C., Roth, A., Buhmann, H., Molenkamp, L.W., Qi, X.L., and Zhang, S.C. Quantum spin Hall insulator state in HgTe quantum wells. *Science*, **318** (5851):766–770, (2007).

[205] Rechtsman, M.C., Zeuner, J.M., Plotnik, Y., Lumer, Y., Podolsky, D., Dreisow, F., Nolte, S., Segev, M., and Szameit, A. Photonic floquet topological insulators. *Nature*, **496**(7444): 196–200, (2013).

[206] Kang, J., Wei, R., Zhang, Q., and Dong, G. Topological photonic states in waveguide arrays. *Advanced Physics Research*, **2**(3):2200053, (2023).

[207] Hafezi, M., Mittal, S., Fan, J., Migdall, A., and Taylor, J. Imaging topological edge states in silicon photonics. *Nature Photonics*, **7**(12):1001–1005, (2013).

[208] Gao, F., Gao, Z., Shi, X., Yang, Z., Lin, X., Xu, H., Joannopoulos, J.D., Soljačić, M., Chen, H., Lu, L., *et al.* Probing topological protection using a designer surface plasmon structure. *Nature Communications*, **7**(1):11619, (2016).

[209] Mittal, S., Goldschmidt, E.A., and Hafezi, M. A topological source of quantum light. *Nature*, **561**(7724):502–506, (2018).

[210] Li, M., Sinev, I., Benimetskiy, F., Ivanova, T., Khestanova, E., Kiriushechkina, S., Vakulenko, A., Guddala, S., Skolnick, M., Menon, V.M., *et al.* Experimental observation of

topological Z2 exciton-polaritons in transition metal dichalcogenide monolayers. *Nature Communications*, **12**(1):4425, (2021).

[211] Guddala, S., Komissarenko, F., Kiriushechkina, S., Vakulenko, A., Li, M., Menon, V., Alù, A., and Khanikaev, A. Topological phonon-polariton funneling in midinfrared metasurfaces. *Science*, **374**(6564):225–227, (2021).

[212] St-Jean, P., Goblot, V., Galopin, E., Lemaître, A., Ozawa, T., Le Gratiet, L., Sagnes, I., Bloch, J., and Amo, A. Lasing in topological edge states of a one-dimensional lattice. *Nature Photonics*, **11**(10):651–656, (2017).

[213] Rezzouk, Y., Khattou, S., El Ghafiani, M., Amrani, M., El Boudouti, E.H., Talbi, A., and Djafari-Rouhani, B. Fabry-Pérot and Friedrich-Wintgen bound states in the continuum in a photonic triple-stub cavity. *Physical Review B*, **109**(23):235431, (2024).

[214] Koshelev, K., Lepeshov, S., Liu, M., Bogdanov, A., and Kivshar, Y. Asymmetric metasurfaces with high-q resonances governed by bound states in the continuum. *Physical Review Letters*, **121**(19):193903, (2018).

[215] van Hoof, N.J., Abujetas, D.R., Ter Huurne, S.E., Verdelli, F., Timmermans, G.C., Sánchez-Gil, J.A., and Rivas, J.G. Unveiling the symmetry protection of bound states in the continuum with terahertz near-field imaging. *ACS Photonics*, **8**(10):3010–3016, (2021).

[216] Gao, Y., Ge, J., Sun, S., and Shen, X. Dark modes governed by translational-symmetry-protected bound states in the continuum in symmetric dimer lattices. *Results in Physics*, **43**: 106078, (2022).

[217] Yang, Y., Peng, C., Liang, Y., Li, Z., and Noda, S. Analytical perspective for bound states in the continuum in photonic crystal slabs. *Physical Review Letters*, **113**(3):037401, (2014).

[218] Doeleman, H.M., Monticone, F., den Hollander, W., Alù, A., and Koenderink, A.F. Experimental observation of a polarization vortex at an optical bound state in the continuum. *Nature Photonics*, **12**(7):397–401, (2018).

[219] Kodigala, A., Lepetit, T., Gu, Q., Bahari, B., Fainman, Y., and Kanté, B. Lasing action from photonic bound states in continuum. *Nature*, **541**(7636):196–199, (2017).

[220] Ha, S.T., Fu, Y.H., Emani, N.K., Pan, Z., Bakker, R.M., Paniagua-Domínguez, R., and Kuznetsov, A.I. Directional lasing in resonant semiconductor nanoantenna arrays. *Nature Nanotechnology*, **13**(11):1042–1047, (2018).

[221] Hwang, M.S., Lee, H.C., Kim, K.H., Jeong, K.Y., Kwon, S.H., Koshelev, K., Kivshar, Y., and Park, H.G. Ultralow-threshold laser using super-bound states in the continuum. *Nature Communications*, **12**(1):4135, (2021).

[222] Krasikov, S., Bogdanov, A., and Iorsh, I. Nonlinear bound states in the continuum of a one-dimensional photonic crystal slab. *Physical Review B*, **97**(22):224309, (2018).

[223] Koshelev, K., Tang, Y., Li, K., Choi, D.Y., Li, G., and Kivshar, Y. Nonlinear metasurfaces governed by bound states in the continuum. *ACS Photonics*, **6**(7):1639–1644, (2019).

[224] Xu, L., Zangeneh Kamali, K., Huang, L., Rahmani, M., Smirnov, A., Camacho-Morales, R., Ma, Y., Zhang, G., Woolley, M., Neshev, D., *et al.* Dynamic nonlinear image tuning through magnetic dipole quasi-BIC ultrathin resonators. *Advanced Science*, **6**(15):1802119, (2019).

[225] Yang, Q., Liu, Y., Gan, X., Fang, C., Han, G., and Hao, Y. Nonlinear bound states in the continuum of etchless lithium niobate metasurfaces. *IEEE Photonics Journal*, **12**(5):1–9, (2020).

[226] Cong, L. and Singh, R. Symmetry-protected dual bound states in the continuum in metamaterials. *Advanced Optical Materials*, **7**(13):1900383, (2019).

[227] Iwahashi, S., Kurosaka, Y., Sakai, K., Kitamura, K., Takayama, N., and Noda, S. Higher-order vector beams produced by photonic-crystal lasers. *Optics Express*, **19**(13):11963–11968, (2011).

[228] Kitamura, K., Sakai, K., Takayama, N., Nishimoto, M., and Noda, S. Focusing properties of vector vortex beams emitted by photonic-crystal lasers. *Optics Letters*, **37**(12):2421–2423, (2012).

[229] Isoniemi, T., Bouteyre, P., Hu, X., Benimetskiy, F., Wang, Y., Skolnick, M.S., Krizhanovskii, D.N., and Tartakovskii, A.I. Realization of Z2 topological photonic insulators made from multilayer transition metal dichalcogenides. *ACS nano*, **18**(47):32547–32555, (2024).

[230] Dirac, P.A.M. The quantum theory of the electron. *Proceedings of the Royal Society of London. Series A, Containing Papers of a Mathematical and Physical Character*, **117**(778):610–624, (1928).

[231] Russell, J.S. Report on waves. In *Report of the fourteenth meeting of the British Association for the Advancement of Science*, volume 25, pages 311–390, (1844).

[232] Jackiw, R. and Rebbi, C. Solitons with fermion number $1/2$. *Physical Review D*, **13**(12):3398, (1976).

[233] Angelakis, D.G., Das, P., and Noh, C. Probing the topological properties of the Jackiw-Rebbi model with light. *Scientific Reports*, **4**(1):6110, (2014).

[234] Shen, S.Q. *Topological Insulators*, volume 174. Springer, (2012).

[235] Li, F.F., Wang, H.X., Xiong, Z., Lou, Q., Chen, P., Wu, R.X., Poo, Y., Jiang, J.H., and John, S. Topological light-trapping on a dislocation. *Nature Communications*, **9**(1):2462, (2018).

[236] Gorlach, A.A., Zhirihin, D.V., Slobozhanyuk, A.P., Khanikaev, A.B., and Gorlach, M.A. Photonic Jackiw-Rebbi states in all-dielectric structures controlled by bianisotropy. *Physical Review B*, **99**(20):205122, (2019).

[237] Tran, T.X. and Biancalana, F. Linear and nonlinear photonic Jackiw-Rebbi states in interfaced binary waveguide arrays. *Physical Review A*, **96**(1):013831, (2017).

[238] Tran, T.X., Nguyen, H.M., and Duong, D.C. Jackiw-Rebbi states in interfaced binary waveguide arrays with Kerr nonlinearity. *Physical Review A*, **100**(5):053849, (2019).

[239] Rice, M. and Mele, E. Elementary excitations of a linearly conjugated diatomic polymer. *Physical Review Letters*, **49**(19):1455, (1982).

[240] Miri, M.A. and Alu, A. Exceptional points in optics and photonics. *Science*, **363**(6422): eaar7709, (2019).

[241] Gupta, N.K., Srinivasu, S., Kumar, M., Tiwari, A.K., Pal, S.S., Wanare, H., and Ramakrishna, S.A. Realization of Jackiw–Rebbi zero-energy modes at photonic crystal domain walls: emergence of polarization-indiscriminate surface states. *Applied Physics Letters*, **124**(9), (2024).

[242] Lee, K.Y., Yoon, S., Song, S.H., and Yoon, J.W. Topological beaming of light. *Science Advances*, **8**(49):eadd8349, (2022).

[243] Yee, K. Numerical solution of initial boundary value problems involving maxwell's equations in isotropic media. *IEEE Transactions on Antennas and Propagation*, **14**(3):302–307, (1966).

[244] Courant, R., Friedrichs, K., and Lewy, H. Über die partiellen Differenzengleichungen der mathematischen Physik. *Mathematische Annalen*, **100**(1):32–74, (1928).

[245] Raman, C. and Nagendra Nathe, N. The diffraction of light by high frequency sound waves: part I. In *Proceedings of the Indian Academy of Sciences-Section A*, volume 2, pages 406–412. Springer, (1935).

[246] Kogelnik, H. Coupled wave theory for thick hologram gratings. *Bell System Technical Journal*, **48**(9):2909–2947, (1969).

[247] Burckhardt, C. Diffraction of a plane wave at a sinusoidally stratified dielectric grating. *Journal of the Optical Society of America*, **56**(11):1502–1508, (1966).

[248] Moharam, M. and Gaylord, T.K. Rigorous coupled-wave analysis of planar-grating diffraction. *Journal of the Optical Society of America*, **71**(7):811–818, (1981).

[249] Li, L. Use of fourier series in the analysis of discontinuous periodic structures. *Journal of the Optical Society of America A*, **13**(9):1870–1876, (1996).

[250] Turunen, J. and Tervo, J. Fourier modal method and its applications to inverse diffraction, near-field imaging, and nonlinear optics. In *Fringe 2013: 7th International Workshop on Advanced Optical Imaging and Metrology*, pages 25–33. Springer, (2014).

[251] Antonakakis, T., Baida, F., Belkhir, A., Cherednichenko, K., Cooper, S., Craster, R., Demésy, G., Desanto, J., Granet, G., Gralak, B., Goray, L., Li, L., Maystre, D., Stout, B., Zolla, F., Schmidt, G., Skeleton, E., Guenneau, S., Nicolet, A., and Vial, B. *Gratings: Theory and Numeric Applications, Second Revisited Edition*. Presses Universitaires de Provence, (2014).

[252] Liu, V. and Fan, S. S4: a free electromagnetic solver for layered periodic structures. *Computer Physics Communications*, **183**(10):2233–2244, (2012).

[253] Castellanos-Gomez, A., Buscema, M., Molenaar, R., Singh, V., Janssen, L., van der Zant, H.S.J., and Steele, G.A. Deterministic transfer of two-dimensional materials by all-dry viscoelastic stamping. *2D Materials*, **1**(1):011002, (2014).

[254] Danielsen, D.R., Lyksborg-Andersen, A., Nielsen, K.E., Jessen, B.S., Booth, T.J., Doan, M.H., Zhou, Y., Bøggild, P., and Gammelgaard, L. Super-resolution nanolithography of two-dimensional materials by anisotropic etching. *ACS Applied Materials & Interfaces*, **13** (35):41886–41894, (2021).

[255] Ocelic, N., Huber, A., and Hillenbrand, R. Pseudoheterodyne detection for background-free near-field spectroscopy. *Applied Physics Letters*, **89**(10):101124, (2006).

[256] Keilmann, F. and Hillenbrand, R. Near-field microscopy by elastic light scattering from a tip. *Philosophical Transactions of the Royal Society of London. Series A: Mathematical, Physical and Engineering Sciences*, **362**(1817):787–805, (2004).

[257] Shen, F., Zhang, Z., Zhou, Y., Ma, J., Chen, K., Chen, H., Wang, S., Xu, J., and Chen, Z. Transition metal dichalcogenide metaphotonic and self-coupled polaritonic platform grown by chemical vapor deposition. *Nature Communications*, **13**(1):5597, (2022).

[258] Popkova, A.A., Antropov, I.M., Tselikov, G.I., Ermolaev, G.A., Ozerov, I., Kirtaev, R.V., Novikov, S.M., Evlyukhin, A.B., Arsenin, A.V., Bessonov, V.O., *et al.* Nonlinear exciton-Mie coupling in transition metal dichalcogenide nanoresonators. *Laser & Photonics Reviews*, **16**(6):2100604, (2022).

[259] Du, J., Bao, W., Zhang, R., Shen, S., Yue, L., Ding, Q., Xie, P., Kuang, X., Zhang, H., and Wang, W. Manipulation of unidirectional side scattering of light in transition metal dichalcogenide nanoresonators. *Physical Review B*, **109**(11):115426, (2024).

[260] Zhang, H., Abhiraman, B., Zhang, Q., Miao, J., Jo, K., Roccasecca, S., Knight, M.W., Davoyan, A.R., and Jariwala, D. Hybrid exciton-plasmon-polaritons in van der Waals semiconductor gratings. *Nature Communications*, **11**(1):3552, (2020).

[261] Kleemann, M.E., Chikkaraddy, R., Alexeev, E.M., Kos, D., Carnegie, C., Deacon, W., Casalis de Pury, A., Große, C., de Nijs, B., Mertens, J., *et al.* Strong-coupling of WSe_2 in ultra-compact plasmonic nanocavities at room temperature. *Nature Communications*, **8** (1):1–7, (2017).

[262] Liu, Y., Zhu, Z., Qian, J., Yuan, J., Yan, J., Shen, Z.X., and Jiang, L. Strong coupling between two-dimensional transition metal dichalcogenides and plasmonic-optical hybrid resonators. *Physical Review B*, **104**(20):205118, (2021).

[263] Shen, S., Wu, Y., Li, Y., Xie, P., Ding, Q., Kuang, X., Wang, W., and Wang, W. Tuning magnetic Mie-exciton interaction from the intermediate to strong coupling regime in a WSe_2 monolayer coupled with dielectric-metal nanoresonators. *Physical Review B*, **105** (15):155403, (2022).

[264] As'ham, K., Al-Ani, I., Alaloul, M., Abdo, S., Abdulghani, A., Lei, W., Hattori, H.T., Huang, L., and Miroshnichenko, A.E. Enhanced strong coupling in the hybrid dielectric-metallic nanoresonator and WS_2 monolayer. *Physical Review Applied*, **19**(5):054049, (2023).

[265] Shibanuma, T., Grinblat, G., Albella, P., and Maier, S.A. Efficient third harmonic generation from metal–dielectric hybrid nanoantennas. *Nano Letters*, **17**(4):2647–2651, (2017).

[266] Sun, S., Zhang, T., Liu, Q., Ma, L., Du, Q., and Duan, H. Enhanced directional fluorescence emission of randomly oriented emitters via a metal–dielectric hybrid nanoantenna. *The Journal of Physical Chemistry C*, **123**(34):21150–21160, (2019).

[267] Xu, L., Rahmani, M., Zangeneh Kamali, K., Lamprianidis, A., Ghirardini, L., Sautter, J., Camacho-Morales, R., Chen, H., Parry, M., Staude, I., *et al.* Boosting third-harmonic generation by a mirror-enhanced anapole resonator. *Light: Science & Applications*, **7**(1):1–8, (2018).

[268] Huang, L., Krasnok, A., Alú, A., Yu, Y., Neshev, D., and Miroshnichenko, A.E. Enhanced light–matter interaction in two-dimensional transition metal dichalcogenides. *Reports on Progress in Physics*, **85**(4):046401, (2022).

[269] Munkhbat, B., Küçüköz, B., Baranov, D.G., Antosiewicz, T.J., and Shegai, T.O. Nanostructured transition metal dichalcogenide multilayers for advanced nanophotonics. *Laser & Photonics Reviews*, **17**(1):2200057, (2023).

[270] Decker, M., Pertsch, T., and Staude, I. Strong coupling in hybrid metal-dielectric nanoresonators. *Philosophical Transactions of the Royal Society A: Mathematical, Physical and Engineering Sciences*, **375**(2090):20160312, (2017).

[271] Lee, E., Seo, I.C., Lim, S.C., Jeong, H.Y., and Jun, Y.C. Active switching and tuning of sharp Fano resonances in the mid-infrared spectral region. *Optics Express*, **24**(22):25684–25696, (2016).

[272] Chen, J., Gan, F., Wang, Y., and Li, G. Plasmonic sensing and modulation based on Fano resonances. *Advanced Optical Materials*, **6**(9):1701152, (2018).

[273] Miroshnichenko, A.E., Flach, S., and Kivshar, Y.S. Fano resonances in nanoscale structures. *Reviews of Modern Physics*, **82**(3):2257, (2010).

[274] Limonov, M.F., Rybin, M.V., Poddubny, A.N., and Kivshar, Y.S. Fano resonances in photonics. *Nature Photonics*, **11**(9):543–554, (2017).

[275] Bernhardt, N., Koshelev, K., White, S.J., Meng, K.W.C., Froch, J.E., Kim, S., Tran, T.T., Choi, D.Y., Kivshar, Y., and Solntsev, A.S. Quasi-BIC resonant enhancement of second-harmonic generation in WS_2 monolayers. *Nano Letters*, **20**(7):5309–5314, (2020).

[276] Tran, K., Moody, G., Wu, F., Lu, X., Choi, J., Kim, K., Rai, A., Sanchez, D.A., Quan, J., Singh, A., *et al.* Evidence for moiré excitons in van der Waals heterostructures. *Nature*, **567** (7746):71–75, (2019).

[277] Huang, D., Choi, J., Shih, C.K., and Li, X. Excitons in semiconductor moiré superlattices. *Nature Nanotechnology*, **17**(3):227–238, (2022).

[278] Grinblat, G., Li, Y., Nielsen, M.P., Oulton, R.F., and Maier, S.A. Efficient third harmonic generation and nonlinear subwavelength imaging at a higher-order anapole mode in a single germanium nanodisk. *ACS Nano*, **11**(1):953–960, (2017).

[279] Liu, T., Xu, R., Yu, P., Wang, Z., and Takahara, J. Multipole and multimode engineering in Mie resonance-based metastructures. *Nanophotonics*, **9**(5):1115–1137, (2020).

[280] Fano, U., Pupillo, G., Zannoni, A., and Clark, C.W. On the absorption spectrum of noble gases at the arc spectrum limit. *Journal of Research of the National Institute of Standards and Technology*, **110**(6):583, (2005).

[281] Bordo, V. Model of Fabry-Pérot-type electromagnetic modes of a cylindrical nanowire. *Physical Review B*, **81**(3):035420, (2010).

[282] Landreman, P.E., Chalabi, H., Park, J., and Brongersma, M.L. Fabry-Perot description for Mie resonances of rectangular dielectric nanowire optical resonators. *Optics Express*, **24** (26):29760–29772, (2016).

[283] Abujetas, D.R., Mandujano, M.A., Méndez, E.R., and Sánchez-Gil, J.A. High-contrast Fano resonances in single semiconductor nanorods. *ACS Photonics*, **4**(7):1814–1821, (2017).

[284] Friedler, I., Sauvan, C., Hugonin, J.P., Lalanne, P., Claudon, J., and Gérard, J.M. Solid-state single photon sources: the nanowire antenna. *Optics Express*, **17**(4):2095–2110, (2009).

[285] Sun, L., Ren, M.L., Liu, W., and Agarwal, R. Resolving parity and order of Fabry–Pérot modes in semiconductor nanostructure waveguides and lasers: Young's interference experiment revisited. *Nano Letters*, **14**(11):6564–6571, (2014).

[286] Frolov, A.Y., Verellen, N., Li, J., Zheng, X., Paddubrouskaya, H., Denkova, D., Shcherbakov, M.R., Vandenbosch, G.A.E., Panov, V.I., Van Dorpe, P., Fedyanin, A.A., and Moshchalkov, V.V. Near-field mapping of optical Fabry–Perot modes in all-dielectric nanoantennas. *Nano Letters*, **17**(12):7629–7637, (2017).

[287] Gromyko, D.A., Dyakov, S.A., Gippius, N.A., Weiss, T., Tikhodeev, S.G., Astrakhantseva, A.S., Fedotova, Y.V., Solovyev, V.V., and Kukushkin, I.V. Strong local field enhancement of Raman scattering observed in metal-dielectric gratings due to vertical Fabry-Perot modes of surface plasmon polaritons. *Physical Review Applied*, **17**(2):024015, (2022).

[288] Liu, W., Tang, Y., Liu, Z., Li, J., Cheng, Y., and Liu, G. Realizing anapole-FP cavity strong coupling in a silicon-based metasurface hybrid system. *IEEE Photonics Journal*, **15**(6):1–5, (2023).

[289] Huang, L., Xu, L., Rahmani, M., Neshev, D., and Miroshnichenko, A.E. Pushing the limit of high-q mode of a single dielectric nanocavity. *Advanced Photonics*, **3**(1):016004–016004, (2021).

[290] Koshelev, K., Favraud, G., Bogdanov, A., Kivshar, Y., and Fratalocchi, A. Nonradiating photonics with resonant dielectric nanostructures. *Nanophotonics*, **8**(5):725–745, (2019).

[291] Gladyshev, S., Frizyuk, K., and Bogdanov, A. Symmetry analysis and multipole classification of eigenmodes in electromagnetic resonators for engineering their optical properties. *Physical Review B*, **102**(7):075103, (2020).

[292] Odit, M., Koshelev, K., Gladyshev, S., Ladutenko, K., Kivshar, Y., and Bogdanov, A. Observation of supercavity modes in subwavelength dielectric resonators. *Advanced Materials*, **33**(1):2003804, (2021).

[293] Nguyen, D.C., Kim, M., Hussain, M., Akhtar, I., Naqvi, B.A., Shehzad, M.A., Jung, J., Seo, Y., *et al.* Visibility of hexagonal boron nitride on transparent substrates. *Nanotechnology*, **31**(19):195701, (2020).

[294] Gorbachev, R.V., Riaz, I., Nair, R.R., Jalil, R., Britnell, L., Belle, B.D., Hill, E.W., Novoselov, K.S., Watanabe, K., Taniguchi, T., *et al.* Hunting for monolayer boron nitride: optical and Raman signatures. *Small*, **7**(4):465–468, (2011).

[295] Tran, T.T., Elbadawi, C., Totonjian, D., Lobo, C.J., Grosso, G., Moon, H., Englund, D.R., Ford, M.J., Aharonovich, I., and Toth, M. Robust multicolor single photon emission from point defects in hexagonal boron nitride. *ACS Nano*, **10**(8):7331–7338, (2016).

[296] Jungwirth, N.R., Calderon, B., Ji, Y., Spencer, M.G., Flatté, M.E., and Fuchs, G.D. Temperature dependence of wavelength selectable zero-phonon emission from single defects in hexagonal boron nitride. *Nano Letters*, **16**(10):6052–6057, (2016).

[297] Castelletto, S., Inam, F.A., Sato, S.i., and Boretti, A. Hexagonal boron nitride: a review of the emerging material platform for single-photon sources and the spin–photon interface. *Beilstein Journal of Nanotechnology*, **11**(1):740–769, (2020).

[298] Sajid, A., Ford, M.J., and Reimers, J.R. Single-photon emitters in hexagonal boron nitride: a review of progress. *Reports on Progress in Physics*, **83**(4):044501, (2020).

[299] Louca, C., Genco, A., Chiavazzo, S., Lyons, T.P., Randerson, S., Trovatello, C., Claronino, P., Jayaprakash, R., Hu, X., Howarth, J., *et al.* Interspecies exciton interactions lead to enhanced nonlinearity of dipolar excitons and polaritons in MoS_2 homobilayers. *Nature Communications*, **14**(1):3818, (2023).

[300] Kumar, S., Brotóns-Gisbert, M., Al-Khuzheyri, R., Branny, A., Ballesteros-Garcia, G., Sánchez-Royo, J.F., and Gerardot, B.D. Resonant laser spectroscopy of localized excitons in monolayer WSe_2. *Optica*, **3**(8):882–886, (2016).

[301] Srivastava, A., Sidler, M., Allain, A.V., Lembke, D.S., Kis, A., and Imamoğlu, A. Optically active quantum dots in monolayer WSe_2. *Nature Nanotechnology*, **10**(6):491–496, (2015).

[302] Koperski, M., Nogajewski, K., Arora, A., Cherkez, V., Mallet, P., Veuillen, J.Y., Marcus, J., Kossacki, P., and Potemski, M. Single photon emitters in exfoliated WSe_2 structures. *Nature Nanotechnology*, **10**(6):503–506, (2015).

[303] Kumar, S., Kaczmarczyk, A., and Gerardot, B.D. Strain-induced spatial and spectral isolation of quantum emitters in mono-and bilayer WSe_2. *Nano Letters*, **15**(11):7567–7573, (2015).

[304] Luo, Y., Shepard, G.D., Ardelean, J.V., Rhodes, D.A., Kim, B., Barmak, K., Hone, J.C., and Strauf, S. Deterministic coupling of site-controlled quantum emitters in monolayer WSe_2 to plasmonic nanocavities. *Nature Nanotechnology*, **13**(12):1137–1142, (2018).

[305] Blauth, M., Jürgensen, M., Vest, G., Hartwig, O., Prechtl, M., Cerne, J., Finley, J.J., and Kaniber, M. Coupling single photons from discrete quantum emitters in WSe_2 to lithographically defined plasmonic slot waveguides. *Nano Letters*, **18**(11):6812–6819, (2018).

[306] Tripathi, L.N., Iff, O., Betzold, S., Dusanowski, Ł., Emmerling, M., Moon, K., Lee, Y.J., Kwon, S.H., Höfling, S., and Schneider, C. Spontaneous emission enhancement in strain-induced WSe_2 monolayer-based quantum light sources on metallic surfaces. *ACS Photonics*, **5**(5):1919–1926, (2018).

[307] He, Y.M., Clark, G., Schaibley, J.R., He, Y., Chen, M.C., Wei, Y.J., Ding, X., Zhang, Q., Yao, W., Xu, X., *et al.* Single quantum emitters in monolayer semiconductors. *Nature Nanotechnology*, **10**(6):497–502, (2015).

[308] Tonndorf, P., Schmidt, R., Schneider, R., Kern, J., Buscema, M., Steele, G.A., Castellanos-Gomez, A., van der Zant, H.S., de Vasconcellos, S.M., and Bratschitsch, R. Single-photon emission from localized excitons in an atomically thin semiconductor. *Optica*, **2**(4):347–352, (2015).

[309] Palacios-Berraquero, C., Kara, D.M., Montblanch, A.R.P., Barbone, M., Latawiec, P., Yoon, D., Ott, A.K., Loncar, M., Ferrari, A.C., and Atatüre, M. Large-scale quantum-emitter arrays in atomically thin semiconductors. *Nature Communications*, **8**(1):1–6, (2017).

[310] Branny, A., Kumar, S., Proux, R., and Gerardot, B.D. Deterministic strain-induced arrays of quantum emitters in a two-dimensional semiconductor. *Nature Communications*, **8**(1): 1–7, (2017).

[311] Hong, X., Kim, J., Shi, S.F., Zhang, Y., Jin, C., Sun, Y., Tongay, S., Wu, J., Zhang, Y., and Wang, F. Ultrafast charge transfer in atomically thin MoS_2/WS_2 heterostructures. *Nature Nanotechnology*, **9**(9):682–686, (2014).

[312] Chen, H., Wen, X., Zhang, J., Wu, T., Gong, Y., Zhang, X., Yuan, J., Yi, C., Lou, J., Ajayan, P.M., *et al.* Ultrafast formation of interlayer hot excitons in atomically thin MoS_2/WS_2 heterostructures. *Nature Communications*, **7**(1):1–8, (2016).

[313] Miller, B., Steinhoff, A., Pano, B., Klein, J., Jahnke, F., Holleitner, A., and Wurstbauer, U. Long-lived direct and indirect interlayer excitons in van der Waals heterostructures. *Nano Letters*, **17**(9):5229–5237, (2017).

[314] Kunstmann, J., Mooshammer, F., Nagler, P., Chaves, A., Stein, F., Paradiso, N., Plechinger, G., Strunk, C., Schüller, C., Seifert, G., *et al.* Momentum-space indirect interlayer excitons in transition-metal dichalcogenide van der Waals heterostructures. *Nature Physics*, **14**(8): 801–805, (2018).

[315] Merkl, P., Mooshammer, F., Steinleitner, P., Girnghuber, A., Lin, K.Q., Nagler, P., Holler, J., Schüller, C., Lupton, J.M., Korn, T., *et al.* Ultrafast transition between exciton phases in van der Waals heterostructures. *Nature Materials*, **18**(7):691–696, (2019).

[316] Kamban, H.C. and Pedersen, T.G. Interlayer excitons in van der Waals heterostructures: binding energy, stark shift, and field-induced dissociation. *Scientific Reports*, **10**(1):1–10, (2020).

[317] Rayleigh, L. XVII. On the maintenance of vibrations by forces of double frequency, and on the propagation of waves through a medium endowed with a periodic structure. *The London, Edinburgh, and Dublin Philosophical Magazine and Journal of Science*, **24**(147):145–159, (1887).

[318] Van der Ziel, J. and Ilegems, M. Multilayer GaAs-Al 0.3 Ga 0.7 As dielectric quarter wave stacks grown by molecular beam epitaxy. *Applied Optics*, **14**(11):2627–2630, (1975).

[319] Orsini, L., Herzig Sheinfux, H., Li, Y., Lee, S., Andolina, G.M., Scarlatella, O., Ceccanti, M., Soundarapandian, K., Janzen, E., Edgar, J.H., *et al.* Deep subwavelength topological edge state in a hyperbolic medium. *Nature Nanotechnology*, **19**(10):1485–1490, (2024).

[320] Choi, Y.S., Lee, K.Y., An, S.C., Jang, M., Kim, Y., Yoon, S., Shin, S.H., and Yoon, J.W. Topological beaming of light: proof-of-concept experiment. *Light: Science & Applications*, **14**(1):121, (2025).

[321] Bouteyre, P., Hu, X., Randerson, S.A., Zotev, P.G., Wang, Y., and Tartakovskii, A.I. Simultaneous observation of bright and dark polariton states in subwavelength gratings made from quasi-bulk WS2. *Optics Express*, **33**(10):21173–21182, (2025).

[322] Huang, L., Jin, R., Zhou, C., Li, G., Xu, L., Overvig, A., Deng, F., Chen, X., Lu, W., Alù, A., *et al.* Ultrahigh-q guided mode resonances in an all-dielectric metasurface. *Nature Communications*, **14**(1):3433, (2023).

[323] Khonina, S., Kazanskiy, N., and Butt, M.A. Spectral characteristics of broad band-rejection filter based on bragg grating, one-dimensional photonic crystal, and subwavelength grating waveguide. *Physica Scripta*, **96**(5):055505, (2021).

[324] Chang-Hasnain, C.J. and Yang, W. High-contrast gratings for integrated optoelectronics. *Advances in Optics and Photonics*, **4**(3):379–440, (2012).

[325] Lu, L., Le-Van, Q., Ferrier, L., Drouard, E., Seassal, C., and Nguyen, H.S. Engineering a light–matter strong coupling regime in perovskite-based plasmonic metasurface: quasi-bound state in the continuum and exceptional points. *Photonics Research*, **8**(12):A91–A100, (2020).

[326] Grann, E.B., Moharam, M., and Pommet, D.A. Artificial uniaxial and biaxial dielectrics with use of two-dimensional subwavelength binary gratings. *Journal of the Optical Society of America A*, **11**(10):2695–2703, (1994).

[327] Orfanidis, S.J. *Electromagnetic Waves and Antennas*. Rutgers University New Brunswick, New Jersey, (2002).

[328] Patnaik, S., InteredgeDistance macro for ImageJ, (2020). URL https://sourceforge.net/projects/interedgedistance. [Accessed on: 2024-12-12].

[329] Heisenberg, W. Über den anschaulichen Inhalt der quantentheoretischen Kinematik und Mechanik. *Zeitschrift für Physik*, **43**(3):172–198, (1927).

[330] Abbe, E. Beiträge zur Theorie des Mikroskops und der mikroskopischen Wahrnehmung. *Archiv für Mikroskopische Anatomie*, **9**(1):413–468, (1873).

[331] Abbe, E. XV. The relation of aperture and power in the microscope (continued). *Journal of the Royal Microscopical Society*, **2**(4):460–473, (1882).

[332] Synge, E. XXXVIII. A suggested method for extending microscopic resolution into the ultra-microscopic region. *The London, Edinburgh, and Dublin Philosophical Magazine and Journal of Science*, **6**(35):356–362, (1928).

[333] Synge, E. XXIII. An application of piezo-electricity to microscopy. *The London, Edinburgh, and Dublin Philosophical Magazine and Journal of Science*, **13**(83):297–300, (1932).

[334] Ash, E. and Nicholls, G. Super-resolution aperture scanning microscope. *Nature*, **237**(5357):510–512, (1972).

[335] Pohl, D.W., Denk, W., and Lanz, M. Optical stethoscopy: image recording with resolution $\lambda/20$. *Applied Physics Letters*, **44**(7):651–653, (1984).

[336] Vincent, T., Liu, X., Johnson, D., Mester, L., Huang, N., Kazakova, O., Hillenbrand, R., and Boland, J.L. snompy: a package for modelling scattering-type scanning near-field optical microscopy. *arXiv preprint, arXiv:2405.20948*, (2024).

[337] Govyadinov, A.A., Amenabar, I., Huth, F., Carney, P.S., and Hillenbrand, R. Quantitative measurement of local infrared absorption and dielectric function with tip-enhanced near-field microscopy. *The Journal of Physical Chemistry Letters*, **4**(9):1526–1531, (2013).

[338] Tranca, D.E., Stanciu, S.G., Hristu, R., Witgen, B.M., and Stanciu, G.A. Nanoscale mapping of refractive index by using scattering-type scanning near-field optical microscopy. *Nanomedicine: Nanotechnology, Biology and Medicine*, **14**(1):47–50, (2018).

[339] Chen, X., Hu, D., Mescall, R., You, G., Basov, D., Dai, Q., and Liu, M. Modern scattering-type scanning near-field optical microscopy for advanced material research. *Advanced Materials*, **31**(24):1804774, (2019).

[340] Dai, S., Fei, Z., Ma, Q., Rodin, A., Wagner, M., McLeod, A., Liu, M., Gannett, W., Regan, W., Watanabe, K., *et al.* Tunable phonon polaritons in atomically thin van der Waals crystals of boron nitride. *Science*, **343**(6175):1125–1129, (2014).

[341] Kim, K.S., Trajanoski, D., Ho, K., Gilburd, L., Maiti, A., van der Velden, L., de Beer, S., and Walker, G.C. The effect of adjacent materials on the propagation of phonon polaritons in hexagonal boron nitride. *The Journal of Physical Chemistry Letters*, **8**(13):2902–2908, (2017).

[342] Dai, S., Fang, W., Rivera, N., Stehle, Y., Jiang, B.Y., Shen, J., Tay, R.Y., Ciccarino, C.J., Ma, Q., Rodan-Legrain, D., *et al.* Phonon polaritons in monolayers of hexagonal boron nitride. *Advanced Materials*, **31**(37):1806603, (2019).

[343] Ramer, G., Tuteja, M., Matson, J.R., Davanco, M., Folland, T.G., Kretinin, A., Taniguchi, T., Watanabe, K., Novoselov, K.S., Caldwell, J.D., *et al.* High-q dark hyperbolic phonon-polaritons in hexagonal boron nitride nanostructures. *Nanophotonics*, **9**(6):1457–1467, (2020).

[344] Chen, J., Badioli, M., Alonso-González, P., Thongrattanasiri, S., Huth, F., Osmond, J., Spasenović, M., Centeno, A., Pesquera, A., Godignon, P., *et al.* Optical nano-imaging of gate-tunable graphene plasmons. *Nature*, **487**(7405):77–81, (2012).

[345] Fei, Z., Rodin, A., Andreev, G.O., Bao, W., McLeod, A., Wagner, M., Zhang, L., Zhao, Z., Thiemens, M., Dominguez, G., *et al.* Gate-tuning of graphene plasmons revealed by infrared nano-imaging. *Nature*, **487**(7405):82–85, (2012).

[346] Gerber, J.A., Berweger, S., O'Callahan, B.T., and Raschke, M.B. Phase-resolved surface plasmon interferometry of graphene. *Physical Review Letters*, **113**(5):055502, (2014).

[347] Woessner, A., Lundeberg, M.B., Gao, Y., Principi, A., Alonso-González, P., Carrega, M., Watanabe, K., Taniguchi, T., Vignale, G., Polini, M., *et al.* Highly confined low-loss plasmons in graphene–boron nitride heterostructures. *Nature Materials*, **14**(4):421–425, (2015).

[348] Schnell, M., Garcia-Etxarri, A., Huber, A.J., Crozier, K.B., Borisov, A., Aizpurua, J., and Hillenbrand, R. Amplitude-and phase-resolved near-field mapping of infrared antenna modes by transmission-mode scattering-type near-field microscopy. *The Journal of Physical Chemistry C*, **114**(16):7341–7345, (2010).

[349] Alonso-Gonzalez, P., Schnell, M., Sarriugarte, P., Sobhani, H., Wu, C., Arju, N., Khanikaev, A., Golmar, F., Albella, P., Arzubiaga, L., *et al.* Real-space mapping of Fano interference in plasmonic metamolecules. *Nano Letters*, **11**(9):3922–3926, (2011).

[350] Schnell, M., Sarriugarte, P., Neuman, T., Khanikaev, A., Shvets, G., Aizpurua, J., and Hillenbrand, R. Real-space mapping of the chiral near-field distributions in spiral antennas and planar metasurfaces. *Nano Letters*, **16**(1):663–670, (2016).

[351] Li, Y., Zhou, N., Kinzel, E.C., Ren, X., and Xu, X. The origin of interferometric effect involving surface plasmon polariton in scattering near-field scanning optical microscopy. *Optics Express*, **22**(3):2965–2972, (2014).

[352] Walla, F., Wiecha, M.M., Mecklenbeck, N., Beldi, S., Keilmann, F., Thomson, M.D., and Roskos, H.G. Anisotropic excitation of surface plasmon polaritons on a metal film by a scattering-type scanning near-field microscope with a non-rotationally-symmetric probe tip. *Nanophotonics*, **7**(1):269–276, (2018).

[353] Klick, A., de la Cruz, S., Lemke, C., Großmann, M., Beyer, H., Fiutowski, J., Rubahn, H.G., Mendez, E.R., and Bauer, M. Amplitude and phase of surface plasmon polaritons excited at a step edge. *Applied Physics B*, **122**:1–8, (2016).

[354] Bozhevolnyi, S.I. Near-field mapping of surface polariton fields. *Journal of Microscopy*, **202**(2):313–319, (2001).

[355] Zhang, C., Hugonin, J.P., Greffet, J.J., and Sauvan, C. Surface plasmon polaritons emission with nanopatch antennas: enhancement by means of mode hybridization. *ACS Photonics*, **6** (11):2788–2796, (2019).

[356] Kaltenecker, K.J., Krauss, E., Casses, L., Geisler, M., Hecht, B., Mortensen, N.A., Jepsen, P.U., and Stenger, N. Mono-crystalline gold platelets: a high-quality platform for surface plasmon polaritons. *Nanophotonics*, **9**(2):509–522, (2020).

[357] Novotny, L. and Hecht, B. *Principles of Nano-Optics*. Cambridge University Press, Cambridge, (2012).

[358] Jang, M., Menabde, S.G., Kiani, F., Heiden, J.T., Zenin, V.A., Asger Mortensen, N., Tagliabue, G., and Jang, M.S. Fourier analysis of near-field patterns generated by propagating polaritons. *Physical Review Applied*, **22**(1):014076, (2024).

[359] Morozov, K., Gubaydullin, A., and Kaliteevski, M. Properties of a Tamm plasmon structure with a subwavelength ring-shaped structuration. In *Journal of Physics: Conference Series*, volume 1199, page 012035. IOP Publishing, (2019).

[360] Chung, H., Zhang, F., Li, H., Miller, O.D., and Smith, H.I. Inverse design of high-NA metalens for maskless lithography. *Nanophotonics*, **12**(13):2371–2381, (2023).

[361] Huang, L., Chen, X., Mühlenbernd, H., Zhang, H., Chen, S., Bai, B., Tan, Q., Jin, G., Cheah, K.W., Qiu, C.W., *et al.* Three-dimensional optical holography using a plasmonic metasurface. *Nature Communications*, **4**(1):2808, (2013).

[362] Scheuer, J. Metasurfaces-based holography and beam shaping: engineering the phase profile of light. *Nanophotonics*, **6**(1):137–152, (2017).

[363] Wan, W., Gao, J., and Yang, X. Metasurface holograms for holographic imaging. *Advanced Optical Materials*, **5**(21):1700541, (2017).

[364] Jiang, Q., Cao, L., Huang, L., He, Z., and Jin, G. A complex-amplitude hologram using an ultra-thin dielectric metasurface. *Nanoscale*, **12**(47):24162–24168, (2020).

[365] Jiang, Q., Hu, L., Geng, G., Li, J., Wang, Y., and Huang, L. Arbitrary amplitude and phase control in visible by dielectric metasurface. *Optics Express*, **30**(8):13530–13539, (2022).

[366] Tang, F., Wu, J., Albrow-Owen, T., Cui, H., Chen, F., Shi, Y., Zou, L., Chen, J., Guo, X., Sun, Y., *et al.* Metasurface spectrometers beyond resolution-sensitivity constraints. *Science Advances*, **10**(49):eadr7155, (2024).

[367] Azzam, S.I., Chaudhuri, K., Lagutchev, A., Jacob, Z., Kim, Y.L., Shalaev, V.M., Boltasseva, A., and Kildishev, A.V. Single and multi-mode directional lasing from arrays of dielectric nanoresonators. *Laser & Photonics Reviews*, **15**(3):2000411, (2021).

[368] Paniagua-Dominguez, R., Ha, S.T., and Kuznetsov, A.I. Active and tunable nanophotonics with dielectric nanoantennas. *Proceedings of the IEEE*, **108**(5):749–771, (2019).

[369] Leykam, D. and Flach, S. Perspective: photonic flatbands. *APL Photonics*, **3**(7):070901, (2018).

[370] Du, L., Molas, M.R., Huang, Z., Zhang, G., Wang, F., and Sun, Z. Moiré photonics and optoelectronics. *Science*, **379**(6639):eadg0014, (2023).

[371] Nguyen, D.X., Letartre, X., Drouard, E., Viktorovitch, P., Nguyen, H.C., and Nguyen, H.S. Magic configurations in moiré superlattice of bilayer photonic crystals: almost-perfect flatbands and unconventional localization. *Physical Review Research*, **4**(3):L032031, (2022).

[372] Baba, T. Slow light in photonic crystals. *Nature Photonics*, **2**(8):465–473, (2008).

[373] Tang, Y., Qin, H., de Ceglia, D., Yang, W., Shameli, M.A., Nauman, M., Morales, R.C., Yan, J., Wang, C., Qiu, S., *et al.* Giant second harmonic generation from 3R-MoS_2 metasurfaces. *arXiv preprint, arXiv:2503.20161*, (2025).